Matthew Thomas Harris

The Study and Replication of Plant Surfaces

Department of Chemistry
Durham University

2018

Declaration

The work undertaken and described in this thesis was undertaken at Durham University Chemistry Department between September 2014 and December 2017. It is the original work of the author except where otherwise stated or acknowledged and has not been submitted for a degree in this, or any other university.

Statement of Copyright

Acknowledgements

Many thanks to the following: Professor Jas Pal Badyal for three years of supervision; the many members of Lab 98 – Angus, Andrea, Sam, Isaias, Hannah, Matt, Rowan, and Bekah – for their ideas, help, support, and secret santa gifts; the members of Newcastle University – Ian Fletcher and Tracey Davey – for all their hard work in analysing the plant surfaces; the catering staff at the university – Wendy, Karen, Emma – who served me the many, many coffees required to make it through my studies; to Annette and Irene for always being there for a chat; and Kate Madden for purchasing Bic's entire supply of purple pen to make this thesis readable.

List of Publications

Collaborative Publications

1. von Spreckelsen, R. M.; Harris, M. T.; Wigzell, J. M.; Fraser, R. C.; Carletto, A.; Mosquin, D. P. K.; Justice, D.; Badyal, J. P. S. Bioinspired Breathable Architecture for Water Harvesting. *Sci. Rep.* **2015**, *5*, 16798.
2. Badyal, J. P. S. von Spreckelsen, R. Harris, M. T. Liquid Movement and/or Collection Apparatus and Method. WO 2016185222 A1. **2016**.
3. Wigzell, J. M.; Racovita, R. C.; Stentiford, B. G.; Wilson, M.; Harris, M. T.; Fletcher, I. W.; Mosquin, D. P. K.; Justice, D.; Beaumont, S. K.; Jetter, R.; Badyal, J. P. S. Smart Water Channelling Through Dual Wettability by Leaves of the Bamboo *Phyllostachys Aurea*. *Colloids and Surfaces A: Physiochemical and Engineering Aspects*. **2016**, *505*, 344–355.
4. Gürsoy, M.; Harris, M. T.; Carletto, A.; Yaprak, A. E.; Karaman, M.; Badyal, J. P. S. Bioinspired Asymmetric-Anisotropic (Directional) Fog Harvesting Based on the Arid Climate Plant Eremopyrum Orientale. *Colloids and Surfaces A.*, **2017**, *529*, 959–965.
5. Gürsoy, M.; Harris, M. T.; Downing, J. O.; Barrientos-Palomo, S. N.; Carletto, A.; Yaprak, A. E.; Karaman, M.; Badyal, J. P. S. Bioinspired Fog Capture and Channel Mechanism Based on the Arid Climate Plant *Salsola crassa*. *Colloids and Surfaces A.*, **2017**, *529*, 195–202.

Abstract

The analysis and replication of surfaces which mimic the behaviour of plants is of importance as it can have a variety of applications. These applications, such as the collection of fog for drinking water, waterproof electronics, and antibiofouling devices have the potential to improve the day to day lives of millions of people. In this thesis the surfaces of multiple plants were analysed and replicated using a variety of techniques to better understand and replicate their wetting mechanisms. Also developed were a range of new analysis and replication techniques which have many potential applications in future projects.

The wetting mechanism and surface of *Xanthosoma sagittifolium* was investigated through the use of analytical techniques such as scanning electron microscopy and time of flight secondary ion mass spectrometry, before being replicated using a nanoimprinting process. This led to the successful production, and testing, of replicas of the leaves of *Xanthosoma sagittifolium*.

These techniques were also employed to aid in the analysis of other plant surfaces, such as that of *Eremopyrum orientale* and *Phyllostachys aurea*, and led to the development of a new technique by which plant surfaces could be analysed using time of flight secondary ion mass spectrometry without the need for a live specimen. Also developed was a new replication method employing 3D printing to replicate the surfaces of *Phyllostachys aurea*. The development of these techniques should prove useful in future analysis and replication of plant surfaces, particularly in countries where resources are limited, or where the plant of interest is in an isolated location.

Contents

Chapter 1 Introduction

1.1 The Utility of Plant Surfaces

The study of plant surfaces has led to the discovery of a range of unique surface properties. Included in these properties are superhydrophobicity, as observed in the lotus leaf (*Nelumbo nucifera*),[1] superhydrophilicity by tropical pitcher plants (*Nepenthes*),[2] fog collection by *Cotulla fallax*,[3] and water channeling by the red cedar tree (*Thuja plicata*).[4] By understanding and replicating these plant surfaces, a range of practical applications can be applied such as, but not limited to, fog collection/harvesting, self-cleaning surfaces, water resistant electronic devices, and anti-biofouling devices.

In order to apply the lessons learnt from studying plant surfaces, the basics of wettability and plants needs to be understood. The following review will focus on those surfaces and the chemistry surrounding them, as well as the analytical techniques and methods used to analyse and replicate the surfaces. It will also explore current replication techniques used to create these types of plant surfaces.

1.2 Plant Surfaces

Leaf surfaces consist of inner cell tissue (the mesophyll) encased by epidermii. Often there is a thin layer of wax that is embedded in the cell cutin where the epidermii is exposed to the atmosphere. This wax, termed the cuticle, is present on both sides of the leaf with the upper epidermus and cuticle referred to as the adaxial surface and the lower epidermus and cuticle termed the abaxial surface (**Figure 1**).[5]

The cuticle serves a number of purposes – it protects the underlying plant cells from mechanical damage, acts as a barrier against microbial attack, and protects the underlying cells from ultraviolet radiation damage.[6] The cuticle's primary function is to regulate the water and gas flow between the plant cells and the surrounding atmosphere. This regulation can cause interesting properties to be displayed on the leaf surface, particularly when considering the interaction with water.[7,8,9]

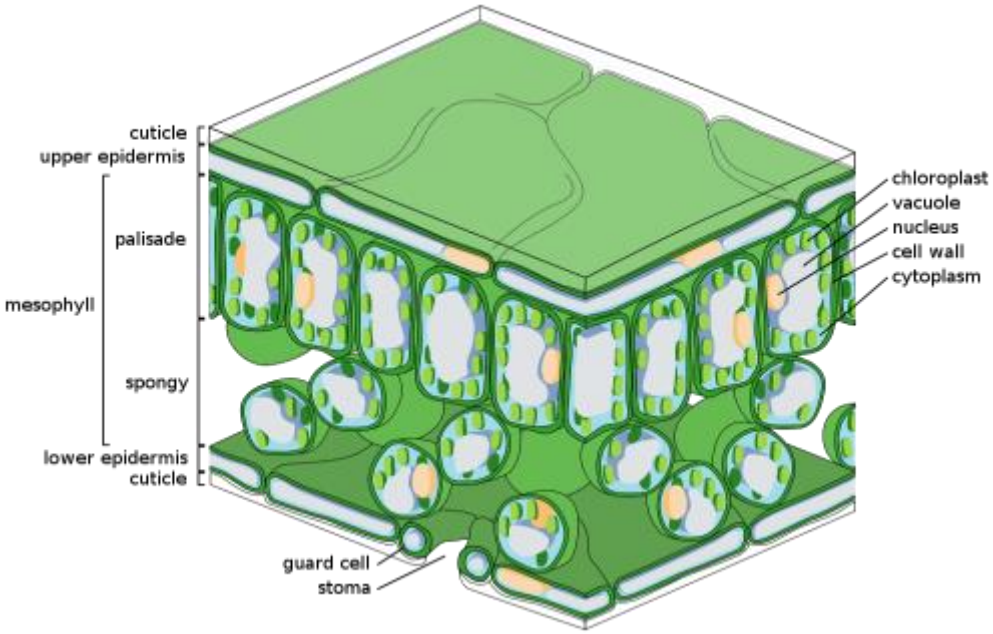

Figure 1: The internal structure of a generic leaf, taken from wikimedia commons[10]

In addition to the cuticle, there is often an additional layer of wax that lies upon its surface secreted by cells in the epidermis.[11] This additional layer of wax, the epicuticular wax, adds additional surface properties to the leaf surface (**Figure 2**). These surface properties can mimic those of the cuticle or drastically alter them, leading to different behaviours depending upon the prescence of the waxes. The ability of the waxes to crystallise into a variety and range of structures, combined with their chemical composition, contribute to the surface properties displayed.[11] The surface chemistry and surface macro and nano structure is therefore altered which alters the surface properties displayed by the leaf.

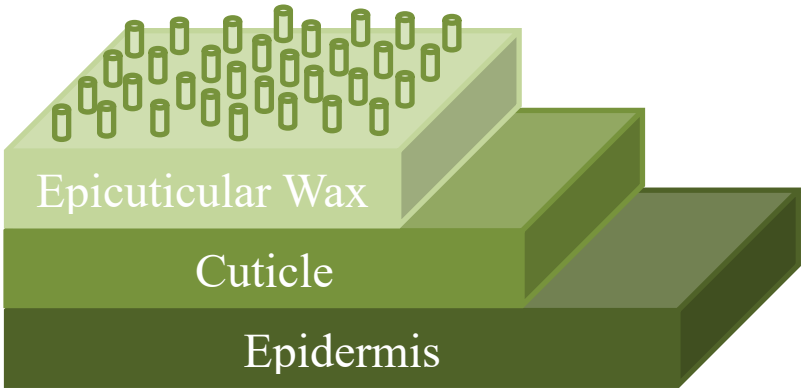

Figure 2: Display showing the three top three layers of the leaf, with cylinders used to represent the epictuticular wax crystals

1.2.1 Epidermis Structure

The overall shape of the epidermis is governed by individual cell structures and their interactions with their neighbouring cells;[12] these interactions govern the cell shape and constitute the bulk of the epidermis structure.

The boundary where two cells meet is termed the anticlinal wall, with the outer cell surface termed the periclinal wall. The interactions at the cell boundary result in two basic types of cell structure – tetragonal and polygonal. A tetragonal cell has four cell boundaries and a polygonal cell has more than four boundaries. Variations in the length, size, and shape of the anticlinal wall boundaries leads to variations in cell structures.[13,14]

Variations at the anticlinal wall boundary can lead to a wide variety of structures which display increased surface roughness and include troughs and peaks as well as non-uniform undulations. Differing anticlinal cell boundary lengths can also lead to different cell shapes, such as elongated cells, where two parallel anticlinal walls are sufficiently longer than the other boundaries. This creates cells that are rectangular in shape.[15]

The central part of the cell, the central field, has a shape determined by the periclinal wall with three main cell curvatures displayed by the central field; flat, convex, and, concave. The central field is one of the main drivers of the overall leaf surface macrostructure, with variations in the three types of cell curvatures leading to a range of cell shapes; a convex outgrowth for example can form papilla or hairs, such as those common found in flower leaves.[16]

1.2.2 Chemical Composition of Plant Waxes

The surface waxes are composed of a variety of different chemical compounds that can be either hydrophilic or hydrophobic in nature. A large majority of plants present hydrophobic waxes on their surface, particularly on the abaxial surface in order to improve photosynthesis efficiency.[17]

The chemical compounds that are present in the surface waxes consist of very-long-chain (VLC) molecules.[18] VLCs are chains with more than eighteen carbon atoms in the backbone and can contain a variety of different functional groups including but not limited to; fatty-acids, aldehydes, ketones, alcohols, and esters (Table 1).[18,19]

Table 1: The generic chemical structure of a variety of of plant waxes

Molecule	Chemical structure
Alcohol	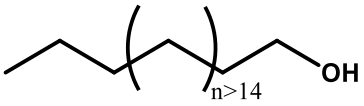
Aldehyde	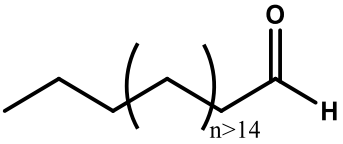
Ester	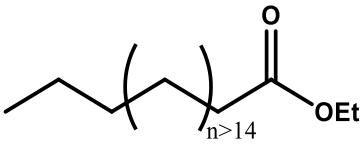
Fatty acid	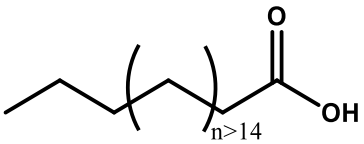
Flavonoid	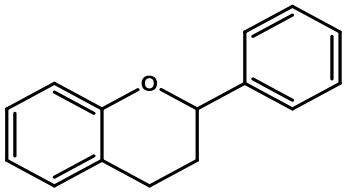
Ketone	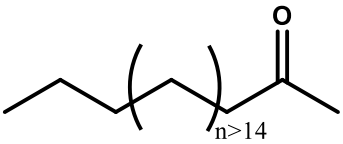
Sterol	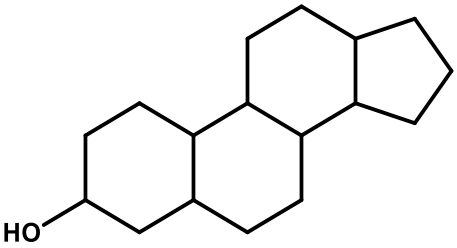
Triterpene	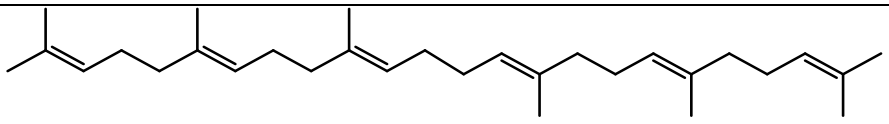

The distribution of these compounds across the surface of a leaf can vary depending on the plant species, within sub species, and within different local environments where the different distribution of the chemical compounds can cause

unique wetting behaviour on different regions of the plant.[20] The exact purpose of this variable wetting behaviour remains unclear.

More clear, is how the chemical composition of the waxes can vary depending upon the environmental conditions the plant is under, with one example of such behaviour seen during periods of water stress.[21] In this case the backbone chain length of the wax increases making the waxes more hydrophobic and serving to reduce water loss in the plant.[21] A second such example involves a change in the functional groups present in the waxes, exchanging alcohol and ketone functional groups for straight chain aliphatic waxes, ultimately serving the same purpose of reducing water loss during periods of water stress.[22]

The epicuticular waxes can crystallise into a range of different structures that can be both two dimensional and three dimensional due to the inherent ability of the waxes to self-assemble; the size of the self-assembled structures can range from 0.5–100 μm and come in a wide variety of different morphologies, the most commonly occuring morphologies are platelets, rodlets, threads, tubules, and granules.[23,24,25,26]

In order to understand how the surface waxes, and the underlying cell structures will affect the leaf interaction with water, the theory behind surface wettability needs to be understood.

1.3 Surface Wettability

With reference to plants and leaf surfaces, wettability is a term often used to describe the interactions between water and the plant or leaf surface.[27] The droplet behaviour is governed by the energy of interaction between the droplet and the surface. More specifically this refers to the three interfacial surfaces observed when the droplet is in contact with the surface.[27] These are the liquid-air interface (γ_{LA}), the liquid-solid interface (γ_{SL}), and the solid-air interface (γ_{SA}) (**Figure 3**).[27,28,29]

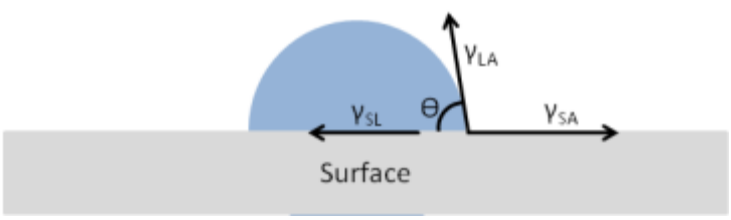

Figure 3: The three surface interfaces observed for a droplet in contact with a surface

When a droplet is placed upon the surface, it will bead, wet, or remain unchanged depending upon the observed equilibrium between the energy of the three interfacial surfaces. This leads to a contact angle, Θ, between the droplet and the surface (**Equation 1**).[27]

$$Cos\,\theta = \frac{(\gamma_{sa} - \gamma_{sl})}{\gamma_{la}} \qquad \textbf{(1)}$$

The wetting process therefore proceeds via a free energy change and is a thermodynamic process. The droplet will alter in shape until an equilibrium is reached between the relative free energies of the three interfaces.[30] Should the solid-liquid interface have the lowest free energy, the droplet will spread out across the surface in order to maximise that interaction and the free energy change. Conversely, if the liquid-air interface has the lowest free energy, then the droplet will bead, taking a more spherical shape.[31] The speed at which the change occurs is determined by the difference in energy between those interfaces – the larger the difference the quicker the change in shape occurs.

Assuming that the energy of the solid-air interface remains constant, whether a droplet beads or spreads, and the rate in which it does so, is governed by the difference between the energy of the surface (γ_{SL}) and the liquid surface tension (γ_{LA}), with the factors affecting the energy of the surface being the surface chemical composition and the surface roughness.[32,33]

1.3.1 Wenzel State

As the energy of a surface is affected by the surface roughness, the surface can be roughened to increase the area of contact with the water droplet and alter the observed droplet behaviour. Assuming that the chemistry of the surface remains unchanged during the roughening process, roughening the surface will amplify the inherent wetting properties of the surface, a phenomenon first described by Wenzel in 1936 (**Figure 4**). This penetration into the surface roughening serves to increase the observed contact angle in the case of hydrophobic surfaces and decreases the contact angle in the case of a hydrophilic surface.[34,35]

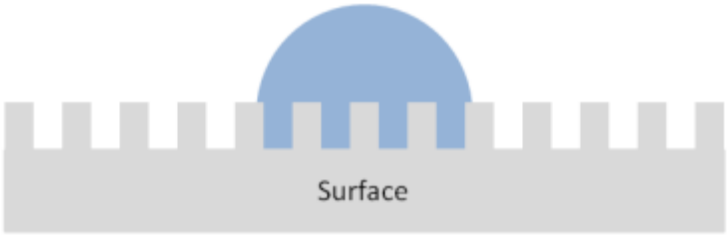

Figure 4: A droplet on a surface under a Wenzel type wetting regime. Here, the droplet penetrates into the surface features

Due to the addition of surface roughness the surface energy term (γ_{SL}) in **Equation 1** must be altered to account for this. The roughness can be represented by a roughness factor "R" (**Equation 2**) which can be measured by scanning electron microscopy (SEM) or atomic force microscopy (AFM) and is defined as;

$$R = \frac{actual\ surface\ area}{apparent\ surface\ area} \qquad \textbf{(2)}$$

When the roughness factor is taken into account this leads to the Wenzel equation (**Equation 3**),[36] where Θ_w is the Wenzel contact angle and Θ_o is the contact angle of the smooth surface. The Wenzel equation can then be used to calculate theoretical contact angles and estimate the effect that changing the surface roughness will have on the surface wettability.

$$\cos\theta_w = R\cos\theta_o \qquad \textbf{(3)}$$

1.3.2 Cassie-Baxter

The Wenzel equation is a useful equation when approximating the contact angle between a droplet and a surface which is non-porous. In the case of a hydrophobic surface however, increasing the surface roughness will eventually lead to a surface that is sufficiently rough that the water droplet cannot penetrate into the fine structure of the surface. This results in a small layer of air between the surface and the water droplet.[37]

The surface roughness means that a small fraction of the liquid-solid interface becomes a solid-air interface, which in turn alters the Wenzel equation, and was first observed by Cassie and Baxter in 1944 (**Figure 5**).[38]

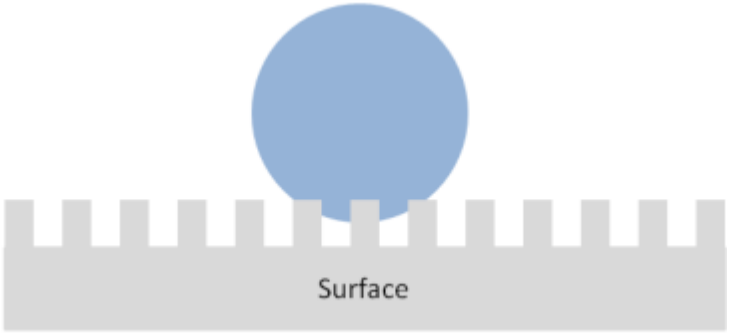

Figure 5: A droplet on a surface under a Cassie-Baxter type wetting regime where the droplet penetrates into the surface features

When the fraction of liquid-solid interface is calculated, the Wenzel equation (**Equation 3**) can then be modified to become:

$$\cos\theta_{CB} = f_{sl}\cos\theta_o - f_{al} \quad \textbf{(4)}$$

Where f_{sl} is the fraction of solid under the drop, and f_{al} is the fraction of air under the drop. This new equation (**Equation 4**), the Cassie-Baxter relationship, remains true for surfaces where the surface roughness features are smaller than the size of the liquid droplet that is placed upon that surface.[39,40] Manipulation of the surface roughness can be used to create surfaces that repel a variety of liquids including those with low surface tensions, such as pentane, creating an omniphobic surface.[41] This is a surface whic can repel multiple different liquids with a range of surface tensions.[42]

1.3.3 Contact Angle Hysteresis

Contact angle hysteresis concerns the behaviour of a droplet as it moves across a surface, where the leading edge of the droplet is the advancing angle, and the trailing edge is the receding angle (**Figure 6**). Subtracting the receding contact angle from the advancing contact angle gives rise to the contact angle hysteresis.[43,44] The contact angle hysteresis gives information as to the movement of a droplet on the surface, with a low contact angle hysteresis signifying the droplet being able to freely move

across the surface, and a high contact angle hysteresis signifying the droplet remaining pinned to the surface.

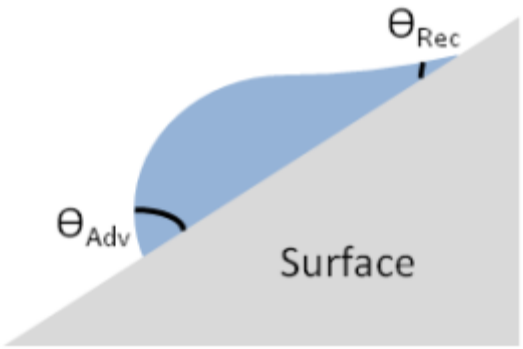

Figure 6: Placing a droplet upon a tilted surface can be used to simulate the advancing and receding contact angles. Here, the advancing edge is where the droplet beads up, and the trailing edge will thin out

The contact angle hysteresis can be measured by a number of different methods. One such method is the sessile drop method (**Figure 7**).[45] First, a droplet of a known size is placed upon the surface and the droplet is then increased and subsequently decreased in size to yield the advancing and receding contact angles respectively. This occurs because the droplet advances across the surface when its size is increased, and retreats across the surface when its size is decreased.[45,46]

A second method which can be used to measure the hysteresis is the tilted stage method, whereby the droplet is placed upon a surface and the surface is tilted. The lowest and highest points on the droplet are measured, yielding the advancing and receding contact angles.[47]

One final example is the captive bubble method which is similar to the sessile drop method but, instead of a droplet of water, a bubble of air is used. The surface is completely submerged in water and a bubble of air is then excreted from a syringe and placed upon the surface, where the contact angle is then measured and subtracted from π to yield the true contact angle (**Equation 5**).[48,49] In this case, Θ_c, is the true contact angle and Θ_o is the observed contact angle.

$$\theta_c = \pi - \theta_o \quad \textbf{(5)}$$

Droplets which have a small contact angle hysteresis will freely roll across a surface as seen in the case of the lotus leaf, whereas droplets that have a large contact angle hysteresis will become attached to the surface.[50]

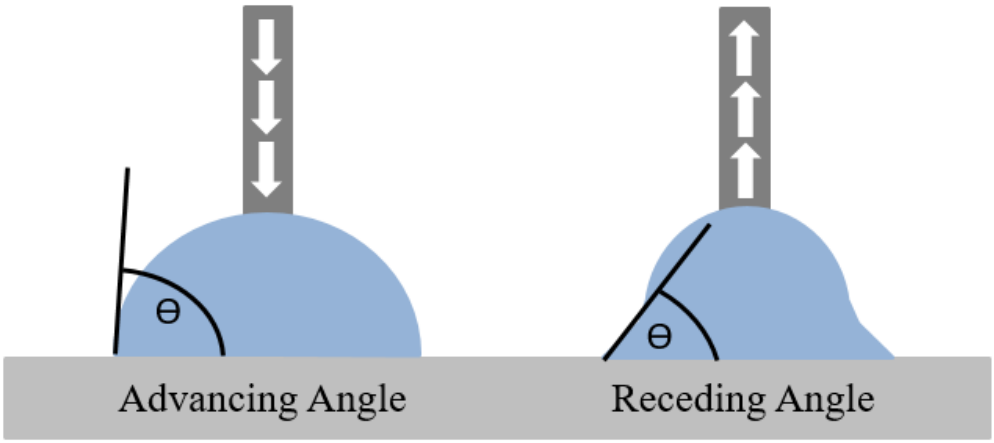

Figure 7: In the sessile drop method the advancing and receding angle can be measured by respectively increasing and decreasing the droplet size. This causes the droplet to advance or recede across the surface and can then be measured, the same theory applies for captive bubble

1.3.4 Droplet Impact

An important factor when considering plant surface behaviour is rain and the velocity of the rain droplets when they impact upon the leaf surface. A droplet impacting upon a surface will deform, and the energy of the droplet will convert from kinetic energy to surface energy and some vibrational energy as the drop oscillates.[51,52] The determing factor in whether or not a droplet will bounce are the interactions between the droplet and the surface, as well as the surface tension of the droplet itself. In some cases the surface will contain small defects where a droplet could become impinged and lose energy.[53] In order for the droplet to bounce, the kinetic energy of the droplet must overcome the energy that it loses upon impinging on surface defects. If it does not overcome the loss, then a solid-liquid interface is formed and the droplet will remain attached to the surface.[53,54] If, however, the energy is sufficient to overcome the surface tension of the droplet it will break apart upon impact.[55]

This relationship between surface tension and the inertia of a water droplet hitting a surface can be described by the Weber number (We) (**Equation 6**).[56]

$$We = \frac{\rho v^2 l}{\sigma} \quad \textbf{(6)}$$

In this instance, ρ is the density of the fluid in kg/m^3, v is the velocity of the droplet in m/s, l is the characteristic length (or droplet diameter), and σ is surface tension of the liquid in N/m.

Consequently, a droplet impacting at a large velocity will overcome the droplet surface tension and result in a spreading or splashing of the droplet, whereas a droplet with sufficient inertia to overcome surface pinning, but not enough to fragment, will bounce off the surface.[56]

The observed deformation of the droplet is also related to the Weber number, where small Weber numbers denote minor deformations and larger Weber numbers denoting larger deformations. In the case of small droplets, the deformation is proportional to a balance between the droplet inertia and capillary force of the surface (**Equation 7**).

$$\tau \propto \sqrt{\frac{\rho}{\sigma}} r^{\frac{3}{2}} \quad \textbf{(7)}$$

Where τ is timescale, ρ is the droplet density, σ is the droplet surface tension, and r the radius of the droplet. The capillary force is an important factor to consider when a surface has micro roughness as the velocity of the droplet when it impacts upon the surface needs to be taken into consideration.[57] Since the droplet has a velocity it may penetrate further into the surface microstructures than those at a lower velocity causing a transition from a Cassie-Baxter regime to a Wenzel regime. It may also leave behind a thin film of water due to the impact, further influencing any subsequent wetting.[58,59]

To maintain surface hydrophobicity it is important that the capillary pressure arising from surface roughness should exceed the pressure exerted by the droplet upon impact, as this prevents surface impingement.[60] The maximum pressure exerted on the surface is defined as the water hammer pressure (**Equation 8**);[61,62] ρ is the

density of the liquid, c is the speed of sound in that liquid and v is the velocity at which the droplet hits the surface.

$$P_{WH} = 0.2\rho cv \quad \textbf{(8)}$$

This is especially important in leaf surfaces which often contain many surface microstructures as, depending upon the speed of the droplet, partial or complete wetting may occur.[63]

1.4 Plant Wetting Mechanisms

Broadly speaking, plant surfaces can be split into four main catagories; superhydrophilic, with contact angles of close to 0°, hydrophilic, with contact angles of less than 90°, hydrophobic, with contact angles of above 90°, and superhydrophobic, with contact angles of greater than 150° (**Figure 8**) as described by Holloway.[64] A variety of factors such as wax composition, surface microstructures, and surface cell structures will govern the wettability observed.[32]

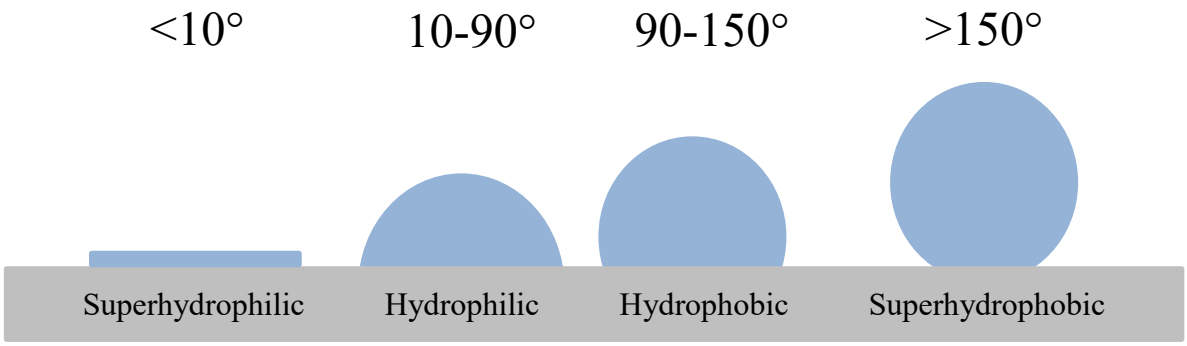

Figure 8: Contact angles for each of the four main categories of wettability

In the case of superhydrophilic plants such as the Nepenthes pitcher plant,[65,2] contact angles were observed of less than 10° by Bauer et al. with a fully wettable surface observed which caused insects to aquaplane across the surface. One way in which plants alter their surfaces to become superhydrophilic, as is the case with the pitcher plant, is to excrete wax compounds that have an affinity for water;[62] alcohols

and fatty acids for example. These types of molecules interact favourably with water and allow a large degree of wetting.

For those leaves that are hydrophilic, such as *Fagus sylvatica* and *Magnolia grandiflora*, they often display little to no epicuticular waxes outside the cuticle. This combined with the smooth nature of the leaf allows them to wet and therefore become hydrophilic, as described by Barthlott and Neuinhuis in 1997.[66] In the case of those leaves that are hydrophobic, they often display a thin 2D layer of wax with only minor surface roughness. The surface roughness creates a hydrophobic surface by providing pockets where air can be trapped underneath a droplet, creating a Cassie-Baxter wetting state.[67]

Plants that are superhydrophobic like the lotus leaf (*Nelumbo*)[1], display both hydrophobic waxes and surface roughness, often with papillose cell structures. As described by Barthlott and Neuinhuis, both of these combine to create a very rough surface with a high roughness factor and strong Cassie-Baxter state, leading to surface super hydrophobicity.[1]

These four general categories, however, do not represent the complete picture; there are many other plant wetting mechanisms which occur in nature. This variation allows a series of sub-categories to be included, which take into account the different structures that can be observed on a plant surface as well as the aforementioned difference in chemical composition of those surfaces.

1.4.1 Hydrophobic Plant Wetting Mechanisms

Of the many plants that display hydrophobicity, perhaps the most famous is the lotus leaf (*Nelumbo*)[1] described by Barthlott and Neuinhuis, which shows superhydrophobicity and self-cleaning properties. Self-cleaning occurs when water droplets travel across the surface and collect surface contaminants as they move, due to the weak attractive force between the contaminant and the surface being overcome by the droplet-contaminant interaction. This is one of three hydrophobic mechanisms mentioned in the literature,[68] which are termed the lotus effect, the petal effect and the salvinia effect respectively.

1.4.1.1 The Lotus Effect

The lotus effect, originally described by Barthlott and Neuinhuis, applies to plants which display superhydrophobicity due to a combination of surface roughness and surface chemistry.[69] Epicuticular wax crystals present on the surface of the leaf cells trap air and form a composite surface with low interfacial tension. This reduces the contact area of the droplet with surface and increases the water/air interface, which creates the archetypal Cassie-Baxter state. Since the surface energy is low, the droplet does not impinge upon the surface and water pinning is not observed.[70] The low contact angle hysteresis allows water to flow freely across the surface, collecting surface contaminants as it flows, creating a self-cleaning surface. In the case of the lotus effect, plants show micro and nano surface structures (**Figure 9**), with a hydrophobic wax component on top of their surface resulting in superhydrophobicity. Other plants which display this effect are the Indian cress (*Tropaeolum Majus. L*), the Prickly pear (*Opuntia angelmannii*), and cane (*Alchemilla*) as described by Wilkinson et al.[71]

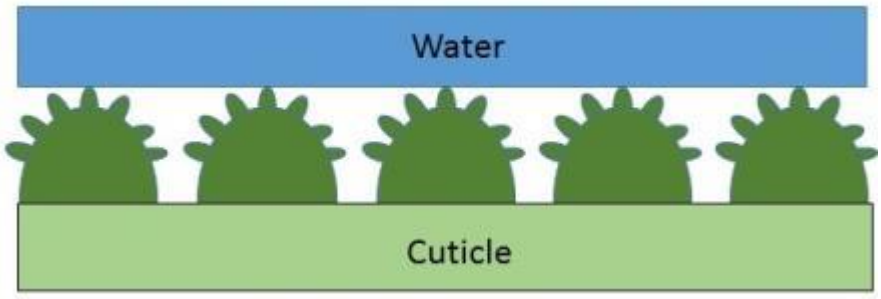

Figure 9: A typical lotus type surface, in this case the cuticle has micro waxes and nano-waxes which result in a Cassie-Baxter state. Here, the water droplet does not penetrate into the surface roughness

Specific to the lotus leaf, the cells on the surface have a papillae type structure with nanoscale waxes attached to the surface, which results in a Cassie-Baxter wetting state and a high contact angle >150°. The lotus effect is therefore used to describe surfaces which show superhydrophobicity and low contact angle hysteresis across the entire surface.

1.4.1.2 The Petal Effect

The petal effect, first described by Feng et al., is not dissimilar from the lotus effect, but in this case water droplets on the surface will pin to it as opposed to rolling off.[72,73,74] In this case the surface structure is very similar with micro and nano-

structures, however, the water droplets are able to penetrate slightly into the surface features due to their larger size. The penetration allows for the droplet to form a contact line with the surface resulting in a high contact angle hysteresis and therefore droplet pinning.[75] Water contact angles were observed of >150° and a high degree of droplet pinning across the entire leaf surface was shown (**Figure 10**).[72] A variety of rose species (*Rosa cv*) and some clubmosses (*Lycopodium*) fall into this category.

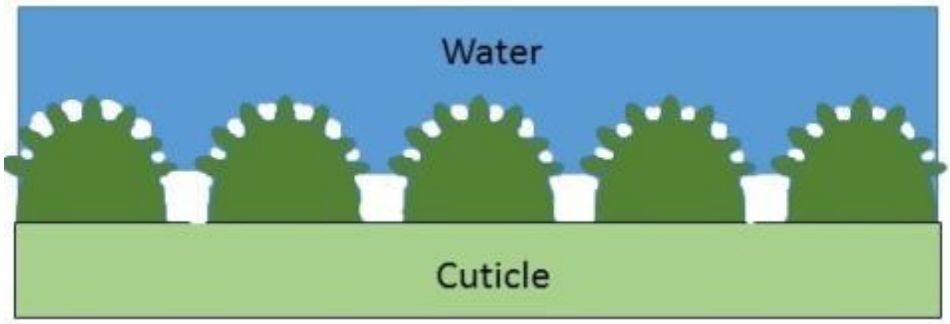

Figure 10: Here, the surface follows a similar structure to the lotus effect, however this time, the water penetrates into the surface roughness resulting in the droplet pinning to the surface. Note the small air layer in the nano structure

1.4.1.3 The Salvinia Effect

The third and final hydrophobic mechanism relates to those plants that live in an underwater environment, and was identified in the *Salvinia* plant species by Barthlott et al. The Salvinia effect is the stabilisation of an air layer on the surface of a leaf.[76,77] Hairs on the surface of the leaf are covered with hydrophobic, nanoscale waxes across their entire surface, except at the tip which is hydrophilic. These hairs cause a thin layer of air to form when placed underwater, resulting in a surface that does not wet.[78,79] The air layer is formed as the water contact line remains pinned to the hydrophilic portion of the hairs whilst being unable to overcome the energy barrier required to form a contact line with the hydrophobic waxes. The hydrophobic waxes, coupled with the increased surface area provided by the unique shape of the hair tip,[76] leads to a water contact angle of >150° and high contact angle hysteresis due to the hydrophilic tip. A variety of Salvinia species (*Salvinia molesta*) and other species of ferns display this type of wetting mechanism (**Figure 11**).[77]

Another plant which displays a similar mechanism is the Lady's Mantle (*Alchemilla mollis*) as described by Herminghaus et al., where tiny hydrophilic hairs

on the surface result in a surface that displays hydrophobicity, and contact angles of >150°.[80] Here the hydrophilic hairs cause a pinning of the contact line and a metastable Cassie-Baxter state at the surface,[81,82] and droplet pinning to the hair tips which results in a surface that is superhydrophobic.[83,84]

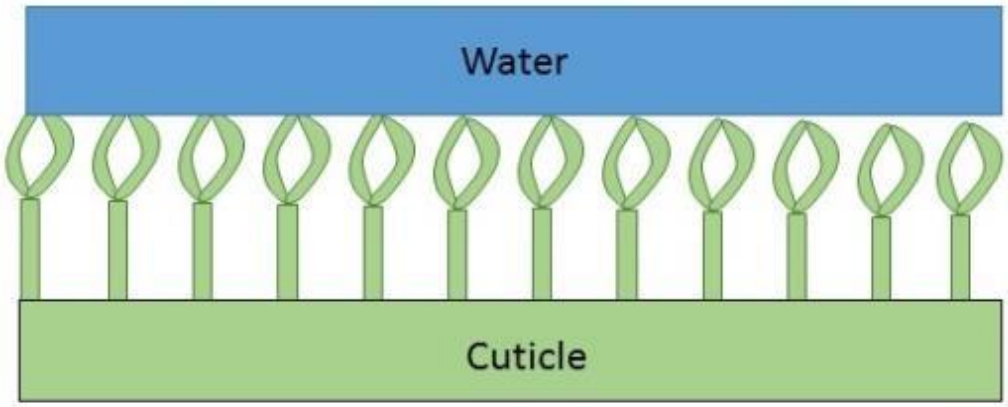

Figure 11: The Salvinia effect, here the hairs on the plant surface cause a metastable Cassie-Baxter state, since the plant is submerged, a thin air layer forms between the water and the cuticle. This allows gas diffusion from the plant to take place

1.4.1.4 Re-entrant curvature

Re-entrant curvature, as described by Tuteja et al., applies to those surfaces where; "the surface topography cannot be described by a simple univalued function $z = h(x,y)$",[85] i.e the surface microstructures are made up of irregular polygons with some form of an overhang. These include "micro-hoodoos", mushroom structures such as those described by Liu et al.,[86] and pillar like structures (**Figure 12**).[87] The structures described are all re-entrant curvatures, named based upon their visual appearance and display superhydrophobicity despite the surface itself being hydrophilic.[88] The superhydrophobicity is a result of the water being unable to overcome the capillary pressure between the surface strcutures generating a local region of low surface energy. The low surface energy observed creates a meta-stable Cassie-Baxter wetting state resulting in superhydrophobicity. The surface can be modified and tuned to react to different liquids by altering the dimensions and chemistry of the surface features, with this type of re-entrant curvature also applying to materials that have been spin coated such as fibres, as demonstrated by Wang et al.[89,90]

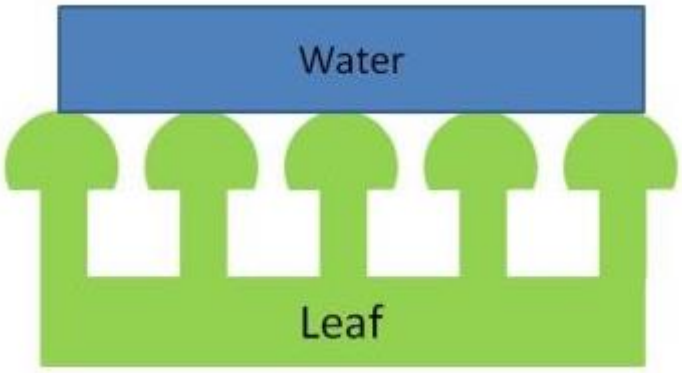

Figure 12: An example of a re-entrant structure, here surface structures (similar in shape to mushrooms) result in hydrophobicity as the water on the surface cannot penetrate the surface due to capillary pressure. These structures can be both micro or nano in scale depending upon the surface

1.4.1.5 Mechanism Comparisons

Comparing the hydrophobic wetting mechanisms there are clear similarities and differences. For example, the lotus and rose petal effect both display micro and nano structures on the leaf surface, with the water droplet sitting atop a trapped air layer in a Cassie-Baxter state. For the rose petal effect, the water penetrates slightly into the surface roughness resulting in a pinning of the contact line, which means the water droplet does not freely move across the surface and therefore displays a high contact angle hysteresis. This is in contrast to the lotus effet where the droplet is able to freely move across the surface.

The salvinia effect, however, is drastically different to the rose petal and lotus effect, as the salvinia effect has large hairs which are easily distinguishable by the naked eye on the surface. The hairs, when submerged, cause a pinning of water to the hydrophilic hair tips whilst being repelled from the hydrophobic waxes present over the rest of the hairs. This creates an air surface between the droplet and the leaf resulting in a surface that displays superhydrophobicity. The combination of surface structure and chemistry differentiates the salvinia from re-entrant curvature, where the surface behaviour is solely a factor of the surface structures. These surface structures prevent wetting of the surface due to the high capillary pressure needed for

the droplet to penetrate between structures independently of the surface chemistry. The differences between mechanisms are summarised below (**Table 2**).

Table 2: The difference between the mechanisms in regards to the surface structure they show and the hysteresis that is observed on the surface

Mechanism	Surface Structure	Hysteresis	Mode of Mechanism
Lotus Effect	Micro and nano structures	Low to none	Cassie-Baxter
Petal Effect	Micro and nano structures	Large	Cassie-Baxter[72]
Salvinia Effect	Micro hairs	Large	Cassie-Baxter[91]
Re-Entrant	Micro and/or nano structures	Variable[92]	Cassie-Baxter[92]

1.4.2 Hydrophilic Plant Wetting Mechanisms

Similarly to hydrophobic plants there are three hydrophilic mechanisms reported in the literature to date: include the wild petunia, the pitcher effect, and the spine effect.

1.4.2.1 Wild Petunia Effect

The wild petunia (*Ruellia devosiana*) possesses a non-homogeneous physical surface which contains many surface features. One such feature is the prescence of embedded wax secreting glands that secrete hydrophilic compounds such as alcohols and esters in order to aid in the surface wetting.[93] This mechanism, as described and characterised by Barthlott et al. follows a Wenzel type arrangement with complete penetration of the water into the surface (**Figure 13**).[93] This penetration results in the droplet spreading through the surface to maximise the surface interaction creating a low observable contact angle, and has even observed to flow up the leaf, against the pull of gravity.

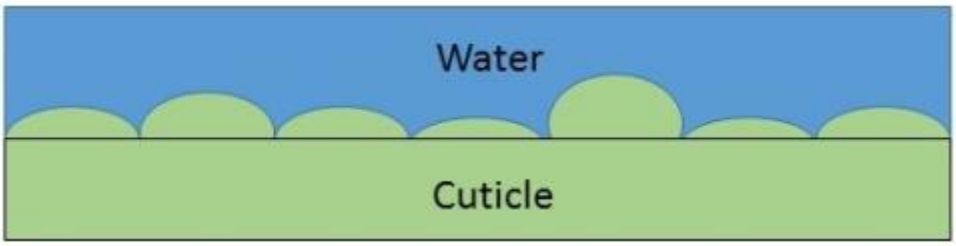

Figure 13: In this case, the water penetrates into the non-homogeneous surface resulting in wetting

1.4.2.2 The Pitcher Effect

The pitcher effect is observed in those plants which have a homogenous surface as opposed to the non-homogenous surface displaced in the wild petunia effect. The surface may display surface waxes to aid in the complete spreading of water.[94] A common feature observed in these plants is a thin film of water that forms across the entire surface, creating a highly slippery surface as shown by Bohn et al. (**Figure 14**). The flat surface lacking microstructures coupled with hydrophilic waxes creates a high energy wenzel surface that causes complete wetting to be observed. This effect has been described across multiple plant species such as the Nepenthes pitcher plant, the prayer plant (*Maranta leuceneura*), and the Zebra plant (*Calthea Zebrina*).[94,95,96]

Figure 14: Since the surface is homogeneous, the water forms a layer atop the surface which aids in surface wetting. In the case of the pitcher plant, this creates a surface nearly impossible to grip onto

1.4.2.3 The Spine Effect

The spine effect corresponds to plants which have spines upon their surface. The spines either cause water wicking, where wicking describes the motion of water independently of external forces like gravity, or direct absorption through the spines themselves, as demonstrated by Jiang et al.[97,98] The water droplet moves from the

thin part of the spine to the wider part in order to maximise the energy of interaction between the surface and the droplet. This effect is maxismised by the spines having a hydrophilic surface which aids in maximising the energy of interaction. Often, once contact is made with the main stem, the water droplet is completely absorbed by the plant. This type of mechanism is most commonly seen on cacti species, such as *Discocactus horshii*.

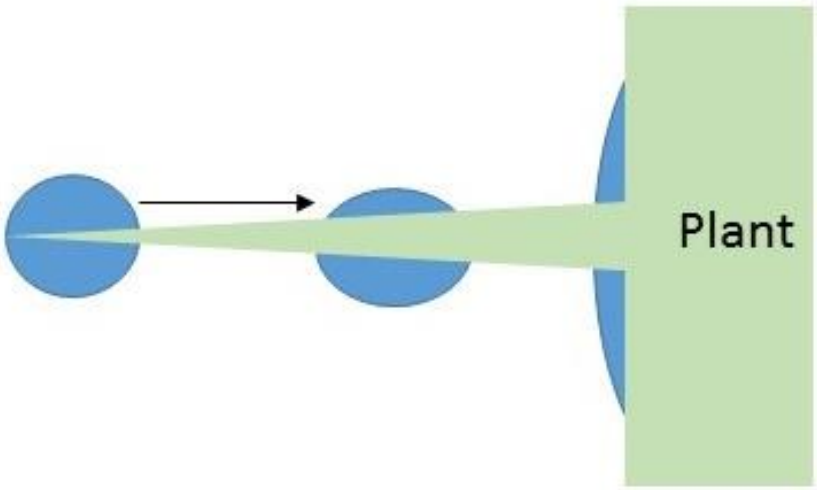

Figure 15: The spine effect occurs when droplets wick up the spine to the main body of the plant. The water droplet wicks in this case to maximise the surface contact between the spin and the water droplet, resulting in a favourable free energy change. This continues until the droplet hits the main body of the plant and wets

1.4.2.4 Mechanism Comparisons

When comparing the three hydrophilic mechanisms it is apparent that the wild petunia and pitcher effects operate under similar mechanisms, just with different surface structures. Both follow a Wenzel type mechanism, where the wild petunia has a non-homogenous surface and the pitcher has a homogeneous surface. The spine effect shows the greatest variability as it displays directional wetting, in this case along the direction of the spines (**Table 3**).

Table 3: Detailing the difference in mechanisms, in the case of the wild petunia and pitcher effect, the hysteresis is low as complete wetting occurs. In the case of the spine effect, the hysteresis is high as the droplets will pin to the spines no matter their orientation

Mechanism	Surface Structure	Hysteresis	Mode of Mechanism
Wild Petunia Effect	Heterogeneous, micro and nano	Low	Wenzel
Pitcher Effect	Homogeneous, micro and nano	Low	Wenzel[99]
Spine Effect	Spines with micro roughness	High	Wenzel

1.5 Fog Collection

Water scarcity, particularly in the developing world, is a growing concern. In many of the arid regions experiencing water scarcity, regular episodes of fog provide water for local plant life. Ordinarily, plants acquire water via uptake through their root system, there are however a number of plants which do not. Often, these plants collect water through the precipitation of fog, such as *Cotula fallax*[3], allowing them to thrive in an arid environment. The analysis and replication of these plant surfaces could provide useful insight into the development of devices which can efficiently collect fog.

1.5.1 Fog Collecting Plant Surfaces

There are a variety of plants which collect water from fog using a range of different mechanisms. *Stipagrostis sabulicola* is a desert grass found in the dunes of Namibia, it has tall, thin leaves which have an array of grooves running the length of the leaf.[100] Fog collects in the furrows on the plant surface before adjacent droplet coalesce to form a large droplet. The larger droplet then overcomes the pinning

forces holding it to the leaf and it rolls down the grooves to the shallow root system below.

The *O. microdasys* species of cactus, found in the deserts of North America, collects fog in a different way to the desert grasses of Namibia. In this case, an array of spines on the surface, located in discrete clusters, allows for the collection and absorption of fog. The spines themselves have grooves running the length, with barbs that are oriented in the direction of the leaf surface, the grooves get wider the closer to the leaf they are which causes water droplets to wick from the tip of the spine to the base. This wicking occurs, even against the pull of gravity and allows the cactus to absorb water present on the spines.[101]

Stipagrostis sabulicola and *O. microdasys* are two examples of plants which collect fog as a source of water. In order to study the fog collecting properties of plants surfaces which are similar, a method by which fog can be produced in a laboratory environment is needed, this method must control for variables that affect fog collection. Such as wind speed, humidity, and size of fog droplet.[102]

1.6 Experimental Techniques

A range of surface replication and analytical techniques can be employed, both to analyse plant surfaces and replicate them. This section includes a brief overview of some of those techniques and methods.

1.6.1 Scanning Electron Microscopy (SEM)

Scanning electron microscopy (SEM) provides details about the surface topography of a sample with much greater resolution than conventional light microscopy.[103] This is due to the use of electrons as opposed to light waves for analysing the surface. The resolution possible is determined by the wavelength of the electrons and the ability to focus the incident beam on the sample.[103]

Usually electrons are emitted from an electron gun via thermionic emission from a tungsten filament cathode, the electrons are then accelerated using an electric field and then focused via a series of magnetic fields which act similar to the lenses in an optical microscope. The distance between the sample and the final magnetic

field determines the depth of the SEM field, thus allowing samples with large variations in depth to be imaged sharply.[104]

When an electron impacts the sample surface, a variety of interactions take place, one of which being the ejection of a secondary electron. Detectors placed in the SEM chamber detect the ejected electrons and compare the energy of those ejected to the electrons emitted from a second electron gun (**Figure 16**).[104]

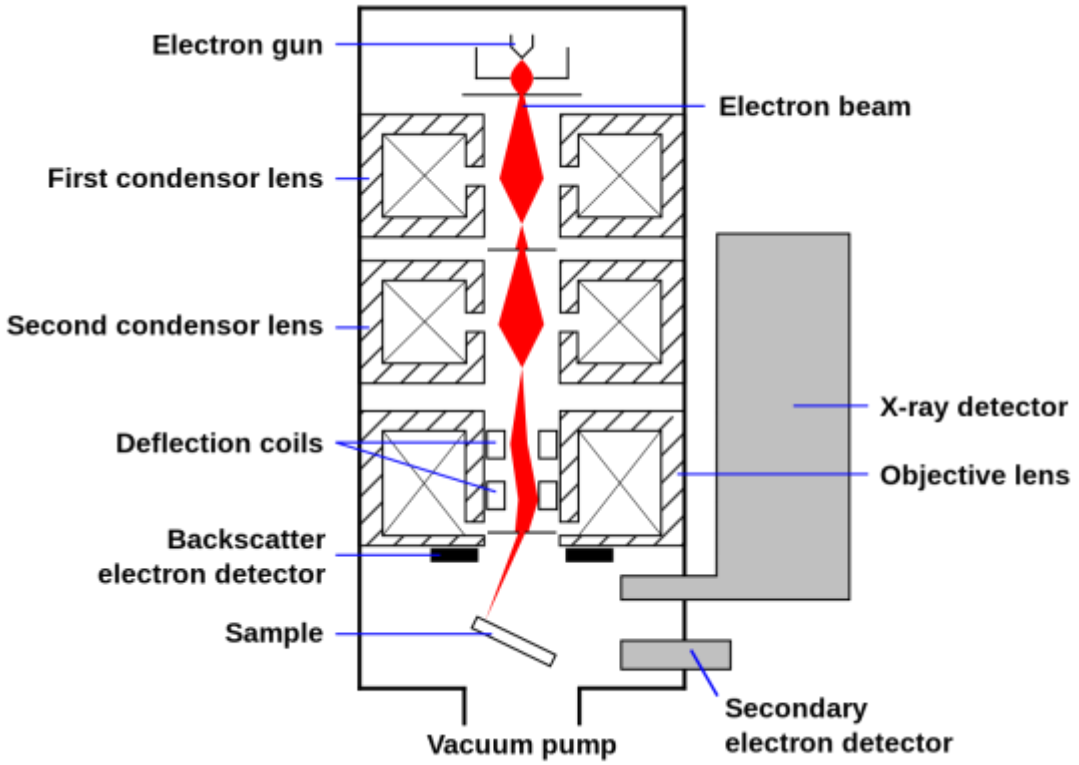

Figure 16: Schematic diagram of a generic SEM. Often for biological samples a nanometre thick coating of gold is often applied to reduce the charge of the surface and allow an accurate image to be created, this occurs if the surface has excess charging resulting in bright "white" spots on the image. The difference in intensities allows the creation of an intensity distribution map, an image of the surface

One issue associated with SEM is that samples may become charged by the repeated bombardment of the surface which results in bright "spots" on the image, a problem which is particularly common in those samples that are good conductors or have water present.[105] In the case of biological samples, occasionally they may need to be coated with a nanometre thick coating of gold in order to reduce the charging of the surface that occurs. The coating is sufficiently thin that it cannot be seen on

the majority of spectrometers as they lack the appropriate resolution. It is possible to analyse plant surfaces without the need for surface coating, using the glycerol substitution technique described by Ensikat et al., making SEM the most common tool used to analyse surface roughness and observe epicuticular waxes.[105]

1.6.2 X-ray Photoelectron Spectroscopy (XPS)

X-ray photoelectron spectroscopy (XPS) is a surface sensitive technique that measures the surface chemical composition using X-rays. Under ultra-high vacuum conditions ($<10^{-9}$ millibar), X-rays are directed at a surface from an X-ray source. The X-rays then interact with electrons in the sample causing their ejection from the atom (**Figure 17**).[106] By measuring the energy of the emitted electron and comparing it to the energy of the initial X-ray, the binding energy of the electron can be measured.[107] By measuring the amount of electrons emitted, and their binding energies, the surface composition can be determined. Whilst this technique has a high resolution,[108] and can analyse the average atomic structure of the surface, the ultra-high vacuum required makes using this technique to analyse plant surfaces difficult. This is because as the leaf dehydrates under the high vacuum conditions it can curl in on itself, altering its shape, occluding the surface. Samples therefore need to be properly secured to prevent this.

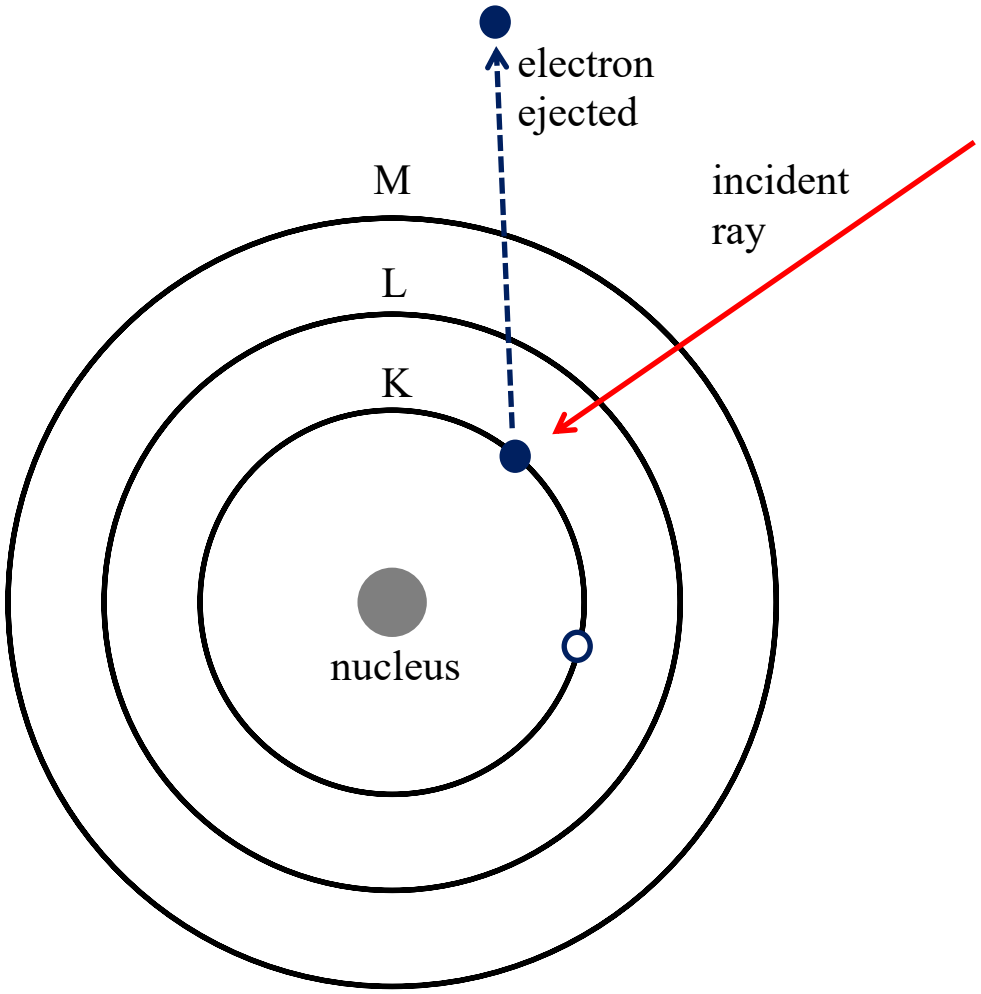

Figure 17: The ejected photoelectron has a kinetic energy that can be measured and compared to the energy of the initial X-ray (incident ray) to ascertain the binding energy and therefore the atomic composition of the sample

1.5.3 Energy Dispersive X-ray Spectroscopy (EDS)

Energy dispersive X-ray spectroscopy (EDS, sometimes referred to as EDX) is commonly used to analyse the chemical or elemental composition of a sample. Under vacuum conditions, electrons or X-rays are directed at the surface from a source. The incident beam interacts with electrons bound in shells and may cause the ejection of an electron from an inner shell, creating an electron hole. Another electron, from a higher energy shell then relaxes to fill the hole left behind emitting an X-ray as it relaxes. The energy and number of X-rays emitted from the sample can then be measured by a spectrometer (**Figure 18**). Since each element has a unique atomic structure, it is possible to determine the elemental composition of the surface.[109,110]

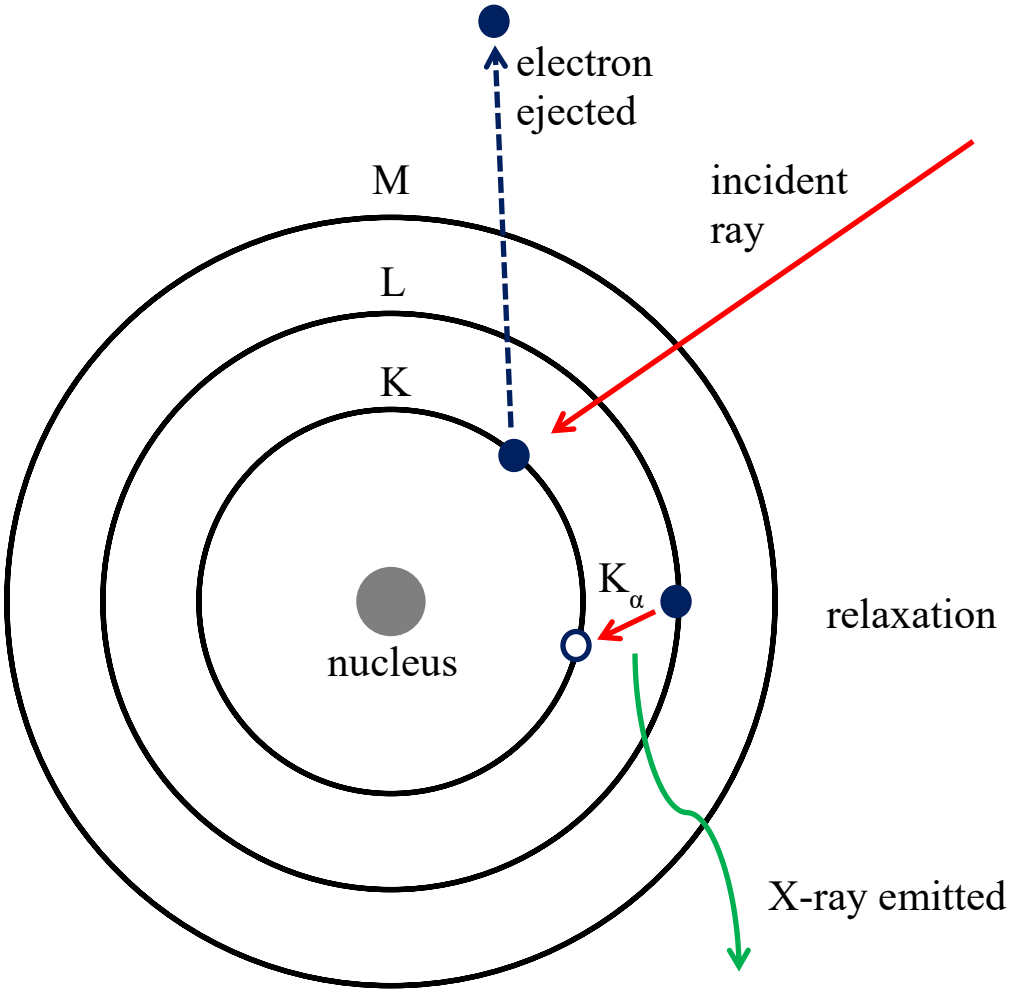

Figure 18: Basic theory behind EDS. The incident ray causes the ejection of an electron from a low energy shell, leaving behind a hole. An electron from a higher energy shell relaxes to fill that hole, emitting a measurable X-ray in the process

The different shells are denoted K, L, and M, with different quantum numbers, n = 1, 2, and 3 respectively. K_α is therefore an electron transition from the "L" shell to the "K" shell and the highest energy type of X-ray emitted. In the case of a fluorine atom, the characteristic K_α value is 0.677 keV.[111]

1.5.4 Time of Flight Secondary Ion Mass Spectrometry (ToF-SIMS)

This technique is particularly useful in analysing the surface waxes which are present on the surface, giving excellent spatial resolution across the leaf surface. Secondary ion mass spectrometry (SIMS) is the creation, collection and analysis of secondary ions that have been ejected from the surface of interest.[112] In SIMS, an ion beam is

focused upon the surface in either a pulsed or a continuous fashion. The ion beam ionises chemical components of the surface resulting in the ejection of charged species. The ejected ions then pass through a mass analyzer to a detector under high vacuum conditions (**Figure 19**).

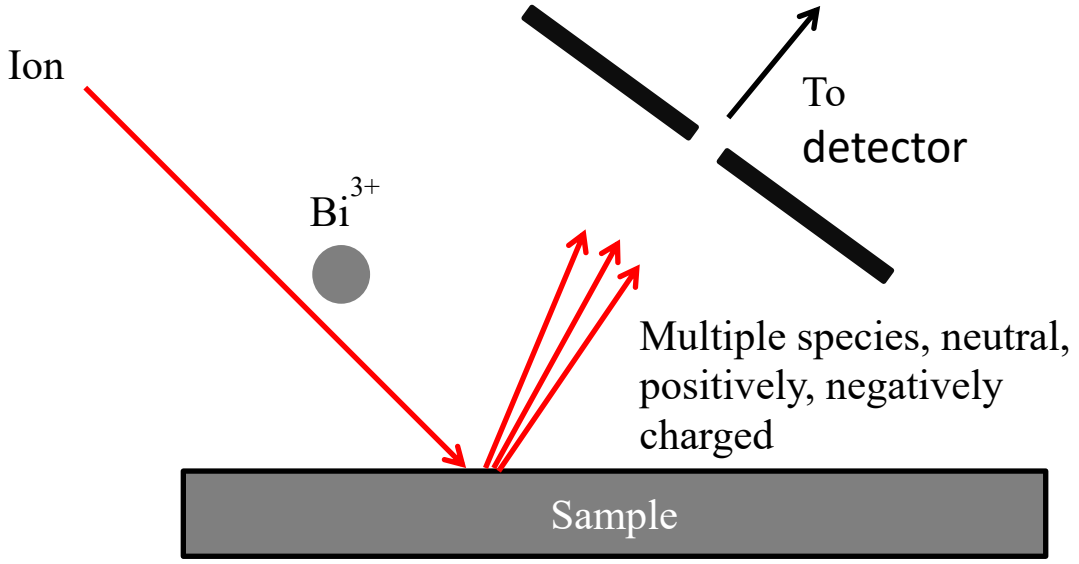

Figure 19: ToF-SIMS utilises an ion gun to generate ions that are directed at the surface. In this example, a bismuth liquid metal ion gun is used to generate Bi^{3+} ions which are directed at the surface. The impact generates a multitude of different species which are then passed through to an analyser

Time of flight (ToF) SIMS is a variation on the type of analyser used. In time of flight, ions are separated according to their velocity; since all ions are given the same energy their velocity, and therefore their time of flight, will change relative to their mass. In the case of plant samples, ToF-SIMS can be used to analyse the chemical composition of the surface, including those compounds embedded within the cuticle and any waxes expressed on the surface.[112,113]

1.6.5 Plasma Surface Modification

Irving Langmuir coined the term "fourth state of matter" late in the 1920s to describe plasma, and is now used to describe gasses which are composed primarily of ionised particles.[114] This includes charged ions, electrons, and neutrals. In order to generate a plasma, an electric field is applied to a dielectric gas which causes separation of

electrons from their parent nucleii if the electric field is strong enough. The now ionized electrons quickly go on to generate a cascade process and a plasma.

The plasma discharge can then be used to alter the chemical and physical properties of a surface through polymer deposition, plasmachemical modification and etching, whilst leaving the bulk material unchanged.[115] An example of such a process is using a CF_4 gas plasma to alter a surface and make it superhydrophobic.[116]

1.6.6 Thickness Measurements

It is possible to measure the thickness of thin films on an opaque substrate by using a spectrophotometer that is capable of measuring reflected and transmitted light from a sample. Measurements obtained can be used to determine a number of factors such as the film thickness (d), the extinction coefficient of the film (k) and the refractive index of the film (n) (**Figure 20**).[117]

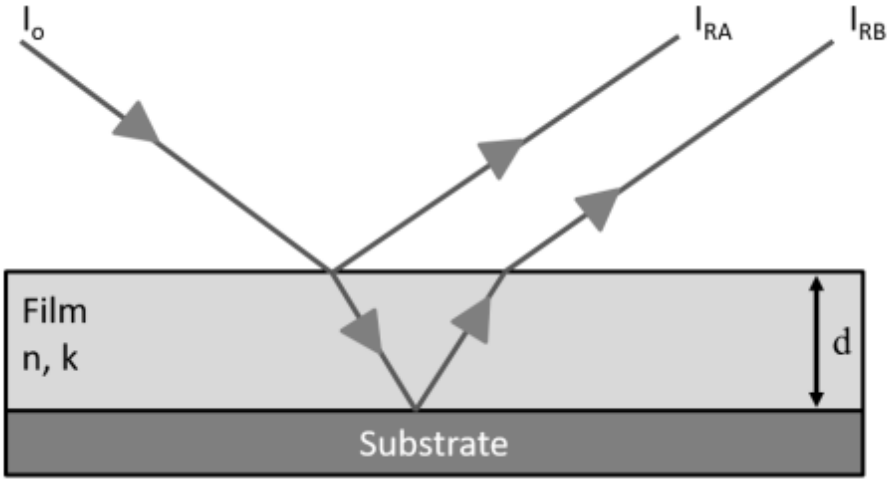

Figure 20: By irradiating the sample using monochromatic light, at a variety of different wavelengths, allows a number of film properties to be measured such as its thickness

I_o is the incident ray of the incoming monochromatic light, I_{RA} is the reflected ray at the top of the film, and I_{RB} is the reflected ray at the bottom of the film. For light with a wavelength of between 350–1000 nm the amount which is reflected by the sample will vary depending up the amount of constructive or destructive interference

between I_{RA} and I_{RB}. This interference leads to a periodical amplification and extinction of some of the wavelengths of light giving an interferance spectra.[117,118]

Since the reflected beam at the bottom of the film I_{RB} must travel through the film it will be affected by the refractive index of the film material (n) and the extinction coefficient of the film material (k). The refractive index is determined by the speed at which light travels through it relative to the speed of light in a complete vacuum. The film will affect the distance the light travels through the film and therefore its path length. Some of the light will also be absorbed by the thin film itself and affect the intenstity of the light which is reflected. It is possible, however, to fit the spectrum using a basic Cauchy model,[119] allowing one to ascertain the film thickness if the refractive index is known.

This technique is important in determining the thickness of deposited films, a technique which is particularly useful when creating surfaces which mimic those of plants. By depositing a layer of material, it becomes possible to impart chemical properties upon the surface of study.[120]

1.6.7 Soft Lithography

One of the most common and widely used methods to replicate the surface of plants is soft-lithography (**Figure 21**). The method was first described by Xia and Whitesides in 1998,[121,122] where they performed soft lithography using a flexible poly-dimethyl siloxane (PDMS) mould that could be removed easily from the master surface. Due to the flexible nature of the PDMS mould it can be used to recreate complex topologies provided the polymer can flow and penetrate into the surface features.[123]

The soft-lithographic approach has been used to create replicas of a variety of plant leaves such as the lotus leaf,[124] and the Colocasia (*Colocasia, esculenta*).[125] This technique can also be used to replicate other surface features such as the fine structures of butterfly wings.[126]

The first stage involves cutting a suitable leaf sample from the parent plant and applying the PDMS to the surface. The PDMS is then allowed to set and carefully separated from the surface to yield a negative mould of the leaf sample. Epoxy resin is then poured into the negative moulds and allowed to cure before also

being separated from the mould. This yields a positive replica of the leaf sample (**Figure 21**).

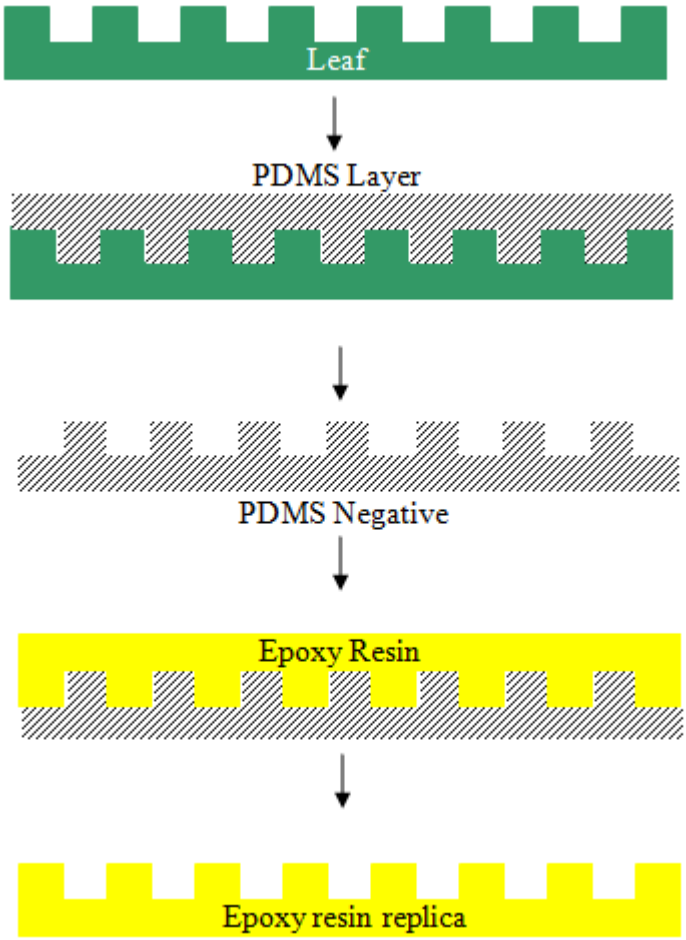

Figure 21: A schematic diagram showing soft lithography of a leaf sample. It works by first creating a PDMS negative of the surface before adding an epoxy resin or a polymer to create a positive replica of the surface

Soft lithography is a useful tool that can be used to accurately replicate surface structures; it is even capable of replicating the 3D waxes that are commonly found upon leaf surfaces, although some accuracy is lost. In the case of the Indian cress (*Tropaeolum Majus L*), additional surface features such as stomata were also replicated, with the resolution on soft lithography in the range of 30 nm, as limited by the wetting properties of the mould material.[122] The penetration into the materials is dependent upon the aspect ratio of the surface feature, allowing penetration into the surface in the range of 30 nm to several hundred nanometres, depending on the surface feature.[122] This resolution is small enough to be able to identify the majority

of micro structures, as well as some of the larger nano wax crystals (**Figure 22**), but the accuracy of the mould will vary from surface to surface. In particular, surfaces which contain features with high aspect ratios will be poorly replicated compared to those with low aspect ratios; this includes plants with hairs for example. Despite these limitations, soft lithography is widely used to replicate plant surfaces, as it is a relatively cheap, quick, and accurate way to replicate plant surfaces as demonstrated by multiple groups such as Barthlott et al. and Wang et al.[127,128]

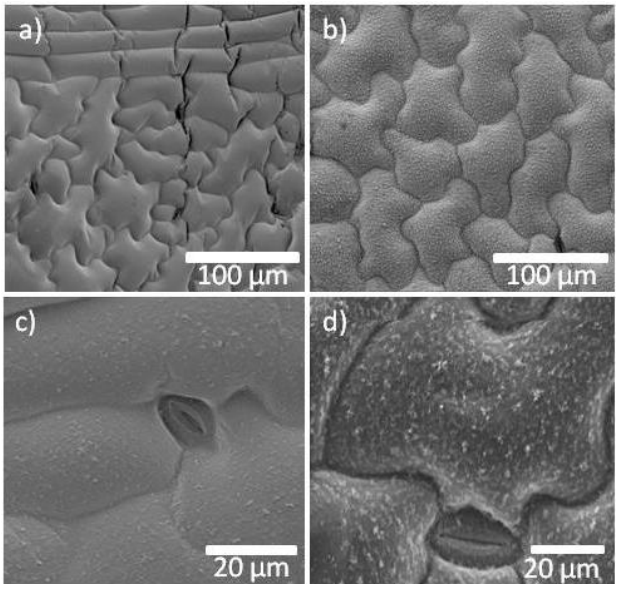

Figure 22: SEM images obtained for replicas (a and c) compared to their leaf counterparts (b and d) for samples of *Tropaeolum Majus L*

1.6.8 3D Printing

3D printing, also commonly known as additive manufacturing, is a way to create a 3D object by successively adding material layer by layer. The process begins by creating a model of the object using computer software, such as Solidworks. Once the model is created it is processed by printer software and sliced into multiple layers which are then printed. There are several applications for this technology, such as medical devices and general manufacturing as described by Rengier et al.[129]

There are several techniques employed in order to print an object, such as extrusion and light polymerisation. In the former, a material such as a thermoplastic is melted and extruded via a small nozzle into the desired shape.[130] The latter uses a photopolymer which undergoes polymerisation when exposed to UV light. Layers of material are added and set by exposing the material to UV light.[130]

This technique has been used previously to create biomimetic surfaces, in particular the creation of artificial shark skin, and can offer several advantages over other techniques such as scaleability and cost.[131] The main advantage of 3D printing is that it allows for more control than moulding. For example, the size and shape of the desired surface features can easily be altered using 3D printing, whereas in moulding they are limited to the underlying substrate used to create the mould. Secondly, 3D printing can quickly produce large surfaces in a few hours, which would be difficult to achieve using the moulding process as the the sample size is a limiting factor. It is also possible to create surfaces where the features overlap or contain overhangs, which is difficult to do using moulding due to the moulding material being unable to penetrate into surface features. One major disadvantage, as discovered by Lauder et al., was that 3D printing lacked the required resolution to accuately print the surfaces required.[131]

1.6.9 Water Contact Angle Analysis

How a droplet of water interacts with a surface is highly dependent upon the roughness of the surface, and the energy of the surface. Contact angle measurements therefore provide a useful tool in analysing the surface, especially plant surfaces. With the sessile drop method being most appropriate for analysing plant surfaces.

The contact angle displayed by a droplet is defined by the interaction between the three interfacial energies as described previously (**1.3 Surface Wettability**). It is also possible to determine the homogeneity of a surface by measuring the contact angle hysteresis, with a more homogenous surface having a lower contact angle hysteresis.

1.6.10 Infrared Analysis (IR)

A common technique which is used to analyse chemical groups is infrared spectroscopy. This technique relies on the chemical bonds absorbing infrared radiation that matches the vibrational frequency of that bond, resulting in an excited state.[132] The energy absorbed is affected by the shape of the bond, the strength of the

bond, and the atoms at either end of the bond. The wavenumber of absorbance can be predicted by considering a simple two molecule system and the equation:

$$\upsilon = \frac{1}{2\pi c}\sqrt{\frac{k}{\mu}} \quad \textbf{(9)}$$

υ is the wavenumber of absorbance, c is the speed of light, k is the spring constant for the bond and μ is the reduced mass of the system. This technique can be useful for obtaining information about the types of bonds found in chemical samples such as plant waxes, as demonstrated by Morzycki et al.[132]

1.7 Conclusion

The wettability of a surface is influenced by the roughness of the surface and its chemical composition as demonstrated by Wenzel and Cassie-Baxter, and can display a wide variety of unique properties such as superhydrophobicity and superhydrophilicity. This is particularly apparent in nature, where plant surfaces display a wide variety of wetting mechanisms and behaviours when interacting with water. These mechanisms include superhydrophobicity displayed by the lotus leaf, superhydrophilicity of the nepenthes pitcher plant, and hydrophobic hairs with hydrophilic tips of salvinia.

There are a range of analytical techniques which can be used to analyse plant surfaces before replication. Most commonly used is SEM, which allows for accurate imaging of leaf surfaces without the need for surface modification. Micrometre scale images can be obtained of surface features, such as cells and waxes, which can then be studied to determine the overall structure of the surface. More recently, XPS and mass spectrometry have been used to analyse the chemical composition of the waxes present on the surface, which whilst difficult to carry out experimentally due to availability of equipment and the need to have samples close to the lab, provide a detailed analysis of the chemical composition of the surface.

In terms of replication of plant surfaces, the most commonly used technique, soft lithography, has been used to replicate multiple plant surfaces such as that of the Indian Cress. The technique, which, when combined with plasmachemical surface modification, allows for the creation of reasonably accurate replicas of the surface

that mimic both surface roughness and surface chemistry. A new technique gaining attention is 3D printing, although replicas of plant surfaces are yet to be achieved.

1.8 Project Aims

The scope of this thesis is to observe, analyse and replicate the wetting behaviour displayed by a number of plant species utilising the techniques described and previously employed in the literature. Work will also be undertaken to further develop these technique and create new novel techniques by which the surfaces of plants can be analysed and replicated. In particular, techniques which focus on the analysis of surface chemistry, particularly plant waxes, will be developed as the underlying wetting behaviour is governed by surface structure and surface chemistry. ToF-SIMS, which allows for the detailed analysis of surface waxes, is an example of one such technique that will be further developed.

Often, plants that display interesting properties may be located in regions that are difficult to obtain samples from due to their geographical isolation, or located in developing countries where surface analysis is impossible. Development of a novel method by which those surfaces can be analysed will be explored. Plants will be chosen for study based upon interesting wetting properties, such as fog collection, dual wettability, or water channelling. The surfaces of these plants will then be studied both structurally and chemically before being replicated to create a surface that biomimics the behaviour observed.

Work will also be conducted to develop new techniques by which plant surfaces can be replicated on a large scale, overcoming some of the limitations of current techniques. Successful replication of plant surfaces is necessary to further develop devices which can collect fog or channel water that have real world applications.

Finally, an experimental method that can test the fog collection properties of the plant surfaces and any replicated surfaces will be developed, which enables the testing and analysis of those surfaces when exposed to fog.

1.8 References

[1] Barthlott, W.; Neuinhuis, C. Purity of the Scared Lotus, or Escape from Contamination in Biological Surfaces. *Planta* 1997, *202*, 1–8.

[2] Bauer, U.; Federle, W. The Insect-Trapping Rim of Nepenthes Pitchers. *Plant Signal Behav.* **2009**, *4(11)*, 1019–1023.

[3] Andrews, H. G.; Eccles, E. A.; Schofield, W. C.; Badyal, J. P. Three-Dimensional Hierarchical Structures for Fog Harvesting. *Langmuir* **2011**, *5(27)*, 3798–3802.

[4] von Spreckelsen, R. M.; Harris, M. T.; Wigzell, J. M.; Fraser, R. C.; Carletto, A.; Mosquin, D. P. K.; Justice, D.; Badyal, J. P. S. Bioinspired Breathable Architecture for Water Harvesting. *Sci. Rep.* **2015**, *5*, 16798.

[5] Bhushan, B.; Burton, Z. Surface Characteriation and Adhesion and Friction Properties of Hydrophobic Leaf Surfaces. *Ultramicroscopy*, **2006**, 709–719.

[6] Krauss P.; Markstädter, C.; Riederer, M. Attenuation of UV radiation by plant cuticles from woody species. *Plant, Cell and Environment* **2005**, *20(8)*, 1079–1085.

[7] Eglington, G.; Hamilton, R. J. Leaf Epicuticular Waxes. *Science* **1967**, *156(3780)*, 1322–1335.

[8] Mariani, C.; Wolters-Arts, M. Complex Waxes. *The Plant Cell* **2000**, *12(10)*, 1795–1798.

[9] Glove, B. J. Differentiation in Plant Epidermal Cells. *Journal of Experimental Botany* **2000**, *51(344)*, 497–505.

[10] https://commons.wikimedia.org/wiki/File:Leaf_Tissue_Structure.svg

[11] Eglington, G.; Hamilton, R. J. Leaf Epicuticular Waxes. *Science* **1967**, *156*, 1332–1335.

[12] Korn, R. W.; Spalding, R. M. The Geometry of Plant Epidermal Cells. *New Phytologist* **1973**, *72(6)*, 1357–1365.

[13] Koch, K.; Bhushan, B.; Barthlott, W. Diversity of Structure, Morphology and Wetting of Plant Surfaces. *Soft Matter* **2008**, *4*, 1943–1963.

[14] Armour, W. J.; Barton, D. A.; Law, A. M. K.; Overall, R. L. Differential Growth in Periclinal and Anticlinal Walls during Lobe Formation in Arabidopsis Cotyledon Pavement Cells. *The Plant Cell* **2015**, *27(9)*, 2484–2500.

[15] Zhang, C.; Halsey, L. E.; Szymanski, D. B. The Development and Geometry of Shape Change in Arabidopsis Thalina Cotyledon Pavement Cells. *Plant biol.* **2011**, *11(23)*.

[16] Martin, C.; Glover, B. J. Functional Aspects and Cell Patterning in Aerial Epidermis. *Curr.Opin. Plant Biol.* **2007**, *10*, 70–82.

[17] Haynes, W. M. *Handbook of Chemistry and Physics*. CRC Press, 93rd **2012**.

[18] Post-Beittenmiller, D. Biochemistry and Molecular Biology of Wax Production in Plants. *Ann. Rev. Plant. Physiol. Plant. Mol. Biol.* **1996**, *47*, 405–435.

[19] Kunst, L.; Samuels, A. L. Biosynthesis and Secretion of Plant Cuticular Wax. *Progress in Lipid Research*. **2003**, *42*, 51–80.

[20] Wigzell, J. M.; Racovita, R. C.; Stentiford, B. G.; Wilson, M.; Harris, M. T.; Fletcher, I. W.; Mosquin, D. P. K.; Justice, D.; Beaumont, S. K.; Jetter, R.; Badyal, J. P. S. Smart Water Channelling Through Dual Wettability by Leaves of the Bamboo *Phyllostachys Aurea*. *Colloids and Surfaces A: Physiochemical and Engineering Aspects*. **2016**, *505*, 344–355.

[21] Macková, J.; Vašková, M.; Macek, P.; Hronková, M.; Schreiber, L.; Šantrůček, J. Plant Response to Drought Stress Simulated by ABA Application: Changes in Chemical Composition of Cuticular Waxes. *Environmental and Experimental Botany*. **2013**, *86*, 70–75.

[22] Kim, K. S.; Park, S. H.; Kin, D. K.; Jenks, M. A. Influence of Water Deficit on Leaf Cuticular Waxes of Soybean. *Int. J. Plant. Sci.* **2007**, *168(3)*, 307–316

[23] Barthlott, W.; Neinhuis, C.; Cutler, D.; Ditsch, F.; Meusel, I.; Theisen, I.; Wilhelmi, H. Classification and Terminology of Plant Epicuticular Waxes. *Bot. J. Linn.Soc.* **1998**, *126(3)*, 237–260.

[24] Koch, Kerstin.; Ensikat, H-J. The Hydrophobic Coatings of Plant Surfaces: Epicuticular Wax Crystals and Their Morphologies, Crystallinity and Molecular Self-Assembly. *Micron* **2008**, *39(7)*, 759–772.

[25] Jeffree, C. E.; Riederer, M.; Müller, C. The Fine Structure of the Plant Cuticle. *Annual Plant Reviews Volume 23: Biology of the Plant Cuticle*. Blackwell Publishing Ltd, Oxford, **2006**

[26] Jeffree, C. E.; Baker, E. A.; Holloway, P. J. Ultrastructure and Recrystallization of Plant Epicuticular Waxes. *New Phytol.* **1975**, *75*, 539–549.

[27] Li, X. M.; Reinhoudt, D.; Crego-Calama, M. What do we Need for a Superhydrophobic Surface? A Review on the Recent Progress in the Preparation of Superhydrophobic Surfaces. *Chem. Soc. Rev.* **2007**, *36(8)*, 1350–1368.

[28] Morra, M.; Occhiello, E.; Garbassi, F. Contact Angle Hysteresis in Oxygen Plasma Treated Poly(tetrafluoroethylene). *Langmui* **1989**, *5(3)*, 872–876.

[29] Chen, L.; Bonaccurso, E. Effects of Surface Wettability and Liquid Viscosity on the Dynamic wetting of Individual Drops. *Phys. Rev. E.* **2014**, *90*, 022401.

[30] Bonn, D.; Eggers, J.; Indekeu, J.; Meunier, J.; Rolley, E. Wetting and Spreading. *Rev. Mod. Phys.* **2009**, *81*, 739–805.

[31] de Gennes, P. G. Wetting: Statics and Dynamics. *Rev.Mod. Phys.* **1985**, *57*, 827–863.

[32] Holloway, P. J. Surface Factors Affecting the Wetting of Leaves. *Pestic. Sci.***1970**, *1*, 156–163.

[33] Zisman, W. A. Relation of the Equilibrium Contact Angle to Liquid and Solid Constitution. *Contact Angle, Wettability, and Adhesion* **1964**, *1*, 1–51.

[34] Wenzel, R. N. Resistance of Solid Surfaces to Wetting by Water. *Ind. Eng. Chem.* **1936**, *28(8)*, 988–994.

[35] Murakami, D.; Jinnai, H.; Takahara, A. Wetting Transition from the Cassie-Baxter State to the Wenzel State on Textured Polymer Surfaces. *Langmuir* **2014**, *30(8)*, 2061–2067.

[36] Shirtcliffe, N. J.; McHuk, G.; Atherton, S.; Newton, M. I.; *Adv. Colloid. Interface. Sci.* **2010**, *161*, 124–138.

[37] Bico, J.; Tordeux, C.; Quéré, D. Rough Wetting. *Europhys. Lett.* **2001**, *55(2)*, 214–220.

[38] Cassie, A. B. D.; Baxter, S. Wettability of Porous Surfaces. *Transactions of the Faraday Society*. **1944**, *40*, 546–551.

[39] Choi, W.; Tuteja, A.; Mabry, J. M.; Cohen, R. E.; McKineley, G. H. A Modified Cassie-Baxter Relationship to Explain Contact Angle Hysteresis and Anisotropy on Non-Wetting Textured Surfaces. *Journal of Colloid and Interface Science* **2009**, *339(1)*, 208–216.

[40] Gao, L.; McCarthy, T. J. How Wenzel and Cassie Were Wrong. *Langmuir* **2007**, *23(7)*, 3762–3765.

[41] Tuteja, A.; Choi, W.; Ma, M.; Mabry, J. M.; Mazzella, S. A.; Rutledge, G. C.; McKinley, G. H.; Cohen, R. E. Designing Superoleophobic Surface. *Science* **2007**, *318(5856)*, 1618–1622.

[42] Tuteja, A.; Choi, W.; Mabry, J. M.; McKinley, G. H.; Cohen, R. E. Robust Omniphobic Surfaces. *PNAS* **2008**, *105(47)*, 18200–18205.

[43] McHale, G.; Shirtcliffe, N. J.; Newton, M. I. Contact-Angle Hysteresis on Super-Hydrophobic Surfaces. *Langmuir* **2004**, *20(23)*, 10146–10149.

[44] Joanny, J. F.; de Gennes, P. G. A Model for Contact Angle Hysteresis. *The Journal of Chemical Physics* **1984**, *81*, 552–562.

[45] Neumann, A. W.; Good, R. J. Techniques of Measuring Contact Angles. *Surface and Colloid Science* **1979**, *11*, 31–91.

[46] Yuan, Y.; Lee, T. R. Contact Angle and Wetting Properties. *Surface Science Techniques.* **2013**, *51*, 3–34.

[47] Macdougall, G.; Ockrent, C. Surface Energy Relations in Liquid/Solid System. I. The Adhesion of Liquids to Solids and a New Method of Determining the Surface Tension of Liquids. *Proc. R. Soc.* **1942**, *180(981)*, 151–172.

[48] Marmur, A. Contact-Angle Hysteresis on Heterogeneous Smooth Surfaces: Theoretical Comparison of the Captive Bubble and Drop Methods. *Colloids Surf. A.* **1998**, *136*, 209–215.

[49] Montes Ruiz-Cabello, F. J.; Rodriguez-Valverde, M. A.; Marmur, A.; Cabrerizo-Vilchez, M. A. Comparison of Sessile Drop and Captive Bubble Methods on Rough Homogeneous Surfaces: A Numerical Study. *Langmuir* **2011**, *27(15)*, 9638–9643.

[50] Wang, F-C.; Wu, H-A. Pinning and Depinning Mechanism of the Contact Line During Evaporation of Nano-Droplets Sessile on Textured Surfaces. *Soft Matter* **2013**, *9*, 5703–5709.

[51] Varanasi, K. K.; Deng, T.; Smith, J. D.; Hsu, M.; Bhate, N. Frost Formation and Ice Adhesion on Superhydrophobic Surfaces. *Appl. Phys. Lett.* **2010**, *97*, 234102.

[52] Richard, D.; Quéré, D. Viscous Drops Rolling on a Tilted Non-Wettable Solid. *Europhys. Lett.* **1999**, *48(3)*, 286–291.

[53] Zorba, V.; Stratakis, E.; Barberoglou, M.; Spanakis, E.; Tzanetakis, P.; Anastasiadis, S. H.; Fotakis, C. Biomimetic Artificial Surfaces Quantitatively Reproduce the Water repellency of a Lotus Leaf. *Adv. Mat.* **2008**, *20(21)*, 4049–4054.

[54] Jansen, H. P.; Sotthewes, K.; Ganser, C.; Teichert, C.; Zandvliet, H. J. W.; Kooij, E. S. Tuning Kinetics to Control Droplet Shapes on Chemically Striped Patterned Surfaces. *Langmuir* **2012**, *28(37)*, 13137–13142.

[55] Richard, D.; Quéré, D. Bouncing Water Drops. *Europhys. Lett.* **2000**, *50(6)*, 769–775.

[56] Denis, R.; Clanet, C.; Quéré, D. Contact Time of a Bouncing Drop. *Nature* **2002**, *417*, 811.

[57] Chen, S. H.; Soh, A. K. The Capillary Force in Micro- and Nano-Indentaion with Different Indenter Shapes. *Int. J. Solids. Structures.* **2008**, *45*, 3122–3137.

[58] Bhushan, B.; Jung, Y. C. Dynamic Effects of Bouncing Water Droplets on Superhydrophobic Surfaces. *Langmuir* **2008**, *24(12)*, 6262–6269.

[59] Li, X.; Ma, X.; Lan, Z. Dynamic Behavior of the Water Dropley Impact on a Textured Hydrophobic/Superhydrophobic Surface: The Effect of the Remaining Liquid Film Arising on the Pillars' Tops on Contact Time. *Langmuir* **2010**, *26(7)*, 4831–4838.

[60] Bartolo, D.; Bouamrirene, F.; Verneuil, E.; Buguin, A.; Silberzan, P.; Moulinet, S. Bouncing or Sticky Droplets: Impalement Transitions on Superhydrophobic Micropatterned Surfaces. *Europhysics Letters* **2006**, *74*, 299–305.

[61] Huang, Y. C.; Hammitt, F. G.; Yang, W-J. Hydrodynamic Phenomena During High-Speed Collision Between Liquid Droplet and Rigid Plane. *J. Fluids Eng.***1973**, *95(2)*, 276–292.

[62] Varanasi, K. K.; Deng, T.; Hsu, M. F.; Bhate, N. Design of Superhydrophobic Surfaces for Optimum Roll-Off and Droplet Impact Resistance. *ASME* **2008**, *13*, 637–645.

[63] Reyssat, M.; Yeomans, J. M.; Quéré, D. Impalement of Fakir Drops. *Europhys. Lett.* **2006**, *74*, 306.

[64] Förch, Renate, Holger Schönherr, and A. Tobias A. Jenkins. *Surface Design: Applications in Bioscience and Nanotechnology*. Weinheim: Wiley-VCH, **2009**.

[65] Ueda, E.; Levkin, P. A. Emerging Applications of Superhydrophilic-Superhydrophobic Micropatterns. *Adv. Mat.* **2013**, *25(9)*, 1234–1247.

[66] Bhushan, B.; Jung, Y. C. Micro- and Nanoscale Characterization of Hydrophobic and Hydrophilic Leaf Surfaces. *Nanotechnology* **2006**, *17*, 2758–2772.

[67] Burton, Z.; Bhushan, B. Surface Characterization and Adhesion and Friction Properties of Hydrophobic Leaf Surfaces. *Ultramicroscopy* **2006**, *106*, 709–719.

[68] Wang, G.; Guo, Z.; Liu, W. Interfacial Effects of Superhydrophobic Plant Surfaces: A Review. *J. Bionic Eng.* **2014**, *11(3)*, 325–345.

[69] Patankar, N. A. Mimicking the Lotus Effect: Influence of Double Roughness Structures and Slender Pillars. *Langmuir* **2004**, *20(19)*, 8209–8213.

[70] Otten, A.; Herminghaus, S. How Plant Keep Dry: A Physicicst's Point of View. *Langmuir* **2004**, *20(6)*, 2405–2408.

[71] Wilkinson, R. E.; Mayeux, H. S. Composition of Epicuticular Wax on Opuntia-Engelmannii. *Bot. Gaz.* **1990**, *151(3)*, 342–347.

[72] Feng, L.; Zhang, Y.; Xi, J.; Zhu, Y.; Wang, N.; Xia F.; Jiang, L. Petal Effect: a Superhydrophobic State with High Adhesive Force. *Langmuir* **2008**, *24(8)*, 4114–4119.

[73] Ebert, D.; Bhushan, B. Wear-Resistant Rose Petal-Effect Surfaces with Superhydrophobicity and High Droplet Adhesion using Hydrophobic and Hydrophilic Nanoparticles. *J. Colloid Interface Sci.* **2012**, *384*, 182–188.

[74] Cheng, Z.; Du, M.; Lai, H.; Zhang, N. Sun, K. From Petal Effect to Lotus Effect: a Facile Solution Immersion Process for the Fabrication of Super-Hydrophobic Surfaces with Controlled Adhesion. *Nanoscale* **2013**, *5(7)*, 2776–2783.

[75] K. L. Mittal, *Advances in contact angle, wettability and adhesion*, John Wiley & Sons, 2013

[76] Barthlott, W.; Schimmel, T.; Wiersch, S.; Koch, K.; Brede, M.; Barczewski, M.; Walheim, S.; Weis, A.; Kaltenmaier, A.; Leder, A.; Bohn, H. F. The Salvinia Paraqdox: Superhydrophobic Surfaces with Hydrophilic Pins for Air Retention Under Water. *Adv. Mater.* **2010**, *22(21)*, 2325–2328.

[77] Cerman, Z.; Striffler, B. F.; Barthlott, W. Dry in Water: the Superhydrophobic Water Ferm Salvinia – a Model for Biomimetic Surfaces *Functional Surf. Bio.* **2009**, *1*, 97–111.

[78] Room, P. M.; Harley, K. L. S.; Forno, I. W.; Sands, D. P. A. Successful Biological Control of the Floating Weed Salvinia *Nature* **1981**, *294*, 78–80.

[79] Hunt, J.; Bhushan, B. Nanoscale Biomimetics Studies of Salvinia Molesta for Micropattern Fabrication *J. Coll. Int. Sci.* **2011**, *363(1)*, 187–192.

[80] Otten, A.; Herminghaus, S. How Plants Keep Dry: A Physicist's Point of View *Langmuir* **2004**, *20(6)*, 2405–2408.

[81] Bernardino, N. R.; Blickle,V.; Dietrich, S. Wetting of Surfaces Covered by Elastic Hairs *Langmuir* **2010**, *26(10)*, 7233–7241.

[82] Tuteja, A.; Choi, W.; Mabry, J. M.; McKinley, G. H.; Cohen, R. E. Robust Omniphobic Surfaces *Proc. Natl.* **2008**, *105(47)*, 18200–18205.

[83] Brewer, C. A.; Smith, W. K.; Vogelmann, T. C. Functional Interaction Between Leaf Trichomes, Leaf Wettability and the Optical Properties of Water Droplets *Plant Cell Environ.* **1991**, *14(9)*, 955–962.

[84] Pierce, S.; Maxwell, K.; Griffiths, H.; Winter, K. Hydrophobic Trichome Layers and Epicuticular Wax Poweders in Bromeliaceae *Am. J. Bot.* **2001**, *88(8)*, 1371–1389.

[85] Tuteja, A.; Choi, W.; Ma, M.; Mabry, J. M.; Mazzella, S. A.; Rutledge, G. C.; McKinley, G. H.; Cohen, R. E. Designing Superoleophobic Surface *Science*, **2007**, *318(5856)*, 1618–1622.

[86] Liu, J–L.; Feng, X–Q,; Wang, G.; Tu, S–W. Mechanisms of Superhydrophobic on Hydrophilic Substrates *J. Phys.: Condes. Matter* **2007**, *19(35)*, 356002.

[87] Liu, K.; Tian, Y.; Jiang, L. Bio-Inspired Superoleophobic and Smart Materials: Design, Fabrication, and Application *Progress in Materials Science* **2013**, *58(4)*, 503–564.

[88] Kang, S. M.; Kim, S. M.; Kim, H. N.; Kwak, M. K.; Tahk, D. H.; Suh, K. Y. Robust Superomniphobic Surfaces with Mushroom like Micropillar Arrays. *Soft Matter* **2012**, *8*, 8563–8568.

[89] Zhu, M.; Zuo, W.; Yu, H.; Yang, W.; Chen, Y. Superhydrophobic Surface Directly Created by Electrospinning Based on Hydrophilic Material *J. Mat. Sci.* **2006**, *41(12)*, 3793–3797.

[90] Wang, T.; Hu, X.; Dong, S. A General Route to Transform Normal Hydrophilic Cloths into Superhydrophobic Surfaces *Chem. Commun* **2007**, *18*, 1849–1851.

[91] Mayser, M. J.; Bohn, H. F.; Reker, M.; Barthlott, W. Measuring Air Layer Volumes Retained by Submerged Floating-Ferns Salvinia and Biomimetic Superhydrophobic Surfaces *J. Nanotechnol* **2014**, *5*, 812–821.

[92] Kim, S.; Cheung, E.; Sitti, M. Wet Self-Cleaning of Biologically Inspired Elastomer Mushroom Shaped Microfibrillar Adhesives *Langmuire*, **2009**, *25(13)*, 7196–7199

[93] Koch, K.; Blecher, I. C.; König, G.; Kehraus, S.; Barthlott, W. The Superhydrophilic and Superoleophilic Leaf Surfaces of Ruellia Devosiana (acanthaceae): a Biological Model for Spreading of Water and Oil on Surfaces *Funct. Plant Biol.* **2009**, *36*, 339–350.

[94] Bohn, H. F.; Federie, W. Insect Aquaplaning: Nepenthes Pitcher Plants Capture Prey with the Peristome, a Fully Wettable Water-Lubricated Anisotropic Surface. *PNAS*, **2004**, *101(39)*, 14138–14143.

[95] Bauer, U.; Bohn, H. F.; Federle, W. Harmless Nectar Source or Deadly Trap: Nepenthes Pitchers are Activated by Rain, Condensation and Nectar *Proc. Biol. Sci.* **2008**, *275(1632)*, 259–265.

[96] Own, T. P. Jr.; Lennon, K. A. Structure and Development of the Pitchers from the Carnivorous Plant Nepenthes Alata (Nepenthaceae) *Am. J. Bot.* **1999**, *86(10)*, 1382–1390.

[97] Ju, J.; Bai, H.; Zheng, Y.; Zhao, T.; Fang, R.; Jiang, L. A Multi-Structural and Multi-Functional Integrated Fog Collection System in Cactus *Nature Commun.* **2012**, *3*, 1247

[98] Hidalgo, P.; Méndez, B.; Piqueras, J. GeO_2 Nanowires and Nanoneedles Grown by Thermal Deposition Without a Catalyst. *Nanotechnology* **2005**, *16(11)*, 2521–2524.

[99] R. J. Crawford, E. P. Ivanova, *Superhydrophobic Surfaces*, Elselvier, Amsterdam, **2015**.

[100] Roth-Nebelsick, A.; Ebner, M.; Miranda, T.; Gottschalk, V.; Voigt, D.; Gorb, S.; Stegmaier, T.; Sarsour, J.; Linke, M.; Konrad, W. Leaf surface structures enable the endemic Namib desert grass Stipagrostis sabulicola to irrigate itself with fog water. *J. R. Soc. Interface* **2012**, *9*, 1965-1974.

[101] Ju, J.; Bai, H.; Zheng, Y.; Zhao, T.; Fang, R.; Jiang, L. A multi-structural and multi-functional integrated fog collection system in cactus. *Nature Communications*, **2012**, *3*, 1247.

[102] Schemenauer, R. S.; Cereceda, P. Fog-Water Collection in Arid Coastal Locations *Ambio*, **1991**, *20(7)*, 303–308.

[103] P. W. Atkins, J. De Paula, *Atkins' Physical chemistry*, 7th ed, Oxford University Press, Oxford, **2002**.

[104] M. H. Loretto, *Electron beam analysis of materials*, 2nd ed, Chapman & Hall, London, **1994**

[105] Ensikat, H. J.; Barthlott, W. Liquid Substitution: a Versatile Procedure for SEM Specimen Preparation of Biological Materials Without Drying or Coating. *J. Microsc*. **1993**, *172*, 195.

[106] Moseley, H. G. J.; Darwin, C. G. XIV. The Reflection of the X-rays *Philosophical Magazine Series* **1913**, *26(151)*, 210–232.

[107] Rutherford, E.; Robinson H.; Rawlinson W. F. XXXIV. Spectrum of the β Rays Excited by γ Rays. *Philosophical Magazine Series 6*, **1914**, *28(164)*, 281–286.

[108] Shirley, D. A. High-Resolution X-ray Photoemission Spectrum of the Valence Bands of Gold *Phys. Rev. B.* **1972**, *5*, 4709–4714.

[109] Bertin, E. P.; *Principles and Practice of X-Ray Spectrometric Analysis*, 2nd ed., Plenum Press, New York, **1975,** Chap. 8, pp. 315–403.

[110] Srnová-Šloufová, I.; Vlčková, B.; Bastle, Z.; Hasslett, T. L. Bimetallic (Ag)Au Nanoparticles Prepared by the Seed Growth Method: Two-Dimensional Assembling, Characterization by Energy Dispersive X-ray Analysis, X-ray Photoelectron Spectroscopy, and Surface Enhanced Raman Spectroscopy, and Proposed Mechanism of Growth. *Langmuir* 2004, *20(8)*, 3407–3415.

[111] Vandi, L-J.; Truss, R.; Veidt, M.; Rasch, R.; Heitzmann, M. T.; Paton, R. Fluorine Mobility During SEM-EDX Analysis: A Challenge for Characterizing Epoxy/Fluorpolymer Interfaces. *J. Phys. Chem.* **2013**, *117*, 16933–16941.

[112] Perkins, M. C.; Roberts, C. J.; Briggs, D.; Davies, M. C.; Friedmannm A.; Hart, C. A.; Bell, G. A. Surface Morphology and Chemistry of Prunus Laurocerasus, L. Leaves: a Study Using X-ray Photoelectron Spectroscopy, Time-of-Flight

Secondary-ion Mass Spectroscopy, Atomic-Force Microscopy and Scanning-Electron Microscopy *Planta*, **2005**, *221(1)*, 123–124.

[113] Perkins, M. C.; Bell, G.; Briggs, D.; Davies, M. C.; Friedman, A.; har, C. A.; Roberts, C. J.; Rutten, F. J. M. The Application of ToF-SIMS to the Analysis of Herbicide Formulation Penetration into and Through Leaf Cuticles. *Colloids and Surfaces B.* **2008**, *67(1)*, 1–13.

[114] Langmuir, I. The Interaction of Electron and Positive Ion Space Charges in Cathod Sheaths. *Phys. Rev.* **1929**, *33*, 954.

[115] Yao, S. C.; Choi, K. J. Heat Transfer Experiments of Mono-Dispersed Vertically Impacting Sprays. *Int. J. Multiphase Flow* **1987**, *13*, 639.

[116] Woodward, I.; Schofield, W. C. E.; Roucoules, V.; Badyal, J. P. S. Seuper-Hydrophobic Surfaces Produced by Plasma Fluorination of Polybutadiene Films. *Langmuir* **2003**, *19(8)*, 3432–3438.

[117] Daughton, W. J.; Givens, F. L. An Investigationof the Thickness Variation of Spun-on Thin Films Commonly Associated with the Semiconductor Industry. *J. Electrochem. Soc.* **1982**, *129(1)*, 173–179.

[118] Ylilammi, M.; Ranta-aho, T. Optical Determination of the Film Thicknesses in Multilayer Thin Film Structures. *Thin Solid Films* **1993**, *232(1)*, 56–62

[119] Antonietti, M.; Conrad, J. Synthesis of Very Highly Ordered Liquid Crystalline Phases by Complex Formation of Polyacrylic Acid with Cationic Surfactants. *Angew. Chem. Int. Ed. Engl.* **1994**, *33*, 1869.

[120] Kim, Y.; Lee, J-H.; Kim, K-J. Surface Characterisation of Hydrophobic Thin Films Deposited by Inductively Coupled and Pulsed Plasma. *J. Vac. Sci. Technol. A.* **2009**, *27(4)*, 900.

[121] Lee, S–M.; Kwon, T. H. Mass-Producible Replication of Highly Hydrophobic Surfaces from Plant Leaves *Nanotechnology* **2006**, *17(13)*, 3189–3196.

[122] Xia, Y.; Whitesides, G. M. Soft Lithography. *Angew. Chem. Int. Ed.* **1998**, *37*, 550–575.

[123] Xia, Y.; Kim, E.; Zhao, X–M, Rogers, J. A.; Prentiss, M.; Whitesides, G. M. Complex Optical Surfaces by Replica Molding against Elastomeric Masters. *Science* **1996**, *273*, 347–349.

[124] Liu, B.; He, Y.; Fan, Y.; Wang, X. Fabricating Super-Hydrophobic Lotus-Leaf-Like Surfaces Through Soft-Lithographic Imprinting. *Macromol. Rapid. Commun.* **2006**, *27*, 1859–1864.

[125] Arvind Singh, R.; Yoon, E–S.; Kim, H. J.; Kim, J.; Jeong, H. E.; Suh, K. Y. Replication of Surfaces of Natural Leaves for Enhanced Micro-Scale Tribological Property *Mat. Sci. Eng. C.* **2007**, *27(4)*, 875–879.

[126] Kang, S–H.; Tai, T–Y.; Fang, T–H. Replication of Butterfly Wing Microstructures Using Molding Lithography. *Current. Apply. Phys.* **2010**, *10*, 626–630.

[127] Wang, F.; Li, S.; Wang, L. Fabrication of Artificial Super-Hydrophobic Lotus Leaf-Like Bamboo Surfaces Through Soft Lithography. *Colloids and Surfaces A.* **2017**, *513*, 389–395.

[128] Liu, B.; He, Y.; Fan, Y.; Wang, X. Fabricating Super-Hydrophobic Lotus-Leaf-Like Surfaces Through Soft-Lithographic Imprinting. *Macromol. Rapid. Comm.* **2006**, *27(21)*, 1859–1864.

[129] Rengier, F.; Mehndritta, A.; von Tengg-Kobligk, H.; Zechmann, C. M.; Unterhinninghofen, R.; Kauczor, H-U.; Giesel, F. L. 3D Printing Based on Imaging Data: A Review of Medical Applications. *International Journal of Computer Assissted Radiology and Surgery* **2010**, *5(4)*, 335–341.

[130] Kruth, J-P.; Leu, M. C.; Nakagawa, T. Progress in Additive Manufacturing and Rapid Prototyping. *CIRP Annals* **1998**, *47(2)*, 525–540.

[131] Wen, L.; Weaver, J. C.; Lauder, G. V. Biomimetic Shark Skin: Design, Fabrication and Hydrodynamic Function. *J. Exp. Biol.* **2014**, *217*, 1656–1666.

[132] Dubis, E. N.; Dubis, A. T.; Morzycki, J. W. Comparative Analysis of Plant Cuticular Waxes Using HATR FT-IR Reflection Technique. *J. Molecular Structure* **1999**, *511*, 173–179.

Chapter 2 The Study and Replication of Plant Surfaces

2.1 Experimental

2.1.1 Preparation of Xanthosoma sagittifolium Samples

A single plant cutting of *Xanthosoma sagittifolium* was collected from Durham University Botanical Garden's Tropical greenhouse where the climate is kept warm and humid to mimic the conditions found in a rainforest. A single leaf was cut from the main plant such that 12–14 inches of stem remained. The stem was then immersed in water (tap water, Northumbrian Water) to prevent dehydration of the leaf during transit to the laboratory. The leaves were washed with deionised water and allowed to air dry in the laboratory. Samples were cut from three regions of each leaf, margin, lamina, and, midrib. Leaves that were young and mature were sampled.

2.1.2 Contact Angle Measurements

Contact angle measurements were taken at room temperature using a video capture apparatus (VCA 2500 XE, AST Products Inc.) and 1.0 μL high purity water droplets (ISO 3696 Grade 1). Advancing and receding contact angle values were determined by respectively increasing and subsequently decreasing the liquid drop volume by a further 1.0 μL until the contact line was observed to move.[1] A minimum of three static, advancing, and receding contact angles were obtained for each sample. Averages and standard deviations were calculated.

2.1.3 Scanning Electron Microscopy (SEM)

Individual leaf specimens were prepared for scanning electron microscopy analysis by using a glycerol substitution process.[2] 2–4 mL of 2% glutaraldehyde (Sigma-Aldrich Co.) solution in phosphate buffer (pH 7.2, Sigma-Aldrich Co.) was dispensed onto a small (~2 cm^2) piece of fabric placed in a petri dish, and a leaf was

placed on top of the soaked fabric for 2 h. The fabric was then replaced with a new piece, and it was soaked with a solution of 10% glycerol (> 99%, Sigma Aldrich Ltd.) in water and left for 2 h. The same process was repeated for increasing concentrations of glycerol up to 90% in 10% steps. Each sample was then mounted onto a carbon disk supported on an aluminium stub. No gold coating was required due to the conductive nature of the glycerol.[3] Surface topography images were taken on a scanning electron microscope (Tescan Vega 3MLU, TESCAN ORSAY HOLDING) operating in a secondary electron detection mode, in conjunction with an 8–20 kV accelerating voltage, and a working distance between 9 and 11 mm.

The epoxy resin positive replica samples were mounted onto a carbon disk supported on an aluminum holder, and coated with a 5 nm gold layer (Model 108 sputter coating unit, Cressington Scientific Instruments Ltd) in order to avoid excess surface charging. Images were taken on a scanning electron microscope (Tescan Vega 3MLU, TESCAN ORSAY HOLDING) operating in secondary electron detection mode, in conjunction with 8 kV accelerating voltage, and a working distance between 8 and 26 mm.

2.1.4 Epoxy Resin Replicas

Samples from three regions (margin, lamina, and midrib) of fresh *Xanthosoma Sagittifolium* leaves (mature and young) were cut from the parent plant and epoxy resin positive replicas were prepared in accordance with prior art.[4,5,6] Plant leaves were rinsed with water to remove any surface debris and allowed to dry in air. Negative moulds of these surfaces were prepared by application of a polyvinylsiloxane base and cure mixture (President Plus Jet Light Body, Coltene/Whaledent AG) to the substrate, and immediately pressing down using a glass slide for a cure period of 10 min. Once the negative mould had hardened, it was carefully peeled away from the natural substrate surface, rinsed with water, and left to dry. Positive replicas from the negative moulds were prepared using epoxy resin (epoxy resin L and hardener S, R&G Faserverbundwerkstoffe GmbH). The epoxy resin was thoroughly mixed in a 5:2 ratio of resin to hardener, and then poured over the negative mould. Any trapped air bubbles were removed by placing under vacuum, and then the mixture was left to cure for 36 h in a desiccator. Finally, the

negative moulds were gently peeled away to reveal the positive replicas of the plant leaves.

2.1.5 1H,1H,2H,2H-Perfluorooctyle acrylate (PFAC-6) Plasmachemical Surface Modification

In the case of nanoimprinting, a functional coating was plasma deposited onto the negative mould prior to the filling with epoxy resin to produce the positive replica. Pulsed plasma deposition of the low surface energy precursor, 1H, 1H, 2H, 2H-perfluorooctyl acrylate (+95%, Fluorochem Ltd, purified using several freeze-pump-thaw cycles) was carried out in an electrodeless cylindrical glass reactor (5 cm diameter, 520 cm^3 volume, base pressure of 1×10^{-3} mbar, and with a leak rate better than 1.8×10^{-9} kg s^{-1}) enclosed in a Faraday cage.[7] The chamber was fitted with a gas inlet, a Pirani pressure gauge, a 30 L min^{-1} two-stage rotary pump attached to a liquid cold trap, and an externally wound copper coil (4 mm diameter, 9 turns, spanning 8–15 cm from the precursor inlet). All joints were grease-free. An L-C network was used to match the output impedance of a 13.56 MHz radio frequency (RF) power generator to the partially ionised gas load. The RF power source was triggered by a signal generator, and the pulse shape monitored with an oscilloscope. Prior to each experiment, the chamber was cleaned by scrubbing with detergent, rinsing in water and propan-2-ol, followed by oven drying. The system was then reassembled and evacuated. Further cleaning consisted of running an air plasma at 0.2 mbar pressure and 50 W power for 30 min. Next, polyvinylsiloxane negative moulds, and reference silicon (100) wafer pieces (Silicon Valley Microelectronics Inc.) were inserted into the centre of the reactor, and the system pumped back down to base pressure. At this stage, 1H,1H,2H,2H-perfluorooctyl acrylate monomer vapour was introduced at a pressure of 0.2 mbar for 5 min prior to ignition of the pulsed electrical discharge. The optimum conditions for functional group retention corresponded to a peak power of 40 W, and a duty cycle on-time of 20 μs and off-time equal to 20 ms. Deposition was allowed to proceed for 150 s to yield nm thick layers.[8] Upon plasma extinction, the precursor vapour continued to pass through the system for a further 3 min, and then the chamber was evacuated back down to base pressure.

2.2 Xanthosoma sagittifolium

Globally, over 1 billion people lack access to clean drinking water, many of whom live in the regions of the planet that are arid and semi-arid.[9] This lack of clean drinking water causes millions of deaths globally and a significant economic impact upon developing countries. The study of plant surfaces and their properties has led to the discovery of new, biomimetic, technological applications in multiple industries.[10] By analysing plant surfaces and their interactions with water, new ways in which water can be collected, such as from fog may be discovered.[11,12] This chapter will focus on the study of the wetting behaviour of plant surfaces as well as their replication, primarily focusing on *Xanthosoma sagittifolium*.

Xanthosoma sagittifolium is a species of tropical plant of the Aracea family found in South America and the tropical regions of Africa. It is cultivated as it produces a starchy, edible corm.[13] It has green leaves that range in size from small (30 cm) to very large (2 m), with primary and secondary veins a pale green colour. The leaves, particularly fresh growth, show a unique wetting behaviour when interacting with water, with water droplets running across the surface yet remaining pinned to the vein regions. This combination of water channelling and geographical wettability was the reason behind this plant being chosen for study.

2.3 Water Capture Behaviour of *Xanthosoma sagittifolium*

Xanthosoma sagittifolium displays hydrophobicity but also, a unique water droplet capture and release mechanism, with water pinning to veins before reaching a critical mass and rolling off the leaf. The water either runs down the veins towards the midrib and then down the midrib towards the leaf stem for the leaf pointing upwards, or towards the tip of the leaf and rolling off for the leaf point downwards due to gravity. The droplets tend to pin around the edges of the leaf (possibly due to the general leaf shape) before reaching a larger size/volume and rolling across the surface (**Figure 23**). This phenomenon remains true for both “young” (less than approximately 30 cm in length) and “mature” (greater than 30 cm in length) leaves. It is also observed that both the “mature” and “young” leaves of *Xanthosoma*

sagittifolium display nearly identical capture and release type mechanisms, with water droplets remaining pinned to the leaf veins.

(a) (b)

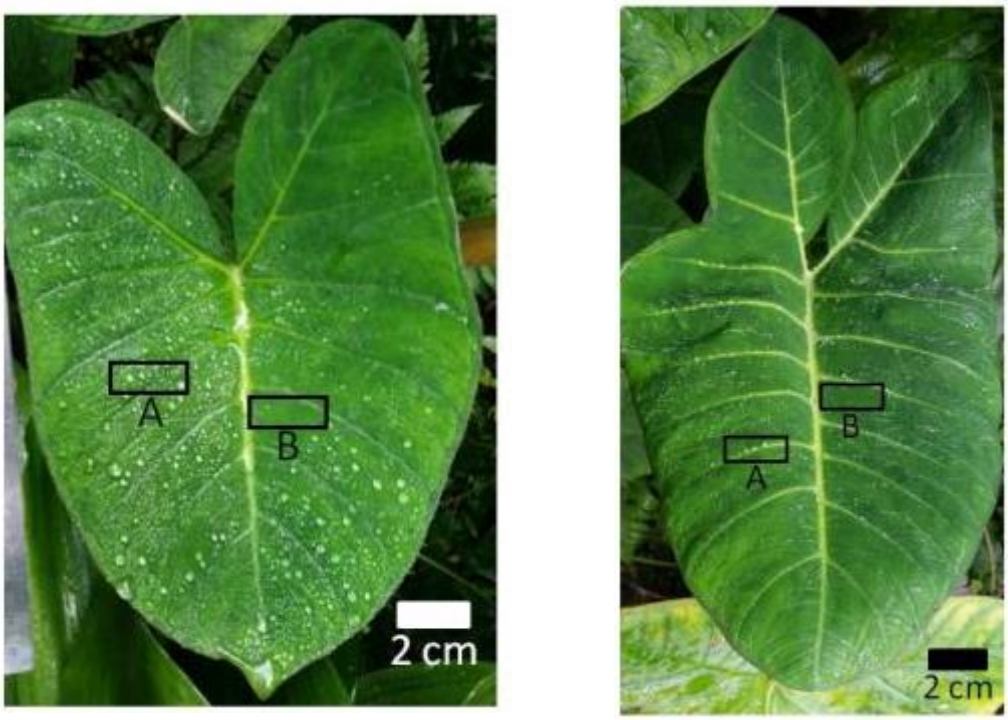

Figure 23: Photographs of (a) Young and (b) Mature *Xanthosoma sagittifolium* leaves after water droplet spraying. Note how the water droplets pin along the veins (box A)

The leaf itself consists of three main regions, the margin, lamina, and midrib, which show unique wetting behaviour when observed. These regions can be seen (**Figure 24**), with the yellow are indicating the margin, blue the lamina, and maroon the midrib.

Figure 24: Image of a leaf of *Xanthosoma sagittifolium* highlighting the three regions of a leaf. The margin (yellow area), lamina (blue region), and midrib (maroon region)

2.4 Water Contact Angle

Samples from each region, margin, lamina, and midrib, were cut from each leaf and water contact angles measured (**Table 4**).

Table 4: Water contact angles measured for a young leaf of *Xanthosoma sagittifolium*

Leaf Region	Static Water Contact Angle /°	Advancing Water Contact Angle /°	Receding Water Contact Angle /°
Margin	166 ± 5	152 ± 8	146 ± 10
Lamina	165 ± 4	152 ± 5	142 ± 10
Midrib	156 ± 8	157 ± 9	132 ± 22

Static water contact angles show a highly hydrophobic surface with contact angles of >150°, this indicates a surface which has a low surface energy, that causes the droplet to bead up in order to maximise the liquid-air intefacial energy (γ_{LA}). This

low surface energy is likely due to a combination of surface roughness, and hydrophobic surface chemistry as described in plants previously. Contact angle hysteresis (**Table 5**) calculated show low values for the margin and lamina region, but higher values for the midrib. The variation in value is also much more pronounced for the midrib region, matching with experimental observations of droplets pinning to the midrib and vein regions of the leaf across. The large variation in hysteresis indicates points on the surface that are high in energy, allowing a contact line to form between the water and the surface, resulting in a pinning of the water droplet.

Table 5: Contact angle hysteresis values for the three regions of a young leaf of *Xanthosom sagittifolium*

Leaf Region	Contact Angle Hysteresis /°
Margin	6 ± 4
Lamina	10 ± 5
Midrib	24 ± 15

The values obtained for the hysteresis of a young leaf of *Xanthosoma sagittifolium* as well as the static contact angle data is indicative of a superhydrophobic wetting state.[14] This wetting state is only present in the margin and lamina regions with low contact angle hysteresis and high static water contact angles, which indicates a low energy surface in these regions. The low variation in the hystersis observed for those two regions also indicates a broadly homogeneous surface with low energy, whereas the larger variaton observed in the midrib indicates a much higher energy surface resulting in a larger hysteresis. Water contact angles were then conducted on a mature leaf of *Xanthosoma sagittifolium* (**Table 6**) and the contact angle hysteresis measured (**Table 7**).

Table 6: Water contact angles measured for a mature leaf of *Xanthosoma sagittifolium*

Leaf Region	Static Water	Advancing Water	Receding Water

	Contact Angle /°	Contact Angle /°	Contact Angle /°
Margin	141 ± 3	146 ± 7	138 ± 3
Lamina	138 ± 4	134 ± 5	123 ± 11
Midrib	126 ± 5	130 ± 10	121 ± 9

Table 7: Contact angle hysteresis values for the three regions of a mature leaf of *Xanthosom sagittifolium*

Leaf Region	Contact Angle Hysteresis /°
Margin	8 ± 6
Lamina	4 ± 1
Midrib	9 ± 3

Static water contact angles show a lower value for the mature leaf when compared to those of a young leaf. This difference could be due to a number of reasons. One such possibility is that the surface cell structures between leaves change over the leaf lifetime, changing shape resulting in a smoother surface and therefore a lower R_f value which results in less of a cassie-baxter type wetting regime. A second possibility is the degradation of surface waxes over time due to physical attrition, again, resulting in a smoother surface as the surface chemistry changes to be more hydrophilic.[15,16] Another possibility is that the chemical composition of the waxes has changed over time as the leaf reaches maturity, the change could involve an increase in hydrophilic functional groups, such as alcohols and carboxylic acids, or a decrease in the chain length of the waxes. This change would ultimately result in a higher energy surface and therefore lower observed contact angle.

When comparing the contact angles and hysteresis for both young and mature leaves (**Figure 25**), the highest values are for the young leaf. With contact angles of >150° and a low contact angle hysteresis everywhere except the midrib region. This is indicative of a superhydrophobic wetting state and could be a reasoning behind the unique wetting behaviour observed for the leaves of *Xanthosoma sagittifolium*. In contrast, the mature leaf shows contact angles of approximately

140° and a low contact angle hysteresis for the midrib region. Despite this lower contact angle hysteresis, the mature leaf lacks the superhydrophobic wetting state seen for a younger leaf. In order to ascertain the cause of these differences, both structural and chemical studies of this surface were required.

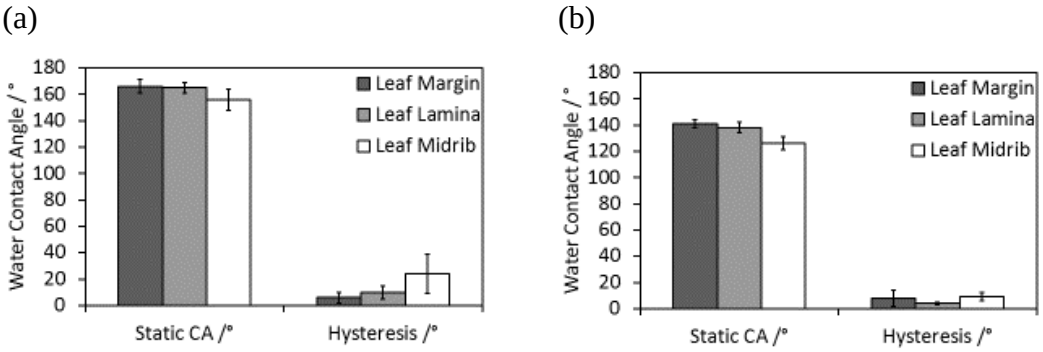

Figure 25: Comparison between the contact angle data obtained for both the young (a) and mature (b) leaves of *Xanthosoma sagittifolium*. Static water contact angles and contact angle hysteresis are shown

2.5 Scanning Electron Microscopy

SEM images were taken from the margin, lamina, and midrib regions of young and mature *Xanthosoma Sagittifolium* leaves. On the nano-scale, epicuticular waxes present on the surface show a similar structure for all three regions (margin, lamina, and midrib). The three regions also present veins across the surface which exhibit different surface structure to the surrounding region. The waxes display the typical irregular platelet type structure often found on plant leaf surfaces.[17] This structure serves to create small pockets of air between water droplets placed on the surface and the surface itself, resulting in a Cassie-Baxter wetting state.

The cell macro structure, however, is different between the non-veined and veined parts of the leaf. The cells have a more circular (convex structures, with sunken anticlinal walls) structure on the regions without veins and an elongated, oblong shaped appearance in the veined regions. The difference in surface structure between the vein/no vein regions reduces the surface roughness (**Section 1.3.2**), which could explain the difference in wettability observed. The 20 μm SEM images show the convex structure is most evident in the margin region, which is also the region with the lowest contact angle hysteresis (Figure 26).

The overall macro-structure of the surface cells shows a papillae type structure (convex in shape, with sunken anticlinal walls), with oblong, as opposed to convex shapes for cells located in the vein regions.[18, 19]

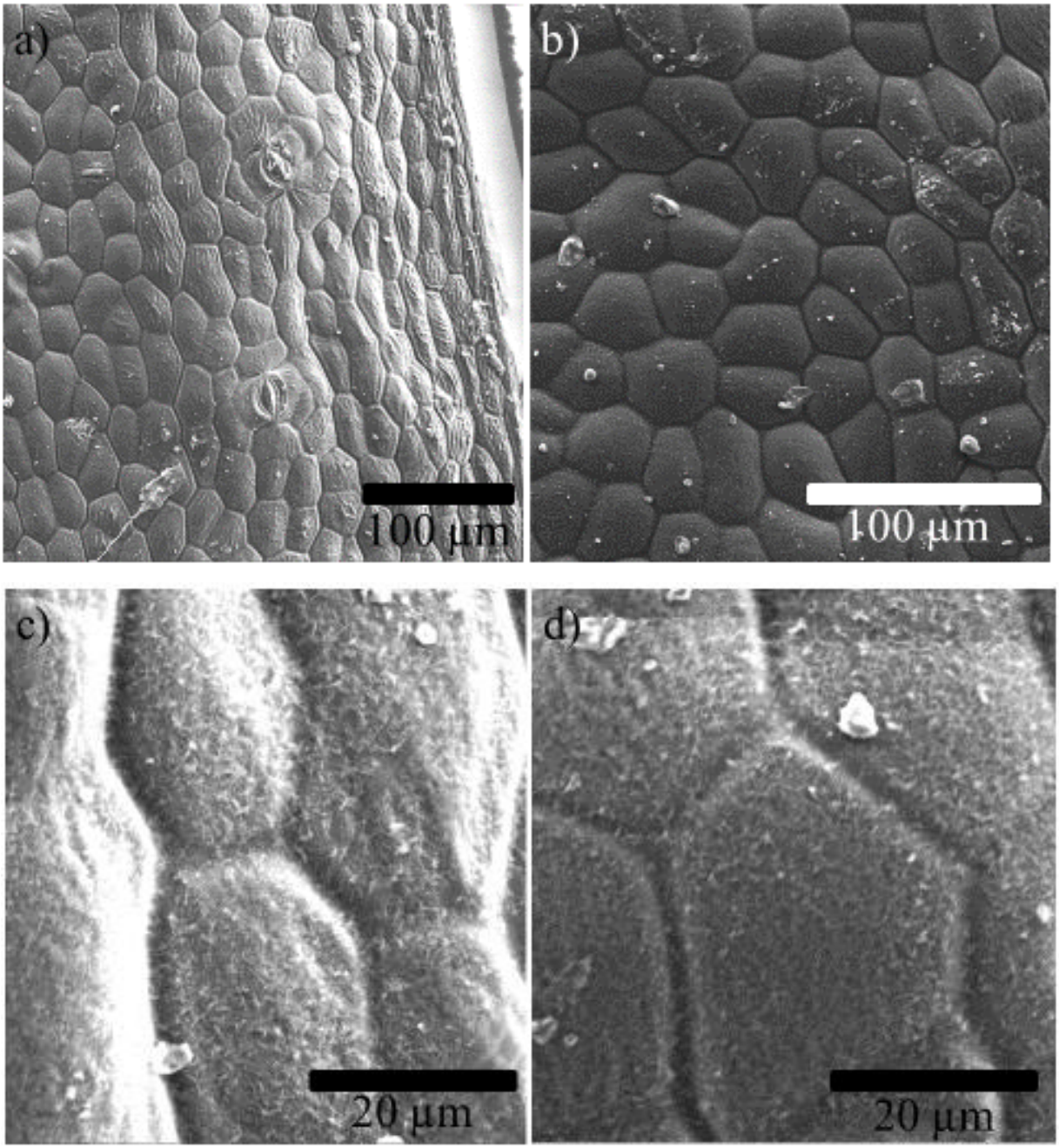

Figure 26: SEM images of a young leaf of *Xanthosoma sagittifolium* showing the leaf margin and a small area adjacent to it. The edge of the leaf (a, c), and the area adjacent to it (b, d) are shown

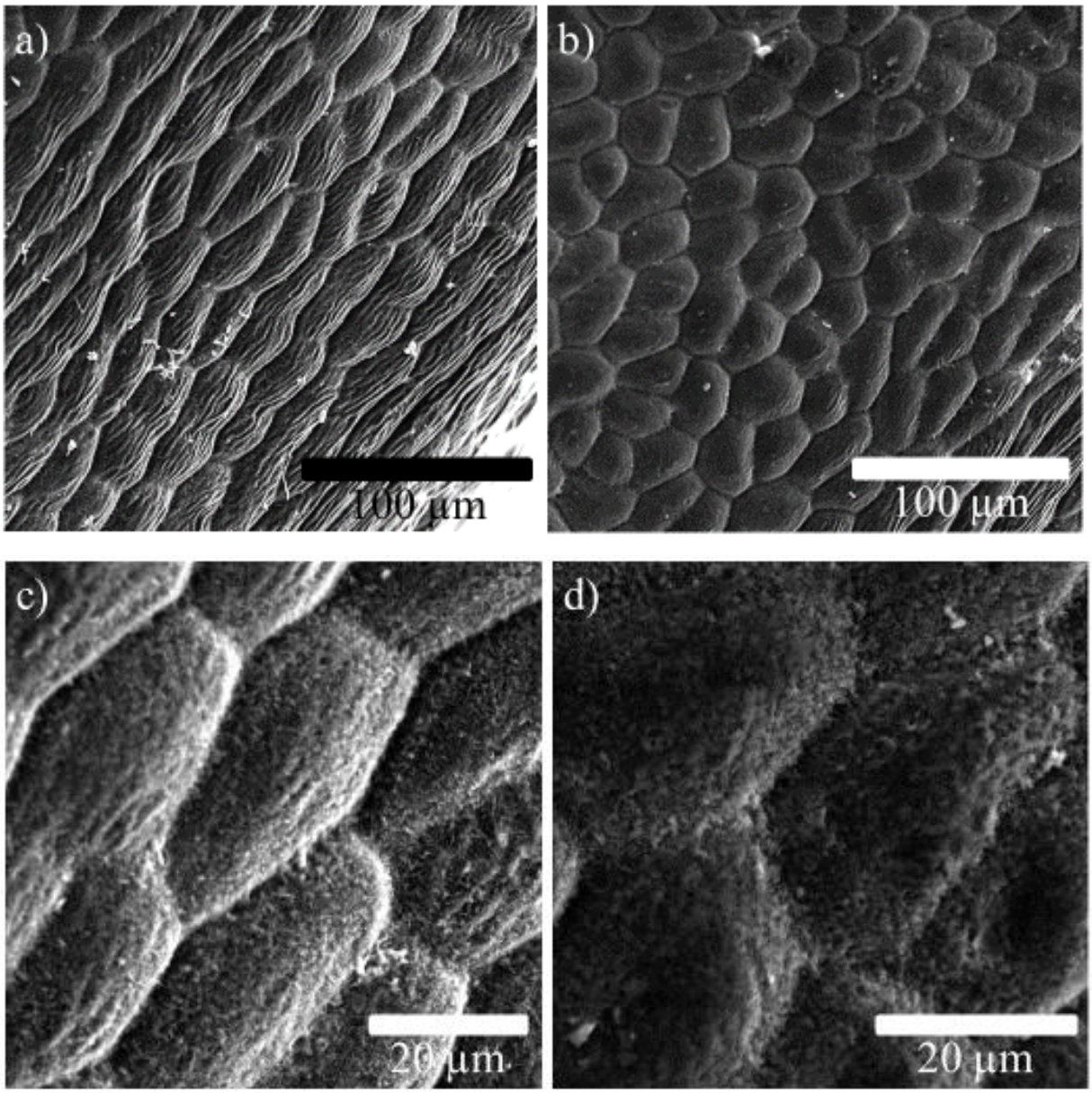

Figure 27: SEM images of a mature leaf of *Xanthosoma sagittifolium* showing the very edge of the leaf and the area immediately adjacent to it. The edge of the leaf (a, c), and the area adjacent to it (b, d) are shown

The two different types of leaves (Figure 26 and Figure 27) show similar surface macrostructures for both the very edge of the leaf and the area immediately adjacent to it. In the case of the mature leave samples, the wrinkling effect seen on the surface of the cells is a result of the cell beginning to dry out during the glycerol substitution process. Both young and mature leaves show a thin band of oblong shaped cells at the edge of the leaf surface, with convex cells shapes present at the region adjacent to the edge. Both young and mature leaves, and both types of cell, show the same epicuticular waxes present on the surface although, in the case of the

mature leaf, these waxes show some signs of wear and degradation resulting in a loss of definition. This difference in cell shape and wax structure explains the wetting behaviour observed for the leaves, with water droplets pinning to the very edge of the leaf (oblong cell shapes) and the mature leaf showing a slightly lower contact angle when compared to its young counterpart.

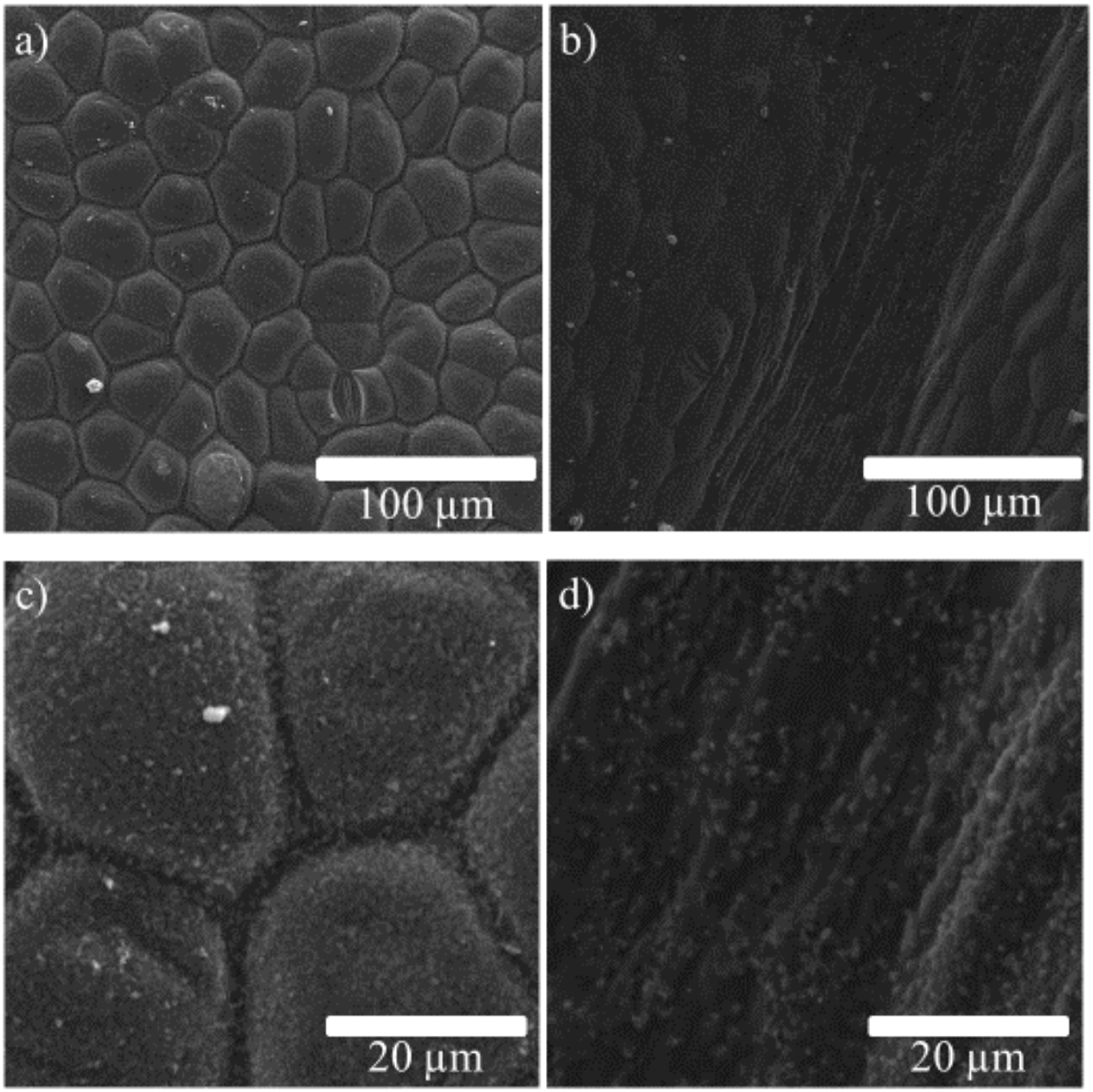

Figure 28: SEM images of a young leaf of *Xanthosoma sagittifolium* showing the margin. The leaf margin (a, c), and a vein region in that margin (b, d) are shown

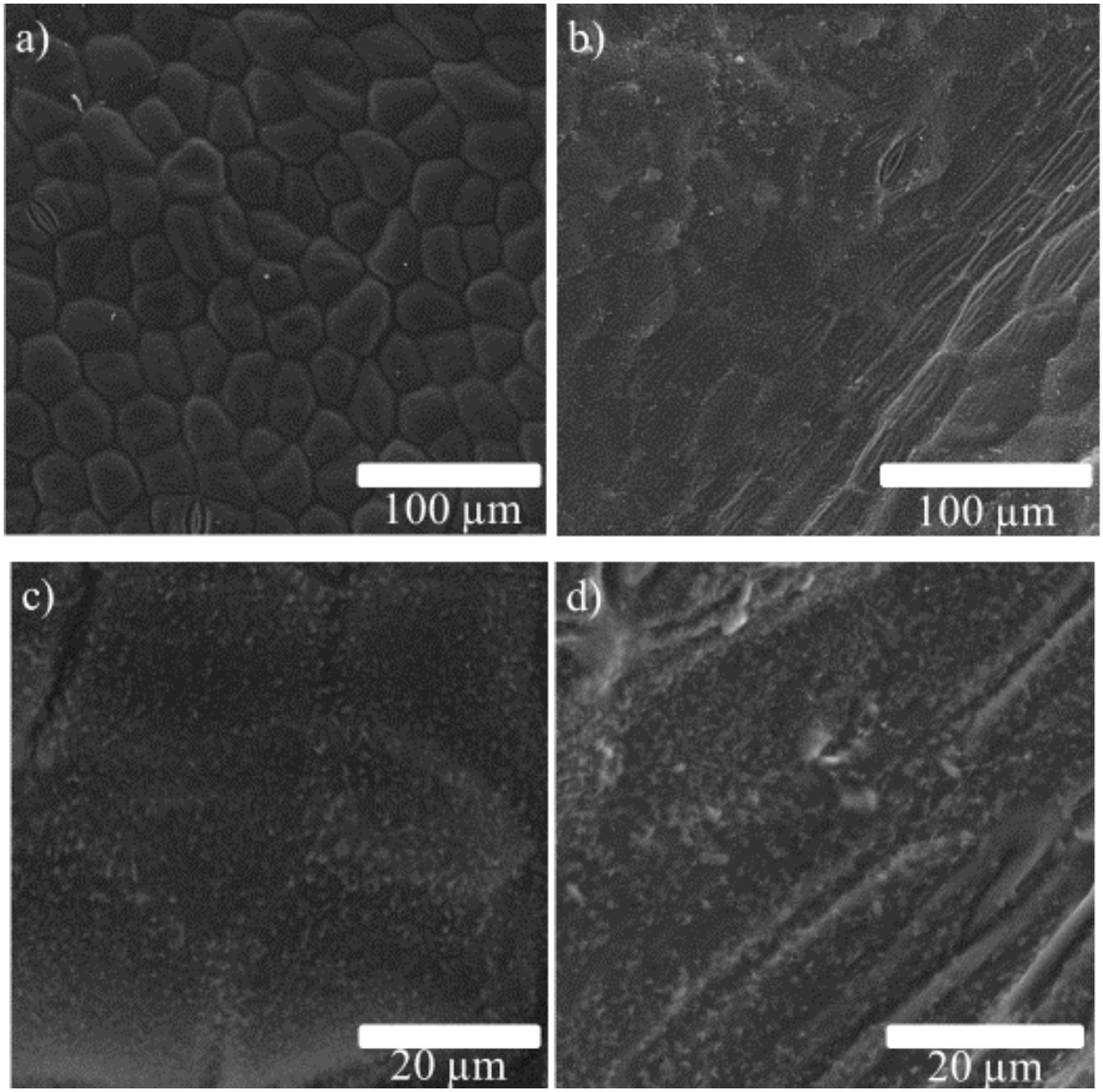

Figure 29: SEM images of a mature leaf of *Xanthosoma sagittifolium* showing the margin region. The leaf margin (a, c), and a vein region in that margin (b, d) are shown

The same cell shapes and patterns are also observed for the margin region of the leaf (**Figure 28 and Figure 29**), with papillae type cell shapes present in the regions without vein, and oblong cell shapes present for the veined regions. Nanoscale waxes are present across the entire surface.

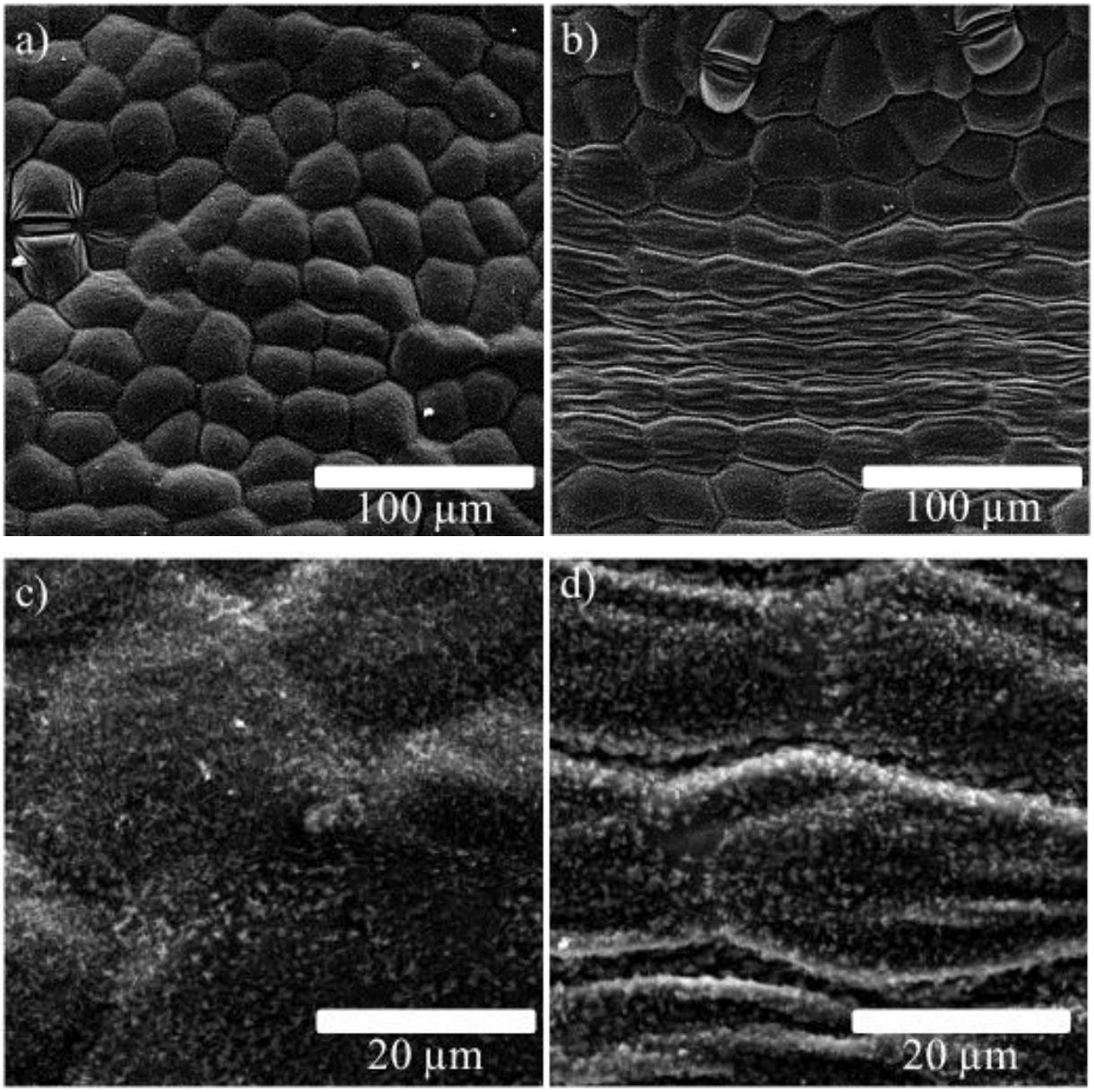

Figure 30: SEM images of a young leaf of *Xanthosoma sagittifolium* showing the lamina region. The leaf lamina (a, c), and a vein region in that lamina (b, d) are shown

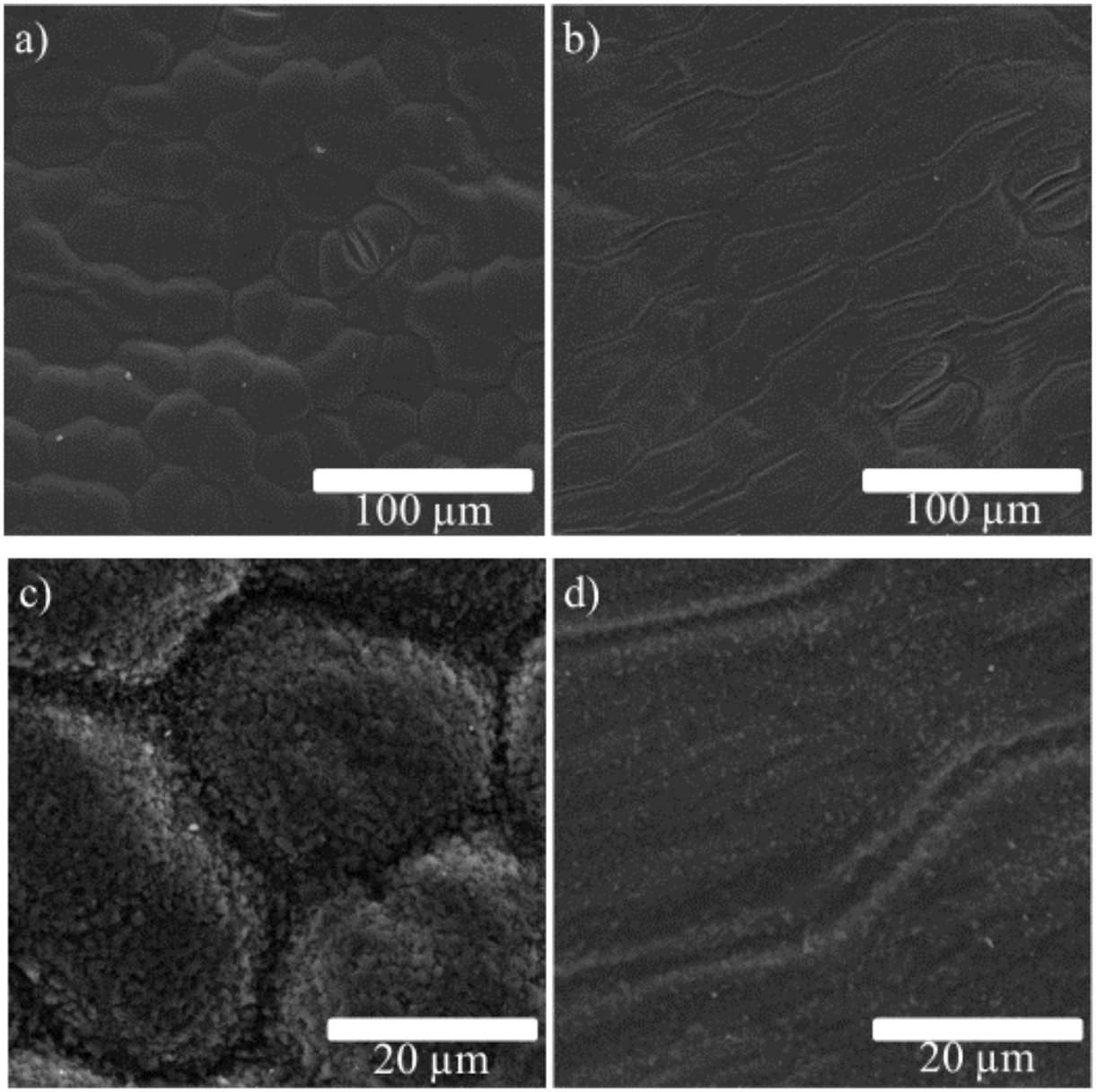

Figure 31: SEM images of a young leaf of *Xanthosoma sagittifolium* showing the midrib region. The leaf adjacent to the midrib (a, c), and the midrib (b, d) are shown

The lamina region for both young and mature leaves (**Figure** 31**30** and **Figure 32**), show very similar cell structures and surface waxes as the margin region. This similarity in structure helps explain why the margin and lamina regions show similar wettability.

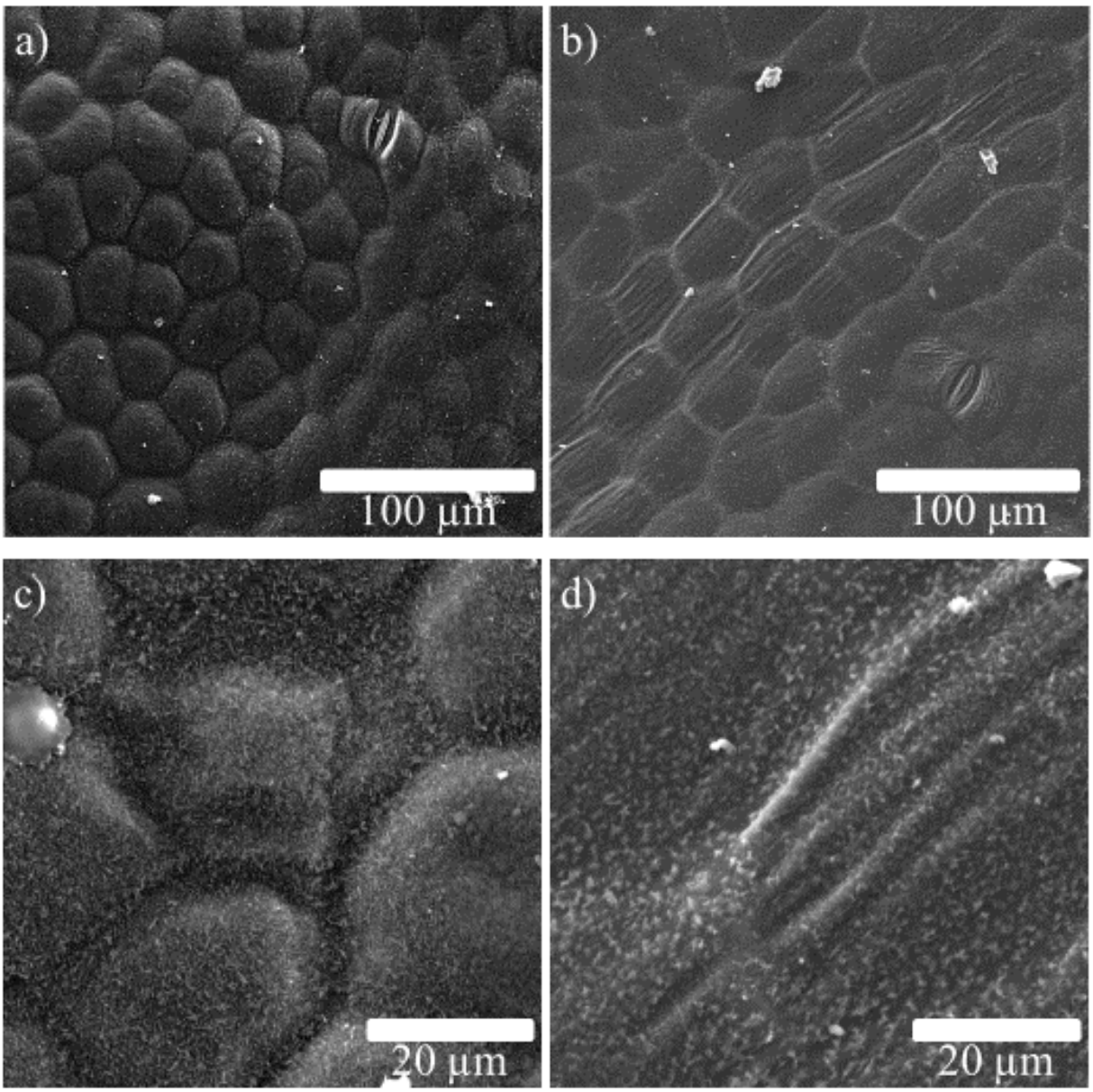

Figure 32: SEM images of a mature leaf of *Xanthosoma sagittifolium* showing the lamina region. The leaf lamina (a, c), and a vein region in that lamina (b, d) are shown

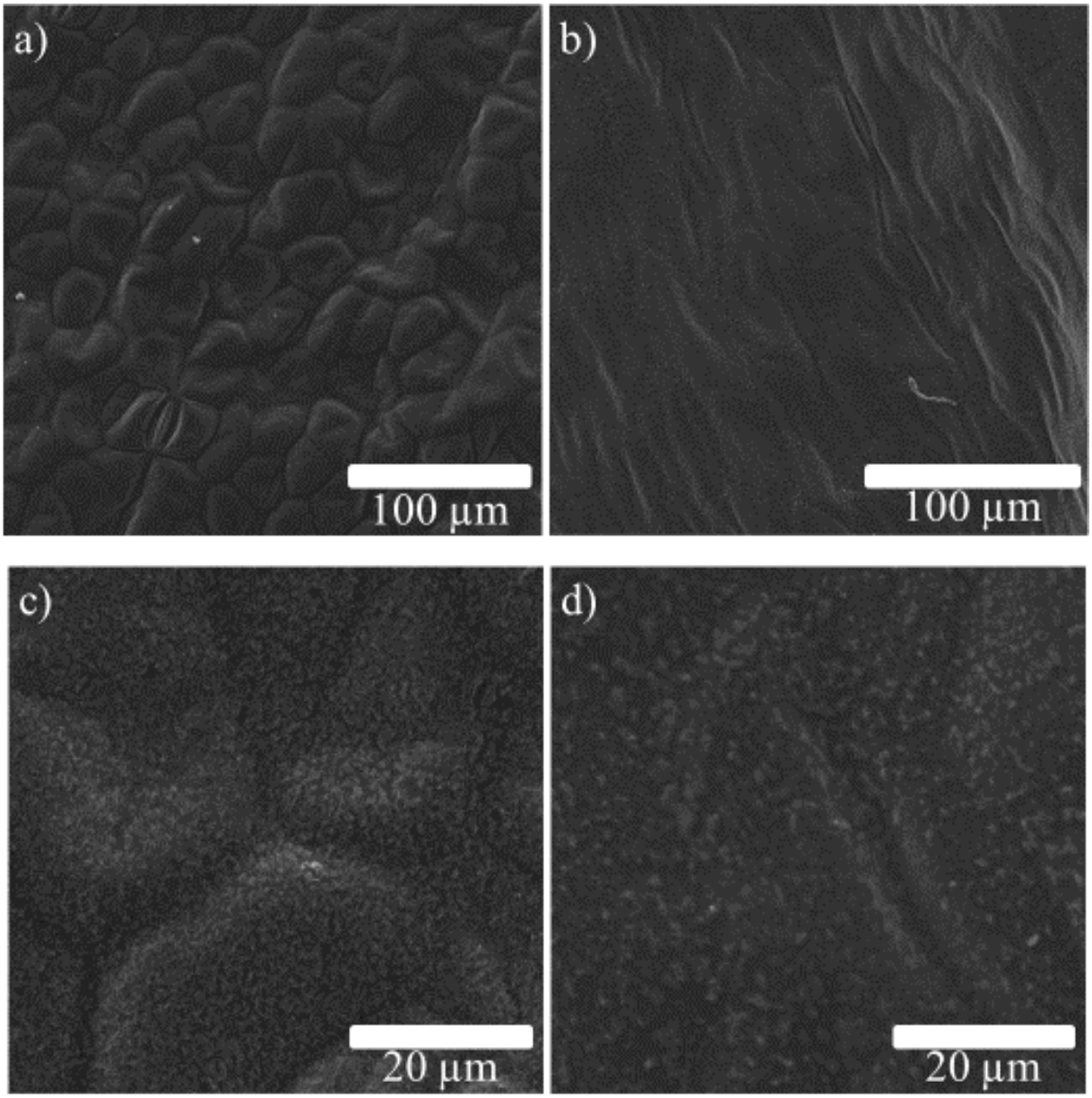

Figure 33: SEM images of a mature leaf of *Xanthosoma sagittifolium* showing the midrib region. The leaf adjacent to the midrib (a, c), and the midrib midrib (b, d) are shown

The largest variability is seen for the midrib region (**Figure 32** and **Figure 33**), with the vein regions showing poorly defined cell shapes. The lack of surface macro-roughness could help explain the difference in wettability observed, both in terms of static water contact angle and contact angle hysteresis. The lack of roughness in the vein regions leads to a poor Cassie-Baxter wetting state, with a lower R_f value and therefore a lower observed contact angle.

2.6 Functional Nanoimprint Replication

Functional nanoimprinting refers to a specific method for surface replication, combining the deposition of a functional nano layer with soft lithography. A negative mould of a sample is first created before the nano layer is deposited on the surface. Once deposition is complete, epoxy resin is poured into the mould and allowed to set before being separated. The separation detaches some of the polymer layer leaving it deposited on the surface of the epoxy resin replica (**Figure 34**).

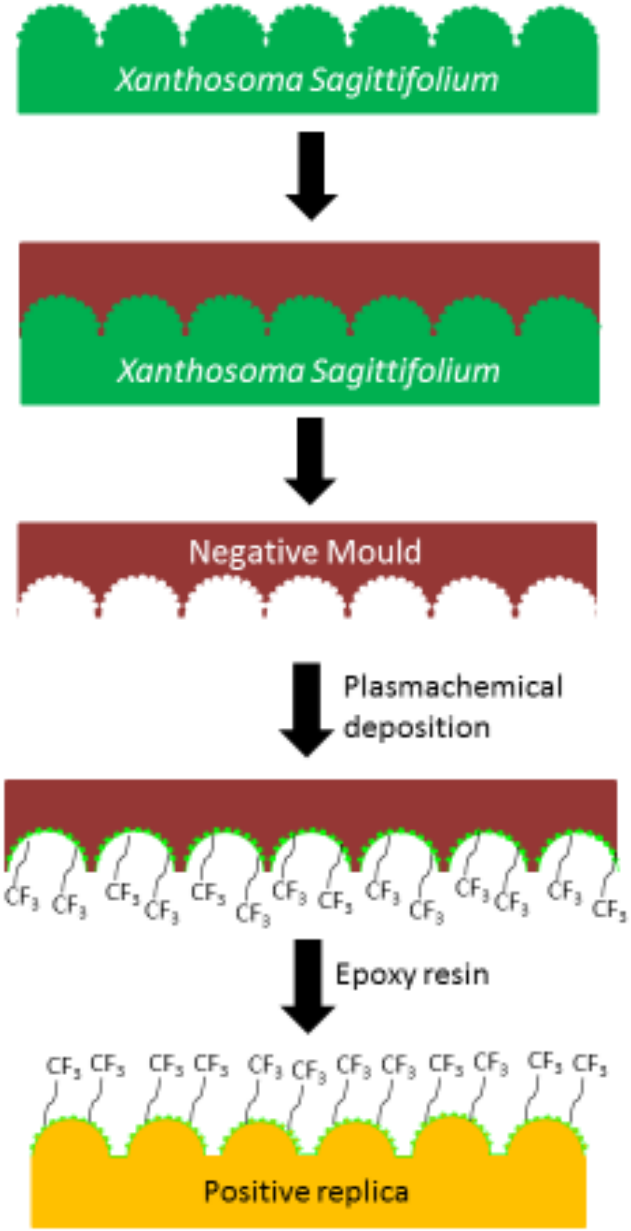

Figure 34: Scheme showing the nanoimprinting process on a leaf of *Xanthosoma sagittifolium*. The deposition of a polymer layer allows for multiple replicas to be made from the same negative mould

2.6.1 Nanoimprint Replication of *Tropaeolum majus*

Tropaeolum majus, commonly referred to as Indian Cress, is a flowering plant originally native to the Andes mountain range. It produces large spherical leaves which are superhydrophobic in nature, and static water contact angles provided from the literature show a contact angle of >150°.

Indian Cress was chosen as a trial plant as its surface macro structure is similar to that of *Xanthosoma sagittifolium* making it a good analogue in the refinement of the nanoimprinting process.Prior to deposition of the polymer layer a series of replicas were made in order to conduct microscopy and contact angle analysis, and these “untreated replicas” were used as a comparison.

Scanning electron microscopy images show that the replication process can be used to accurately replicate the surface of the Indian Cress, with the nanoscale waxes present on the surface detected, albeit with limited resolution (**Figure 35**).

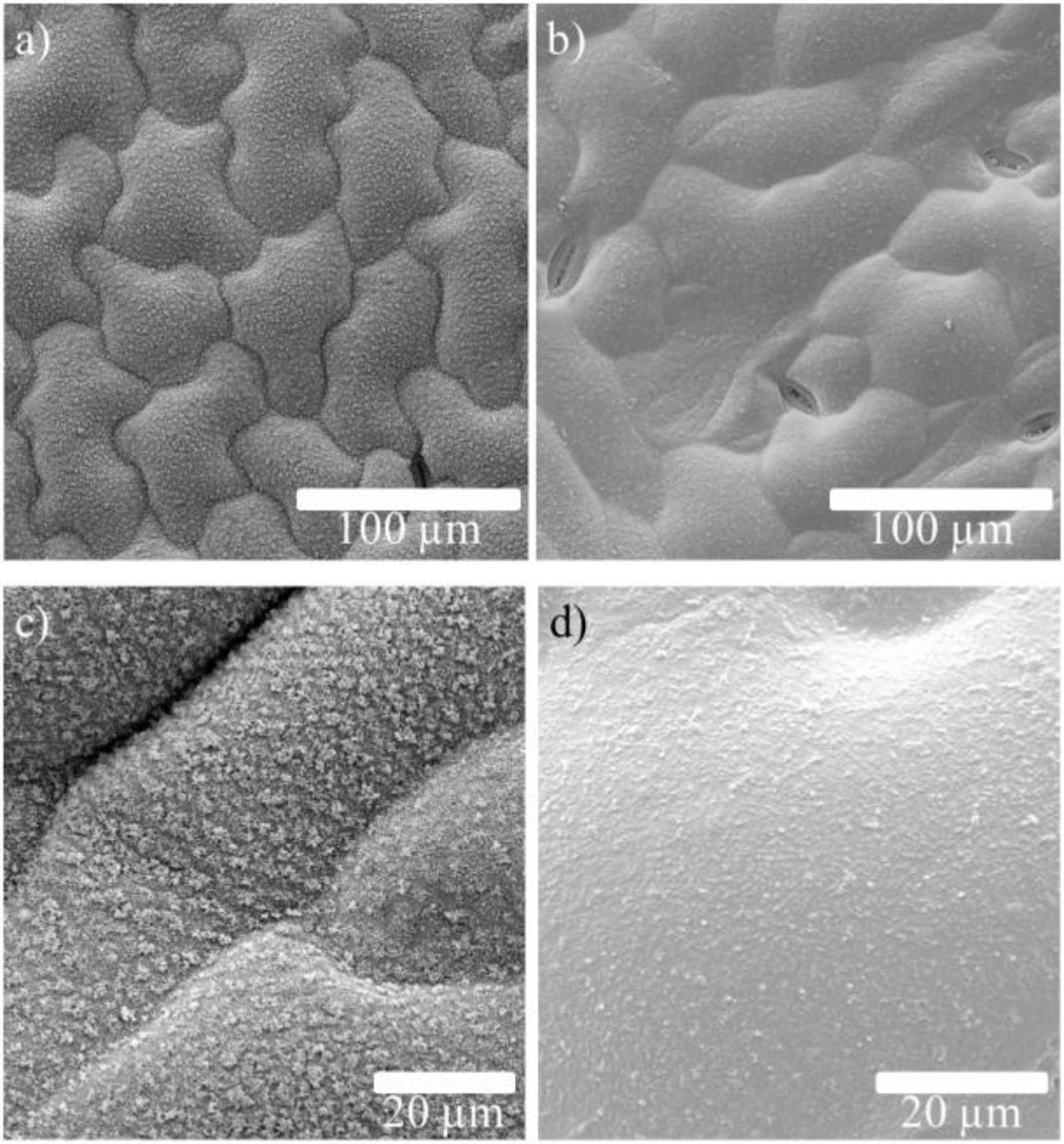

Figure 35: SEM images of the leaf of Indian Cress (a, c) and a corresponding replica at the same scale (b, d). Note how it is possible to detect the nanoscale waxes present on the surface of the leaf, with limited accuracy

As the SEM images show, it is possible to replicate the surface macro structure to a reasonable degree of accuracy using this technique, and is even able to replicate stomata in the leaf surface. It is also possible to distinguish the nanoscale waxes present on the surface, although a significant loss of accuracy occurs. This loss of accuracy is seen more generally across the mould with small surface defects

occurring regularly across the surface of the replica, resulting in localised areas of relatively high surface energy. Replication of the surface roughness alone is not sufficient to mimic the surface energy of the plant and the contact angles displayed. Contact angles on the epoxy resin replicas were then measured (**Table 8**).

Table 8: Water contact angles taken on epoxy resin positive replicas of Indian Cress

Static Water Contact Angle /°	**Advancing Water Contact Angle /°**	**Receding Water Contact Angle /°**
108 ± 11	112 ± 4	Pin

The static water contact of 108 ± 11 indicates a slightly hydrophobic surface was created, with an advancing contact angle of 112 ± 4 and a receding contact angle which resulting in a pinning of the contact line indicating a high surface energy. Pinning of the contact line occurs because the epoxy resin is a mixture of polymer chains and as such does not form a chemically homogenous surface. The lack chemical homogeneity causes a random distribution of surface energy across the surface and therefore pinning of the contact line. In order to ascertain how the surface roughness has affected the water contact angle, contact angle data needs to be obtained on a flat epoxy resin sample. Flat epoxy resin samples were created by taking 20 mm x 20 mm silicon wafer (Silicon valley, Microelectronics Inc.) and creating a negative mould of the surface. Epoxy resin was prepared as described previously and 23 replicas were created. Contact angles were then measured (**Table 9**).

Table 9: Contact angle data for flat epoxy resin squares created using moulds of silicon wafers

Sample Code	Static Water Contact Angle /°	Advancing Water Contact Angle /°	Receding Water Contact Angle /°
1	76 ± 2	85 ± 2	Pin
2	77 ± 3	82 ± 2	Pin
3	83 ± 3	88 ± 2	Pin
4	78 ± 1	81 ± 2	Pin
5	79 ± 1	85 ± 1	Pin
6	80 ± 7	86 ± 4	Pin
7	80 ± 1	86 ± 2	Pin
8	81 ± 2	83 ± 1	Pin
9	78 ± 4	83 ± 3	Pin
10	74 ± 4	78 ± 6	Pin
11	75 ± 6	75 ± 7	Pin
12	70 ± 9	71 ± 7	Pin
13	79 ± 3	85 ± 2	Pin
14	78 ± 2	84 ± 2	Pin
15	81 ± 2	83 ± 5	Pin
16	81 ± 2	81 ± 4	Pin
17	85 ± 6	81 ± 4	Pin
18	77 ± 3	84 ± 2	Pin
19	81 ± 1	85 ± 3	Pin
20	76 ± 2	82 ± 1	Pin
21	79 ± 8	86 ± 4	Pin
Average	78 ± 5	82 ± 5	Pin

An average static water contact angle across all samples of 78 ± 5 shows flat epoxy resin to be slightly hydrophilic, again with a pinning of the contact line occurring during receding angle measurements. This pinning of the contact line is again due to the non homogeneity of the surface chemistry due to the random

distribution of polymer chains. Comparison between the replicas of Indian Cress and flat squares indicates a large increase in static contact angle of 30°, sufficient to switch the surface from hydrophilic to hydrophobic. This shows that mimicking the surface macro structure has imported hydrophobic activity.

A series of negative moulds of Indian Cress were then treated with 1H,1H,2H,2H-Perfluorooctyle acrylate (PFAC-6) using a pulsed plasma. This deposited a nanometre thick layer of polymer on the surface of the mould. By altering experiment conditions it was possible to deposit films of different thicknesses. A polymer layer of approximately 150 nm, 100 nm, and 50 nm, was deposited on separate negative moulds of Indian Cress. Epoxy resin positive replicas were created from each mould and contact angles measured on the replicas (**Table 10**). The PFAC-6 layer was deposited to mimic the surface chemistry and a range of thicknesses used to test the optimal coating.

Table 10: Water contact angles for three replicas of Indian Cress, each made from a mould with a different thickness of PFAC-6 deposited on the surface

PFAC-6 Thickness /nm	Static Water Contact Angle /°	Advancing Water Contact Angle /°	Receding Water Contact Angle /°
163	130 ± 5	139 ± 5	Pin
94	133 ± 2	142 ± 2	Pin
58	143 ± 6	152 ± 4	Pin

Observed contact angles are the same for samples with 163 nm and 94 nm thick PFAC-6 layers deposited on the negative mould, showing a hydrophobic surface with a contact angle over 20° higher than that of an untreated replica. The largest improvement in static water contact angle is observed for the 58 nm PFAC-6 layer, showing an improvement of nearly 40° over the replica and a combined improvement of nearly 70° over a flat square, now approaching the contact angles typical of a superhydrophobic surface. The presence of a layer of CF_2 functionalities on the surface of the replica lowers the surface energy causing an increase in hydrophobicity as the liquid-air interface becomes a more favourable interaction, which explains the improvement in static water contact angle observed for all samples.

The difference in observed contact angles between the different thicknesses is likely due to the PFAC-6 being sufficiently thick that it obscures surface macro features present in the replicas. This serves to lower the overall surface roughness resulting in a lower contact angle for the thicker films. Since the contact angle of the original leaf is >150° a thinner PFAC-6 layer leads to replicas that more closely match the native plant, therefore when depositing PFAC-6 on the negative moulds of *Xanthosoma sagittifolium* 50–100 nm thicknesses are desirable.

Since the separation of the epoxy resin positive replica from the negative mould removes only a portion of the deposited PFAC-6 layer, it is possible to create multiple iterations using the same mould and observe similar wetting behaviour. Contact angles were then measured on the multiple iterations created (**Table 11**).

Table 11: Contact angle data for multiple iterations of epoxy resin replicas for multiple moulds of Indian Cress. A total of five iterations were created for each mould

PFAC-6 Thickness /nm	Iteration No.	Static Water Contact Angle /°	Advancing Water Contact Angle /°	Receding Water Contact Angle /°
163	1	130 ± 5	139 ± 5	Pin
	2	131 ± 3	138 ± 5	Pin
	3	133 ± 11	134 ± 6	Pin
	4	139 ± 5	142 ± 4	Pin
	5	131 ± 6	135 ± 6	Pin
94	1	133 ± 2	142 ± 2	Pin
	2	131 ± 3	139 ± 5	Pin
	3	132 ± 8	138 ± 7	Pin
	4	136 ± 2	144 ± 5	Pin
	5	136 ± 5	146 ± 7	Pin
58	1	143 ± 6	152 ± 4	Pin
	2	139 ± 3	136 ± 9	Pin
	3	132 ± 1	143 ± 6	Pin
	4	143 ± 2	152 ± 1	Pin
	5	142 ± 3	143 ± 5	Pin

A total of five separate iterations were made from each mould of Indian Cress, contact angles measured on the replicas showed similar water contact angles for each successive iteration apart from the third iteration of the 58 nm mould. This is likely due to a defect occurring during the peeling process where a low amount of PFAC-6 polymer was transferred to the epoxy resin replica.

It was also observed that the negative moulds became mechanically degraded over time, with one disintegrating after the fifth iteration was made, likely due to repeated stress incurred during the peeling process. Nevertheless, these experiments have shown it is possible to create a reasonable surface mimic which demonstrates similar surface properties to that of the leaf through multiple iterations. Therefore

this appears to be a suitable method to be used for replicating the leaves of *Xanthosoma sagittifolium* and potentially other plants (**Figure 36**). White, grey, and dark grey bars correspond to the 163 nm, 94 nm, and 58 nm replicas respectively.

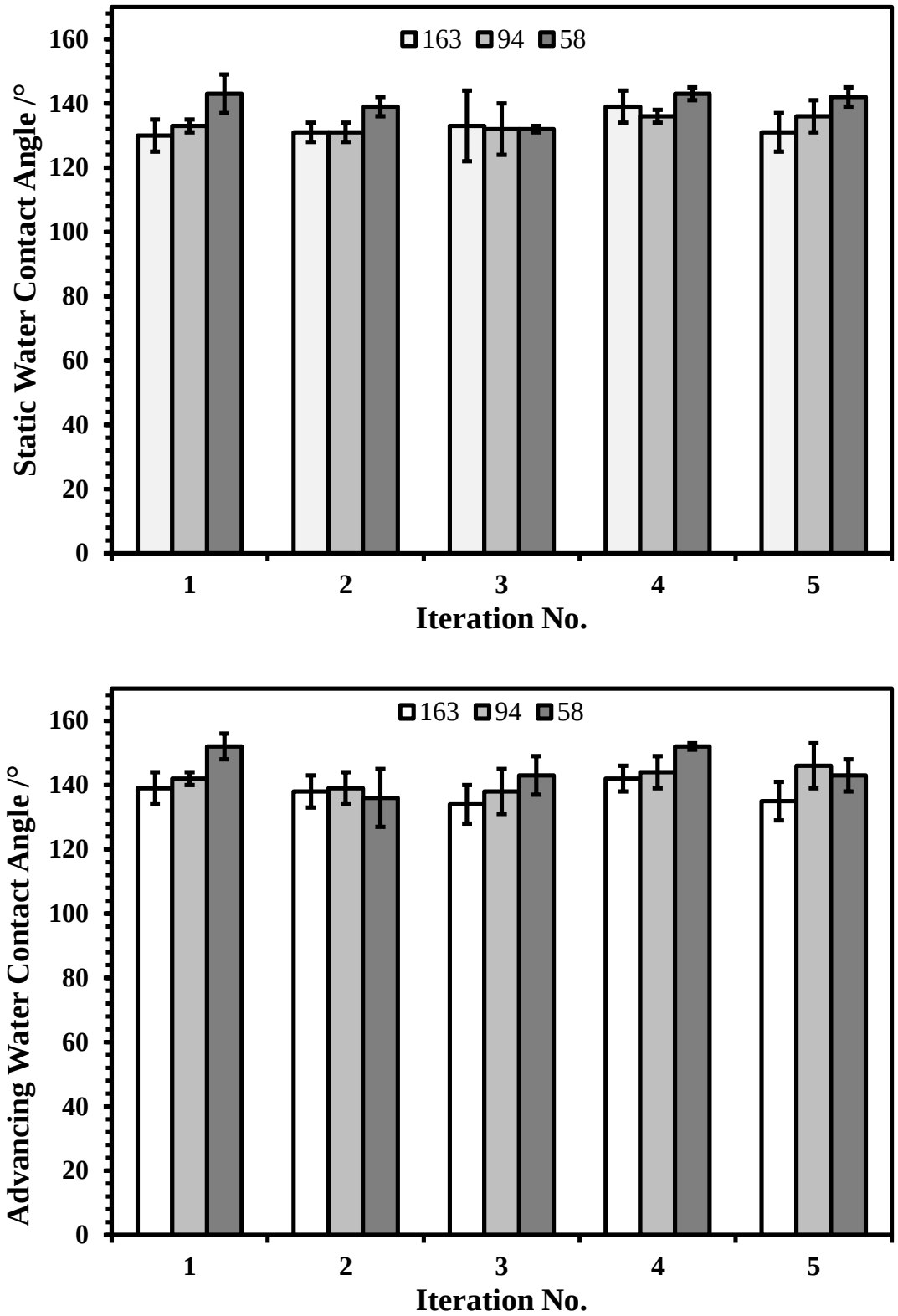

Figure 36: Graphs summarising the contact angles observed for each successive iteration of plant replication, all receding contact angles resulted in a pinning of the contact line and so are not shown. Coating thickness are shown

2.6.2 Nanoimprint Replication of *Xanthosoma sagittifolium*

As described previously there are three main regions on the leaves of *Xanthosoma sagittifolium*, the margin, lamina, and midrib, as well as two different ages of leaf. The leaves were rinsed with deionised water (to remove surface contaminants) and allowed to air dry before sample cuttings were taken. Three negative moulds were made for each of the three regions on each leaf to yield nine negative moulds per leaf. Epoxy resin replicas were made using all samples and contact angles measured (**Table 12** and **Table 13**).

Table 12: Water contact angles for epoxy resin replicas of *Xanthosoma sagittifolium*, in this case, contact angles of a young leaf are shown

Sample Region	Sample No.	Static Water Contact Angle /°	Advancing Water Contact Angle /°	Receding Water Contact Angle /°
Margin	1	89 ± 5	93 ± 3	Pin
	2	90 ± 3	92 ± 2	Pin
	3	89 ± 7	88 ± 6	Pin
Lamina	1	90 ± 3	91 ± 3	Pin
	2	88 ± 4	90 ± 6	Pin
	3	88 ± 3	90 ± 5	Pin
Midrib	1	78 ± 3	77 ± 6	Pin
	2	96 ± 10	92 ± 4	Pin
	3	101 ± 6	100 ± 4	Pin

Table 13: Water contact angles for epoxy resin replicas of *Xanthosoma sagittifolium*, in this case, contact angles of a mature leaf are shown

Sample Region	Sample No.	Static Water Contact Angle /°	Advancing Water Contact Angle /°	Receding Water Contact Angle /°
Margin	1	92 ± 9	97 ± 10	Pin
	2	95 ± 9	95 ± 12	Pin
	3	101 ± 4	105 ± 5	Pin
Lamina	1	86 ± 6	86 ± 8	Pin
	2	96 ± 4	94 ± 5	Pin
	3	107 ± 3	108 ± 2	Pin
Midrib	1	97 ± 5	96 ± 8	Pin
	2	93 ± 3	94 ± 3	Pin
	3	92 ± 7	92 ± 7	Pin

Static water contact angles for the epoxy resin positive replicas show contact angles that are mostly hydrohpobic. The static contact angles observed are in line with the behaviour expected for the three regions, with the margin and the lamina showing similar values and the midrib showing lower values. This behaviour matches that observed for the leaf as described previously.

There are some anomalous contact angles however, particularly for the mature leaf, showing a higher variation in measured contact angle and a higher degree of hydrophilicity. This difference is expected as the mature leaf is likely to have a higher proportion of surface defects due to its age. Replicas were then washed successively in H_2O (**Table 14** and **Table 15**) and a 50:50 v/v isopropyl alcohol/cyclohexane solution (**Table 16** and **Table 17**), then contact angles measured. This was to remove any surface contaminants that may be present, resulting in the anomalous contact angles observed.

Table 14: Water contact angles for epoxy resin replicas of *Xanthosoma sagittifolium*, in this case, contact angles of a young leaf are shown after a H_2O wash

Sample Region	Sample No.	Static Water Contact Angle /°	Advancing Water Contact Angle /°	Receding Water Contact Angle /°
Margin	1	100 ± 9	103 ± 12	Pin
	2	97 ± 7	101 ± 6	Pin
	3	92 ± 8	98 ± 1	Pin
Lamina	1	100 ± 3	103 ± 4	Pin
	2	97 ± 3	101 ± 4	Pin
	3	93 ± 9	100 ± 6	Pin
Midrib	1	88 ± 5	85 ± 16	Pin
	2	100 ± 5	101 ± 6	Pin
	3	95 ± 11	99 ± 8	Pin

Table 15: Water contact angles for epoxy resin replicas of *Xanthosoma sagittifolium*, in this case, contact angles of a mature leaf are shown after a H_2O wash

Sample Region	Sample No.	Static Water Contact Angle /°	Advancing Water Contact Angle /°	Receding Water Contact Angle /°
Margin	1	114 ± 4	114 ± 6	Pin
	2	107 ± 6	107 ± 3	Pin
	3	108 ± 2	112 ± 4	Pin
Lamina	1	111 ± 4	111 ± 4	Pin
	2	101 ± 9	109 ± 6	Pin
	3	106 ± 7	111 ± 4	Pin
Midrib	1	100 ± 4	101 ± 5	Pin
	2	101 ± 5	102 ± 1	Pin
	3	91 ± 8	91 ± 12	Pin

Table 16: Water contact angles for epoxy resin replicas of *Xanthosoma sagittifolium*, in this case, contact angles of a young leaf are shown after an IPA/CY wash

Sample Region	Sample No.	Static Water Contact Angle /°	Advancing Water Contact Angle /°	Receding Water Contact Angle /°
Margin	1	93 ± 6	95 ± 1	Pin
	2	85 ± 10	90 ± 9	Pin
	3	82 ± 13	88 ± 13	Pin
Lamina	1	81 ± 1	82 ± 6	Pin
	2	77 ± 7	86 ± 6	Pin
	3	86 ± 12	89 ± 9	Pin
Midrib	1	85 ± 3	86 ± 3	Pin
	2	88 ± 5	92 ± 3	Pin
	3	61 ± 7	60 ± 2	Pin

Table 17: Water contact angles for epoxy resin replicas of *Xanthosoma sagittifolium*, in this case, contact angles of a mature leaf are shown after an IPA/CY wash

Sample Region	Sample No.	Static Water Contact Angle /°	Advancing Water Contact Angle /°	Receding Water Contact Angle /°
Margin	1	102 ± 1	101 ± 3	Pin
	2	99 ± 5	103 ± 2	Pin
	3	114 ± 7	117 ± 6	Pin
Lamina	1	96 ± 4	97 ± 5	Pin
	2	90 ± 7	91 ± 7	Pin
	3	102 ± 6	106 ± 4	Pin
Midrib	1	88 ± 3	84 ± 5	Pin
	2	94 ± 8	93 ± 6	Pin
	3	100 ± 6	99 ± 1	Pin

After washing, static contact angles range from slightly hydrophilic (young leaf) to slightly hydrophobic (mature leaf). This data is similar in relation to the contact angles of the Indian Cress showing the similarity in underlying surface structure for the two leaves and corresponding replicas. Negative moulds were then treated using a pulsed plasma deposition as described previously (**Section 2.1**) by Andrea Carletto.

Negative moulds were made of both young and mature leaves of *Xanthosoma sagittifolium* and in the case of the replicas of the young leaf, average PFAC-6 thickness was 42 nm, with replicas of the mature leaf averaging 108 nm PFAC-6 thickness.

Table 18: Water contact angles for epoxy resin replicas of young *Xanthosoma sagittifolium* where the negative mould was pre-treated with PFAC-6. A total of three iterations for each region were made

Iteration No.	Iteration No.	Static Water Contact Angle /°	Advancing Water Contact Angle /°	Receding Water Contact Angle /°
Margin	1	144 ± 5	145 ± 7	121 ± 17
	2	147 ± 2	148 ± 3	118 ± 9
	3	144 ± 4	150 ± 2	123 ± 13
Lamina	1	146 ± 2	145 ± 3	113 ± 4
	2	146 ± 2	149 ± 5	126 ± 5
	3	128 ± 17	142 ± 6	102 ± 18
Midrib	1	134 ± 4	149 ± 5	117 ± 11
	2	135 ± 8	143 ± 4	110 ± 5
	3	118 ± 9	135 ± 6	94 ±4

Table 19: Water contact angles for epoxy resin replicas of mature *Xanthosoma sagittifolium* where the negative mould was pre-treated with PFAC-6. A total of three iterations for each region were made

Iteration No.	Iteration No.	Static Water Contact Angle /°	Advancing Water Contact Angle /°	Receding Water Contact Angle /°
Margin	1	134 ± 7	141 ± 3	108 ± 4
	2	130 ± 1	141 ± 2	100 ± 6
	3	135 ± 10	144 ± 5	110 ± 8
Lamina	1	131 ± 2	133 ± 2	113 ± 8
	2	127 ± 3	143 ± 5	108 ± 9
	3	135 ± 1	147 ± 2	118 ± 4
Midrib	1	114 ± 2	126 ± 6	106 ± 10
	2	114 ± 1	132 ± 5	101 ± 10
	3	130 ± 5	141 ± 3	108 ± 6

Water contact angles obtained for the replicas of *Xanthosoma sagittifolium* are summarised (**Figure 37**). The static contact angles of a young leaf show superhydrophobic values for all regions >150° and hydrophobic values for the mature leaf ~140°. Replicas of the leaf surface that are untreated epoxy show similar static contact angles and a high contact angle hysteresis for all samples, by using the nanoimprinting process to alter the surface chemistry, the hydrophobicity of the surface can be improved and the observed difference between the margin/lamina and midrib region better mimicked. An increase in static contact angle is observed for all samples, with values greater than 140° and a much lower contact angle hysteresis. The lower contact angle hysteresis is observed as the surface becomes more homogeneous due to the polymer layer now present on the surface, resulting in a lower observed contact angle hysteresis when compared to untreated replicas. The polymer layer is not however uniform, resulting in some lack of homogeneity on the surface and therefore higher contact angle hysteresis than *Xanthosoma sagittifolium*. These values are not drastically dissimilar from the plant surface and the reduction in surface hydrophobicity due to limitations within the replication technique,

particularly in mimicking surface roughness. Of particular note is the increased tendency of water to pin to the replica surface, a limitation of this technique that is likely to persist when replicating other plant surfaces due to the surface being non homogenous.

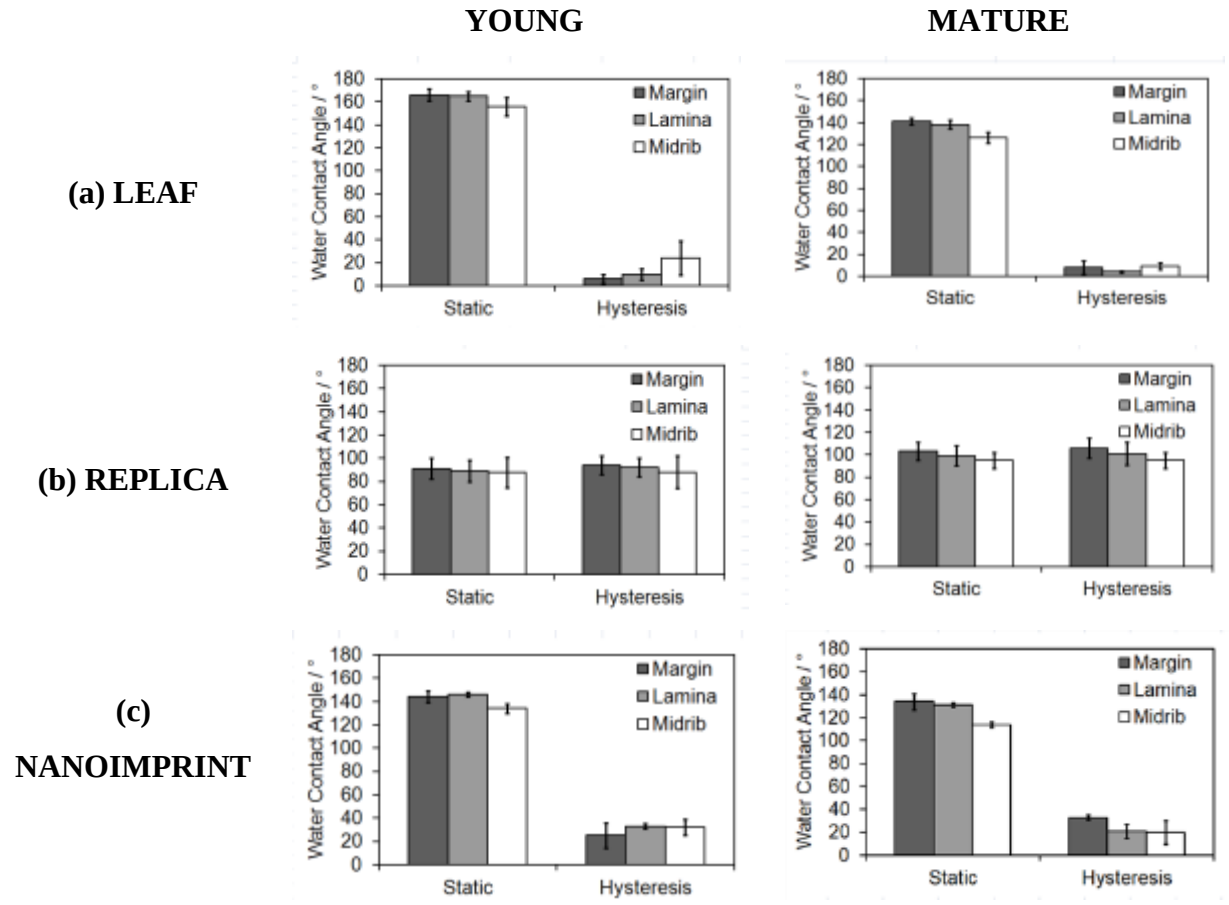

Figure 37: Graphical summary of the observed contact angles and hysteresis for both the young and mature replicas of *Xanthosoma sagittifolium*, first nanoimprint iterations are shown, with the 42 nm PFAC-6 thickness for the young leaf and the 108 nm PFAC-6 thickness for the mature leaf shown

The leaves of *Xanthosoma sagittifolium* have been successfully replicated to a reasonable degree of accuracy using functional nanoimprinting, with static contact angles similar in value to those of the leaf. Nanoimprinted replicas also show an improved contact angle hysteresis over the untreated replicas, with PFAC-6 coating thicknesses of between 50–100 nm showing the best results.

2.6.2 Nanoimprint Replication of *Eremopyrum orientale*

Eremopyrum orientale is a plant found in the arid regions of North Africa, southern Europe and Asia.[20] It displays a unique asymmetric-anisotropic wetting mechanism along grooves present upon the leaf surface. SEM images were taken by collaborating partners in Turkey (**Figure 38**), which show the presence of these grooves (approximately 100 nm apart) which run the surface of the leaf, as well as small cones which point towards the leaf tip, increasing in intensity closer to the leaf tip. These cones aid in the directional water spreading observed, as well as the hydrophobicity of the surface. SEM images also show the presence of nanoscale waxes over the entirety of the leaf surface (apart from the cones). This combination of grooves, cones, and waxes, allows the surface to display hydrophobicity (Cassie-Baxter state) and direct the surface water in the direction of the cones present on the surface. The cones also vary in their density depending upon their location on the leaf, with the density increasing the closer the location towards to leaf tip.

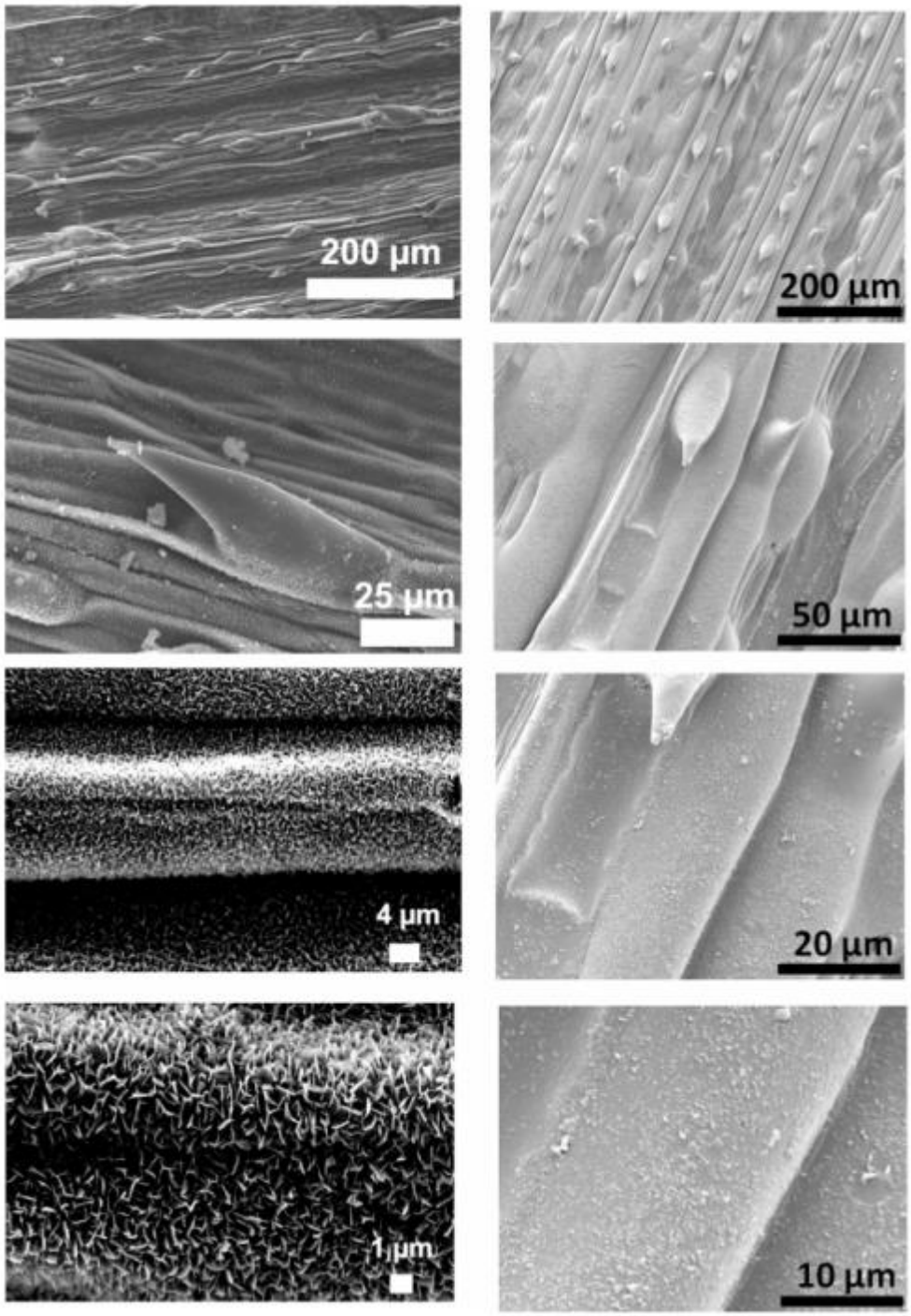

Figure 38: SEM images taken of both the leaf of *Eremopyrum orientale* (left hand images) and epoxy resin positive replicas (right hand images) taken of the leaf. SEM images of the leaf were taken by collaborators in Turkey[21]

Negative replicas were provided by collaborators in Turkey (Mehmet Gürsoy et al.) and positive replicas were made of the plant samples. Contact angles were then measured on the replicas. It was observed that directional spreading occurred in the direction of the grooves present on the surface resulting in anisotropic

wetting.[22,23,24] It therefore became necessary to measure contact angles both perpendicular and parallel to the grooves present on the surface (**Figure 39**).

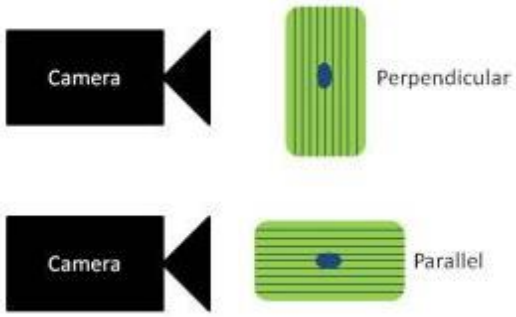

Figure 39: Diagram showing the orientation of the samples relative to the camera and the directional spreading of the droplet on the surface

A total of three epoxy resin replicas were made using three separate negative moulds of the leaf of *Eremopyrum orientale*. Water contact angles were then measured across all three replicas (**Table 20**) both parallel and perpendicular to the surface grooves.

Table 20: Water contact angles for epoxy resin positive replicas of *Eremopyrum orientale*. Contact angles parallel and perpendicular to the surface grooves were measured

Orientation	Sample No.	Static Water Contact Angle /°	Advancing Water Contact Angle /°	Receding Water Contact Angle /°
Parallel	1	134 ± 5	135 ± 1	Pin
	2	127 ± 3	129 ± 4	Pin
	3	134 ± 4	138 ± 7	Pin
Perpendicular	1	68 ± 5	78 ± 6	Pin
	2	80 ± 10	96 ± 2	Pin
	3	82 ± 2	91 ± 3	Pin

One negative mould (sample 1) was then treated with a pulsed plasma deposition to deposit a layer of PFAC-6 upon the surface. NKD measurements were taken as described previously to measure the average thickness of the deposition, with an average thickness of 58 nm. Contact angles were again measured both perpendicular and parallel to the surface grooves present on the surface (**Table 21**).

Table 21: Water contact angles for epoxy resin positive replicas of *Eremopyrum orientale* where the negative mould was pre-treated with PFAC-6 (58 nm). Contact angles parallel and perpendicular to the surface grooves were measured, brackets indicate contact angles of original plant surface

Orientation	Sample No.	Static Water Contact Angle /°	Advancing Water Contact Angle /°	Receding Water Contact Angle /°	Contact Angle Hysteresis /°
Parallel	1	159 ± 3 (164 ± 1)	161 ± 2 (163 ± 1)	110 ± 3 (157 ± 1)	52 ± 4 (5 ± 1)
Perpendicular	1	152 ± 3 (148 ± 1)	154 ± 3 (153 ± 1)	102 ± 3 (145 ± 1)	53 ± 4 (8 ± 1)

The observed contact angles for the nanoimprinted replica show good correlation with the leaf surface for both the static and advancing water contact angles. The receding and hysteresis values show the largest difference, being much larger than the native plant surface, which is as expected when using this technique to replicate plant surfaces. The wetting behaviour observed however, shows the same directional water droplet spreading along the direction of the grooves present on the leaf surface.

The leaves of *Eremopyrum orientale* display a unique wetting behaviour with asymmetric-anisotropic (directional) water spreading. This behaviour is underpinned by the combination of hierarchical surface structure of grooves and cones as well as nanoscale waxes superimposed across much of the surface. The density and direction of cones as well as the direction of the grooves govern the directional water spreading from the leaf petiole to the leaf tip. The surface of the leaf as well as the wetting behaviour was replicated using soft lithography and the nanoimprinting process.

2.7. Conclusion

The wetting behaviour of both *Xanthosoma sagittifolium* and *Eremopyrum orientale* has been observed and replicated by using a nanoimprinting technique. Both show interesting wetting mechanisms with *Eremopyrum orientale* showing asymmetric-

anisotropic (directional) water spreading. The behaviour of both leaves is underpinned by the surface structure they display, with the differences in cell macrostructure between the vein/no vein region in *Xanthosoma sagittifolium*, and the presence of regularly spaced surface grooves with cones in *Eremopyrum orientale* affecting the behaviour.

In the case of *Xanthosoma sagittifolium* the elongated cell shapes present in the vein regions cause a decrease in the Cassie-Baxter state present in those locations resulting in a higher surface energy and contact angle hysteresis and consequently pinning of the contact line. This behaviour is particularly prevalent in the younger leaves of the plant, which may indicate a self-cleaning property present in order to improve the photosynthesis of the leaf or prevent infection from microorganisms. For *Eremopyrum orientale*, the directional nature of the cones and surface grooves allows for water droplets present in fog to be collected and directed towards the tip of the leaf before falling off to the plant's root system below. This allows for the highly efficient collection of water from fogs allowing the plant to thrive in the arid regions of North Africa and Southern Europe.

Both plants were replicated using the nanoimprinting technique which offers several advantages as well as disadvantages for a replication technique. Most notably, it is able to provide a reasonably accurate representation of the surface strcuture through the moulding process, which is easy to carry out experimentally and produces repeatable results. Treating the moulds with a PFAC-6 plasma deposition allows for the altering of surface chemistry of the replicas to better mimic those of the leaf surfaces. Most notably, the PFAC-6 coating lowers the observed contact angle hysteresis by increasing the homogeneity of the surface when compared to untreated replicas. The PFAC-6 treated moulds provide the best replication of plant surfaces in both contact angle and contact angle hysteresis. Major drawbacks of the technique include scalability, as well as the need for delicate coating to be deposited on the moulds prior to casting, with too thick a coating resulting in a lower contact angle. The moulds all show increased contact angle hystersis relative to the parent plant though do successfully mimic the static contact angles observed to a reasonable degree of accuracy. This behaviour was observed both in the template plant Indian Cress as well as the leaves studied and is inherently a large limitation of this technique.

The work undertaken on both these plants is a novel approach to both understanding their wetting mechanisms and replicating their surfaces.

2.8 References

[1] Johnson Jr, R. E.; Dettre, R. H. Wettability. Berg, J. C., Eds.; Marcel Dekker, Inc., New York, 1993; pp 1–75

[2] Ensikat, H. J.; Barthlott, W. Liquid Substitution: a Versatile Procedure for SEM Specimen Preparation of Biological Materials Without Drying or Coating. *J. Microsc*. **1993**, *172*, 195.

[3] Ensikat, H. J. Liquid Substitution Methods. In *Procedures in Electron Microscopy*; Robards A.W., Wilson A.J., Eds.; John Wiley & Sons: York, UK, 1996; pp 66–76.

[4] Andrews, H. G.; Wood, T. J.; Schofield, W. C. E.; Badyal, J. P. S. Functional Nanoimprinting. *Chem. Vap. Depos.* **2012**, *18* (7–9), 239–244.

[5] Xia, Y. N.; Kim, E.; Zhao, X. M.; Rogers, J. A.; Prentiss, M.; Whitesides, G. M. Complex Optical Surfaces Formed by Replica Molding Against Elastomeric Masters. *Science* **1996**, *273*, 347–349.

[6] Koch, K.; Sculte, A. J.; Fischer, A.; Gorb, S. N.; Barthlott, W.; Fast, A. Precise and Low-Cost Replication Technique for Nano- and High-Aspect-Ratio Structures of Biological and Artificial Surfaces. *Bioinspiration Biomimetics* **2008**, *3*, 046002.

[7] Coulson, S. R.; Woodward, I. S.; Brewer, S. A.; Willis, C.; Badyal, J. P. S. Ultra-Low Surface Energy Plasma Polymer Films. *Chem. Mater.*, **2000**, *12*, 2031–2038.

[8] Fraser, R. C.; Carletto, A.; Wilson, M.; Badyal, J. P. S. Plasmachemical Double Click Thiol-Ene Reactions for Wet Electrical Barrier. *ACS Appl. Mater. Interfaces* **2016**, *8*, 21832–21838.

[9] The United Nations World Water Development Report: Managing Water Under Uncertainty and Risk. **2012**, UNESCO, Paris.

[10] Spaeth, M.; Barthlott, W. Lotus-Effect: Biomimetic Super-Hydrophobic Surfaces and Their Application. *Adv. Sci. Technol.*, **2008**, *60*, 38–46.

[11] Roth-Nebelsick, A.; Ebner, M.; Miranda, T.; Gottschalk, V.; Voigt, D.; Gorb, S.; Stegmaier, T.; Sarsour, J.; Linke, M.; Konrad, W. Leaf Surface Structures Enable the Endemic Namib Desert Grass Stipagrostis sabulicola to Irrigate Itself with Fog Water. *Interface* **2012**, *9*, 1965–1974.

[12] Gürsoy, M.; Harris, M. T.; Downing, J. O.; Barrientos-Palomo, S. N.; Carletto, A.; Yaprak, A. E.; Karaman, M.; Badyal, J. P. S. Bioinspired Fog Capture and Channel Mechanism Based on the Arid Climate Plant *Salsola crassa*. *Colloids and Surfaces A.*, **2017**, *529*, 195–202.

[13] Lawal, O. S. Composition, Physiochemical Properties of Retrogradation Characteristics of Native, Oxidised, Acetylated, and Acid-Thinned New Cocoyam (Xanthosoma Sagittifolium) Starch. *Food Chemistry*, **2004**, *87(2)*, 205–218.

[14] Òner, D.; McCarthy, T. J. Ultrahydrophobic Surfaces: Effects of Topography Length Scales on Wettability. *Langmuir* **2000**, *16*, 7777–7782.

[15] Mackerron, D. K. L. Wind Damage to Surface of Strawberry Leaves. *Ann. Bot.* **1976**, *40*, (January 1975), 351–354.

[16] Wigzell, J. M.; Racovita, R. C.; Stentiford, B. G.; Wilson, M.; Harris, M. T.; Fletcher, I. W.; Mosquin, D. P. K.; Justice, D.; Beaumont, S. K.; Jetter, R.; Badyal, J. P. S. Smart Water Channelling Through Dual Wettability by Leaves of the Bamboo Phyllostachys Aurea. *Colloids and Surfaces A.*, **2016**, *506*, 344–355.

[17] Barthlott, W.; Neinhuis, C.; Cutler, D.; Ditsch, F.; Meusel, I.; Theisen, I.; Wilhelmi, H. Classification and Terminology of Plant Epicuticular Waxes. *Bot. J. Linn. Soc.* **1998**, *126*, 237–260.

[18] Koch, K.; Bhushan, B.; Barthlott, W. Diversity of Structure, Morphology and Wetting of Plant Surfaces. *Soft Matter* **2008**, *4*, 1943–1963.

[19] McWhorter, C. G.; Ouzts, C.; Paul, R. N. Micromorphology of Johnsongrass (Sorghum halepense) Leaves *Weed Science*, **1993**, *41(4)*, 583–589.

[20] Cabi, E.; Doğan, M. Taxonomic Study on the Genus Eremopyrum (Ledeb.) Jaub. et Spach (Poaceae) in Turkey. *Plant Syst. Evol.*, **2010**, *287*, 129–140.

[21] Gürsoy, M.; Harris, M. T.; Carletto, A.; Yaprak, A. E.; Karaman, M.; Badyal, J. P. S. Bioinspired Asymmetric-Anisotropic (Directional) Fog Harvesting Based on the Arid Climate Plant Eremopyrum Orientale. *Colloids and Surfaces A.*, **2017**, *529*, 959–965.

[22] Kannan, R.; Sivakumar, D. Drop Impact Process on a Hydrophobic Grooved Surface. *Colloids Surf. A.* **2008**, *317*, 694–704.

[23] Xia, D.; Johnson, L. M.; Lopez, G. P. Anisotropic Wetting Surfaces with One-Dimensional and Directional Structures: Fabrication Approaches, Wetting Properties and Potential Applications. *Adv. Mater.*, **2012**, *24*, 1287–1302.
[24] Kim, T–I.; Suh, K. Y. Unidirectional Wetting and Spreading on Stooped Polymer Nanohairs. *Soft Matter* **2009**, *5*, 4131–4135.

Chapter 3 ToF-SIMS Analysis on Negative Moulds of *Phyllostachys aurea*

3.1. Introduction

It has been well documented that surface waxes present on leaves influence their wettability[1,2] with multiple techniques being employed to analyse surface waxes.[3] One useful technique is Time of Flight Secondary Ion Mass Spectrometry (ToF-SIMS) which has been previously used to analyse surface compounds on leaf cuticles[4] as it provides sub-micro resolution and highly accurate chemical specificity.[5] The leaves of *Phyllostachys aurea* (golden bamboo) show a unique wetting behaviour on their adaxial surface with young leaves showing two different wetting regimes across the surface. Water present on the leaf margin shows hydrophobicity (~140°), whilst the middle of the leaf and the margin show hydrophilicity (~80°). This dual wettability is only present in young leaves and disappears as the leaf reaches maturity. ToF-SIMS was conducted on the surface of both young and mature leaves by previous members of the Badyal group and proved a useful tool in the analysis of plant surfaces.[5]

One of the main limitations of this technique is that plants samples which were analysed were freshly cut from the parent plant. This was done in order to minimise surface contamination and dehydration of the plant cells which would result in inaccurate surface analysis. A second limitation is access to the equipment to run ToF-SIMS analysis is limited, especially in the developing world. For future work in this area it becomes difficult to analyse the chemical composition of plant surfaces if the plant cannot be easily grown or found locally, therefore it was envisioned that potential removal of the surface waxes by the nanoimprinting process may allow for samples to be transported large distances without compromising the analysis, eliminating the two main diasadvantages of using this technique, as moulds can be sent off for analysis without the need to grow the plant locally, or buy the equipment necessary to run this experiment. This would involve the waxes being removed mechanically, similar to other techniques employed by

other groups.[6,7] To this end, leaves of the golden bamboo were used to create a PDMS negative replica which was subsequently analysed using ToF-SIMS, which should allow for surface analysis of the leaf to be undertaken.

3.2 Experimental

3.2.1 ToF-SIMS Analysis

Leaves of the golden bamboo were analysed as described previously in the literature.[5]

The PDMS mould and leaf samples for ToF-SIMS analysis were mounted directly to a suitable sample holder using clean stainless steel clips.

Static SIMS analyses were carried out using an ION-TOF 'TOF-SIMS IV – 200' instrument (ION-TOF GmbH, Münster, Germany) of single-stage reflectron design. Positive and negative ion spectra and images of the leaf samples were obtained using a Bi_3^{2+} focused liquid metal ion gun at 25 keV energy, incident at 45° to the surface normal and operated in 'bunched' mode for high mass resolution. This mode used ca. 20ns wide ion pulses at 6.7kHz repetition rate. Charge compensation was effected by low-energy (ca. 20 eV) electrons provided by a flood gun. The total ion dose density was less than 1×10^{16} ions m^{-2} in all cases. The topography of the sample surface and the ion gun mode of operation limited the mass resolution in this work to ca. $m/\Delta m = 4000$ in the case of the PDMS mould samples.

Positive and negative ion static SIMS spectra and images of the PDMS mould samples were recorded at room temperature with a 128 × 128 pixel raster and a field of view of 200μm × 200μm.

Positive and negative ion static SIMS spectra and images were recorded from the margin, lamina and mid-rib regions of the leaf sample at room temperature. Raw data containing the secondary ions recorded at each pixel was acquired with a 256 × 256 pixel raster and a field of view of 500μm × 500μm.

3.2.2 Contact Angle Measurements

Contact angle measurements were taken at 20 °C using a video capture apparatus (VCA 2500 XE, AST Products Inc.) and 1.0 μL high purity water droplets (ISO 3696 Grade 1). Advancing and receding contact angle values were determined by respectively increasing and subsequently decreasing the liquid drop volume by a further 1.0 μL until the contact line was observed to move.[8] A minimum of three

static, advancing, and receding contact angles were obtained for each sample. Averages and standard deviations were calculated.

3.3 Golden Bamboo Leaves

3.3.1 Previous Work

The dual wettability observed for the leaves of *Phyllostachys aurea* were measured using contact angle analysis in previous work undertaken in the Badyal group[5], showing a highly hydrophobic surface for the margin of young leaves and a hydrophilic surface for the midrib of young leaves (**Table 22**). Old leaves showed a hydrophilic surface over the entire leaf surface.

Table 22: Water contact angle analysis of the adaxial surface of young and old leaves of *Phyllostachys aurea*. Data taken from Wigzell, J. M.; Racovita, R. C.; Stentiford, B. G.; Wilson, M.; Harris, M. T.; Fletcher, I. W.; Mosquin, D. P. K.; Justice, D.; Beaumont, S. K.; Jetter, R.; Badyal, J. P. S. Smart Water Chanelling Through Dual Wettability by Leaves of the Bamboo Phyllostachys aurea *Colloids and Surfaces A: Physiochem. Eng. Aspects* 2016, *506*, 344–355

Leaf Area	**Water Contact Angle / °**			
	Static	Advancing	Receding	Hysteresis
Young Leaf (Margin)	141 ± 3	142 ± 2	136 ± 4	5 ± 4
Young Leaf (Midrib)	77 ± 13	84 ± 12	62 ± 10	23 ± 8
Old Leaf (Margin)	69 ± 12	83 ± 12	51 ± 11	32 ± 6
Old Leaf (Midrib)	69 ± 14	87 ± 12	60 ± 10	27 ± 7

Experiments then identified the chemical composition of the surface waxes present on young and mature leaves of golden bamboo. The surface waxes which were found to be present were a wide range of very long chain (VLC) molecules, with a multitude of different moieties. These moieties include alkyl esters, carboxylic acids, aldehydes, acids, and amines with chain lengths of up to 48 carbon atoms (C_{48}) as described by Wigzell et al.[5] The distribution of some of the waxes varied between leaf regions (midrib compared to margin), as well as between young/old leaves. The m/z values for the surface waxes present can be seen (**Figure 40**), which provide a basis and reference point for the PDMS negative mould analysis.

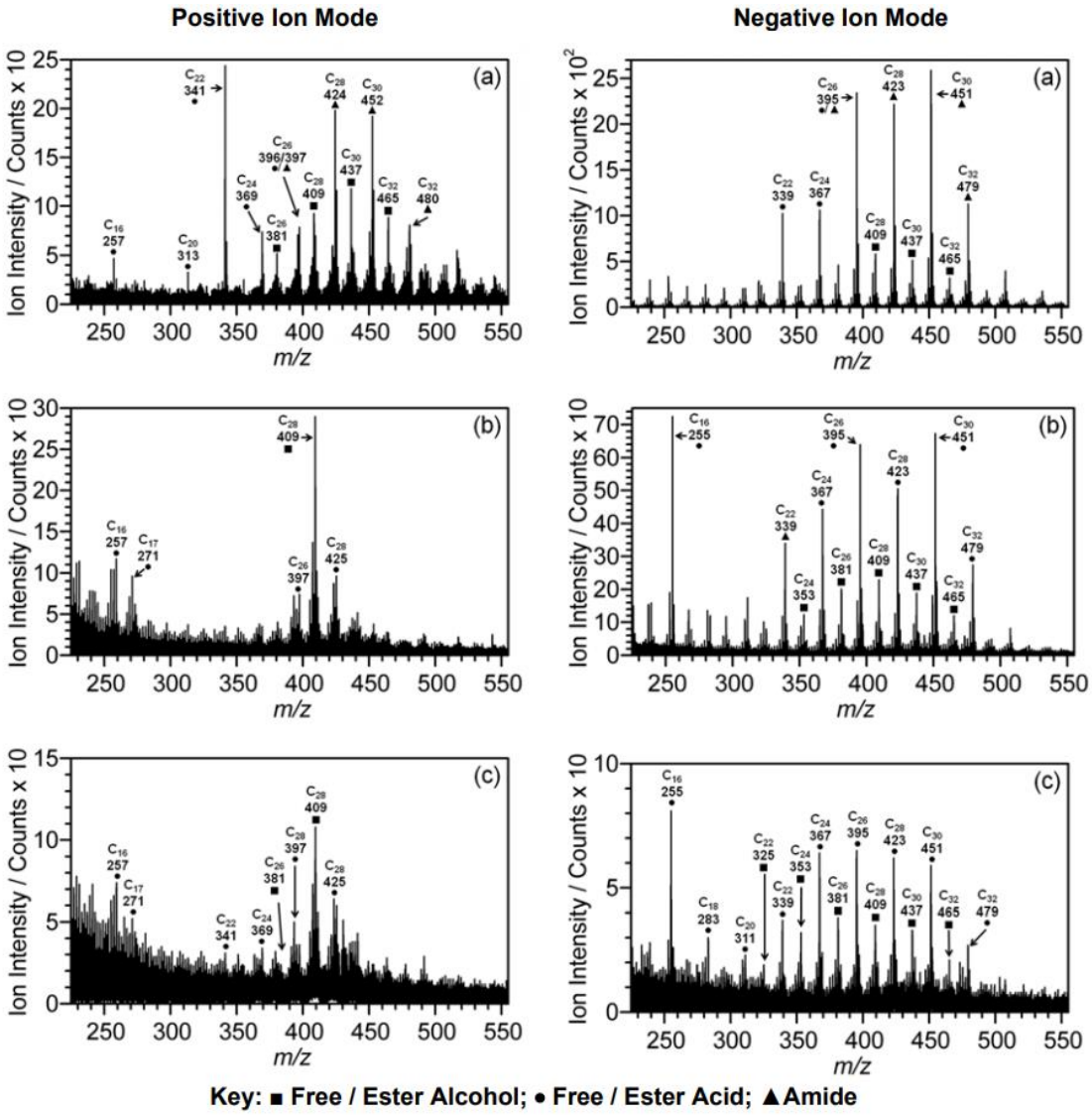

Figure 40: ToF-SIMS data for the leaves of *Phyllostachys Aurea*, showing the main fragmentation assignments for: (a) the margin of the young leaf; (b) the middle of the young leaf; and (c) a raster scan across both the margin and middle of the old leaf. Image taken from Wigzell, J. M.; Racovita, R. C.; Stentiford, B. G.; Wilson, M.; Harris, M. T.; Fletcher, I. W.; Mosquin, D. P. K.; Justice, D.; Beaumont, S. K.; Jetter, R.; Badyal, J. P. S. Smart Water Chanelling Through Dual Wettability by Leaves of the Bamboo Phyllostachys aurea *Colloids and Surfaces A: Physiochem. Eng. Aspects* 2016, *506*, 344–355

The values obtained when analysing a live speciment will be used as a reference point for the negative mould replicas. By comparing the experimental results obtained from the negative moulds with those from a leaf surface will show whether mechanical removal and analysis of surface waxes is possible. A variety of

different moieties, chain lengths, and compounds is present on the surface of *Phyllostachys aurea* which provides a good range of molecules to check for on the moulds.

3.3.2 ToF-SIMS on Moulds

First, contact angle measurements were taken of young leaves of *Phyllostachys aurea* in order to compare the contact angles obtained with those in previous work (**Table 23**). Contact angles obtained show good correlation with those in previous work showing that they exhibit similar behaviour.

Table 23: Water contact angle analysis of the adaxial surface of young and old leaves of *Phyllostachys aurea*, brackets indicate previous data obtained by Wigzell et al.

Leaf Area	**Water Contact Angle / °**			
	Static	Advancing	Receding	Hysteresis
Young Leaf (Margin)	136 ± 8 (141 ± 3)	138 ± 5 (142 ± 2)	134 ± 6 (136 ± 4)	4 ± 7 (5 ± 4)
Young Leaf (Midrib)	58 ± 10 (77 ± 13)	69 ± 6 (84 ± 12)	55 ± 7 (62 ± 10)	14 ± 9 (23 ± 8)
Old Leaf (Margin)	75 ± 3 (69 ± 12)	83 ± 2 (83 ± 12)	69 ± 6 (51 ± 11)	14 ± 6 (32 ± 6)
Old Leaf (Midrib)	68 ± 6 (69 ± 14)	80 ± 5 (87 ± 12)	66 ± 4 (60 ± 10)	14 ± 6 (27 ± 7)

Negative replicas were then taken of two separate young bamboo leaves using nanoimprinting techniques described previously (**Chapter 2**). The samples were allowed to cure and the leaf removed to leave behind a negative replica of the adaxial surface. Two separate regions, Area 1 and 2 were sampled (**Figure 41**) approximately halfway between the leaf stem and tip, either side of the midrib region.

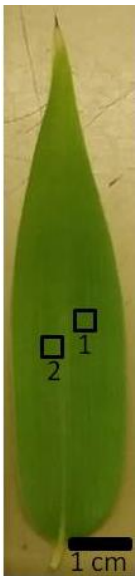

Figure 41: Image showing a young leaf of golden bamboo. The two areas, 1 and 2, are shown, these correspond to the negative mould regions which were analysed

Two negative moulds were created, each which require positive ion and negative ion sampling. This sampling produced a total of four data sets through which to compare to previously published work.[5] The first set of data is shown (**Figure 42**) with positive ion spectra for both samples at area 1 analysed. As previously ■ corresponds to free / ester alcohol, ● corresponds to free / ester acid, ▲corresponds to amide.

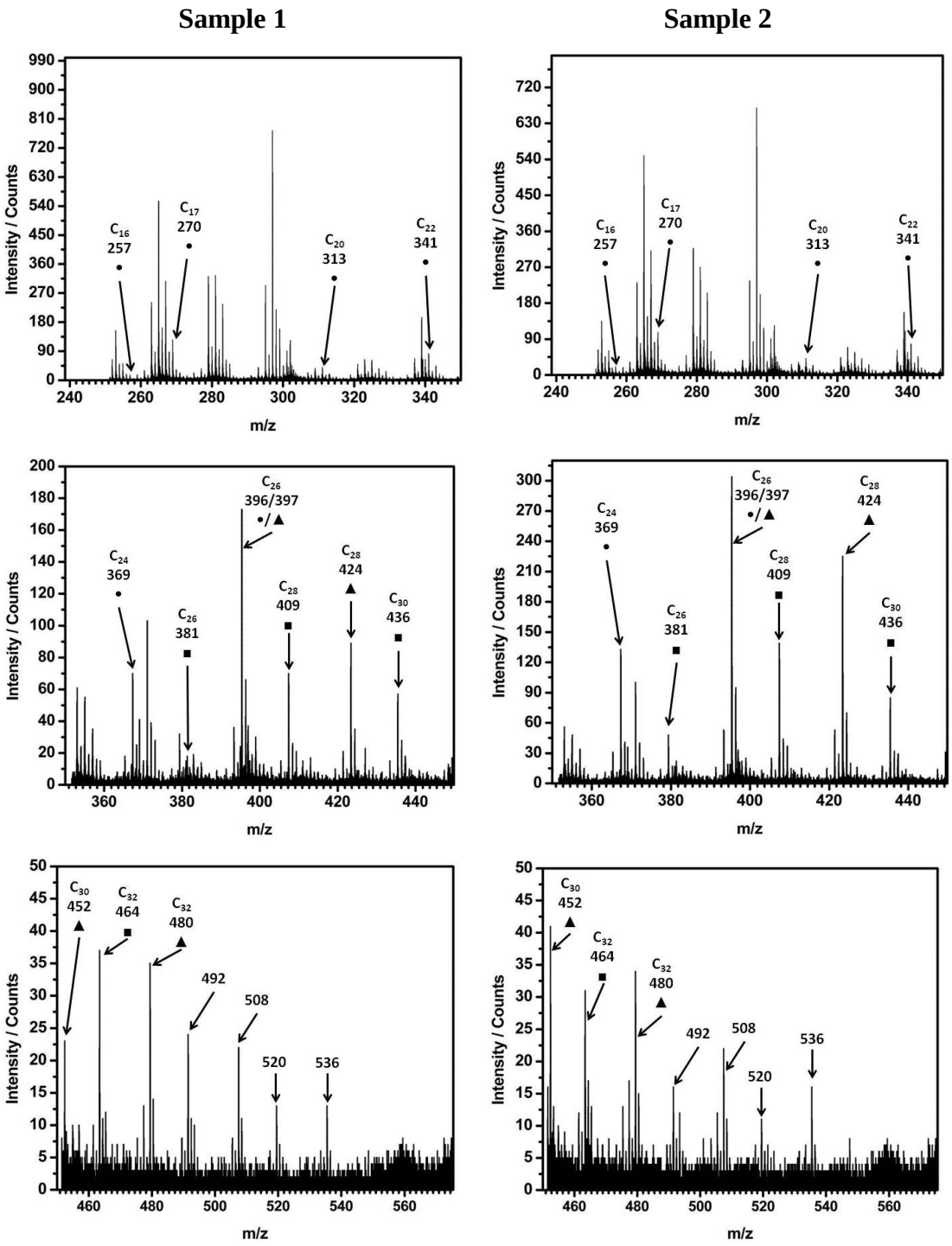

Figure 42: ToF-SIMS graphs showing the positive ion spectra for two separate negative mould samples, area 1 was analysed in both cases. As before ■ corresponds to free / ester alcohol, ● corresponds to free / ester acid, ▲corresponds to amide

The ToF-SIMS analysis detected several compounds which were also found in the fresh leaf of *Phyllostachys aurea* as decribed by Wigzell et al., the compounds detected are summarised (**Table 24**). Given the areas sampled a range of compounds from both the midrib and margin were detected.

Table 24: Collation of the m/z values obtained from the ToF-SIMS analysis for area 1 of both samples. The positive ion spectra are collated

m/z Value Detected	No. C Atoms	Functional Group
257	16	Free / ester acid
270	17	Free / ester acid
313	20	Free / ester acid
341	22	Free / ester acid
369	24	Free / ester acid
381	26	Free / ester alcohol
396	26	Free / ester acid
397	26	Amide
409	28	Free / ester alcohol
424	28	Amide
436	30	Free / ester alcohol
452	30	Amide
464	32	Free / ester alcohol
480	32	Amide

The compounds detected are the same as those detected on the fresh plant surface, with VLC compounds of esters, alcohols, and amides detected. Also present is the characteristic fragmentation pattern observed when VLCs fragment and have a successive CH_2 or C_2H_4 loss, resulting in a decrease of 14 amu and 28 amu respectively. An example of this can be seen when comparing m/z 313 and m/z 341, a loss of 28 amu.[9]

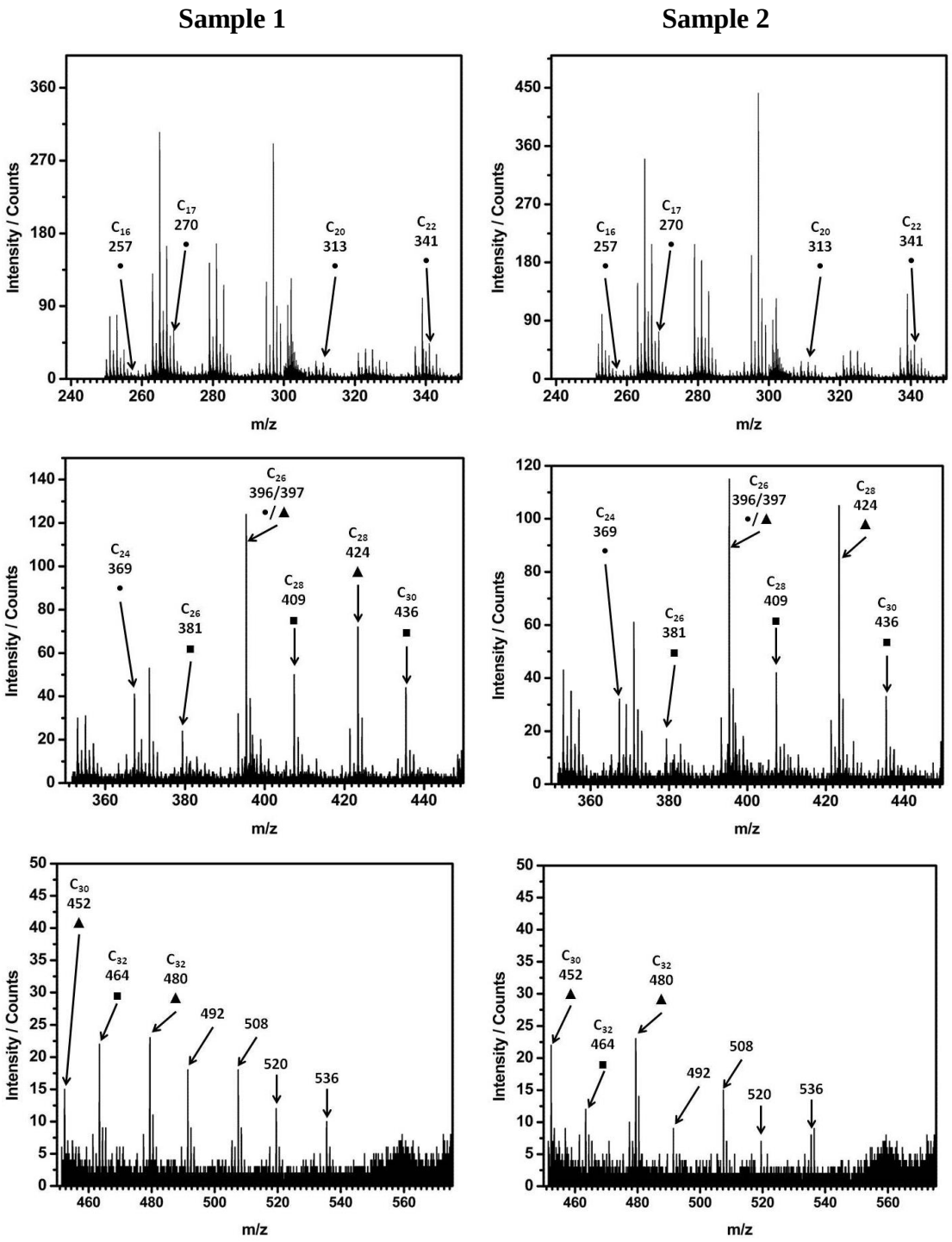

Figure 43: ToF-SIMS graphs showing the positive ion spectra for two separate negative mould samples, area 2 was analysed in both cases. As before ■ corresponds to free / ester alcohol, ● corresponds to free / ester acid, ▲corresponds to amide

As before, the compounds present in both the mould and the negative replica are summarised (**Table 25**).

Table 25: Collation of the m/z values obtained from the ToF-SIMS analysis for area 2 of both samples. The positive ion spectra are collated

m/z Value Detected	No. C Atoms	Functional Group
257	16	Free / ester acid
270	17	Free / ester acid
313	20	Free / ester acid
341	22	Free / ester acid
369	24	Free / ester acid
381	26	Free / ester alcohol
396	26	Free / ester acid
397	26	Amide
409	28	Free / ester alcohol
424	28	Amide
436	30	Free / ester alcohol
452	30	Amide
464	32	Free / ester alcohol
480	32	Amide

The compounds detected in the negative mould are the same as those detected on the fresh plant surface, with VLC compounds of esters, alcohols, and amides observed. The characteristic fragmentation pattern observed when VLCs fragment and have a successive CH_2 or C_2H_4 losses, resulting in a decrease of 14 amu and 28 amu respectively is also observed. Both regions sampled, area 1 and area 2, show good correlation with one another in regards to the m/z values detected.[10]

However, in order to compare the data to the plant surface, the observed peaks as well as their intensities relative to total ion counts need to be compared to those of a blank sample. For that reason, a blank PDMS negative mould of a glass slide was analysed using ToF-SIMS to see if any of the observed fragmentation patterns were due to the PDMS rather than waxes present on the surface. This data

was compared and contrasted against the obtained data for the negative moulds of *Phyllostachys aurea* (**Figure 44**).

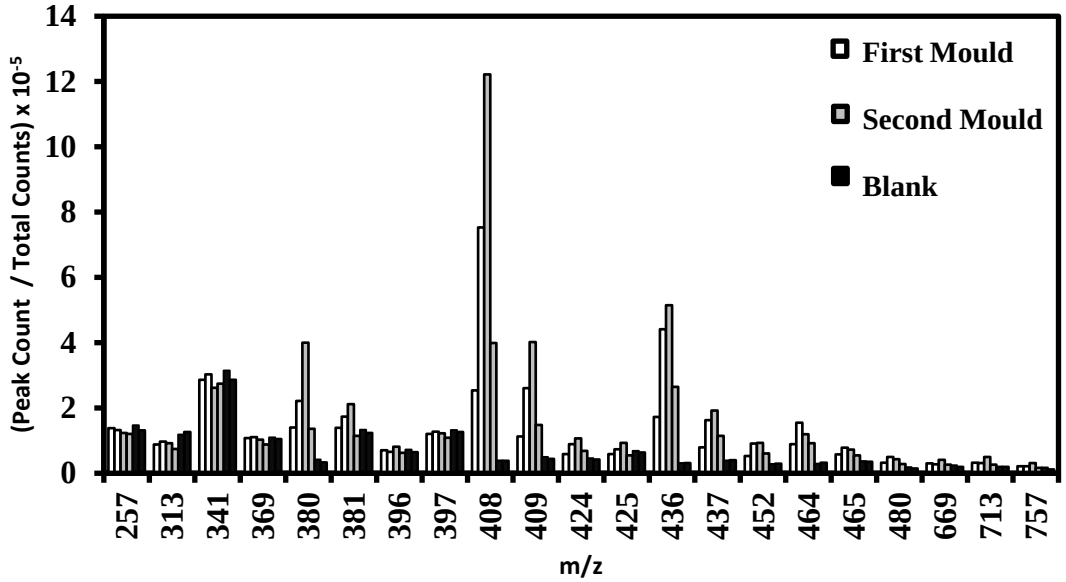

Figure 44: Graph showing the respective m/z peaks found in the original ToF-SIMS data. First mould (white), second mould (grey), and blank mould (black) data is shown. All peaks were normalised relative to total ion count. Positive ion spectra is shown

By comparing the peak counts of the first and second samples to a blank sample the m/z values which correspond to waxes on the surface can be determined. In the case of the positive ion spectra, at known m/z values, several clearly distinct peaks can be seen. These include m/z values of; 380, 408, 409, 436, 437, 452, and 464. The peaks of 464, 436, 408, and 380 are typical of a homologous series, with successive C_2H_4 (28 amu) losses due to alkyl chain fragmentation of the free / ester alcohol, and m/z value of 452 corresponding to a C_{30} very long chain amide. The observed m/z values present on the surface show good correlation with the observed compounds on the natural leaf surface, particularly in the case of detecting free / ester alcohol fragments at m/z 408 and 436.[11]

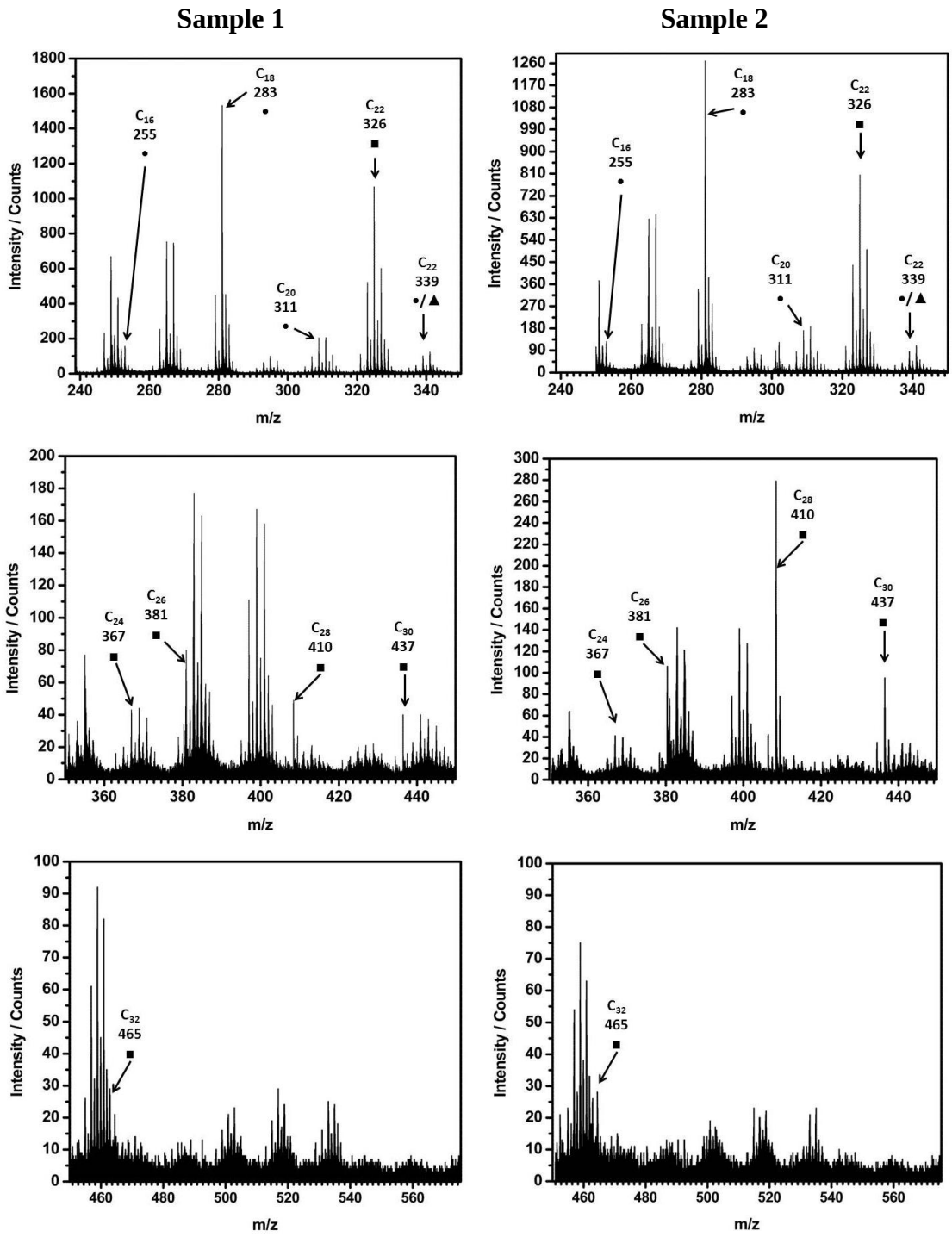

Figure 45: ToF-SIMS graphs showing the negative ion spectra for two separate negative mould samples, area 1 was analysed in both cases. As before ■ corresponds to free / ester alcohol, ● corresponds to free / ester acid, ▲corresponds to amide

Compounds which are found in both the leaf analysis and the negative mould analysis are highlighted (**Figure 45**) and collated (**Table 26**).

Table 26: Collation of the m/z values obtained from the ToF-SIMS analysis for area 1 of both samples. The negative ion spectra are collated

m/z Value Detected	No. C Atoms	Functional Group
255	16	Free / ester acid
283	18	Free / ester acid
311	20	Free / ester acid
326	22	Free / ester alcohol
339	22	Free / ester acid or Amide
367	24	Free / ester acid
381	26	Free / ester alcohol
410	28	Free / ester alcohol
437	30	Free / ester alcohol
465	32	Free / ester alcohol
479	32	Free / ester acid or Amide

Again, as with the case of the positive ion spectra, a range of m/z values which were present on the leaf surface were also detected on the negative mould, these include free /ester alcohol, free / ester acid, and amides. Also observed is the characteristic fragmentation pattern observed for VLC molecules.

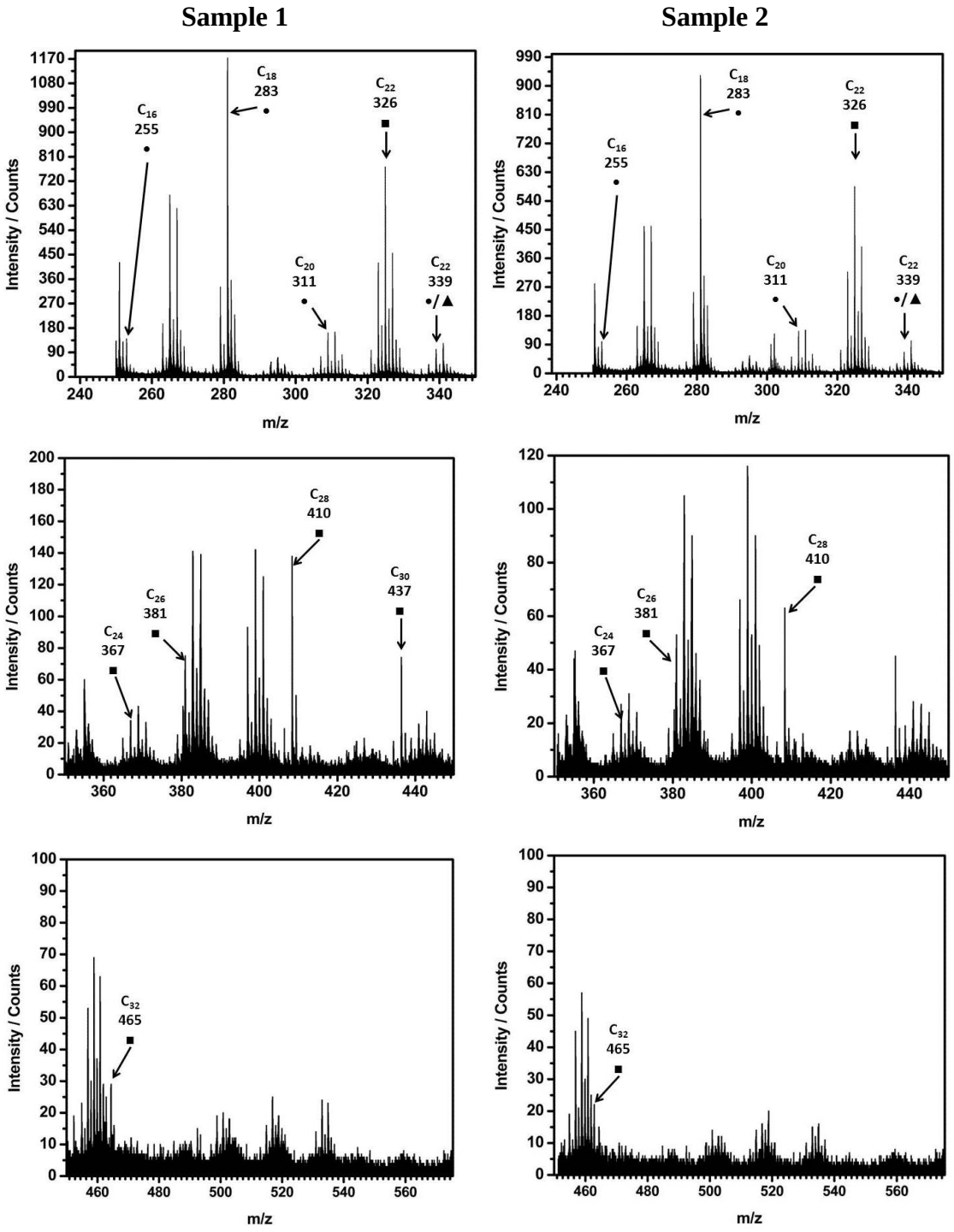

Figure 46: ToF-SIMS graphs showing the negative ion spectra for two separate negative mould samples, area 2 was analysed in both cases. As before ■ corresponds to free / ester alcohol, ● corresponds to free / ester acid, ▲corresponds to amide

Compounds which are found in both the leaf analysis and the negative mould analysis are highlighted (**Figure 46**) and collated (**Table 27**).

Table 27: Collation of the m/z values obtained from the ToF-SIMS analysis for area 2 of both samples. The negative ion spectra are collated

m/z Value Detected	No. C Atoms	Functional Group
255	16	Free / ester acid
283	18	Free / ester acid
311	20	Free / ester acid
326	22	Free / ester alcohol
339	22	Free / ester acid or Amide
367	24	Free / ester acid
381	26	Free / ester alcohol
410	28	Free / ester alcohol
437	30	Free / ester alcohol
465	32	Free / ester alcohol
479	32	Free / ester acid or Amide

The second area (area 2) showed the same m/z values as the first area (area 1). With the same m/z values for free / ester acid, free / ester alcohol and amides detected. As described previously these detected m/z values were compared with a blank PDMS sample (**Figure 47**).

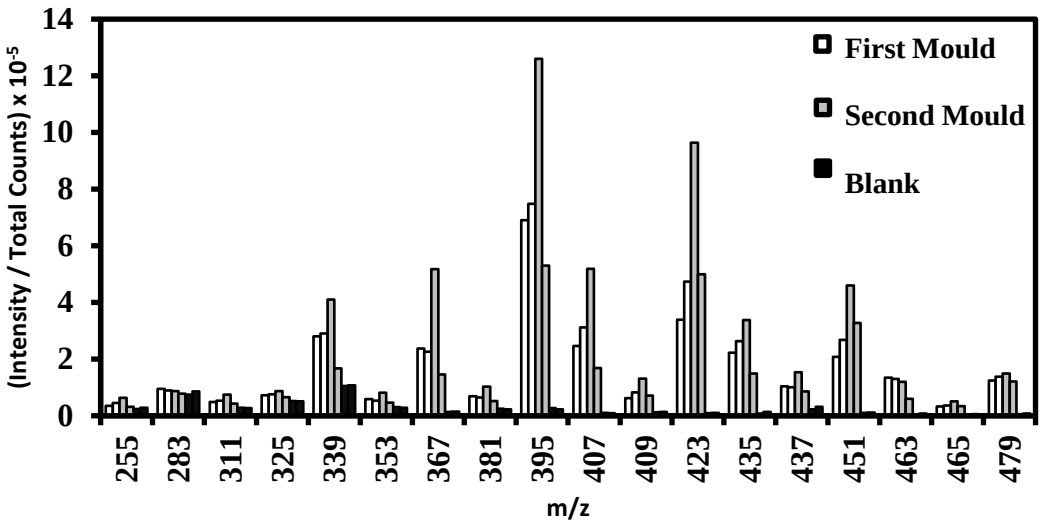

Figure 47: Graph showing the respective m/z peaks found in the original ToF-SIMS data. First mould (white), second mould (grey), and blank mould (black) data is shown. All peaks were normalised relative to total ion count. Negative ion spectra is shown

Comparing the m/z values for known compounds present on the surface, multiple distinguishable peaks can be seen, these include; 339, 367, 381, 395, 407, 409, 423, 435, 437, 451, 463, 465, and 479. With 479 corresponding to a C_{32} amide or ester acid and their relative homologues after successive alkyl fragmentation displayed at 451 (C_{30}), 423 (C_{28}), 395 (C_{26}), and 339 (C_{22}). m/z values of 465/463 correspond to C_{32} free / ester alcohol peaks, with successive homologues seen at m/z 437/435 (C_{30}), and 409/407 (C_{28}). Also seen are peaks at m/z 381 (C_{26} free / ester acid) and 367 (C_{24} ester / alcohol). This data shows that it is possible to detect surface waxes by using a PDMS negative mould to mechanically remove them from the surface. The dual wettability observed is due to the different waxes present on the surface, with more hydrophilic compounds present in the centre of the leaf compared with aliphatic compounds at the edges.

3.5 Conclusion

The difference in chemical composition of plant surfaces has been documented previously, in particular the chemical differences observed on the leaves of *Phyllostachys aurea* area which result in a unique dual wettability present on the leaf surface. Different areas of the leaf show different chemical compositions and spatial

differences in the waxes combined with an underlying macro structure governing the surface properties observed.

Using the nanoimprinting process, two leaves of *Phyllostachys aurea* were used to create negative moulds of the entire leaf surface, these moulds were subsequently analysed using ToF-SIMS to anlalyse the surface compounds (if any) which were present. The analysis showed that it was possible to detect a majority of the surface compounds present on the leaf surface (**Figure 44** and **Figure 47**) as well as characteristic fragmentation patterns observed for VLC molecules, in particular, the amides present on the leaf surface were also detected on the negative mould. This preliminary experiment shows that the nanoimprinting process can be used to detect surface waxes present through the action of mechanical removal, and is a novel approach leading the way for ToF-SIMS analysis of plant surfaces which are located in difficult to reach parts of the world and cannot be easily transported or grown. This technique should allow for the surface chemical characterisation of plant surfaces that would otherwise be impossible in developing countries, as moulds can be sent to laboratories that have the required equipment.

VLC molecules have been reported previously in the literature by Jetter et al.[12] on a number of plant leaves. In particular, fatty acid, alcohol, and ester compounds with similar chain lengths (n = 30+) were found to be present on the leaves of *Kalonchoe daigremontiana*.

Future work in this area will include a more detailed analysis of the PDMS negative moulds of *Phyllostachys aurea*, in particular the regions of the moulds sampled will mimic those analysed in previously published work (margin and midrib), as well as conducting a raster scan across the surface to createa heat map of compound locations. Finally, spatial imaging of the moulds will be undertaken to compare the spatial distribution of the VLC amide (m/z of 451) and C_{22} free / ester acid in accordance with previously published work. This analysis can be conducted on the same negative moulds currently obtained.

Additional experiments will also include using this method to analyse the old leaves of *Phyllostachys aurea* to build a complete picture in comparison with published work. This technique can then be used to analyse the leaf surfaces of other plants in a similar manner. Coupled with the novel use of moulds to analyse the surface waxes present on the leaves should provide a useful tool for future work in this field.

3.6 References

[1] Hunsche, M.; Noga, G. Cuticular Wax Load and Surface Wettability of Leaves and Fruits Collected from Sweet Cherry (Prunus avium) Trees Grown Under Field Conditions or Inside a Polytunnel. *Acta Physiologiae Plantarum* **2011**, *33(5)*, 1785–1792.

[2] Barthlott, W.; Mail, Matthias.; Bhushan, B.; Koch, K. Plant Surfaces: Structures and Functions for Biomimetic Innovations. *Nano-Micro Lett.* **2017**, *9(23)*.

[3] Dove, H.; Mayes, R. W. Protocol for the Analysis of n-Alkanes and other Plant-Wax Compounds and for their use as Markers for Quantifying the Nutrient Supply of Large Mammalian Herbivores. *Nature Protocols* **2006**, *1*, 1680–1697.

[4] Perkins, M. C.; Bell, G.; Briggs, D.; Davies, M. C.; Friedmann, A.; Hart, C. A.; Roberts, C. J.; Rutten, F. J. M. The Application of ToF-SIMS to the Analysis of Herbicide Formulation Penetration into and Through Leaf Cuticles. *Colloids and Surfaces B: Biointerfaces* **2008**, *15(1)*, 1–13.

[5] Wigzell, J. M.; Racovita, R. C.; Stentiford, B. G.; Wilson, M.; Harris, M. T.; Fletcher, I. W.; Mosquin, D. P. K.; Justice, D.; Beaumont, S. K.; Jetter, R.; Badyal, J. P. S. Smart Water Chanelling Through Dual Wettability by Leaves of the Bamboo Phyllostachys aurea *Colloids and Surfaces A: Physiochem. Eng. Aspects* **2016**, *506*, 344–355.

[6] Jetter, R.; Schäffer, S. Chemical Composition of the Prunus Laurocerasus Leaf Surface, Dynamic Changes of the Epicuticular Wax Film During Leaf Development. *Plant Physiol.* **2001**, *126(4)*, 1725–1737.

[7] Vogg, G.; Fischer, S.; Leide, J.; Emmanuel, E.; Jetter, R.; Levy, A. A.; Riederer, M. Tomato Fruit Cuticular Waxes and their Effects on Transpiration Barrier Properties: Functional Characterization of a Mutant Deficient in a Very-Long-Chain Fatty Acid β-Ketoacyl-CoA-Synthase. *J. Exp. Botany* **2004**, *55(401)*, 1401–1410.

[8] Johnson Jr, R. E.; Dettre, R. H. Wettability. Berg, J. C., Eds.; Marcel Dekker, Inc., New York, 1993; pp 1–75

[9] The SurfaceSpectra Static SIMS Library Version 4; John C Vickerman; David Briggs; Alex Henderson, SurfaceSpectra Ltd.

[10] Perkins, M. C.; Bell, G.; Briggs, D.; Davies, M. C.; Friedman, A.; Hart, C. A.; Roberts, C. J.; Rutten, F. J. M. The Application of ToF-SIMS to the Analysis of Herbicide Formulation Penetratio into and Through Leaf Cuticles. *Colloids and Surfaces B: Biointerfaces* **2008**, *67(1)*, 1–3.

[11] Jetter, R.; Sodhi, R. Chemical Composition and Microstructure of Waxy Plant Surfaces: Triterpenoids and Fatty Acid Derivatives on Leaves of Kalanchoe Daigremoniana. *SIMS Proceedings Papers* **2011**, *43(1-2)*, 326–330.

[12] van Maarseveen, C.; Jetter, R. Composition of the Epicuticular and Intracuticular Wax Layers on Kalonchoe daigremontiana (Hamet et Perr. de la Bathie) Leaves. *Phytochemistry* **2009**, 899–906.

Chapter 4 ToF-SIMS Analysis on *Xanthosoma sagittifolium*

4.1 Introduction

A combination of surface roughness and surface chemsitry contributes to the observed wetting behaviour of different surfaces. In the case of plant leaves, the underlying cell structure as well as surface waxes present will determine the wettability observed. ToF-SIMS has proven a useful technique to accurately analyse the surface chemistry of *Phyllostachys aurea* and replicas of those surfaces giving an insight into how the surface chemistry affected the surface wettability observed. The technique was able to distinguish between different compounds in different geographical regions of the bamboo leaf and provide quantitative analysis as to the composition of the waxes present in those regions. Since ToF-SIMS can accurately analyse the surface waxes, this technique can then be applied to other leaves and replicas of plant leaves, such as those of *Xanthosoma sagittifolium* to ascertain if the different wettability observed is due to chemical or structural variations between the different leaf regions. *Xanthosoma sagittifolium* was chosen as it displayed an interesting wetting property when exposed to water. The water droplets remained pinned to surface veins before growing in size as droplets coalesce before rolling off the leaf surface. ToF-SIMS could potentially determine if surface waxes are the cause of the droplet pinning, which could potentially lead to the development of efficient water collecting devices.

4.2 Experimental

4.2.1 ToF-SIMS Analysis

The PDMS mould and leaf samples for ToF-SIMS analysis were mounted directly to a suitable sample holder using clean stainless steel clips.

Static SIMS analyses were carried out using an ION-TOF 'TOF-SIMS IV – 200' instrument (ION-TOF GmbH, Münster, Germany) of single-stage reflectron

design. Positive and negative ion spectra and images of the leaf samples were obtained using a Bi_3^{2+} focused liquid metal ion gun at 25 keV energy, incident at 45° to the surface normal and operated in 'bunched' mode for high mass resolution. This mode used ca. 20ns wide ion pulses at 6.7kHz repetition rate. Charge compensation was effected by low-energy (ca. 20 eV) electrons provided by a flood gun. The total ion dose density was less than 1×10^{16} ions m^{-2} in all cases. The topography of the sample surface and the ion gun mode of operation limited the mass resolution in this work to ca. $m/\Delta m = 4000$ in the case of the PDMS mould samples.

Positive and negative ion static SIMS spectra and images of the PDMS mould samples were recorded at room temperature with a 128 × 128 pixel raster and a field of view of 200μm × 200μm.

Positive and negative ion static SIMS spectra and images were recorded from the margin, lamina and mid-rib regions of the leaf sample at room temperature. Raw data containing the secondary ions recorded at each pixel was acquired with a 256 × 256 pixel raster and a field of view of 500μm × 500μm.

4.2.2 Preparation of Samples

Samples from three regions (margin, lamina, and midrib) of fresh *Xanthosoma sagittifolium* leaves (young leaf) were cut from a leaf which had been separated from the parent plant and rinsed with deionised water to remove any surface debris and allowed to dry in air. Samples were immediately transported to local analytical facilities.

4.3 Results and Discussion

Fresh, young leaf samples of *Xanthosoma sagittifolium* were analysed using ToF-SIMS, with both positive and negative ion spectra for the three plants regions (margin, lamina, and midrib) recorded, up to a m/z value of 1500.

4.3.1 Positive Ion Spectra

The positive ion spectra show clear differences between the margin/lamina regions and the midrib, including the relative peak intensities of the various compounds present on the surface. A common feature between all three regions is the large peak at 39 m/z corresponding to potassium, as well as a range of likely inorganic species present up to approximately 200 m/z. These species include various sulphur

containing compounds such as SO_2, SO_3, and SO_4. In particular there are strong peaks at 137 m/z, 153 m/z and 233 m/z, which, given the large potassium peak likely correspond to potassium-sulphur containing material KH_2SO_4, KH_2SO_5 and $KH_2(SO_4)_2$ respectively. The presence of these species on the surface is likely due to surface contamination of the leaves themselves, most likely from the sprinkler system present in the greenhouse where the parent plant is located.

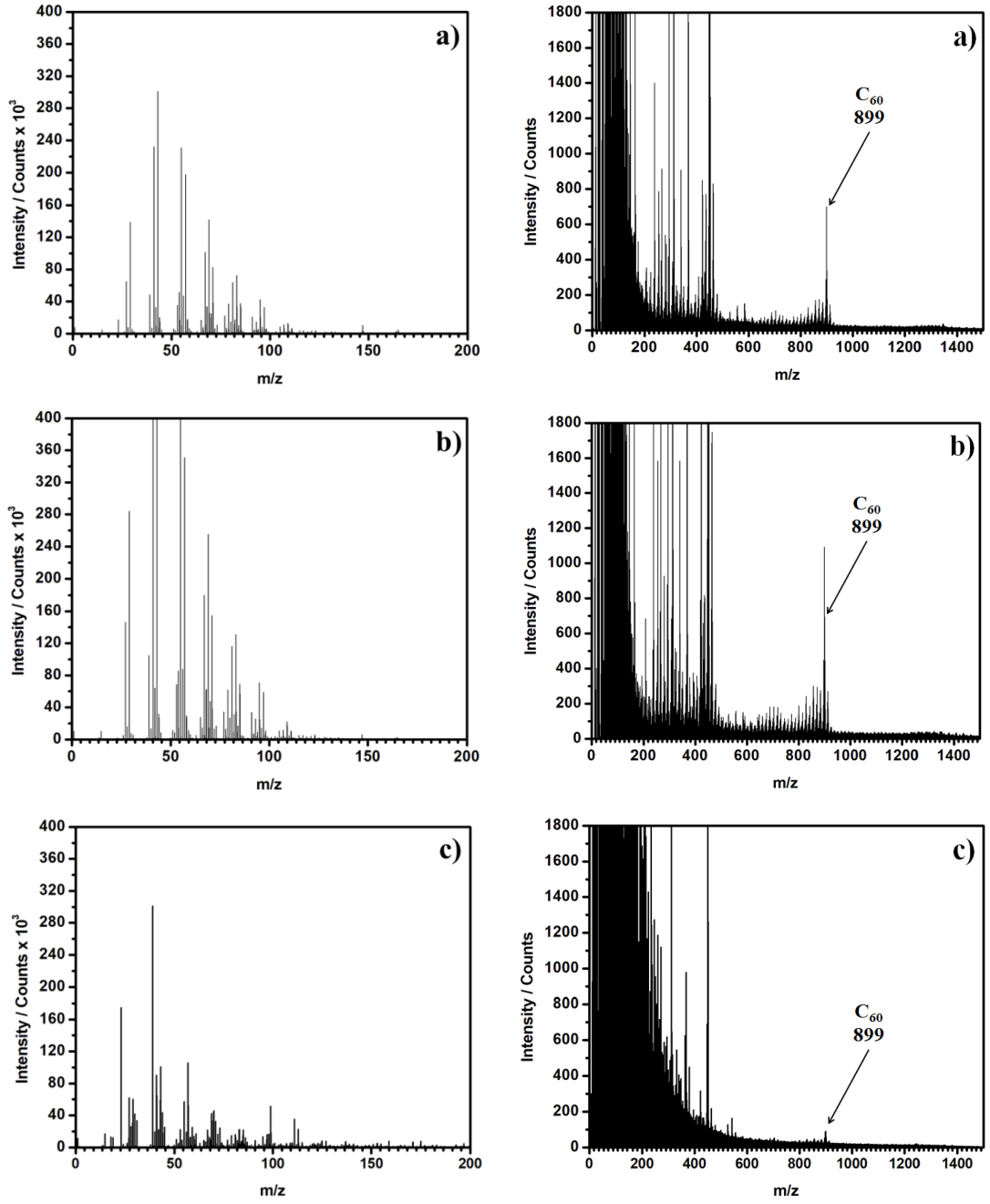

Figure 48: ToF-SIMS spectra for a single leaf sample of *Xanthosoma sagittifolium*, three regions of the leaf are shown; a) margin, b) lamina, c) midrib. Complete spectra are shown

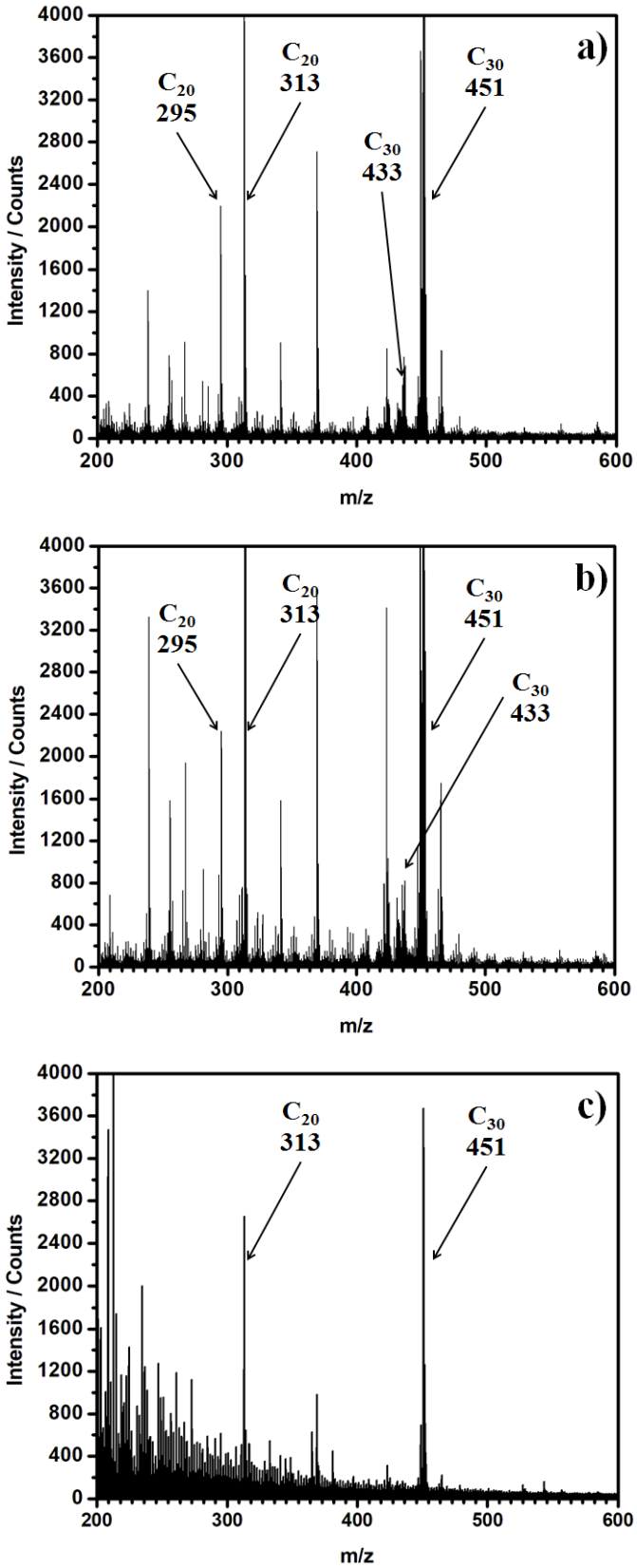

Figure 49: ToF-SIMS spectra for a single leaf sample of *Xanthosoma sagittifolium*, three regions of the leaf are shown; a) margin, b) lamina, c) midrib. Mass range from 200–600 m/z is shown

When analysing the spectra between 200–600 m/z (**Figure 49**), there are differences between the margin/lamina regions and the midrib, with the former showing a much clearer fragmentation pattern consistent with a long alkyl chain. Present on the surface of all regions are two families of compounds, with the parent ion occuring at m/z 313 and 451. The compounds present are consisten with carboxylic acid functionalities although it is possible that the peaks could also be due to esters, with the first peak at 313 m/z consistent with a saturated carboxylic acid $[C_{19}H_{39}COOH_2]^+$ and homologues. A peak 295 m/z, consistent with $[H_2O]^+$ loss at the carboxylic acid group is also observed as well as successive fragmentation of the alkyl chain. This fragmentation pattern is much higher in intensity for the margin/lamina regions than the midrib indicating a higher relative intensity of this compound present on those surfaces. The presence of high amounts of long alkyl chains would increase surface hydrophobicity and would be expected in leaves that show hydrophobicity.

The second compound present occurs at m/z 451, which is consistent with an unsaturated carboxylic acid and homologues with a single unsaturated bond. The main compounds peak $[C_{29}H_{57}COOH_2]^+$ also shows a characteristic fragmentation pattern of a long alkyle chain, with successive $[CH_2]^+$ or $[C_2H_4]^+$ losses. Also observed in the spectra is a peak at 433 m/z, corresponding to the loss of $[H_2O]^+$ to form a characteristic $[RCO]^+$ ion. The two carboxylic acid families and homologues should also be seen in the negative ion spectra, with parent ions occuring at 311 m/z and 449 m/z respectively, which correspond to the deprotonated acids $[C_{19}H_{39}COO]^-$ and $[C_{29}H_{57}COO]^-$.

Also present in the spectra are much smaller peaks at m/z values 529, 557, and 585, which could correspond to acid or amide functionalities with multiple unsaturated bonds such as $[C_{39}H_{71}COOH_2]^+$ or $[C_{39}H_{71}CONH_3]^+$. These peaks would also be present in the negative ion spectra at m/z 529, 555, and 583.

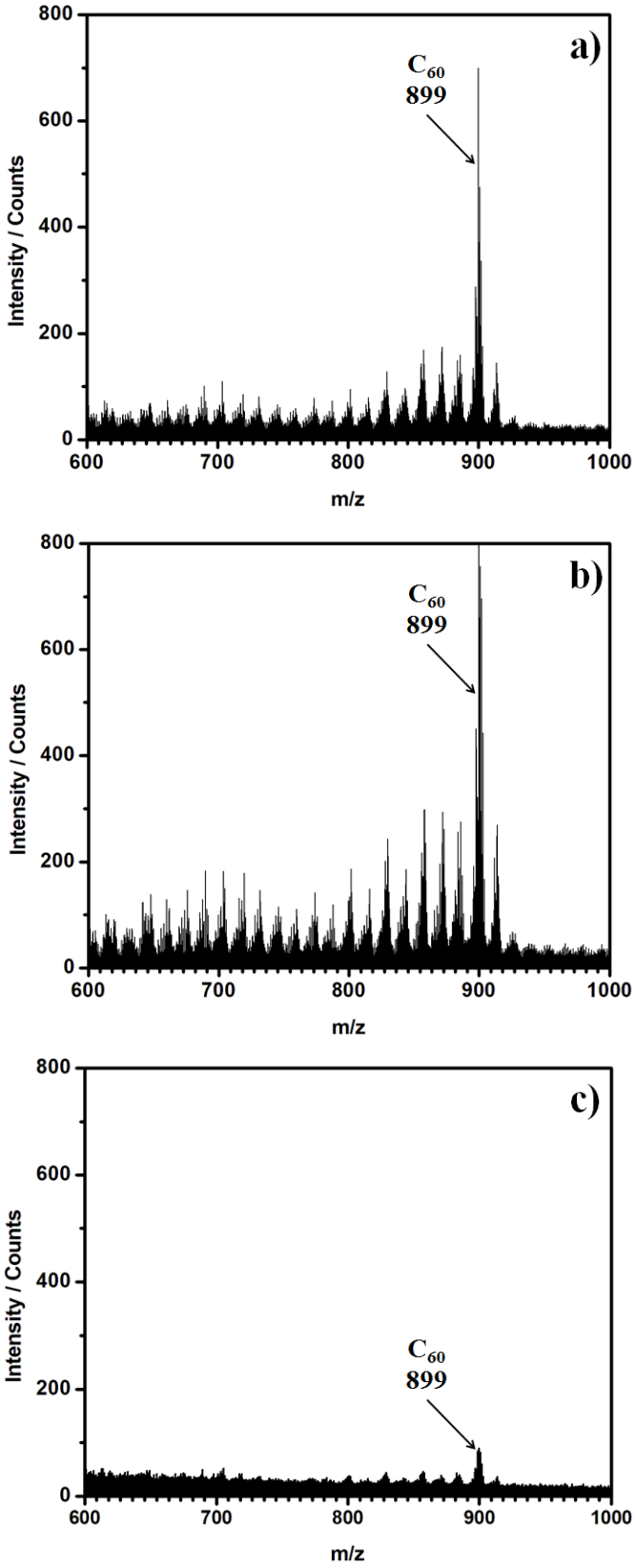

Figure 50: ToF-SIMS spectra for a single leaf sample of *Xanthosoma sagittifolium*, three regions of the leaf are shown; a) margin, b) lamina, c) midrib. Mass range from 600–1000 m/z is shown

For the spectra between 600–1000 m/z (**Figure 50**) there is a clear peak present in the margin/lamina region at m/z 899 which shows weak relative intensity for the midrib region. This peak, given its relative intensity to the other peaks present in the spectra could be a dimer of the compounds present at 451 m/z, which would explain the characteristic alkyl fragmentation pattern observed prior to the peak.

4.3.2 Negative Ion Spectra

The negative ion spectra (**Figure 51**) also show clear differences with respect to margin/lamina compared to the midrib region, as well as when compared to their positive ion spectra. There are a number of inorganic compounds present at lower m/z values, particularly in the midrib region. In particular, peaks are observed at 153 m/z and 233 m/z corresponding to inorganic, sulphur containing compounds previously described. Other peaks which are observed in the midrib region are low mass nitrogen compounds such as $[CN]^-$ and $[CH_2NH_2]^-$. All spectra show similar peaks compared to the positive ion spectra, as well as an observable fragmentation pattern between 500–100 m/z, characteristic of a long alkyl chain.

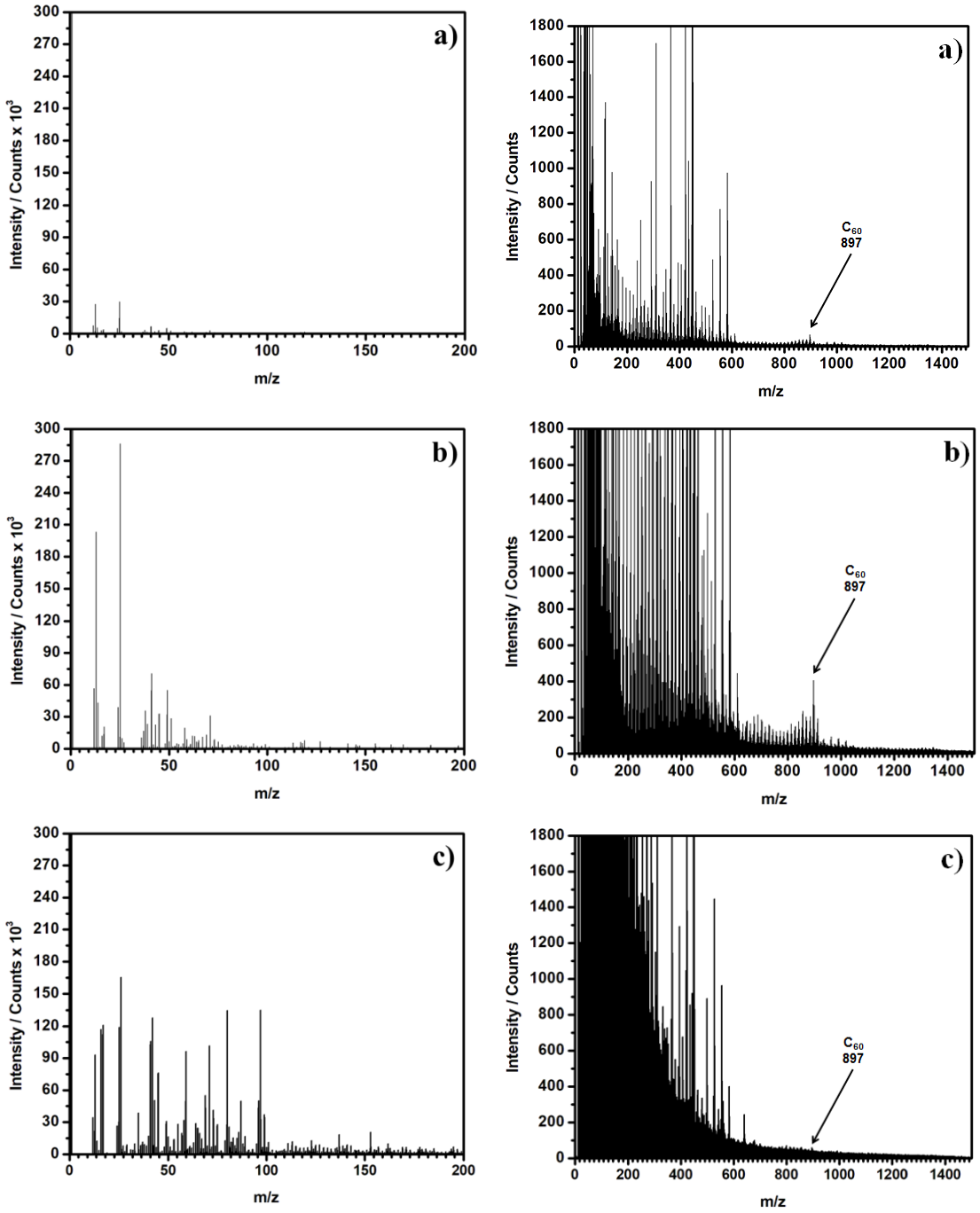

Figure 51: ToF-SIMS spectra for a single leaf sample of *Xanthosoma sagittifolium*, three regions of the leaf are shown; a) margin, b) lamina, c) midrib. Complete spectra are shown

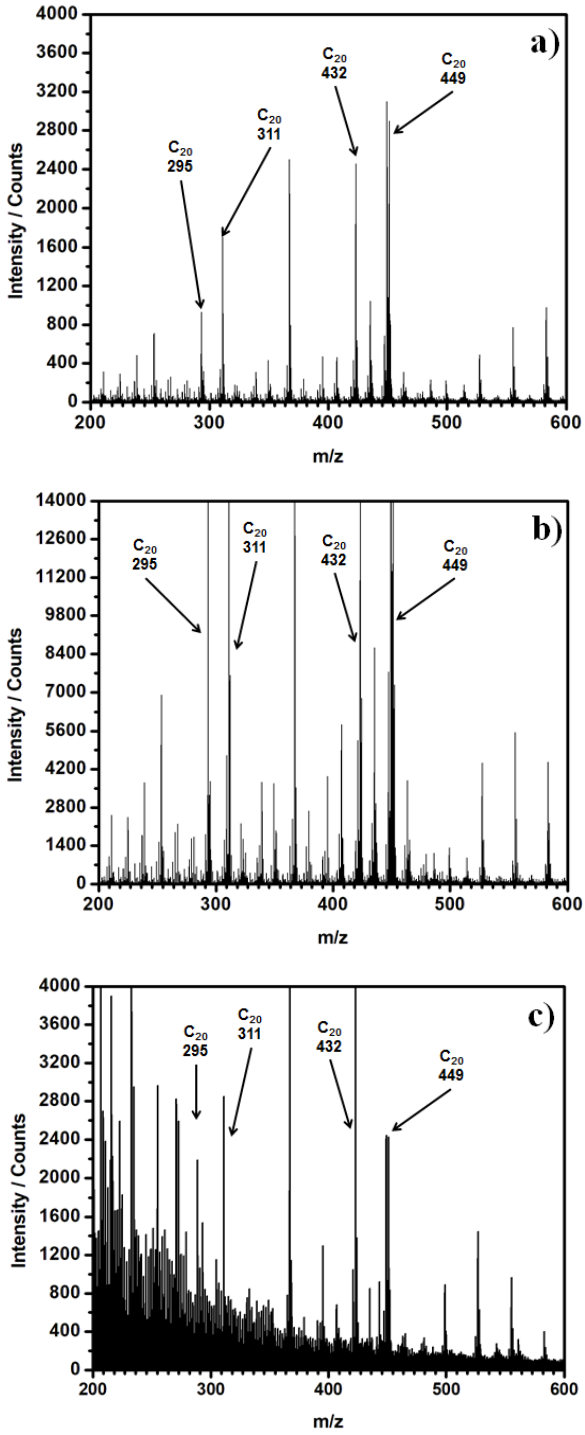

Figure 52: ToF-SIMS spectra for a single leaf sample of *Xanthosoma sagittifolium*, three regions of the leaf are shown; a) margin, b) lamina, c) midrib. Mass range from 200–600 m/z is shown

When comparing the spectra for mass range between 200–600 m/z (**Figure 52**) there are observable differences between the margin/lamina and midrib regions. The former regions show a much clearer fragmentation pattern, at much higher relative intensities compared to the midrib region, although there are some peaks

which are present in all three spectra. As described previously there are peaks corresponding to two families of compounds, likely carboxylic acids at 311 m/z $[C_{19}H_{39}COO]^-$ and 449 m/z $[C_{29}H_{57}COO]^-$ as expected. With fragmentation patterns characteristic to those compounds, such as loss of $[OH]^-$ also observed. Also present is a family of compound at m/z values 527, 555, and 583, which could correspond to acid or amide functionalities with multiple unsaturated bonds such as $[C_{39}H_{71}COO]^-$ or $[C_{39}H_{71}CONH]^-$, although the relative intensities of the peaks are weaker when compared to those at 311 m/z and 449 m/z.

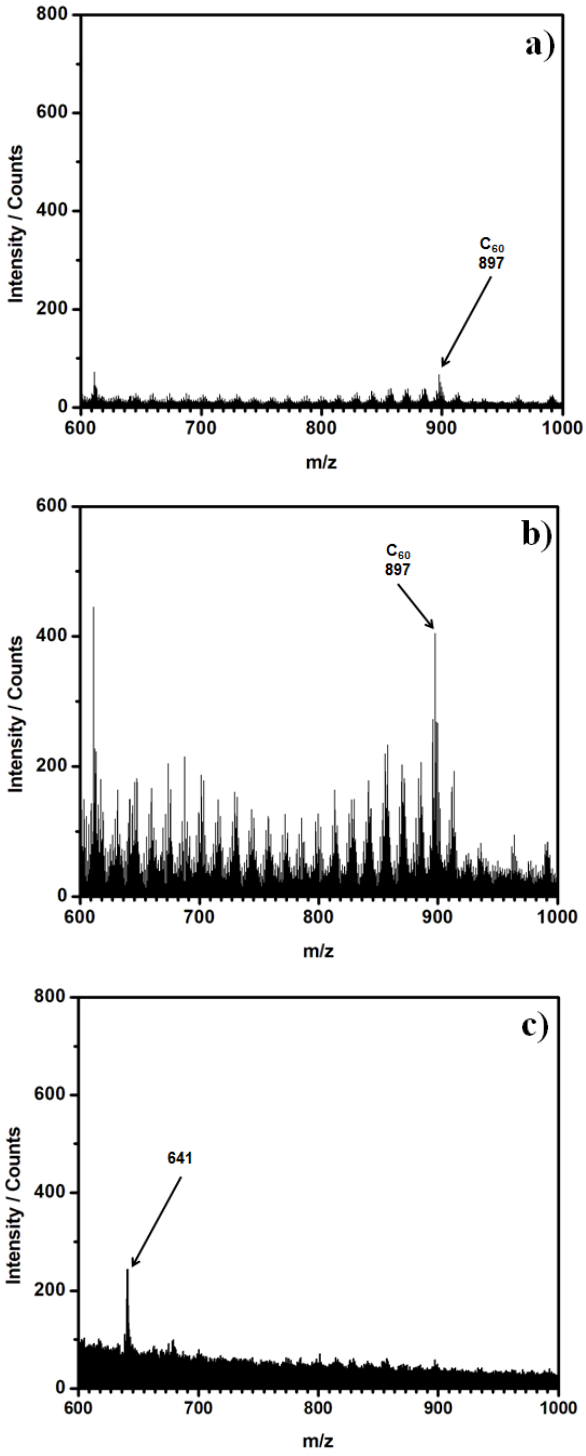

Figure 53: ToF-SIMS spectra for a single leaf sample of *Xanthosoma sagittifolium*, three regions of the leaf are shown; a) margin, b) lamina, c) midrib. Mass range from 600–1000 m/z are shown

For a 600–1000 m/z range, again there is the prescence of a mass peak at 897 m/z, likely a dimer of the 449 m/z carboxylic acid compound, as well as a characteristic fragmentation pattern accompanying it. The intensity of these peaks

are much lower in the midrib and margin region when compared to the lamina, indicating a lower amount present on the surface at the midrib and margin.

For the midrib region, there is a clear peak at 641 m/z with a much higher intensity than surrounding peaks which could be due to fragmentation of the dimer at 897 m/z, although the accurate mass of 641.02 indicates the peak is hydrogen defficient. A typical long hydrocarbon chain would show mass of around 646.6 and a large peak present 561.09 could indicate loss of SO_3. This is more likely the case due to the large presence of oxidised S species present at lower mass values, indicating a contaminant, possibly a surfactant.

4.4 Conclusion

ToF-SIMS has been used to provide a strong indication of the prescence of a variety of compounds present on the leaf surface. Most notably one saturated $C_{19}H_{39}COOH$ and one unsaturated $C_{29}H_{57}COOH$ carboxylic acid compound and their various homologues. These compounds match those that have been detected in other plants, such as *Phyllostachys aurea* by Wigzell et al. and *Kalonchoe daigremontiana* by Jetter et al. Characteristic alkyl chain fragmentation patterns are also observed as well as the prescence of a large amount of low mass, sulphur containing inorganic compounds such as KH_2SO_4. The relative intensities of the compounds between the three regions gives an indication as towards their concentration across the leaf surface (**Figure 54** and **Figure 55**). In particular, the lower intensity observed in the midrib region relative to margin/lamina points towards a differing distribution of surface waxes across the different regions, which may help to explain the differing wettabilities observed. The presence of longer alkyl chains would create a surface that is hydrophobic and therefore repellent to water, which explain the difference in wettability observed between the margin/lamina and midrib regions. Spatial differences in plant waxes have been observed in other plant species, such as *Phyllostachys aurea*.

The difference in peak intensity also shows that the compound is poorly ionised in the positive spectra, showing a much strong ionisation in the negative ion likely due to the carbonyl functionality. Additional analysis of the surface waxes, such as using gas chromatography-mass spectrometry will need to be undertaken in

order to ascertain for certain, as well as surface imaging using ToF-SIMS to measure the spatial distribution of various compounds.

This work shows how ToF-SIMS can be succesfully used to analyse the surface waxes present on a variety of different leaves, with multiple different functional groups and chain lengths detected, as well as inorganic contaminants and characteristic fragmentation patterns. More importantly, this work proves how ToF-SIMS is an important analytical tool in understanding the surface chemistry of plant surfaces which can then be applied in future by other researchers to multiple other plant surfaces.

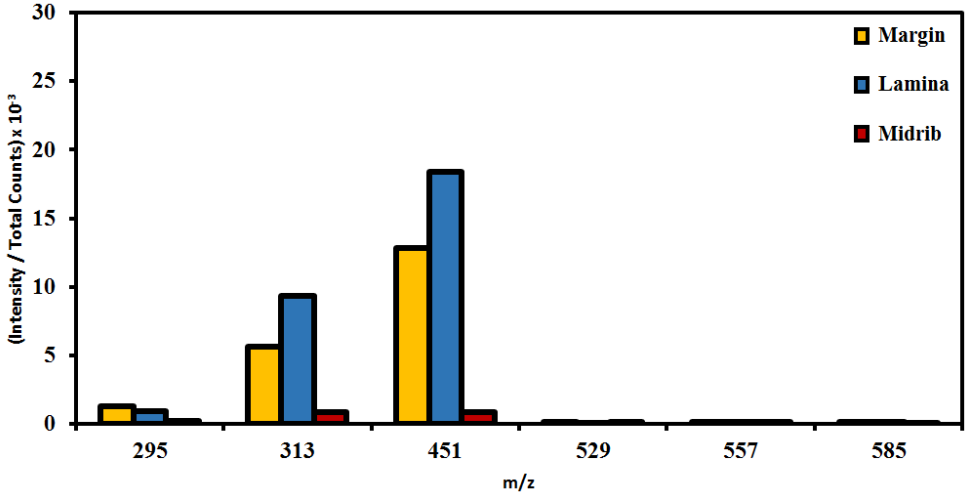

Figure 54: Comparison of the relative intensities of key peaks across the three leaf regions, positive ion spectra is shown

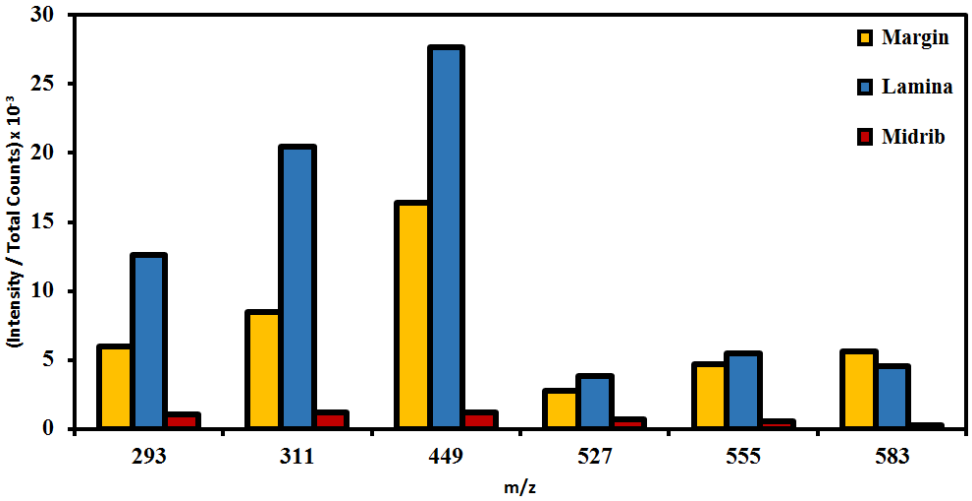

Figure 55: Comparison of the relative intensities of key peaks across the three leaf regions, negative ion spectra is shown

Chapter 5 Development of Fog Collection Methodology

5.1 Introduction

Climate change and a growing global population is placing stress on current water supplies with an estimated 62% of the global population set to experience water scarcity by 2030.[1] In order to solve this issue the development of new, accessbile water sources is essential. One such water source is fog which has already been successfully collected in multiple countries globally.[2]

In order to study and test plant surfaces that are adapted to collect fog, a reliable and repeatable fog collection method is therefore required in order to test the fog collection ability of both artificial and natural fog collecting surfaces.

5.2 Theory

There are a number of ways in which to generate fog in a laboratory setting, each with their advantages and disadvantages. Once generated, the fog can be directed at a sample and the amount of water collected measured experimentally.

5.2.1 Nebulizer

Nebulizers are traditionally used to turn liquid medication/suspensions into an aerosol form. This is particularly useful for treatments directed towards the lungs as it allows the medication to penetrate deep into the lungs themselves. There are two commonly used types of nebulizer, jet nebulizers, and ultrasonic nebulizers.[3]

Jet nebulizers use pressurised gas (air) passed through a small device which contains a liquid suspension, the pressurised gas converting the liquid into an aerosol form which can then pass through an outlet. Typically the gas flow is around 2–10 L min^{-1} and can be supplied via gas cylinder or compressor, with the outlet taking the form of tubing or a medical mouthpiece. The particle size of the aerosol can vary between nebulizers but is predominately contained of droplets micrometres in scale.[4]

Ultrasonic nebulizers use high frequency (1–3 MHz) vibrations of a piezoelectric crystal to generate the aerosol spray. The vibrations cause a fountain to appear at the air-liquid interface of a water reservoir which generates a variety of droplet sizes.[5]

There are advantages and disadvantages to these methods, jet nebulizers require a compressed air stream from a cylinder or compressor whereas ultrasonic nebulizers do not. Ultrasonic nebulizers are easy to use and maintain, but slowly heat up the liquid in the reservoir over time whereas jet nebulizers do not.[8]

5.2.2 Fog Harvesting

Fog collection is initiated when a droplet of fog impacts and is captured by a surface.[6,7,8] The droplet then grows by either coalescing with adjacent droplets on the surface, or when fog impacts surface droplets causing droplet growth. The collection of fog droplets is dependent upon the droplet diameter, the wind speed of the fog, fog density and the surface used in collection.[9]

One example of droplet size influencing fog collection was shown by Park et al. when optimizing the design of wire mesh fog collectors. More efficient collectors proved to be those with a wire diameter size less than that of the water droplet.[10]

A factor that affects the collection of fog is the relevant humidity of the fog. The humidity is affected by the water droplet concentration in the fog and the surrounding air temperature, with higher temperatures resulting in less humidity and therefore lower fog collection.[11] This is important when considering which nebulizer to use for fog collection, as heating up the water stream could alter experimental results.

Another factor in fog collection is the height the collector is placed above the ground. Studies conducted in Chile by Cereceda et al. showed that fog collectors placed 2 metres above the ground collected significantly more than those placed 0.2 metres above the ground. This trend also remained true for those collectors placed at different altitudes along a cliff edge, with those collectors placed at higher altitudes collecting the most water.[12]

5.2.3 Conclusion

Taking the above theory into consideration, a jet nebulizer would appear to be the most appropriate method for the generation of fog particles for two main reasons. Firstly, it is easy to control variables in the system, such as air flow rate and particle size which govern the amount of fog collected by a sample.[9] The flow rate can be controlled by placing a flow meter between the nebulizer and compressed air source and the particle size can be controlled by varying the type of nebulizer used. Secondly, an ultrasonic nebulizer would slowly increase the temperature of the water reservoir over time affecting the generation of fog throughout the course of the experiment and likely resulting in a variable fog stream.

5.3 Experimental

5.3.1 Fog Collection

Fog was generated using an air compressor unit Clement Clarke, MEDIX Econoneb, 3605040HW). Flow rate 7–9 x 10^3 cm^3 min^{-1} at 138 kPa (1.38 bar), and a nebuliser (Cirrus Nebulizer, 1501000, Intersurgical Ltd.) connected in series. A flow meter (NGVB211-GTF2AHD-B, 1–12 L min-1, ¼ inch BSPP angled connections, CT PLATON SAS) was connected between the air compressor and nebuliser to measure the flow rate. A section of flexible (expandable) plastic tubing (58 mm length, 158 mm expanded length, Repti Fogger Expandable hose, Zoo Med Laboratories Inc.) with a circular outlet 19 mm in diameter was used to direct the fog flow at the sample. For some experiments a piece of custom designed glassware, “L” shaped, approximately 90 mm x 90 mm was used to direct the fog stream at the sample.

30 mm x 30 mm samples were affixed to a small sample stand consisting of a red/orange rubber stopper (24 mm length x 13 mm top diameter x 16 mm bottom diameter, Phillip Harris Ltd.), into which is inserted a length of metal wire (80 mm length, wire copper tinned, 1.626 mm diameter, Rowan Cable Products Ltd. TCW16 500 g) such that the top of the wire is a total of 88 mm high. Soldered to this wire is a copper square (10 mm x 10 mm x 1 mm, RS Components Ltd., Copper Sheet, 300

mm x 300 mm x 0.45 mm, 680-695). The samples were affixed using a small amount of glue (Pritt Stick, Henkel Ltd.).

Samples consisted of a variety of materials; polyethylene (HDPE natural, Gilbert Curry Industrial Plastics Co Ltd.), cotton wool (Apaks, 100% Pur Coton, 100 gr, S.N.003.URT.24.03.15, İpek İdrofil Pamuk San. ve Tic. A.Ş., Turkey), and non woven polypropylene (Avoca Technical Ltd, spunbond, 70 g m^{-2}), non-woven polypropylene masks (middle layer (white) of the mask , SDMedical50pk, Blue, SecurityDirect.co.uk), and varying grades of silicon carbide abrasive paper (3M / Wetordry™ 734 Tri-Mite™).

Samples were placed on an analytical balance (Mettler AJ150, Mettler-Toledo Ltd.) at a distance of 50 mm away from the fog outlet, with the centre of the sample in line with the centre of the fog outlet. The nebuliser was filled with 9 cm^3 of deionised water, and experiment times conducted over a period of 20 minutes. The experiments were conducted in a temperature (18–22°C) and humidity (40–50%) controlled room.

5.3.2 Scanning Electron Microscopy

The non-woven polypropylene samples were mounted onto a carbon disk supported on an aluminum holder, and coated with a 5 nm gold layer (Model 108 sputter coating unit, Cressington Scientific Instruments Ltd) in order to avoid excess surface charging. Images were taken on a scanning electron microscope (Tescan Vega 3MLU, TESCAN ORSAY HOLDING) operating in secondary electron detection mode, in conjunction with 8 kV accelerating voltage, and a working distance between 8 and 26 mm.

5.4. Results

Samples were cut to the desired dimensions (30 mm x 30 mm) and mounted on a custom built stand as described previously. Using flexible plastic tubing the fog stream was directed at the sample and placed such that the distance between the mouth of the tubing and sample was 50 mm. In-between the nebulizer and compressor unit, a flow meter was inserted in series to control the air flow (5.5 L min^{-1}) to the nebuliser unit (**Figure 56**). This produced a consistent fog stream in

which 74% of the droplets have diameters of <5 μm, similar in size to those occurring in nature.[13]

Figure 56: Image highlighting the experimental setup with the custom built stand, sample, nebulizer, tubing, and flow meter. The compressor unit is mounted on an adjacent bench

The entire apparatus was placed in a temperature and humidity controlled room, with environmental controls set to a temperature of 20 °C and a relative humidity of 50%. Multiple experiments were then conducted on a variety of materials to test their fog collection abilities. These materials were used to test a variety of different properties, such as how fibre size and surface roughness affects fog collection.

5.4.1 Polyethylene

The first sample which was run using this method was a reference sample of high density polyethylene (**Figure 57**); contact angle measurements were taken on the polyethylene samples yielding a contact angle of 73° ± 3°, showing the samples to be slightly hydrophilic.

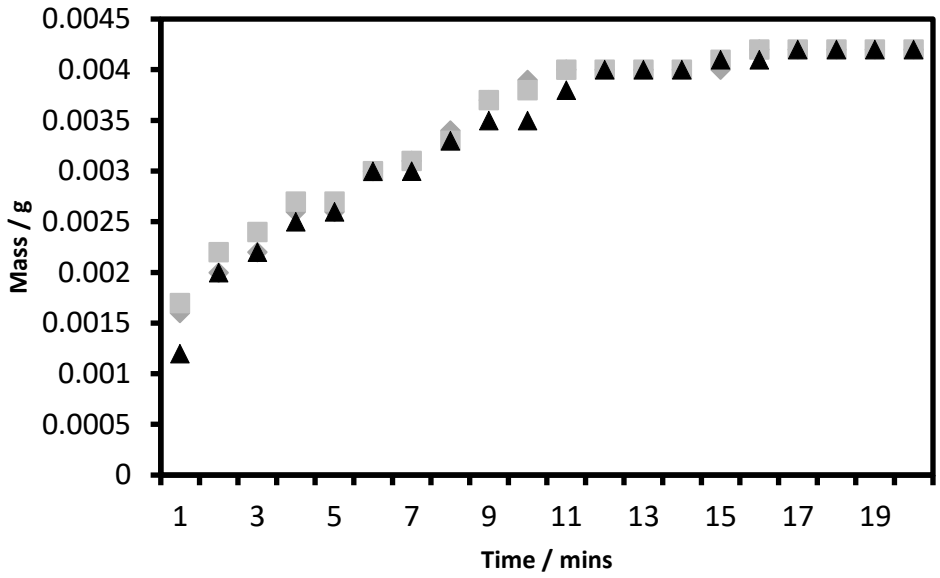

Figure 57: Data obtained for the polyethylene (30 mm x 30 mm) experiments, a total of three different experiments were conducted with a fresh sample used for each successive experiment

A total of three individual experiments were conducted (**Figure 57**), and mass of water collected over a time period measured. The data shows a gradual linear increase before the mass of water collected begins to level off. This could be due to the sample reaching steady state, with water present on the surface evaporating as quickly as it is forming.

5.4.2 Cotton Wool

A total of three cotton wool samples were run and data collected (**Figure 58**). Prior to analysis, static water contact angle measurements were conducted which showed complete absorption of the water droplet into the cotton wool, showing a highly hydrophilic surface.

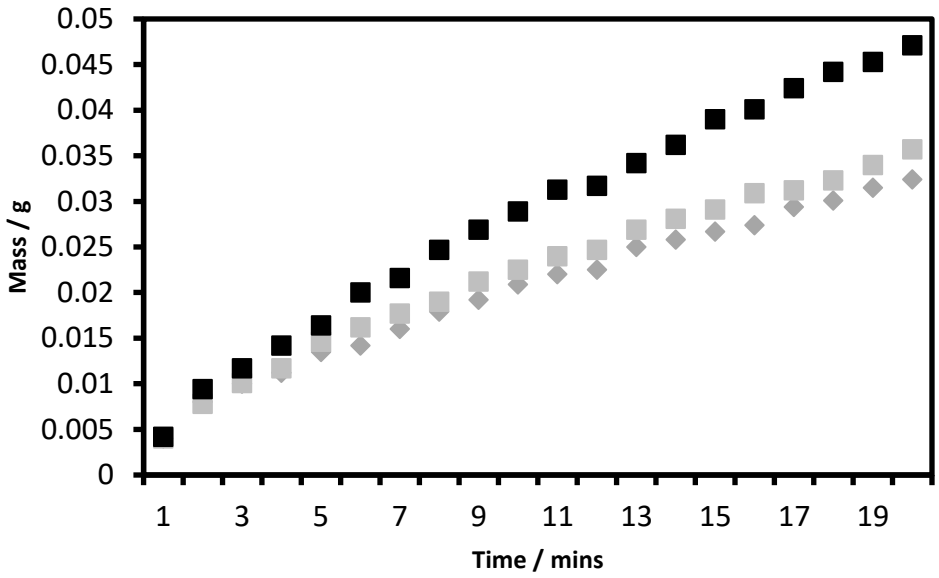

Figure 58: Fog collection data for three individual cotton wool samples (30 mm x 30 mm), with a fresh sample used each time

It was observed during the experiment that small droplets of water grew and nucleated on the sample, particularly around the edges of the sample on the individual cotton fibres, indicating a high degree of surface collection, particularly along individual exposed fibres. The consistent increase in amount collected could be due to the highly absorbant nature of the cotton wool meaning it has not reached a steady state as in polyethylene.

5.4.3 SP180 Grade Sand Paper

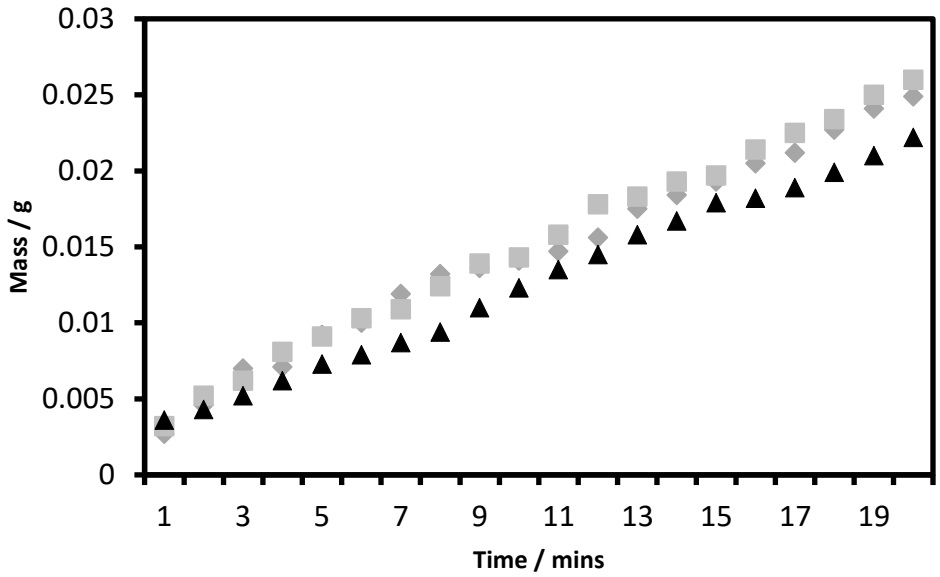

Figure 59: Fog collection data for three individual samples (30 mm x 30 mm), with a fresh sample used for each successive experiment

Three samples of SP180 grade sand paper were run (**Figure 59**) and contact angles measured yielding a contact angle of 55° ± 7°, showing a more hydrophilic surface than that of the polyethylene standard. During the experiment significant deflection of the fog stream by the sample was observed, which would lower the effective flow rate experienced at the surface, which was not as pronounced in the case of the cotton wool sample. The deflection observed appears to have little effect on the rate of water collection, with SP180 grade collecting more water than the polyethylene sample.

5.4.4 SP1200 Grade Sand Paper

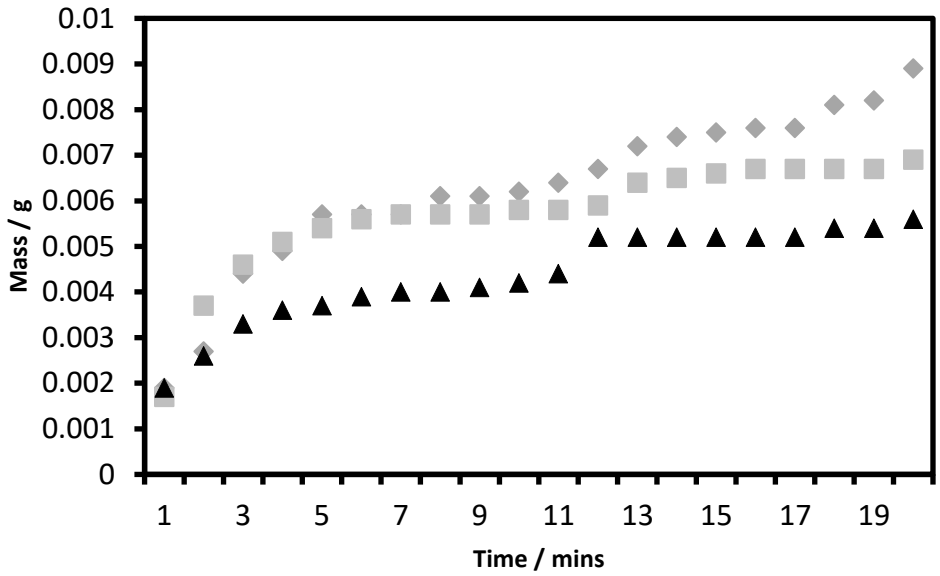

Figure 60: Data for the SP1200 grade sandpaper (30 mm x 30 mm)

Static water contact angles measured on the SP1200 sandpaper were 131° ± 1°, showing the samples to be hydrophobic in nature, likely due to the fine particle size leading to a Cassie-Baxter wetting state. The average particle size on the surface was 15.3 µm in diameter, the smallest particle size of all sandpaper grades tested. The hydrophobic nature of the surface helps explain why it collects less water than the SP180 grade sand paper which is hydrophilic, as surfaces that are hydrophillic collect more fog than those that are hydrophobic. The change in particle size could also play an effect in nucleation of droplets on the surface. It was also observed that the rate of water collection (**Figure 60**) was less consistent than the SP180 grade, potentially reaching steady state towards the end of the experiment.

5.4.5 Non-woven Polypropylene Sheet

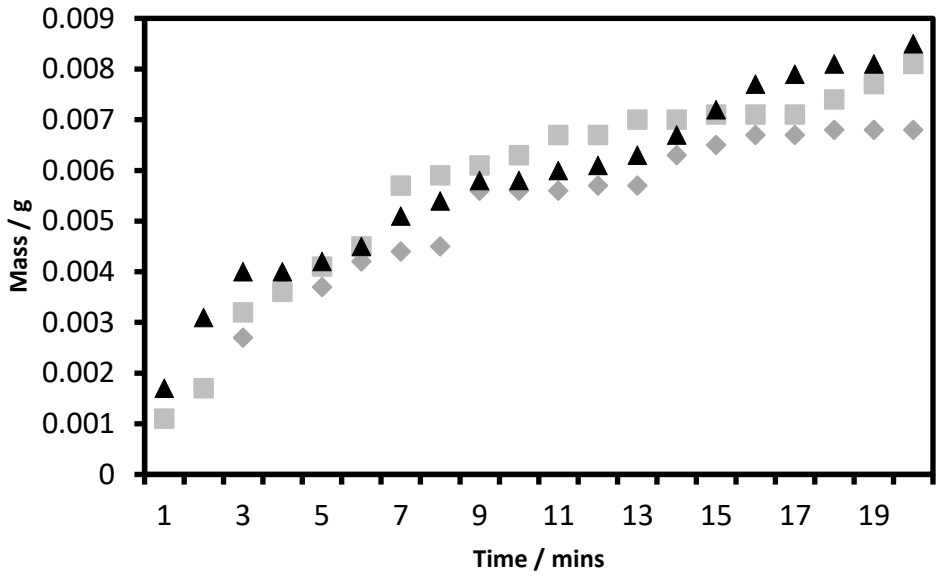

Figure 61: Data obtained for sample of non-woven polypropylene sheet (Avoco) (30 mm x 30 mm)

Contact angle measurements on the non-woven polypropylene sheet yielded a contact angle of 110° ± 2°, showing the samples to be slightly hydrophobic. This case again be explained by a formation of a Cassie-Baxter type wetting regime, with water droplets unable to penetrate into the fibres present on the surface resulting in a stable air layer. It was observed during contact angle measurements that water droplets preferentially self-orientated into the dimples observed on the surface (**Figure 62**), resulting in a lower observed contact angle than the non-woven polypropylene mask counterpart. When collecting fog (**Figure 61**) samples showed a variable collection rate throughout the experiment. The samples overall collected similar amounts of fog to the SP1200 sandpaper, and slightly more than the polyethylene standard.

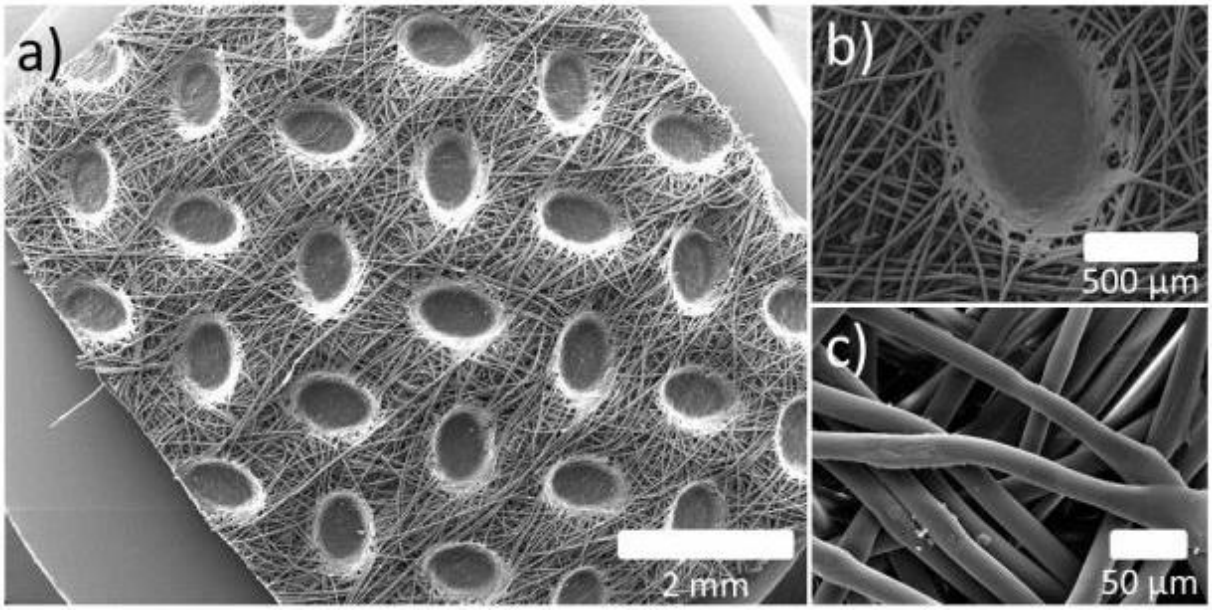

Figure 62: SEM images taking of the non-woven polypropylene mask at a range of magnifications. Average fibre diameters were (18 ± 1) µm

The SEM images (**Figure 62**) show the surface features and patterned dimples present on the sample surface. The average fibre size was measured to be (18 ± 1) µm, larger than the average diameter of water droplets in the fog stream, with a random distribution of fibres across the surface. The dimples themselves showed a flat polypropylene surface where the fibres had been melted together to provide structural cohesion to the material.

5.4.6 Non-woven Polypropylene Mask

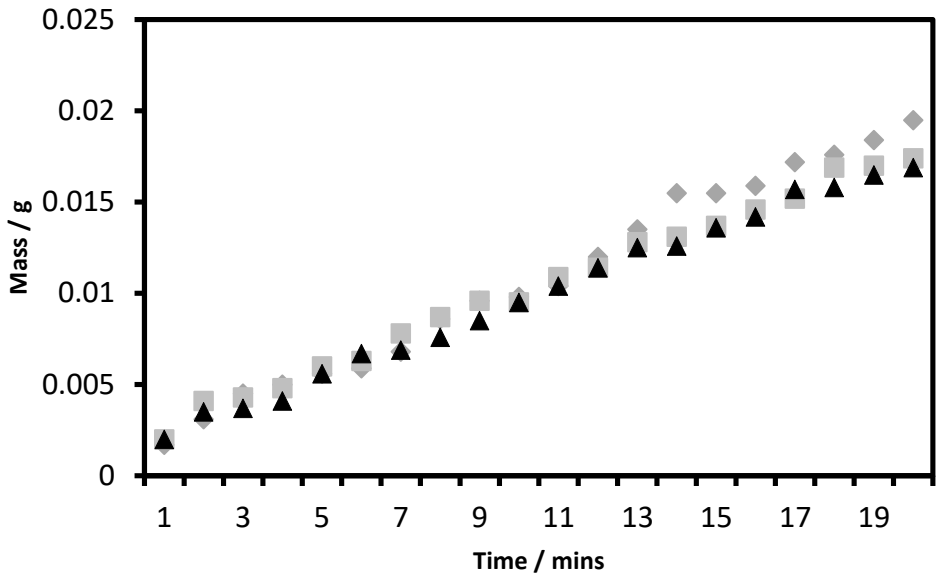

Figure 63: Water collection data for the non-woven polypropylene mask (30 mm x 30 mm)

Contact angle measurements were taken on the non-woven polypropylene mask samples yielding a contact angle of 147° ± 1°, which is more hydrophobic than the non-woven polypropylene sheet. This is likely due to the smaller fibre size (6 ± 1 µm), as well as the lack of dimples in the surface (as shown by SEM) resulting in a more efficient Cassie-Baxter state and a higher observed water contact angle, despite the two samples being chemically identical. The fibre sizes are closer in diameter to those of the fog stream relative to the mask sample. The collection of fog (**Figure 63**) proceeds at a steady rate with the samples collecting more than the polypropylene sheet. The smaller fibre sizes, which are closer to the diameter of the fog could explain why the mask collects more water than the polypropylene sheet as well as explain the increase in hydrophobicity observed. It was also observed that the fog stream deflectd less around the mask than the other samples which may also explain the increased collection rate, as there is an increased flow rate present at the surface of the material.

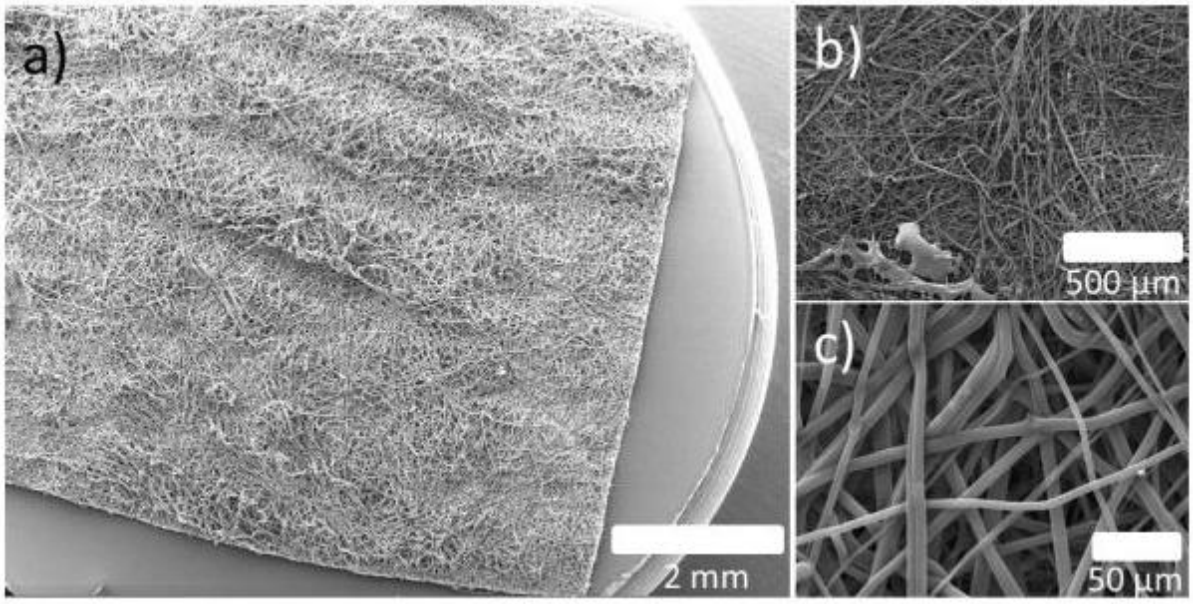

Figure 64: SEM images taking of the non-woven polypropylene sheet at a range of magnifications. Average fibre diameters were (6 ± 1 µm)

The SEM images for the mask (**Figure 64**) show a much smaller average diameter when compared to the non-woven polypropylene sheet. This smaller diameter may help to explain why this samples collected a higher mass of water, with the size matching more closely the diameter of the water droplets in the fog stream, allowing for easier nucleation and capture of the droplets from the fog stream.

5.4.7 Conclusion

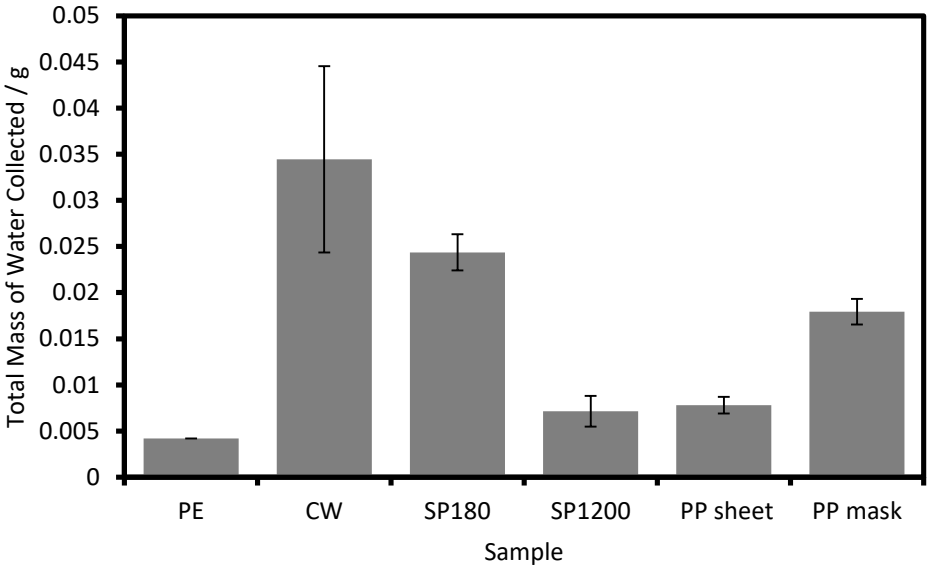

Figure 65: Comparison of overall masses of water collected for each sample (30 mm x 30 mm) over total 20 min duration

When comparing between the samples (**Figure 65**) trends can be seen, for example, the non-woven polypropylene mask collects more water than the non-woven polypropylene sheet despite being chemically identical. The difference in mass collected, is therefore likely due to the difference in surface structure and difference in flow rates. The different fibre size observed, with a smaller fibre size (6 ± 1 µm) collecting more water than the larger fibre size (18 ± 1), as well as the fog stream being deflected less by the mask sample resulting in a higher effective flow rate at the surface could all contribute to the difference in mass collected. This shows that fibrous fog collectors are more efficient if the fibres are similar in diameter to the diameter of fog droplets they are exposed too.

When comparing the sandpaper samples, the trends follow an expected pattern, with the more hydrophilic sample collecting the most water.

Cotton wool collected the most amount of water (in line with experimental observations as the only sample with visible water on the surface), although some variability in results makes a true comparison between it and SP180 grade sandpaper difficult. This variability, as well as the difference in rates observed throughout the experiments across multiple different materials, could be indicative of an experimental error.

It was observed during the course of the experiments that a significant amount of water condensed in the plastic tubing used to direct the fog stream, which could have had an impact on the amount of fog which made contact with the sample as it condensed inside the tubing instead. The tubing proved to be very difficult to dry between individual runs and therefore could have introduced some variability with subsequent experiments.

The expandable nature of the tubing could also have provided a source of error as it was not expanded the same amount for every experiment resulting in a different internal surface area and shape. This will have affected the flow rate and amount of fog which condensed inside the tubing. This could help explain the variability seen in the rate of fog collection for some of the samples. For these reasons, the tubing will need to be changed such that it eliminates these errors.

5.5 Glass Tube to Direct Fog Stream

5.5.1 Experimental

For that reasons described previously, custom made glass tubing (**Figure 66**) was used instead of the expandable tubing and all samples were run again, with the glass tube being dried in-between experiments.

Figure 66: The custom built glass tubing, approximate 90 mm x 90 mm. The glass tube was dried in between each sample

5.5.2 Results

The fog collection experiments were re-run utilising the glass tubing in place of the flexible tubing. Additional samples were also run in order to better observe any trends. The average rate of water collection was also measured for each material.

5.5.3 Polyethylene

Samples of high density polyethylene were again used as a reference sample (**Figure 67**) and the rate of water collection measured. The polyethylene experiments showed a stark difference to those prior to the addition of the glass tubing, with a steady linear increase over time of the mass of water collected, with no levelling off observed. Had the sample reached steady state, as previously hypothesised with water evaporating as quick as it nucleated, this behaviour would not have been observed.

This observation and experiment supports the theory that the flexible tubing previously used was introducing an error into the experiment which altered the amount of water collected on the samples.

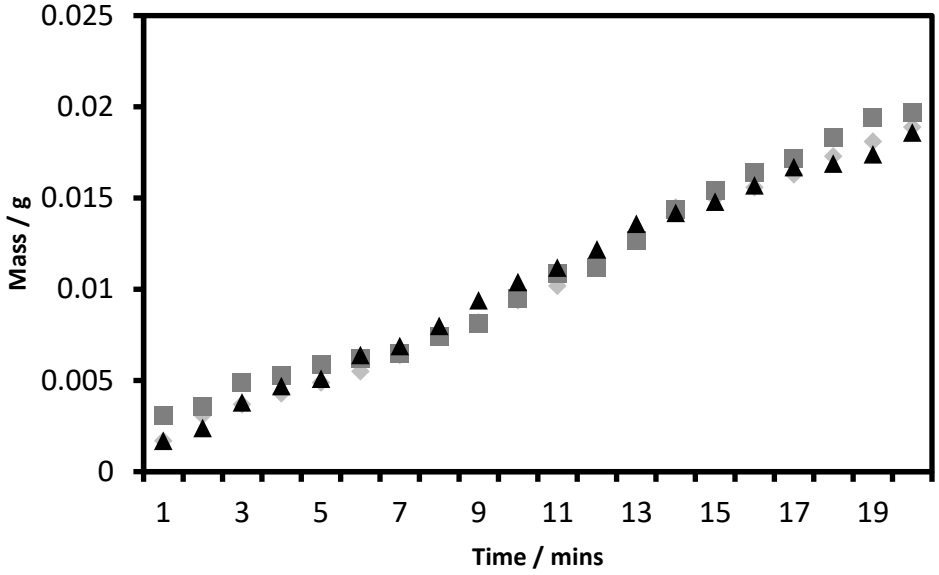

Figure 67: Data obtained for the polyethylene (30 mm x 30 mm) experiments. Rate of water collection for the period between 5–20 min = (91.7 ± 1.7) x 10^{-5} g min^{-1}. No of different experiments using fresh samples = 3

5.5.4 Cotton Wool

Again, as previously described, small water droplets were observed around the edges of the cotton wool sample during the course of the experiment. In particular, droplets nucleated on the fine hairs that occasionally protruded from the edge of the sample. All three cotton wool samples showed good correlation with each other, collecting similar amounts of water and at a similar rate, with a clear linear trend.

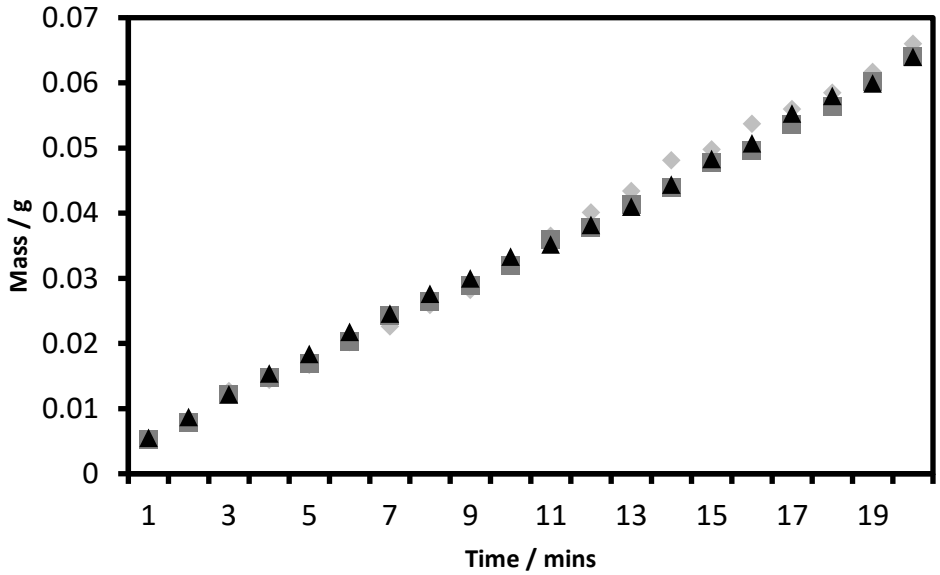

Figure 68: Data obtained for water collection on cotton wool (30 mm x 30 mm). Rate of water collection for the period 5–20 min = (31.6 ± 1.2) x 10^{-4} g min^{-1}. No. of different experiments using fresh samples = 3

5.5.5 SP80 Grade

A total of five different samples of SP80 grade sandpaper were run, with a new sample being used for each experiment. The samples show steady increase over time with no steady state being reached. SP80 grade sandpaper was included in the experiment as it showed complete hydrophilicity, with contact angles of <10° and so should in theory collect the most water out of all sandpaper samples.

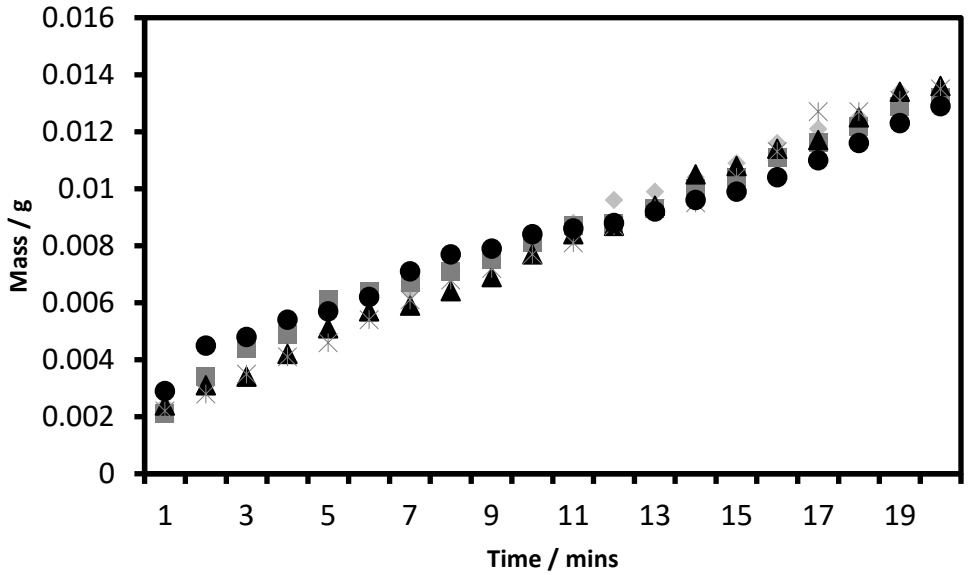

Figure 69: Data results for the SP80 grade (30 mm x 30 mm). Rate of water collection for the period between 5–20 min = (53 ± 4.6) x 10^{-5} g min^{-1}. No of different experiments using fresh samples = 5

5.5.6 SP180 Grade

The SP180 grade sandpaper showed a similar linear trend, although there is some small divergence between samples, as can be seen (**Figure 70**). The difference in fog collection between the cotton wool and SP180 grade can now be clearly seen with cotton wool collecting significantly more water. SP180 grade sandpaper also collects more water than the SP80 grade sandpaper despite being less hydrophilic. This could be due to difference surface roughness between the two grades with SP80 having a larger particle size embedded in the surface.

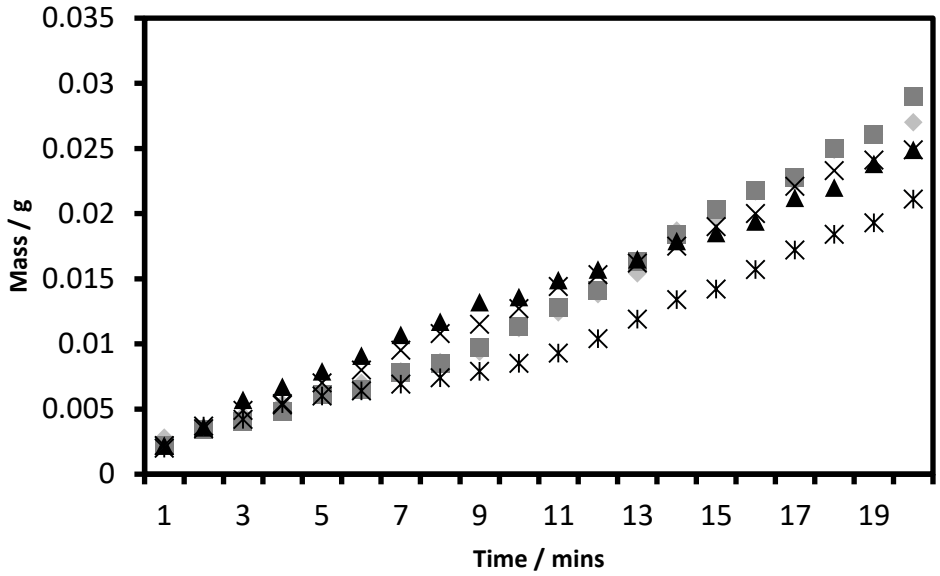

Figure 70: Three experiments were conducted on the SP180 grade (30 mm x 30 mm). Rate of water collection for the period between 5–20 min = (12.5 ± 2.1) x 10^{-4} g min^{-1}. No of different experiments using fresh samples = 5

5.5.8 SP1200 Grade

A total of five experiments were conducted using five fresh samples of SP1200 grade sandpaper (**Figure 71**), again, as with all the previous samples, a clear linear trend can be observed in the data. The amount of fog collected has increased relative to the previous experiment, with the amount collected similar to that of the SP180 grade sandpaper. This indicates that a signifcant amount of fog was condensing inside the tubing leading to lower masses of water collected. The trend in mass collected by the samples has also changed with hydrophilic surfaces collecting the least amount of water out of the sandpaper samples. This reversal in trend indicates a more complex picture and could be due to the different particle sizes present on the surface of the sandpaper, rather than the hydrophillic/hydrophobic nature of the samples with a large particle size (201 µm in the case of SP80) unable to facilitate droplet nucleation due to being much larger than the droplet diameter.

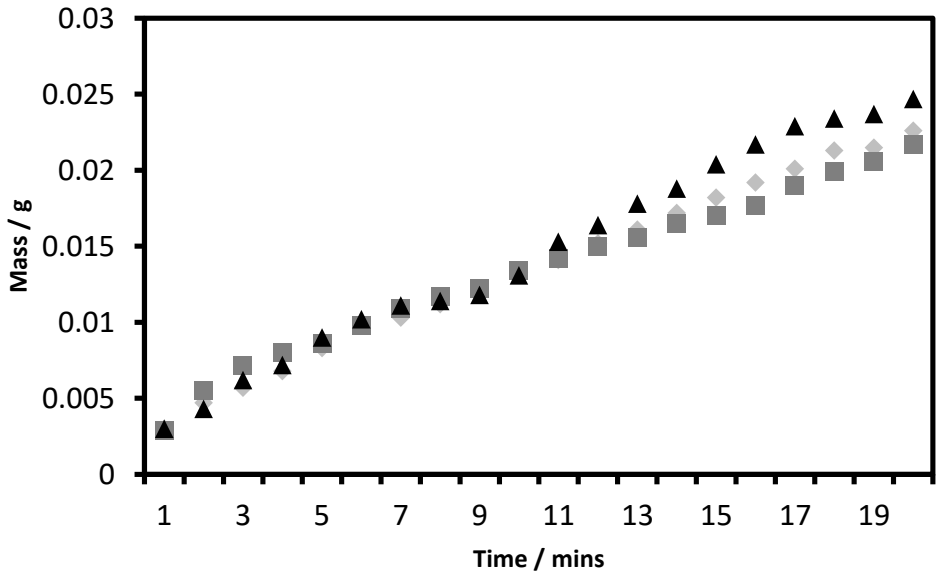

Figure 71: Data for the SP1200 grade (30 mm x 30 mm). Rate of water collection for the period between 5–20 min = (95.8 ± 8.7) x 10^{-5} g min^{-1}. No of different experiments using fresh samples = 5

5.5.9 Non-woven Polypropylene Sheet (Avoco)

The non-woven polypropylene sheet samples (**Figure 72**) showed small divergence in the amount collected between the individual samples. All samples did however show a linear trend in the mass of water collected over time, in line with other experimental observations, as well as an increased amount of water collected, again showing fog was condensing inside the plastic tubing.

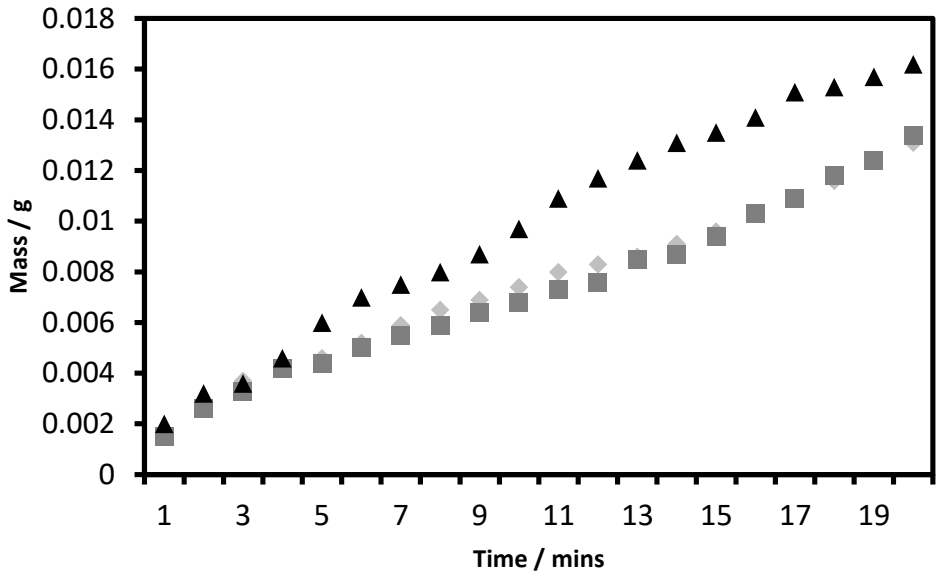

Figure 72: Data obtained for sample of non-woven polypropylene sheet (Avoco) (30 mm x 30 mm). Rate of water collection for the period between 5–20 min = (61.6 ± 5.8) x 10^{-5} g min^{-1}. No of different experiments using fresh samples = 3

5.5.10 Non-woven Polypropylene Mask

The non-woven polypropylene mask (**Figure 73**) collected more water than the polypropylene sheet, it also showed less variation and matched previous experimental trends observed. The increase in water collected is similar for both samples with the fiber size likely playing a signifcant role in the fog collection.

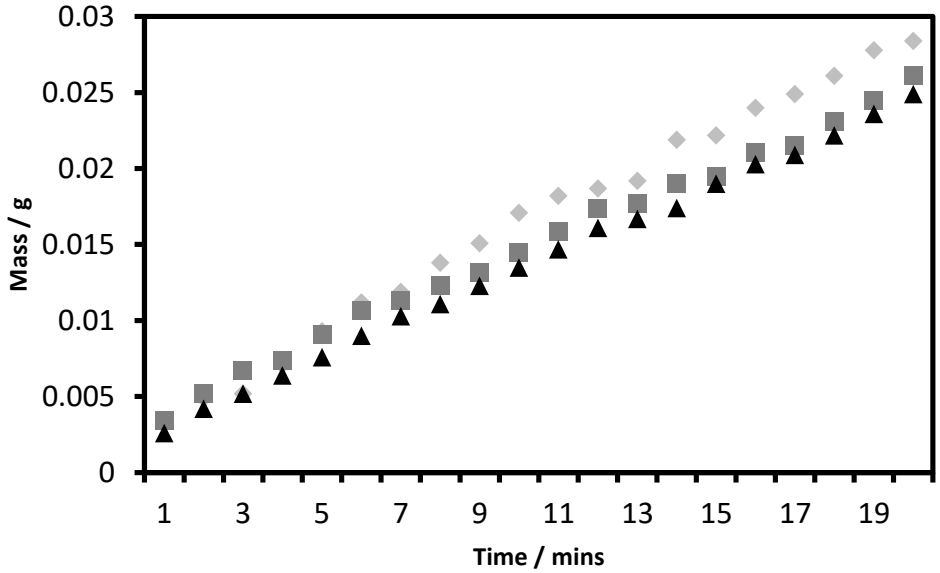

Figure 73: Water collection data for the non-woven polypropylene mask (30 mm x 30 mm). Rate of water collection for the period between 5–20 min = (11.8 ± 0.8) x 10^{-4} g min^{-1}. No of different experiments using fresh samples = 3

5.5.11 Conclusions

When the final readings for each sample are taken into account, it is possible to compare the overall amount of water collected after the full duration of the experiment has been completed (**Figure 74**).

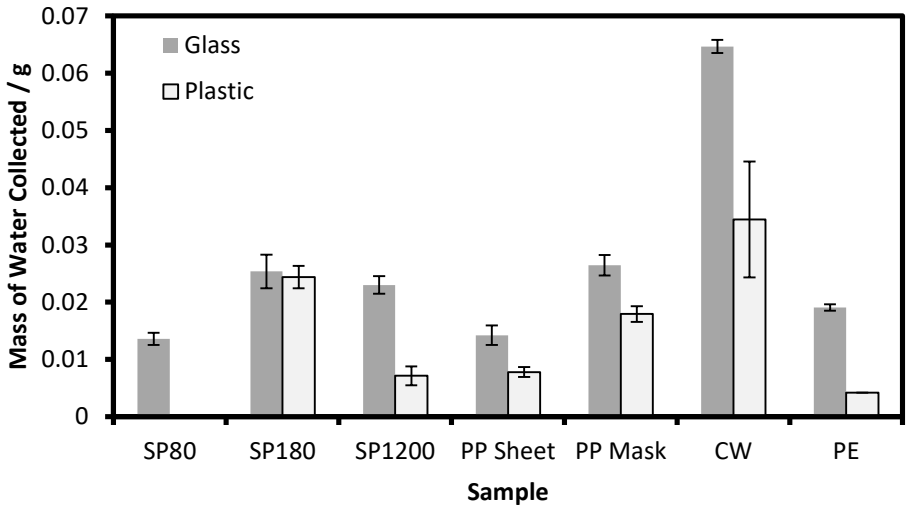

Figure 74: Comparison of overall masses of water collected for each sample (30 mm x 30 mm) over total 20 min duration. Grey bars indicate experiments using glass tube, white bars those using the plastic tubing

When compared with the flexible tubing using the glass tubing results (**Figure 74**) in an increased mass of water collected for all samples barring SP180 grade sandpaper. This strongly indicates that some fog was collecting inside the tubing rather than being directed at the sample. The largest improvement comes in the error associated with the cotton wool samples, with the glass tubing dramatically reducing the variation in the amount of mass collected by the cotton wool.

It was also observed for individual experiments that the rate of water collection followed a linear trend, with a steady increase over time for all samples. Previously, some samples showed a large variability in the rate of water collected, with some remaining flat and no increase in mass observed. These observations lend support to the hypothesis that the plastic tubing was introducing some error into the experiments, either through the variable shape or the water which condensed inside,

in-between experiments. Although the factors determining the amount of fog collection are more nuanced than simply hydrophlic vs hydrophobic, with clear differences observed between different materials, as well as different fiber sizes for chemically identical samples. When comparing samples with variable fibre sizes, those with fibre sizes closer in diameter to the diameter of the fog droplets collected the most fog, in this case the polypropylene mask collected more than the polypropylene sheet. Cotton wool collected the most water likely due to its increased surface area. In the case of the sandpaper samples, a smaller particle size present on the surface improves collection rate, with SP80 having the largest particle size and also the poorest water collection. SP180 and SP1200 sandpaper show similar values (within error) making it difficult to distinguish between the two materials, although both collect more fog than SP80 grade sandpaper.

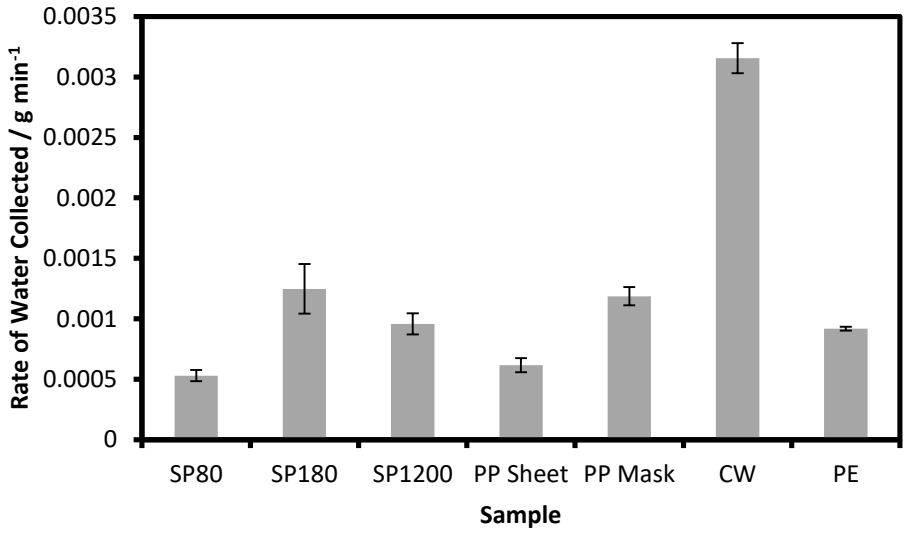

Figure 75: Comparison of rate of water collection (g min^{-1}) for the period between 5–20 min. 30 mm x 30 mm) sample size using the glass tube

In order to test the efficiency of each sample, comparing the rate of water collection becomes important. By comparing the amount collected between 5–20 min (once steady state is achieved) yields a rate of water collection per minute. As **Figure 75** shows, the most effective at water collection is cotton wool, followed by SP180 grade sandpaper and the non-woven polypropylene mask.

This method is able to distinguish between multiple different samples, with different chemistry and surface features, it also produces repeatable and reliable

results with a small margin of error over numerous samples. Some of the larger variance in data has been accounted for and corrected by switching some experimental parameters (tubing). It is also possible to use this method to distinguish between surface features, such as fibre size in the case of the non woven polypropylene, and particle size in the case of the sandpaper samples. This method is therefore appropriate for use in measuring the amount of water collected from a fog stream, with the next stage being to test this method on plant samples and replicas. The method is sensitive enough to distinguish between small surface structure changes (fibre sizes) which is important when applying to different plant surfaces. This is because plants often contain small surface features such as hairs, which show fine variability across the plant surface.

5.6 References

[1] Falkenmark, M.; Lundqvist, J.; Widstrand, C. Macro-Scale Water Scarcity Requires Micro-Scale Approaches *Natural Resources Forum* **1989**, *13(4)*, 258–267.

[2] de Dior Rivera, J. Aerodynamic Collection Efficiency of Fog Water Collectors *Atmospheric Research* **2011**, *102(3)*, 335–342.

[3] Ari, A. Jet, Ultrasonic, and Mesh Nebulizers: An Evaluation of Nebulizers for Better Clinical Outcomes. *Eurasian J. Pulmonology* **2016**, *14*, 1–7.

[4] Elhissi, A. M. A.; Faizi, M.; Naji, W. F.; Gill, H. S.; Taylor, K. M. G. Physical Stability and Aerosol Properties of Liposomes Delivered Using and Air-Jet Nebulizer and a Novel Micropump Device with Large Mesh Apertures. *International Jounral of Pharmaceutics* **2007**, *334(1)*, 62–70.

[5] O'Callaghan, C.; Barry, P. W. The Science of Nebulised Drug Delivery. *Thorax* **1997**, *52*, S31–S34.

[6] Ebner, M.; Miranda, T.; Roth-Nebelsick, A. Efficient Fog Harvesting by Stipagrostis Sabulicola (Namib Dune Bushman Grass) *Journal of Arid Environments* **2011**, *75(6)*, 524–531.

[7] Guha, A. Transport and Deposition of Particles in Turbulent and Laminar Flow *Ann. Rev. Fluid Mechanics* **2008**, *40*, 311–341.

[8] White, B.; Sarkar, A.; Kietzig, A-M. Fog-Harvesting Inspired by the Stenocara Beetle - An Analysis of Drop Collection and Removal from Biomimetic Samples With Wetting Contrast *Applied Surface Science* **2013**, *284*, 826–836.

[9] Schemenauer, R. S.; Cereceda, P. Fog-Water Collection in Arid Coastal Locations *Ambio*, **1991**, *20(7)*, 303–308.

[10] Park, K-C.; Chhatre, S. S.; Srinivasan, S.; Cohen, R. E.; McKinley, G. H. Optimal Design of Permeable Fiber Network Structures for Fog Harvesting *Langmuir*, **2013**, *29*, 13269–13277.

[11] Cáceres, L.; Gómez-Silva, B.; Garró, X.; Rodríguez, V.; Monardes, V.; McKay, C. P. Relative Humidity Patterns and Fog Water Precipitation in the Atacama Desert and Biological Implications *Journal of Geophysical Research* **2007**, *112*, G04S14.

[12] Cereceda, P.; Larrain, H.; Osses, P.; Farias, M.; Egaña, I. The Spatial and Temporal Variability of Fog and its Relation to Fog Oases in the Atacama Desert, Chile *Atmospheric Research* **2008**, *87*, 312–323.

[13] http://www.intersurgical.co.uk/products/oxygen-and-aerosol-therapy/cirrus2-nebuliser-and-nebuliser-mask-kits

Chapter 6 Fog Collection on Plant Samples and Replicas

6.1 Introduction

Using the method described previously in **Chapter 2**, several plant samples of *Xanthosoma sagittifolium* were used to measure their fog collection ability in order to further validate the fog collection method. Positive epoxy resin replicas, as well as replicas which were treated with the nanoimprinting process were also studied. It is expected that both the leaves and replicas show poor fog collection efficiency as *Xanthosoma sagittifolium* is not specialised to collect fog.

6.2 Experimental

6.2.1 Fog Collection

Fog was generated using an air compressor unit Clement Clarke, MEDIX Econoneb, 3605040HW). Flow rate 7–9 x 10^3 cm^3 min^{-1} at 138 kPa (1.38 bar), and a nebuliser (Cirrus Nebulizer, 1501000, Intersurgical Ltd.) connected in series. A flow meter (NGVB211-GTF2AHD-B, 1–12 L min-1, ¼ inch BSPP angled connections, CT PLATON SAS) was connected between the air compressor and nebuliser to measure the flow rate. A section of flexible (expandable) plastic tubing (58 mm length, 158 mm expanded length, Repti Fogger Expandable hose, Zoo Med Laboratories Inc.) with a circular outlet 19 mm in diameter was used to direct the fog flow at the sample. For some experiments a piece of custom designed glassware, “L” shaped, approximately 90 mm x 90 mm was used to direct the fog stream at the sample.

30 mm x 30 mm samples were affixed to a small sample stand consisting of a red/orange rubber stopper (24 mm length x 13 mm top diameter x 16 mm bottom diameter, Phillip Harris Ltd.), into which is inserted a length of metal wire (80 mm length, wire copper tinned, 1.626 mm diameter, Rowan Cable Products Ltd. TCW16

500 g) such that the top of the wire is a total of 88 mm high. Soldered to this wire is a copper square (10 mm x 10 mm x 1 mm, RS Components Ltd., Copper Sheet, 300 mm x 300 mm x 0.45 mm, 680-695). The samples were affixed using a small amount of glue (Pritt Stick, Henkel Ltd.).

Samples consisted of a variety of materials; polyethylene (HDPE natural, Gilbert Curry Industrial Plastics Co Ltd.), cotton wool (Apaks, 100% Pur Coton, 100 gr, S.N.003.URT.24.03.15, İpek İdrofil Pamuk San. ve Tic. A.Ş., Turkey), and non woven polypropylene (Avoca Technical Ltd, spunbond, 70 g m^{-2}), non-woven polypropylene masks (middle layer (white) of the mask , SDMedical50pk, Blue, SecurityDirect.co.uk), and varying grades of silicon carbide abrasive paper (3M / Wetordry™ 734 Tri-Mite™).

Samples were placed on an analytical balance (Mettler AJ150, Mettler-Toledo Ltd.) at a distance of 50 mm away from the fog outlet, with the centre of the sample in line with the centre of the fog outlet. The nebuliser was filled with 9 cm^3 of deionised water, and experiment times conducted over a period of 20 minutes. The experiments were conducted in a temperature (18–22°C) and humidity (40–50%) controlled room.

6.2.2 Epoxy Resin Replicas

Samples from three regions (margin, lamina, and midrib) of fresh *Xanthosoma sagittifolium* leaves (mature and young) were cut from the parent plant and epoxy resin positive replicas were prepared as described previously (**Chapter 2**). Plant leaves were rinsed with water to remove any surface debris and allowed to dry in air. Negative moulds of these surfaces were prepared by application of a polyvinylsiloxane base and cure mixture (President Plus Jet Light Body, Coltene/Whaledent AG) to the substrate, and immediately pressing down using a glass slide for a cure period of 10 min. Once the negative mould had hardened, it was carefully peeled away from the natural substrate surface, rinsed with water, and left to dry. Positive replicas from the negative moulds were prepared using epoxy resin (epoxy resin L and hardener S, R&G Faserverbundwerkstoffe GmbH). The epoxy resin was thoroughly mixed in a 5:2 ratio of resin to hardener, and then poured over the negative mould. Any trapped air bubbles were removed by placing under vacuum, and then the mixture was left to cure for 36 h in a desiccator.

6.2.3 1H,1H,2H,2H-Perfluorooctyle acrylate (PFAC-6) Plasmachemical Surface Modification

PFAC-6 treatments were carried out courtesy of Andrea Carletto. Poly vinyl siloxane negative moulds of *Xanthosoma sagittifolium* were rinsed with deionised water followed by drying in air.

In the case of nanoimprinting, a functional coating was plasma deposited onto the negative mould prior to the filling with epoxy resin to produce the positive replica. Pulsed plasma deposition of the low surface energy precursor, 1H,1H,2H, 2H-perfluorooctyl acrylate (+95%, Fluorochem Ltd, purified using several freeze-pump-thaw cycles) was carried out in an electrodeless cylindrical glass reactor (5 cm diameter, 520 cm^3 volume, base pressure of 1×10^{-3} mbar, and with a leak rate better than 1.8×10^{-9} kg s^{-1}) enclosed in a Faraday cage. The chamber was fitted with a gas inlet, a Pirani pressure gauge, a 30 L min^{-1} two-stage rotary pump attached to a liquid cold trap, and an externally wound copper coil (4 mm diameter, 9 turns, spanning 8–15 cm from the precursor inlet). All joints were grease-free. An L-C network was used to match the output impedance of a 13.56 MHz radio frequency (RF) power generator to the partially ionised gas load. The RF power source was triggered by a signal generator, and the pulse shape monitored with an oscilloscope. Prior to each experiment, the chamber was cleaned by scrubbing with detergent, rinsing in water and propan-2-ol, followed by oven drying. The system was then reassembled and evacuated. Further cleaning consisted of running an air plasma at 0.2 mbar pressure and 50 W power for 30 min. Next, polyvinylsiloxane negative moulds, and reference silicon (100) wafer pieces (Silicon Valley Microelectronics Inc.) were inserted into the centre of the reactor, and the system pumped back down to base pressure. At this stage, 1H,1H,2H,2H-perfluorooctyl acrylate monomer vapour was introduced at a pressure of 0.2 mbar for 5 min prior to ignition of the pulsed electrical discharge. The optimum conditions for functional group retention corresponded to a peak power of 40 W, and a duty cycle on-time of 20 μs and off-time equal to 20 ms. Deposition was allowed to proceed for 150 s to yield nm thick layers. Upon plasma extinction, the precursor vapour continued to pass through the

system for a further 3 min, and then the chamber was evacuated back down to base pressure.

6.3 Fog Collection on Plant Samples

Samples of fresh *Xanthosoma sagittifolium* leaves were cut from their parent plant and transported to the laboratory. Samples from each of the three regions of the plant (margin, lamina, and midrib) were cut and fog collection measurements conducted. Both young and mature leaves of *Xanthosoma sagittifolium* were analysed.

It is expected that the leaves of *Xanthosoma sagittifolium* will make for poor fog harvesters due to the natural environment of the parent plant being located in a tropical region, where access to ground water is not limited, however should provide a useful reference experiment in validating the fog collecting method.

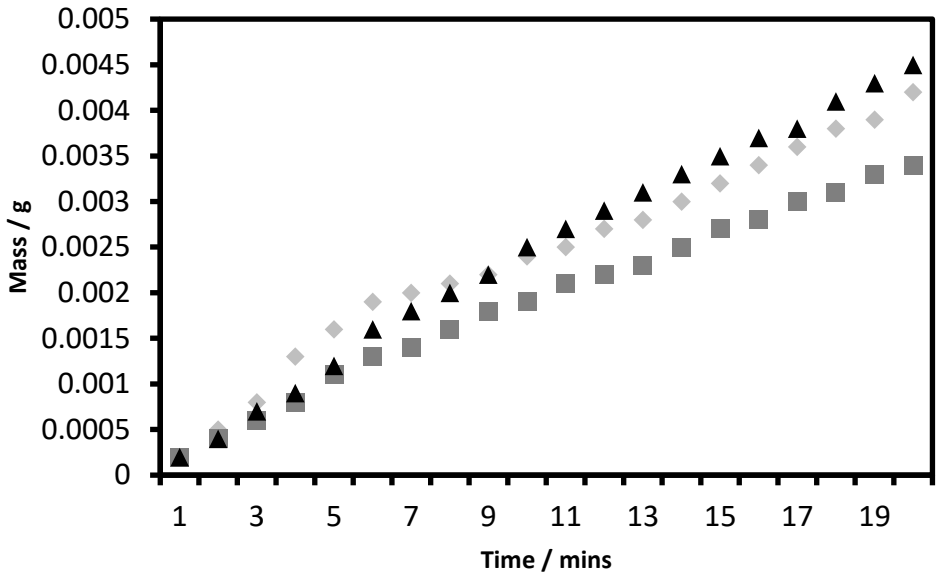

Figure 76: Water collection data for a young leaf of *Xanthosoma sagittifolium*, three separate 30 mm x 30 mm samples of the margin region were analysed

The first set of experiments on the young, margin region shows an overall steady linear increase across all samples (**Figure 76**) throughout the experiment. No water was observed coalescing on the leaf surface and the total amount collected is much lower than the polyethylene standard (**Figure 83**).

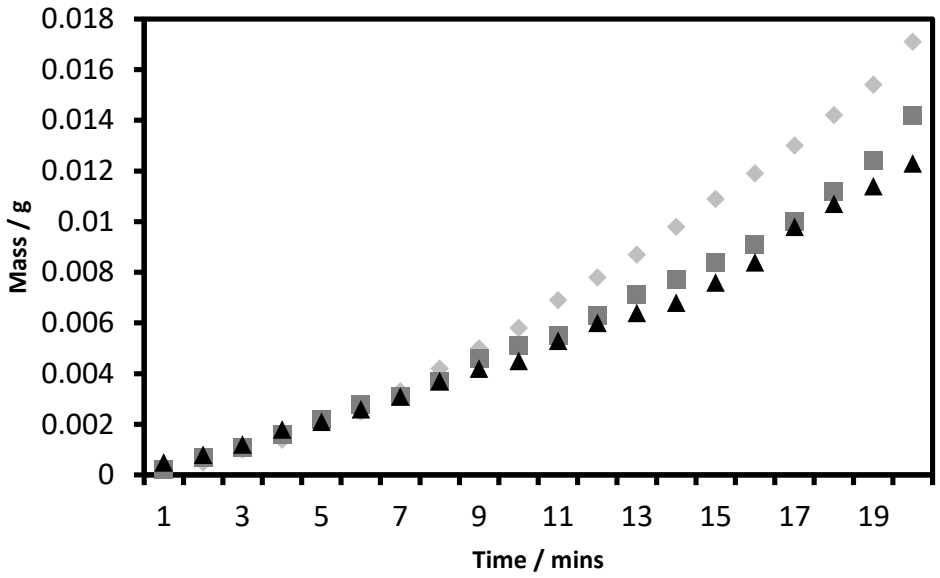

Figure 77: Water collection data for a young leaf of *Xanthosoma sagittifolium*, three separate 30 mm x 30 mm samples of the lamina region were analysed

The experiments conducted for the lamina region showed a deal of variability in the rate at which water was collected, with a steady linear increase during the first half of the experiment, before rising more rapidly in the second half of the experiment, particularly towards the end. It was observed during the experiment that over time, large droplets began coalescing around the edges of the leaf sample, which could have contributed to the increased rate of water collection.

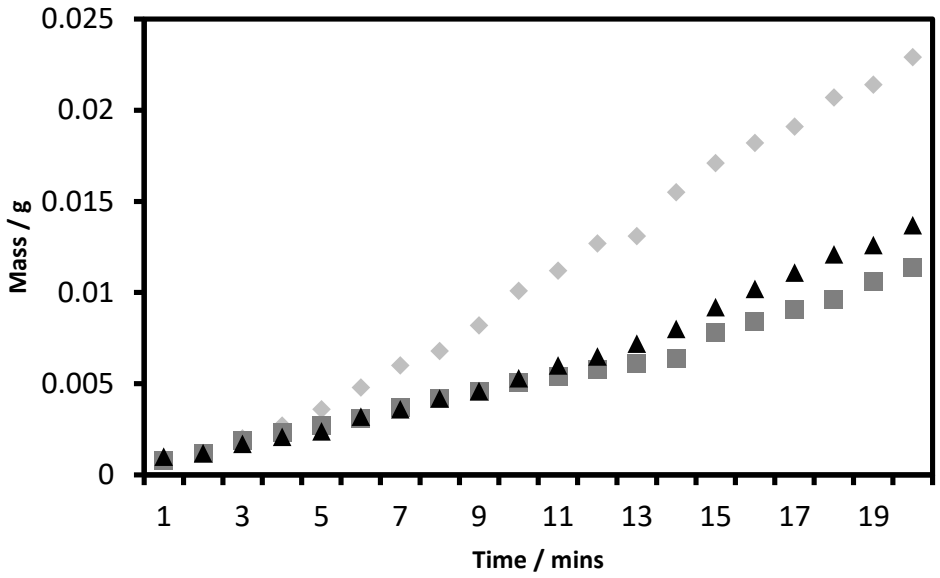

Figure 78: Water collection data for a young leaf of *Xanthosoma sagittifolium*, three separate 30 mm x 30 mm samples of the midrib region were analysed

A similar observation can be made regarding a single sample of the midrib region, with the first sample showing a large disparity in the amount collected when compared to the other two samples. This matches previous expermental observations which show a higher variation in the midrib region, contact angles being an example of such a variation. The samples do however, show a more linear trend across all three samples.

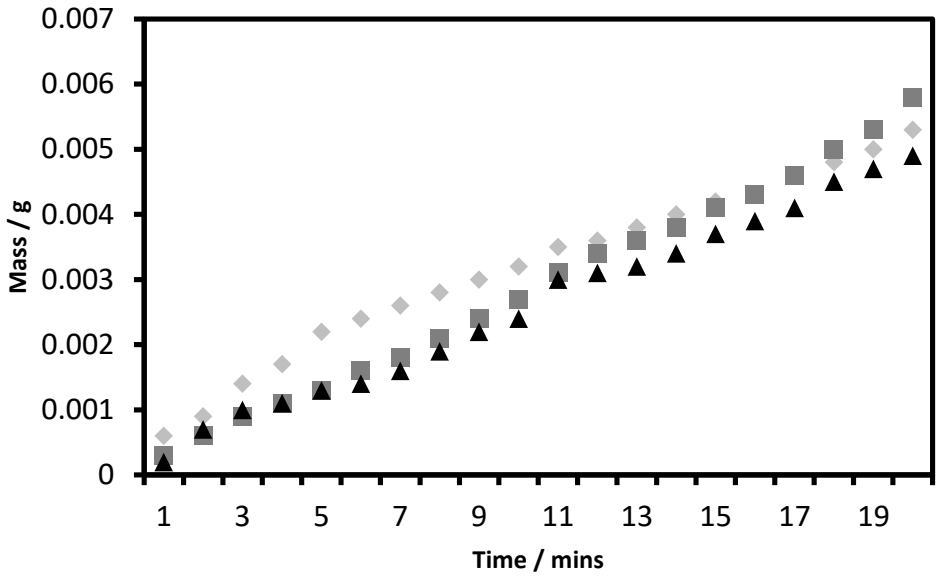

Figure 79: Water collection data for a mature leaf of *Xanthosoma sagittifolium*, three separate 30 mm x 30 mm samples of the margin region were analysed

The mature leaf margin samples show a similar trend to their young leaf counterparts, with a steady linear increase in the amount of water collected. All three samples show similar rates as well as total masses of water collected.

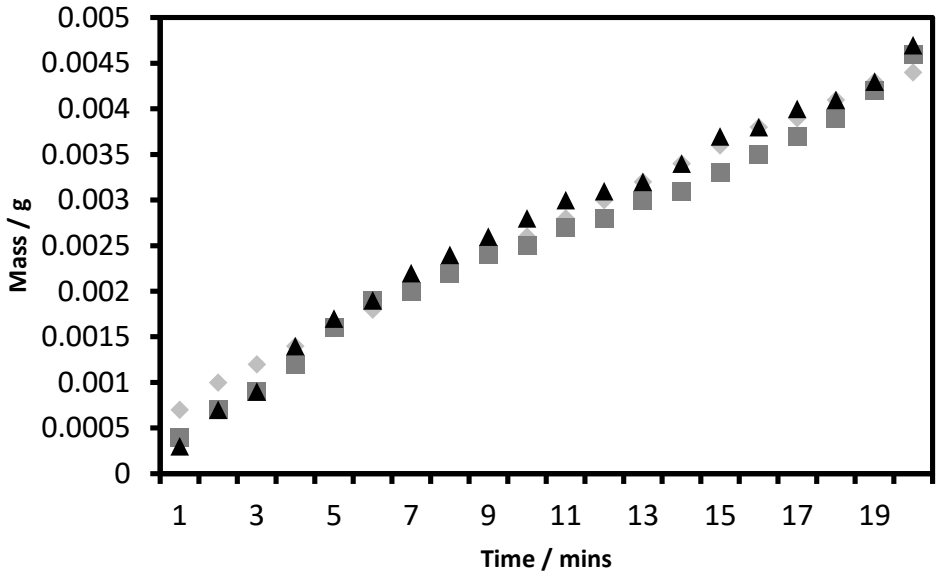

Figure 80: Water collection data for a mature leaf of *Xanthosoma sagittifolium*, three separate 30 mm x 30 mm samples of the lamina region were analysed

The lamina region, as with the young leaf samples shows different rates of water collection during the experiment, with the samples initially collected water at a faster rate than later in the experiment. The rate of water collection does however remain steady for the latter part of the experiment, with the overall masses collected showing similar values across all samples.

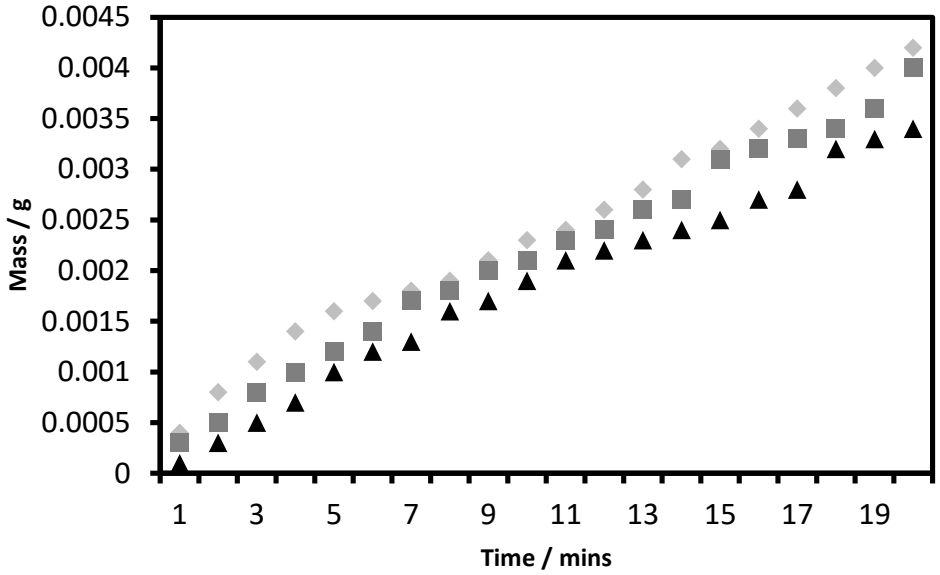

Figure 81: Water collection data for a mature leaf of *Xanthosoma sagittifolium*, three separate 30 mm x 30 mm samples of the midrib region were analysed

The midrib region shows a larger variation across samples and across the rate of water collection when compared to the margin and lamina regions. This increase in variation is in line with previous experimental observations, particularly regarding contact angles for example. It still broadly collects across a linear increase, however there are several regions of larger increases. This could be due to the nature of the samples themselves, with varying midrib thickness between samples due to the nature of the midrib vein shape.

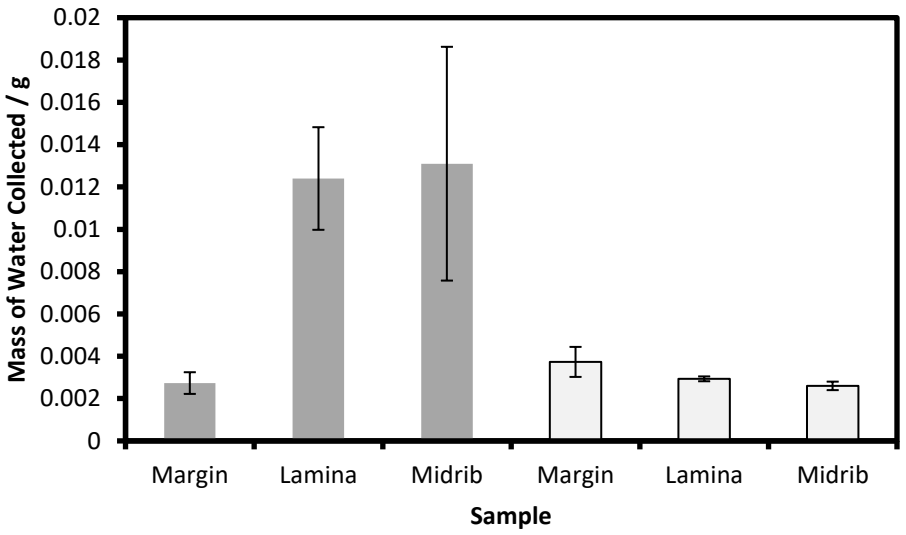

Figure 82: Comparison of the average overall mass of water collected for the period between 5–20 min. Standard deviations are shown. Dark grey bars correspond to young leaves of *Xanthosoma sagittifolium*, light grey for mature leaves

When comparing the total amount of water collected between the period of 5–20 mins it becomes possible to compare the different regions of the plant and between plants. There was a large variation in results observed for a young leaf of *Xanthosoma sagittifolium*, with the lamina and midrib regions collecting a large amount of water relative to the margin, but also showing a large variation in the total amount collected.

The mature leaf shows similar water collection across all three regions, with the margin collecting slightly more than the lamina, which in turn collects more than the midrib. Overall, the mature leaf collects much less water than the samples of the young leaf.

By comparing the rate of water collection, it is possible to compare these samples to those of the polyethylene standard (**Figure 83**) to ascertain their water collection efficiency.

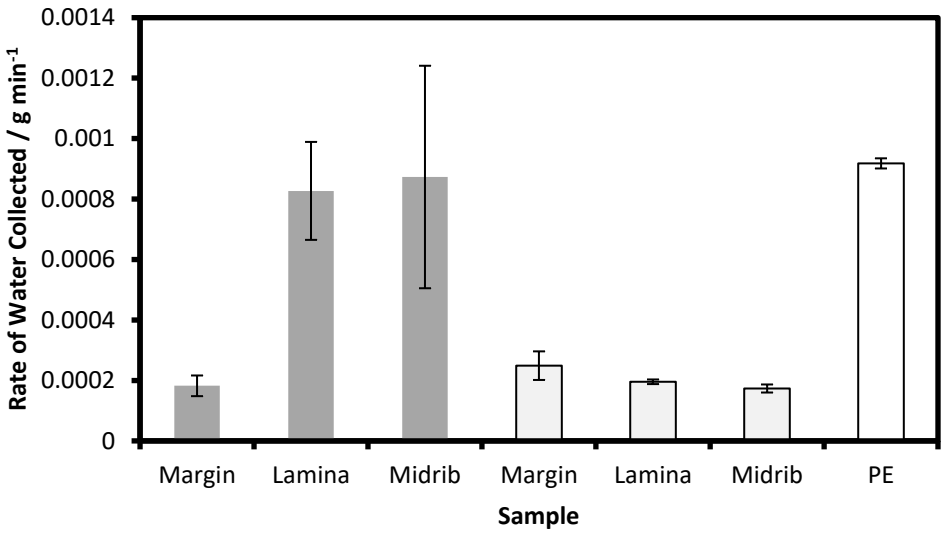

Figure 83: Comparison of the rate of water collection for the period between 5–20 min. Standard deviations are shown. Dark grey bars correspond to young leaves of *Xanthosoma sagittifolium*, light grey for mature leaves. Comparison to polyethylene standard is shown

All regions show poor collection efficiency when compared to the polyethylene standard. This matches experimental observations, a lack of visible water present on the leaf surface, the hydrophobic surface chemistry present on the leaves also likely play a factor, with solely hydrophobic surfaces being poor collectors of fog. As expected, the leaves of *Xanthosoma sagittifolium* are poor at collecting fog.

6.4 Fog Collection on Replicas

Epoxy resin positive replicas were then made of the three regions of *Xanthosoma sagittifolium*, with both young and mature leaves sampled. Flat epoxy resin squares were also made to allow for a comparison between those surfaces and one which is imprinted with the macro structure of the leaf surface.

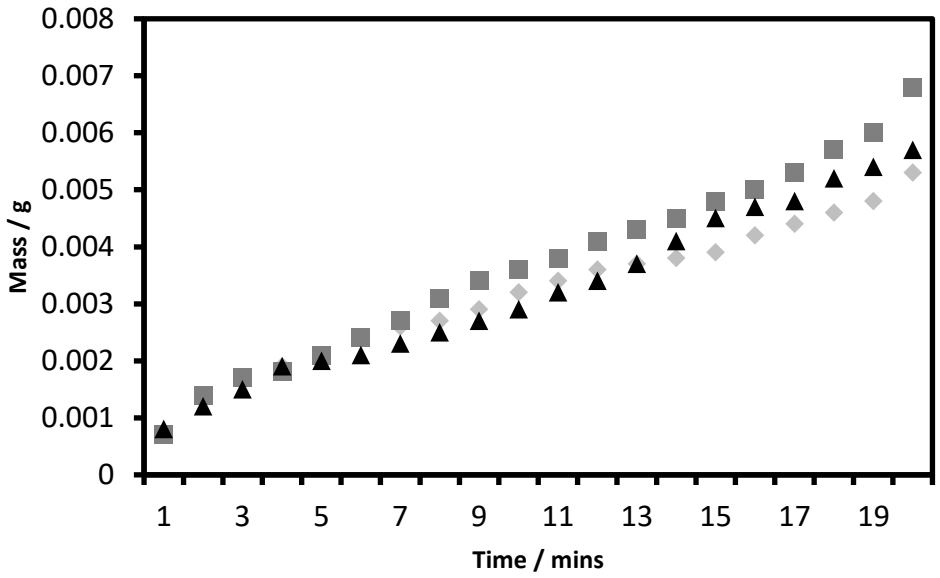

Figure 84: Water collection on three flat epoxy resin squares. Squares were 20 mm x 20 mm in size

Flat epoxy resin squares were created by making a negative mould of a 20 mm x 20 mm sample of silicon wafer (100 mm diameter, P/Boron, orientation <100>, Resistivity 5–20 Ω cm, thickness 525 ± 25 μm, front side polished, rear side surface etched, Semi-standard, Silicon valley Microelectronics Inc.) using methods described previously. Once cured the epoxy resin was rinsed with deionised water and allowed to air dry, static water contact angles obtained for the squares showed contact angles of 78 ± 5°.

Fog collection measurements on the epoxy resin squares showed a linear increase across all samples with a similar total amount of water collected at the end of the experiment. This data can then be used as a comparison for the replica samples of *Xanthosoma sagittifolium* along with the leaf samples.

Epoxy resin replicas of the three regions of both young and mature leaves were made using three separate negative moulds for each region. The moulds used were the same moulds that were used previously to create positive replicas (b). Due to the nature of the moulding process, as well as creating the positive replicas, the replicas contain sections where the leaf isn't imprinted because the resin overflowed the mould (**Figure 85**).

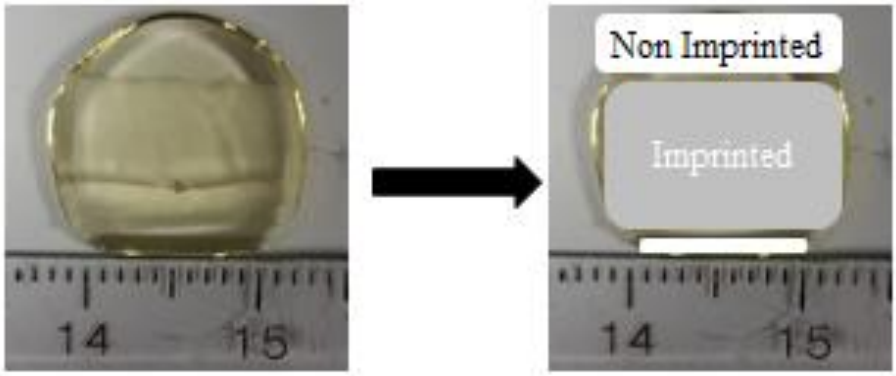

Figure 85: Image showing a single replica for a young leaf of *Xanthosoma sagittifolium*, the margin region is shown. Roughly highlighted are the imprinted (grey) and non-imprinted (white) regions which occur when the epoxy resin overflows the mould. Scale markings are seperated by 1 mm, the distance between 14 and 15 is 10 mm

By comparing the amount of water collected per unit area for the flat epoxy resin squares with the amount of water per unit area for the imprinted/non imprinted regions of the replicas it is possible to determine the amount collected due to the imprinted region.

All the samples were analysed using image analysis software (imageJ) to determine the amount of imprinted/non imprinted regions for each sample. This was done for all three regions across both young and mature leaves (**Table 28**).

Table 28: The amount of each replica which constituted non imprinted epoxy is shown, data corresponds to both young and mature leaf replicas of *Xanthosoma sagittifolium*

Region	Sample No.	Area of non imprinted region / mm^2	
		Young Leaf	Mature Leaf
Margin	1	69	60
	2	23	55
	3	55	52
Lamina	1	24	56
	2	31	23
	3	43	17
Midrib	1	8	7
	2	31	14
	3	26	54

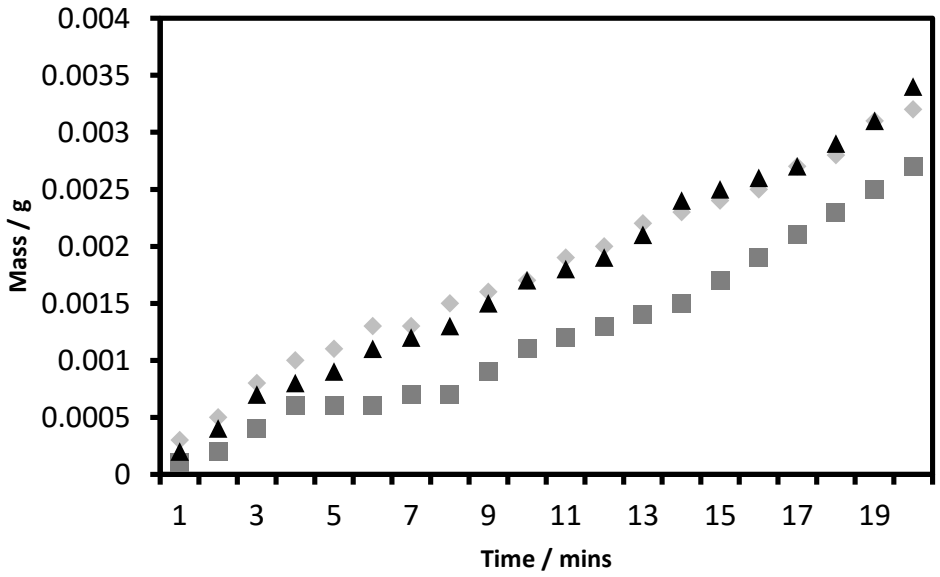

Figure 86: Water collection on epoxy resin replicas of the margin region of a young leaf of *Xanthosoma sagittifolium*. Three separate replicas were sampled

The amount of fog collected by the epoxy resin squares, for the period between 5–20 min was (9.67 ± 1.91) x 10^{-6} g mm^{-2} which can be used to approximate the amount of water collected by the non imprinted regions of the leaf replicas. Using the calculated value, the mass of water collected by the non imprinted regions ranges from 2.2 x 10^{-4} g to 6.7 x 10^{-4} g across the three samples. This reduces the average amount of water collected across the margin (**Figure 86**) replicas to (1.76 ± 0.32) x 10^{-3} g for the period between 5–20 min.

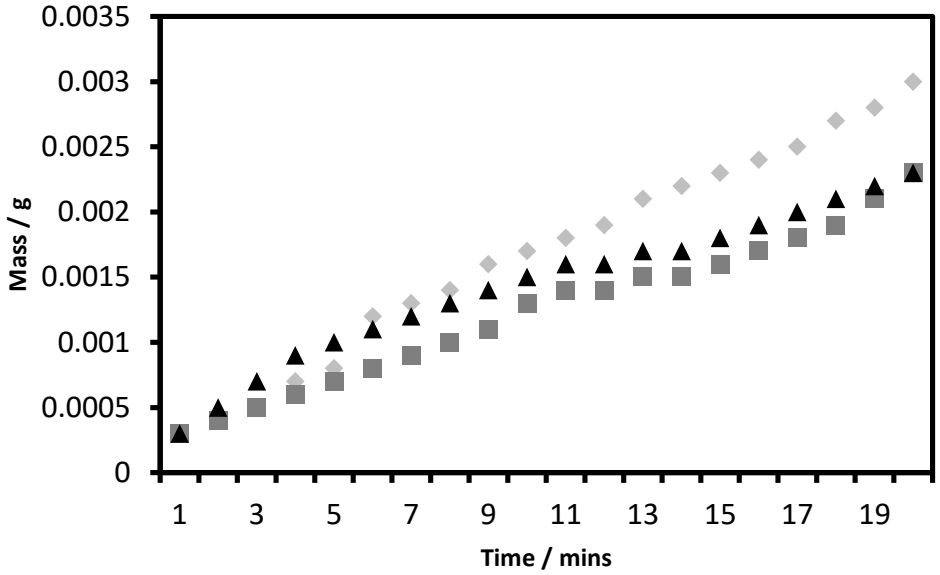

Figure 87: Water collection on epoxy resin replicas of the lamina region of a young leaf of *Xanthosoma sagittifolium*. Three separate replicas were sampled

For the lamina region of a young leaf replica (**Figure 87**), the calculated values for the contribution towards the total mass collected by the non imprinted regions was found to be between 2.3 x 10^{-4} g to 4.2 x 10^{-4} g, which reduces the average mass of water collected across all samples to (1.38 ± 0.55) x 10^{-3} g for the period between 5–20 min.

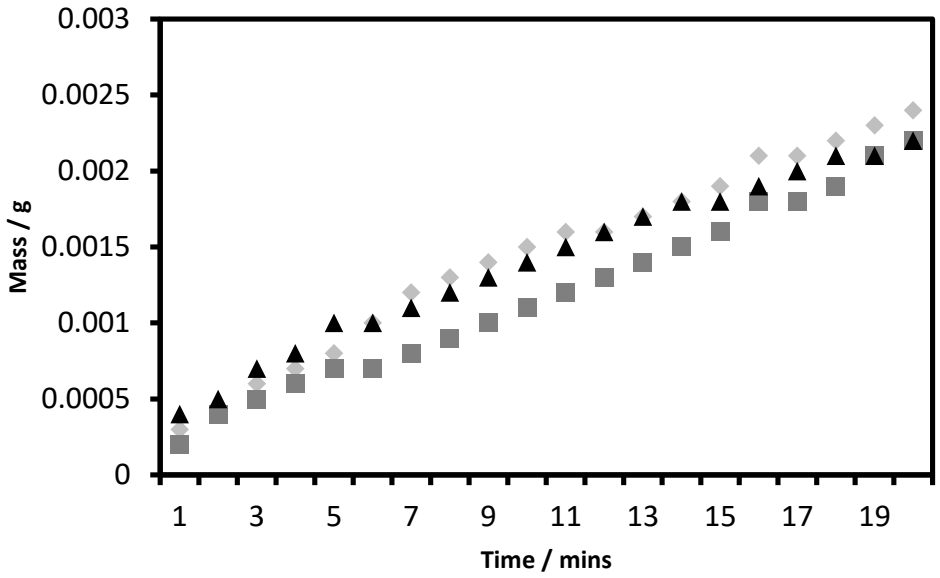

Figure 88: Water collection on epoxy resin replicas of the midrib region of a young leaf of *Xanthosoma sagittifolium*. Three separate replicas were sampled

The midrib replicas of a young leaf (**Figure 88**) have non imprinted regions with a total mass collected by the non imprinted regions of between 7.7 x 10^{-5} g to 3.0 x 10^{-4} g, which reduces the average mass of water collected across all samples to (1.22 ± 0.29) x 10^{-3} g for the period between 5–20 min.

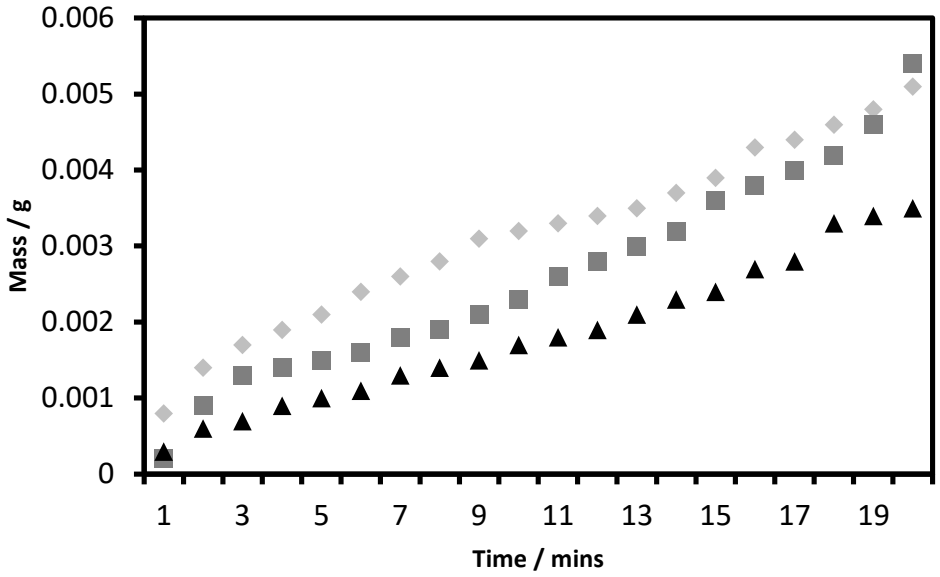

Figure 89: Water collection on epoxy resin replicas of the margin region of a mature leaf of *Xanthosoma sagittifolium*. Three separate replicas were sampled

As calculated for the young leaf replicas, the calculated values for the margin region of a mature leaf (**Figure 89**) was found to be between 5.0 x 10^{-4} g to 5.8 x 10^{-4} g, which reduces the average mass of water collected across all samples to (2.60 ± 0.71) x 10^{-3} g for the period between 5–20 min.

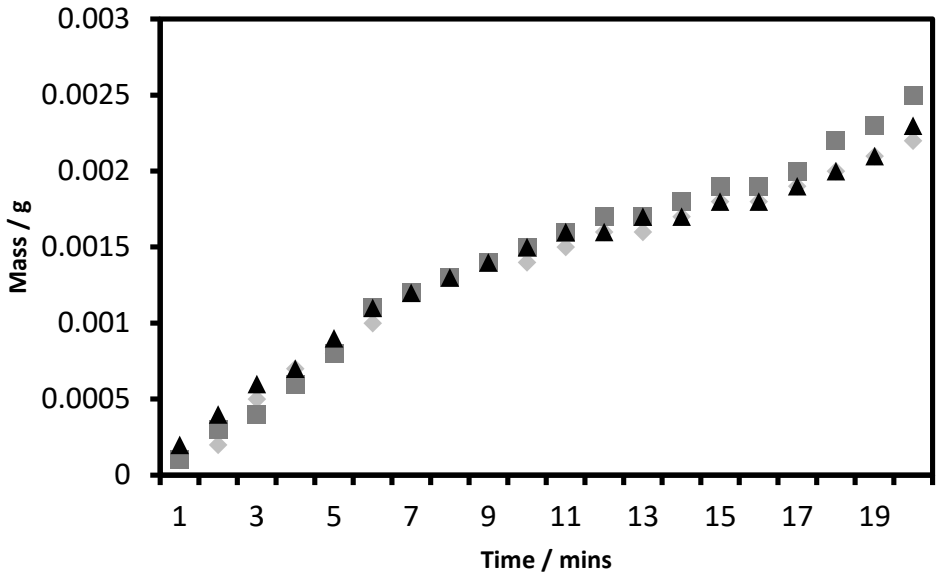

Figure 90: Water collection on epoxy resin replicas of the lamina region of a mature leaf of *Xanthosoma sagittifolium*. Three separate replicas were sampled

As calculated for the young leaf replicas, the calculated values for the lamina region of a mature leaf (**Figure 90**) was found to be between 1.6 x 10^{-4} g to 5.4 x 10^{-4} g, which reduces the average mass of water collected across all samples to (1.19 ± 0.33) x 10^{-3} g for the period between 5–20 min.

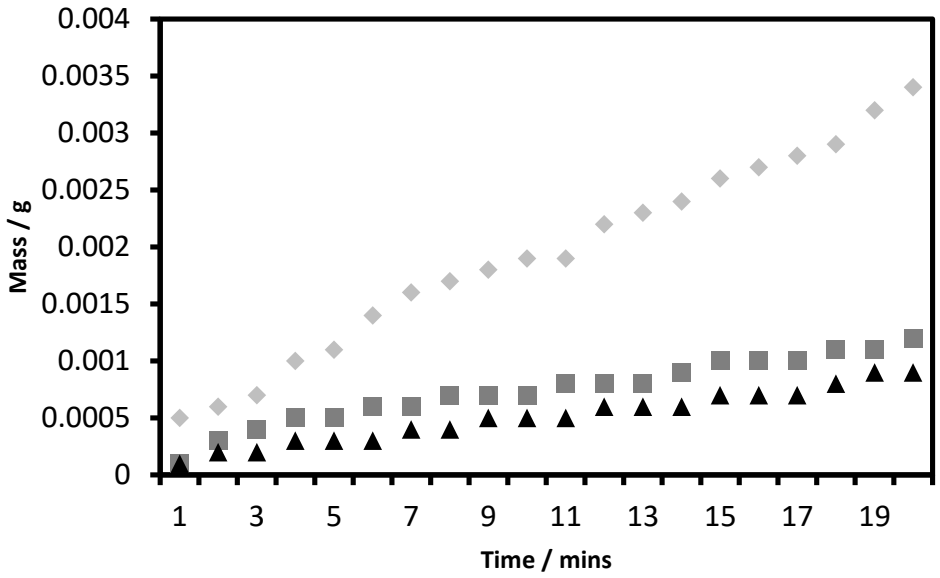

Figure 91: Water collection on epoxy resin replicas of the midrib region of a mature leaf of *Xanthosoma sagittifolium*. Three separate replicas were sampled

As calculated for the young leaf replicas, the calculated values for the midrib region of a mature leaf (**Figure 91**) was found to be between 6.8 x 10^{-5} g to 5.2 x 10^{-4} g, which reduces the average mass of water collected across all samples to (9.58 ± 11.3) x 10^{-4} g for the period between 5–20 min.

The total amount of water collected by each region, across both young and mature replicas can now be compared as the contribution arising from non imprinted regions has been taken into account. The overall mass collected for the period between 5–20 min for the margin, lamina, and midrib region for young and mature epoxy resin positive replicas of *Xanthosoma sagittifolium* is shown (**Figure 92**).

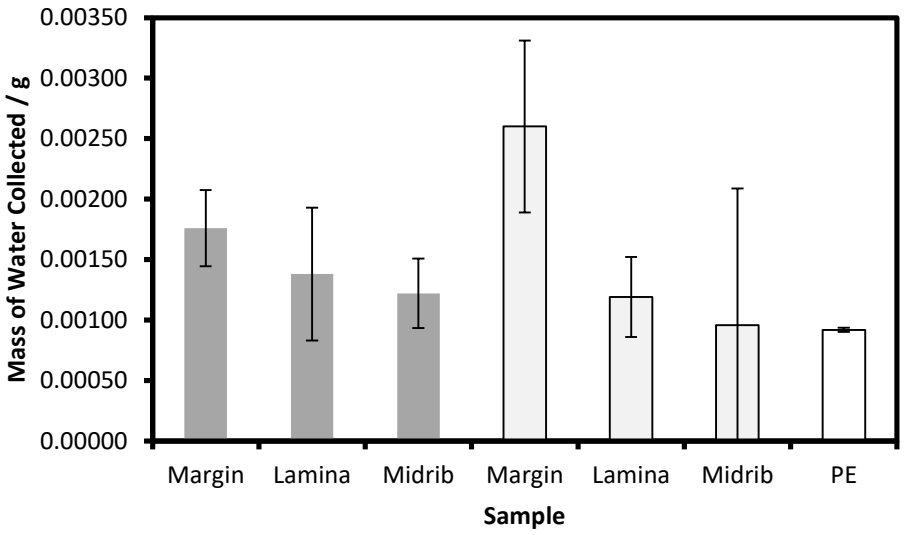

Figure 92: Comparison of the rate of water collection for the period between 5–20 min for positive replicas of *Xanthosoma sagittifolium*. Standard deviations are shown. Dark grey bars correspond to young leaves of *Xanthosoma sagittifolium*, light grey for mature leaves. Comparison to polyethylene standard is shown

When comparing the different leaf replicas, the young leaf shows the most consistent value collected across the margin, lamina, and midrib, with similar amounts collected (within error) for all three regions. This data corresponds with the previous contact angle data (**Chapter 2**) showing similar static water contact angles for all three regions. This was expected as the underlying surface chemistry as well as surface structures should be similar due to the nanoimprinting process.

When comparing the mature replicas, the largest variation seen is with the midrib region and a very large variation in collected data. One sample obtained shows significantly more water collected when compared to the others resulting in the large variation seen. This variation is consistent with previous experiments where the midrib showed the largest variation when exposed to the fog stream for live plant samples (**Figure 83**), which could be due to the region sampled and surface contamination/defects present. Additional experiments will need to be conducted to gather more accurate data for the midrib region.

When comparing the remaining regions and samples against the polyethylene standard, they collect more water over the duration of the experiment than the polyethylene, despite the reduced surface area, proving to be a more efficient fog

collector than the live plant itself. This could be due to the change in surface chemistry, being hydrophilic and a polymer composite rather than hydrophobic, as well as having less surface roughness.

The next stage would be to create samples which mimic the surface hydrophobicity in order to probe a truer representation of the plant surface.

6.5 Fog Collection on Nanoimprinted Replicas

Using the nanoimprinting process, as described previously, multiple PFAC-6 coated samples were analysed and their fog collection efficiencies recorded. The samples used were the same samples for which contact angle data was measured previously (**Chapter 2**), with the first iterations being tested. Contact angles were measured to determine if the surface had degraded however they showed no change from previously measured values.

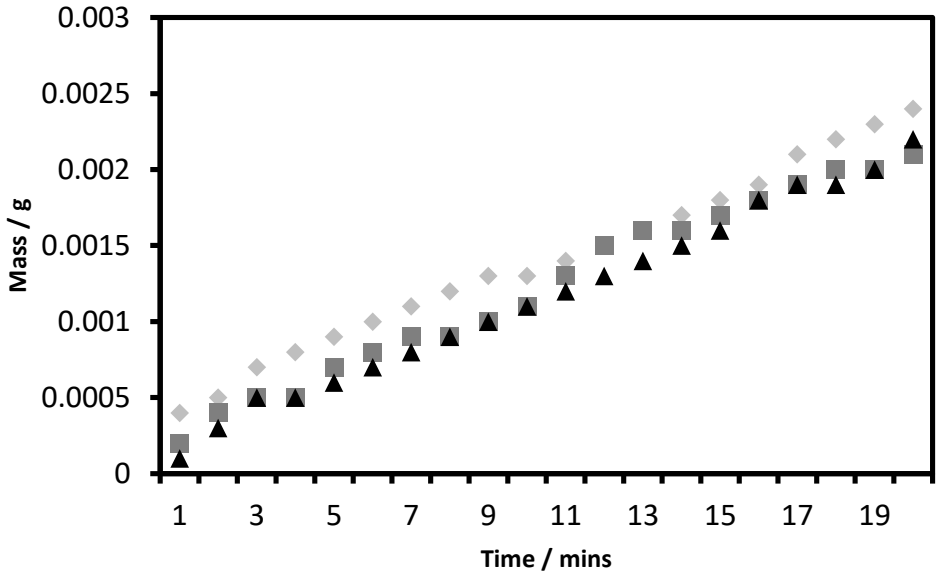

Figure 93: Water collection on epoxy resin replicas of the margin region of a young leaf of *Xanthosoma sagittifolium*. Three separate replicas were sampled and the negative moulds were pre-treated with PFAC-6 before addition of epoxy resin occurred

All three samples show a steady linear increase in the amount of water collected, with an average mass of water collected for between 5–20 min of (1.5 ± 0.1) x 10^{-3} across all samples.

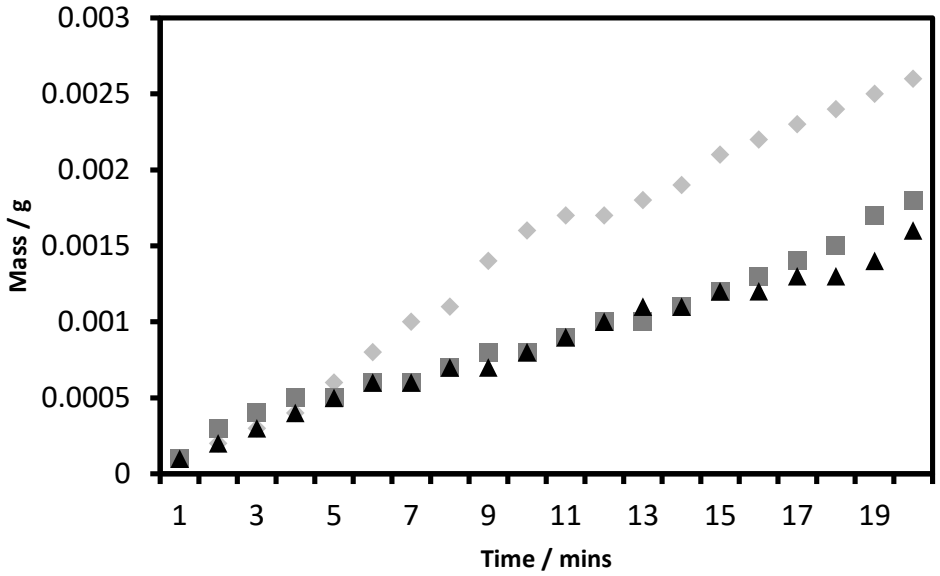

Figure 94: Water collection on epoxy resin replicas of the lamina region of a young leaf of *Xanthosoma sagittifolium*. Three separate replicas were sampled and the negative moulds were pre-treated with PFAC-6 before addition of epoxy resin occurred

The average mass of water collected between 5–20 min is (1.5 ± 0.5) x 10^{-3} across all samples, which is similar in value to the amount collected by the margin region, which is expected as the two regions have similar surface structures and show similar water contact angles.

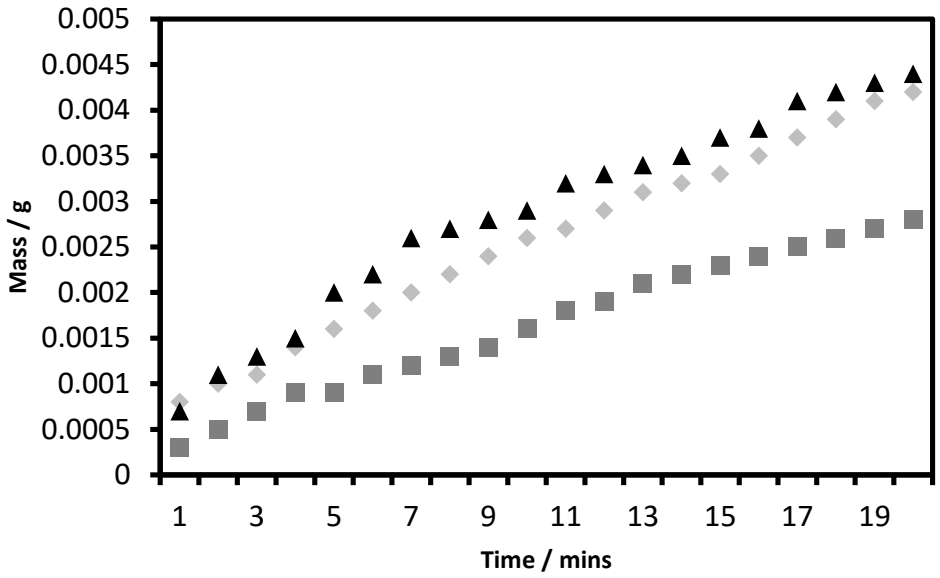

Figure 95: Water collection on epoxy resin replicas of the midrib region of a young leaf of *Xanthosoma sagittifolium*. Three separate replicas were sampled and the negative moulds were pre-treated with PFAC-6 before addition of epoxy resin occurred

The average mass of water collected over the period of 5–20 min is (2.3 ± 0.4) x 10^{-3} across all samples.

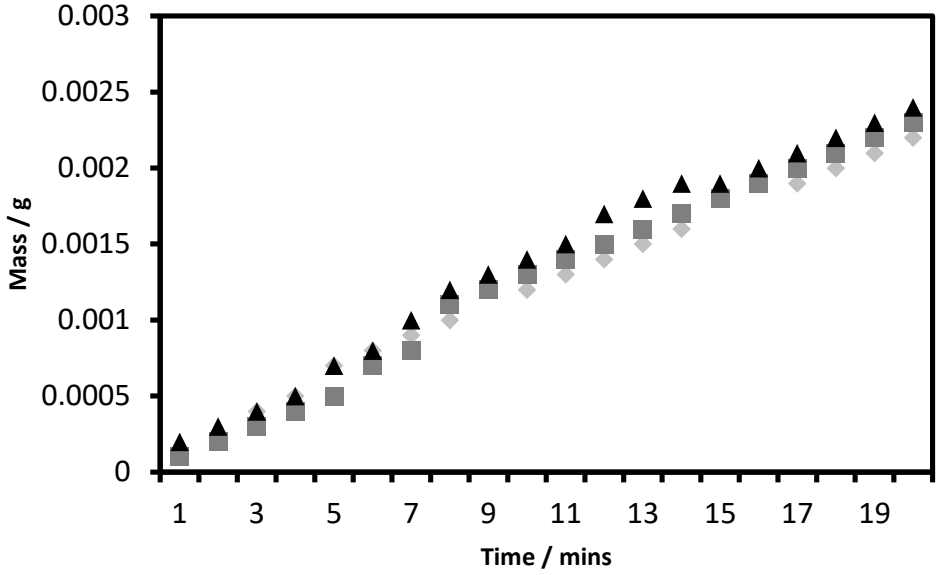

Figure 96: Water collection on epoxy resin replicas of the margin region of a mature leaf of *Xanthosoma sagittifolium*. Three separate replicas were sampled and the

negative moulds were pre-treated with PFAC-6 before addition of epoxy resin occurred

The average mass of water collected over the period of 5–20 min is (1.6 ± 0.2) x 10^{-3} across all samples.

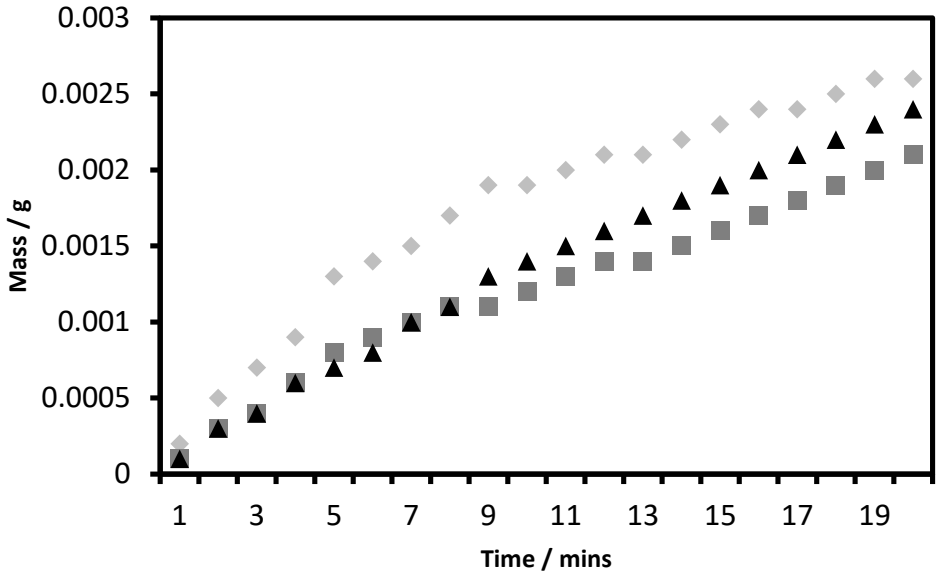

Figure 97: Water collection on epoxy resin replicas of the lamina region of a mature leaf of *Xanthosoma sagittifolium*. Three separate replicas were sampled and the negative moulds were pre-treated with PFAC-6 before addition of epoxy resin occurred

The average mass of water collected over the period of 5–20 min for the lamina replicas from a mature leaf is (1.4 ± 0.2) x 10^{-3} across all samples.

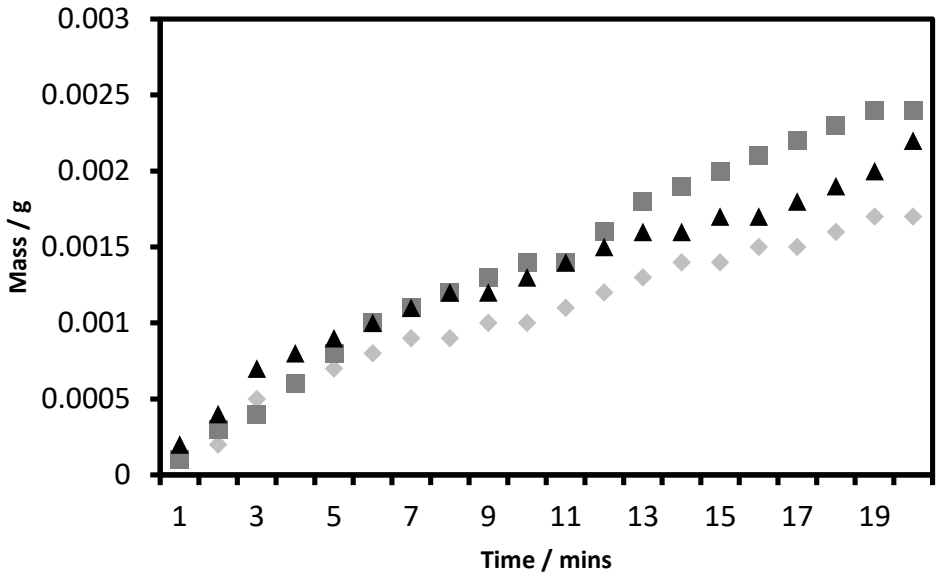

Figure 98: Water collection on epoxy resin replicas of the midrib region of a mature leaf of *Xanthosoma sagittifolium*. Three separate replicas were sampled and the negative moulds were pre-treated with PFAC-6 before addition of epoxy resin occurred

The average mass of water collected over the period of 5–20 min for the midrib replicas from a mature leaf is $(1.3 \pm 0.3) \times 10^{-3}$ across all samples. The total amount of water collected over the duration of the experiment can then be compared (**Figure 99**).

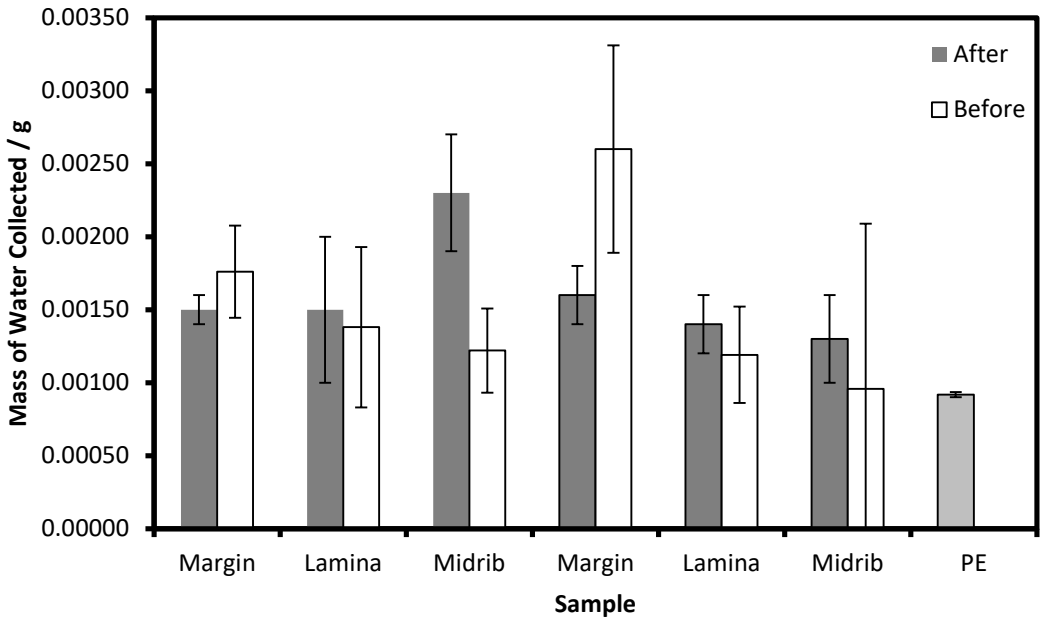

Figure 99: Comparison of the total amount of water collected for the PFAC-6 treated replicas for the period between 5–20 min. Standard deviations are shown. The first three pairs of bars correspond to young leaves of *Xanthosoma sagittifolium*, the next three pairs correspond to mature leaves. Dark grey bars show post nanoimprinting, white bars prior. Comparison to polyethylene standard is also included

When comparing the mass of water collected relative to the PE standard, all samples collect more water than the polyethylene, with the midrib region for the young leaf collecting the most. The main improvement seen is for mature midrib samples, which a much lower error associated with the experiment. One of the limitations of this analysis is that the amount of water collected due to the non imprinted regions present was not measured, however since they account for approx 5–10% of the total area sampled the amount of water collected is likely to be small and therefore the above analysis makes for a useful approximation of the expected results. Additional experiments will need to be conducted to ascertain a more accurate value however.

6.6 Conclusion

As expected, the leaves of *Xanthosoma sagittifolium* showed poor fog collection ability, in many cases much lower than that of PE, with the untreated and treated replicas showing an increased efficiency despite their much smaller size for most samples. The increased efficiency observed in the replicas relative to the polyethylene surface could be due to the increased surface roughness resulting in higher nucleation rate present on the surface of the replicas, increasing the amount of fog collected. Overall, the results obtained are as expected for leaves and replicas of *Xanthosoma sagittifolium*, highlighting how this fog collection ~~colelction~~ method can be used in future experiments. One further method of validation for future work, would be to conduct fog collection measurements on plants known to be efficient fog collectors, such as *Eremopyrum orientale* or *Cotulla fallax*.

Chapter 7 Development and Testing of 3D Printing Methodology

7.1 Introduction

3D printing is a relatively new technique that is gaining attention in the replication of biomimetic surfaces, with a wide variety of applications.[1,2] The technique has useful advantages in the context of fog collection, as it becomes possible to produce fog collecting surfaces on site without the need for expensive and cumbersome manufacturing equipment. It also provides similar advantages over the nanoimprinting process described in this thesis, with scalability and ease of manufacture being primary advantages. This chapter explores the work towards using this technique to replicate plant surfaces, a new and novel approach to their replication. In particular, the replication of two plant surfaces will be attempted, the leaves of *Phyllostachys aurea* as well as the leaves of *Thuja plicata*.

7.2 Experimental

7.2.1 3D Printed Meshes

3D printed meshes were designed on Solidworks software (Dassault Systémes SolidWorks Corp.) before being printed on Objet Eden 500V 3D printer (Stratasys Ltd.) using an acrylic compound (Objet Fullcure 720 (RGD720), Stratasys Ltd.). Once printed, meshes were removed from the print bed and soaked in a solution of Cream Cleaner (Tesco PLC.) and water (Tap, Northumbrian Water Ltd.) in a 1:10 v/v ratio to remove residual support material.

7.2.2 Laser Cut Meshes

Meshes were designed using Solidworks software (Dassault Systémes SolidWorks Corp.) before being laser cut using a HPLC Laser Script LS6840 laser cutter. Laser cutting was carried out on a variety of materials; non woven polypropylene (Avoca Technical Ltd, spunbond, 70 g m^{-2}), non-woven polypropylene masks (middle layer (white) of the mask, SDMedical50pk, Blue, SecurityDirect.co.uk), and varying grades of silicon carbide abrasive paper (3M / Wetordry™ 734 Tri-Mite™).

7.2.3 Plasmachemical Surface Functionalisation

Plasmachemical surface functionalisation was carried out in an electrodeless cylindrical glass reactor (5 cm diameter, 470 cm^3 volume, base pressure of 1×10^{-3} mbar, and with a leak rate better than 1.8×10^{-9} kg s^{-1}) enclosed in a Faraday cage. The chamber was fitted with a gas inlet, a Pirani pressure gauge, a 30 L min^{-1} two-stage rotary pump attached to a liquid cold trap, and an externally wound copper coil (4 mm diameter, 9 turns, spanning 8–15 cm from the precursor inlet). All joints were grease-free. An L-C network was used to match the output impedance of a 13.56 MHz radio frequency (RF) power generator to the partially ionised gas load. The RF power source was triggered by a signal generator, and the pulse shape monitored with an oscilloscope. Prior to each experiment, the chamber was cleaned by scrubbing with detergent, rinsing in water and propan-2-ol, followed by oven drying. The system was then reassembled and evacuated. Further cleaning consisted of running an air plasma at 0.2 mbar pressure and 50 W power for 30 min. 3D printed mesh samples were inserted into the chamber before subsequent pumping down to base pressure. Next, precursor gas was introduced to the chamber via needle control valve at 0.2 mbar pressure and the electrical discharge was ignited. Precursors include: 1H,1H,2H,2H-perfluorooctyl acrylate monomer (+95%, Fluorochem Ltd, purified using several freeze-pump-thaw cycles) and air.

7.2.4 Water Collection and Contact Angle Measurements

Water collection was conducted in accordance with prior art.[3]

7.2.5 Fog Collection

Fog was generated using an air compressor unit Clement Clarke, MEDIX Econoneb, 3605040HW). Flow rate 7–9 x 10^3 cm^3 min^{-1} at 138 kPa (1.38 bar), and a nebuliser (Cirrus Nebulizer, 1501000, Intersurgical Ltd.) connected in series. A flow meter (NGVB211-GTF2AHD-B, 1–12 L min-1, ¼ inch BSPP angled connections, CT PLATON SAS) was connected between the air compressor and nebuliser to measure the flow rate. A section of flexible (expandable) plastic tubing (58 mm length, 158 mm expanded length, Repti Fogger Expandable hose, Zoo Med Laboratories Inc.) with a circular outlet 19 mm in diameter was used to direct the fog flow at the sample. For some experiments a piece of custom designed glassware, “L” shaped, approximately 90 mm x 90 mm was used to direct the fog stream at the sample.

30 mm x 30 mm samples were affixed to a small sample stand consisting of a red/orange rubber stopper (24 mm length x 13 mm top diameter x 16 mm bottom diameter, Phillip Harris Ltd.), into which is inserted a length of metal wire (80 mm length, wire copper tinned, 1.626 mm diameter, Rowan Cable Products Ltd. TCW16 500 g) such that the top of the wire is a total of 88 mm high. Soldered to this wire is a copper square (10 mm x 10 mm x 1 mm, RS Components Ltd., Copper Sheet, 300 mm x 300 mm x 0.45 mm, 680-695). The samples were affixed using a small amount of glue (Pritt Stick, Henkel Ltd.). Samples consisted of a variety of materials; non woven polypropylene (Avoca Technical Ltd, spunbond, 70 g m^{-2}), non-woven polypropylene masks (middle layer (white) of the mask, SDMedical50pk, Blue, SecurityDirect.co.uk), and varying grades of silicon carbide abrasive paper (3M / Wetordry™ 734 Tri-Mite™).

7.2.5 X-Ray Scanning of Leaf Surface

Live samples of *Phyllostachys aurea* were cut from their parent plant and transported to the laboratory before a cross section (approx 15 mm x 15 mm) was cut and immediately placed inside an X-Ray Computer Tomography machine (XRadia/Zeiss VersaXRM 410). The leaf sample was scanned for a 24 h period to generate a computerised image of the sample. Image processing was carried out using AvizoFire software (Thermo Fischer Scientific) and Netfabb (Autodesk) before being printed on Objet Eden 500V 3D printer (Stratasys Ltd.) using an acrylic compound (Objet Fullcure 720 (RGD720), Stratasys Ltd.).

7.3 3D Printed Meshes

Thuja plicata, commonly known as Canadian red cedar, is a large coniferous tree native to North America. During torrential rainfall, the ground beneath the tree remains dry despite an open structure present in the leaves above. Canadian red cedar grows in a conical shape with branches that overlap regularly, forming an array of overlapping leaves that channel the heavy rainfall away from the base of the tree. 3D printed meshes were designed and printed in accordance with prior work that mimic the overlapping branch structure of *Thuja plicata*; **Figure 100** shows the shape of an individual unit within the 3D printed mesh.[3]

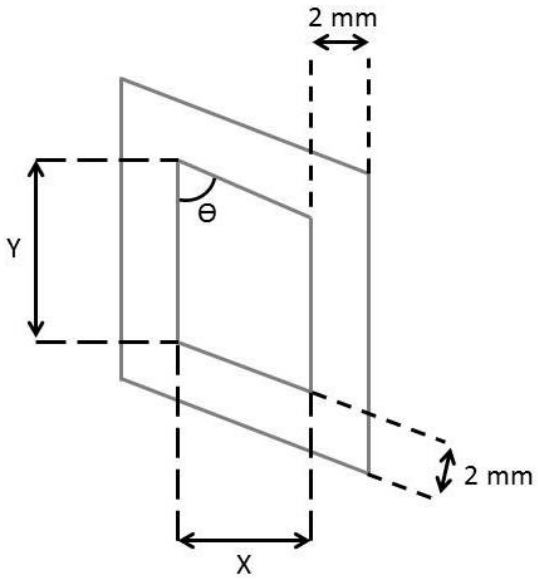

Figure 100: Schematic diagram showing the dimension of an individual unit of the 3D printed mesh. The internal angle, Θ, and internal dimensions, X and Y, can be altered to produce a variety of different mesh shapes. The thickness of the walls are set to 2 mm. This mesh mimics the shape and structure of the leaves of *Thuja plicata*

Utilising a 3D printed mesh based upon the leaf structure of *Thuja plicata* allowed for a novel approach to the mimicking of the plant behaviour in a laboratory environment. It then became possible to measure how the internal angle, mesh orientation, and mesh pore size affected the water collecting behaviour observed.

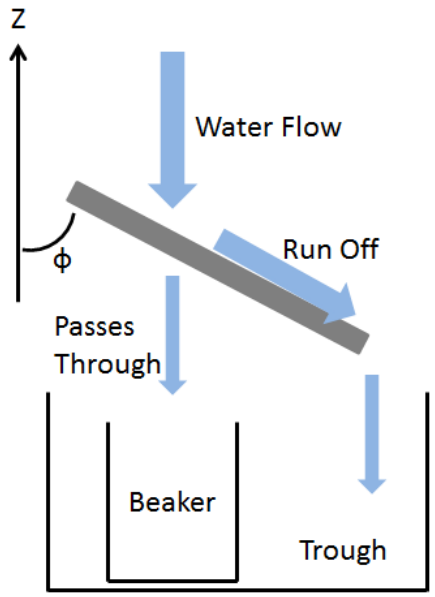

Figure 101: Schematic diagram showing the experimental setup, here, water is directed as the mesh surface using either a sprinkler or burette. The water that passes

through and runs off is measured at a variety of ϕ values and mesh sizes. Double layer, as well as plasma treated single layers were measured[3]

By altering the surface wetting properties of the mesh the water channelling behaviour observed may also be altered. Meshes were 3D printed and underwent plasmachemical surface modification to alter their surface properties using PFAC-6 or air. Static water contact angles were increased from 93° ± 8° to 132° ± 3° in the case of PFAC-6 plasmachemical surface modification, and decreased to 65° ± 5° in the case of air plasmachemical surface modification.

The change increase in static contact angle after treatment with PFAC-6 showed a small change in water collection efficiencies for the single layer mesh (**Table 29**). It was observed that all the water which passed through the mesh occurred at the start of the experiment when contact was initially made with the water stream and the mesh. One or two droplets would bounce off the surface and through the holes in the mesh due to the hydrophobic nature of the mesh surface.

Table 29: Amount of water collected by single mesh, mesh was pre-treated with PFAC-6 make it hydrophobic. Chi = 60°, 4 mm x 4 mm at 45° mesh. Beta = 0°. Static water contact angles as measured were 132° ± 3°

	1	**2**	**3**	**4**	**5**	**6**	**7**	**8**	**9**	**10**
Vol. Dispensed / ml	28.7	28.7	28.7	28.7	28.7	28.7	28.7	28.7	28.7	28.7
Time Taken / s	45.3	46.8	44.7	44.6	46.2	45.2	44.8	44.9	44.4	45.2
Vol. From Trough / ml	24.65	24.5	24.4	23.65	24.3	24.0	24.4	23.3	24.7	24.8
Vol. From Beaker / ml	0.05	0.1	0.05	1.0	0.3	0.6	0.4	1.0	0.1	0.0
Vol. Retained on Surfaces / ml	0.3	0.4	0.55	0.35	0.4	0.4	0.2	0.7	0.2	0.2

A mesh which had a hydrophilic surface also showed negligible difference in water collection efficiencies compared to an untreated mesh, with the water stream running directly off the mesh. No droplets bounced off the surface during initial contact of the water with the mesh, resulting in no water passing through the mesh (**Table 30** and **Table 31**).

Table 30: Amount of water collected by single mesh, mesh underwent plasmachemical surface modification using air to make the surface hydrophilic. Chi = 60°, 4 mm x 4 mm at 45° mesh. Beta = 0°. Static water contact angles as measured were 65° ± 5°

	1	**2**	**3**	**4**	**5**	**6**	**7**	**8**	**9**	**10**
Vol. Dispensed / ml	28.7	28.7	28.7	28.7	28.7	28.7	28.7	28.7	28.7	28.7
Time Taken / s	45.6	45.6	45.8	45.4	44.8	44.4	45.9	44.7	44.9	44.4
Vol. From Trough / ml	28.5	28.6	28.55	28.55	28.6	28.65	28.65	28.6	28.65	28.6
Vol. From Beaker / ml	0	0	0	0	0	0	0	0	0	0
Vol. Retained on Surfaces / ml	0.2	0.1	0.15	0.15	0.1	0.05	0.05	0.1	0.05	0.1

Table 31: Amount of water collected by single mesh, mesh underwent plasmachemical surface modification using air to make the surface hydrophilic. Chi = 60°, 4 mm x 4 mm at 45° mesh. Beta = 0°. Static water contact angles as measured were 65° ± 5°

	1	**2**	**3**	**4**	**5**	**6**	**7**	**8**	**9**	**10**
Vol. Dispensed / ml	28.7	28.7	28.7	28.7	28.7	28.7	28.7	28.7	28.7	28.7
Time Taken / s	48.1	44.8	45.3	45.2	44.7	44.8	45.0	45.2	45.1	45.6
Vol. From Trough / ml	28.5	28.2	28.5	28.2	28.2	28.5	28.5	28.6	78.1	28.4
Vol. From Beaker / ml	0.1	0	0	0	0	0	0	0	0.2	0.4
Vol. Retained on Surfaces / ml	0.1	0.5	0.2	0.5	0.5	0.2	0.2	0.1	0.4	0.2

In the case of a single layer mesh, using a single water stream that impacts the mesh is not an accurate representation of rain, nor is it an accurate representation of the overlapping branch structure of *Thuja plicata*. By replacing the single layer mesh and using a double layer mesh, as well as a water stream that more accurately mimics rain, a more accurate representation of the behaviour of *Thuja plicata* as well as more practical applications of water collection can be applied. It was found that larger holes significantly reduce the water capture ability of the double layer~~k~~ meshes (**Table 32**–**Table 35**).

Table 32: Amount of water collected layered mesh consisting of two layers, Chi = 70°, 3 mm mesh spacing, 9 mm x 9 mm at 45° mesh. Beta = 0°

	1	2	3	4	5	6	7	8	9	10
Vol. Dispensed / ml	20.0	20.0	21.0	20.0	19.0	21.0	17.5	20.0	21.0	20.0
Time Taken / s	6.4	7.1	7.4	7.6	7.4	8.1	7.5	7.6	7.0	7.4
Vol. From Trough / ml	16.0	11.5	19.0	19.0	16.5	18.5	13.0	5.0	9.5	13.0
Vol. From Beaker / ml	3.5	8.0	0.5	0.5	0.5	1.5	2.0	13.0	10.5	5.5
Vol. Retained on Surfaces / ml	0.5	0.5	1.5	0.5	2.0	1.0	2.5	2.0	1.0	1.5

As the dimensions of the internal holes increased, so too did the amount of water which passed through the mesh, as shown by the increased amount collected in the beaker.

Table 33: Amount of water collected layered mesh consisting of two layers, Chi = 70°, 3 mm mesh spacing, 12 mm x 12 mm at 45° mesh. Beta = 0°

	1	2	3	4	5	6	7	8	9	10
Vol. Dispensed / ml	20.0	20.0	20.0	20.0	21.0	21.0	20.0	20.0	20.0	21.0
Time Taken / s	6.9	7.3	7.5	7.6	7.0	7.2	7.0	7.4	6.7	6.9
Vol. From Trough / ml	6.5	10.5	8.0	6.5	6.5	11.0	7.0	10.5	12.5	12.0
Vol. From Beaker / ml	12.5	9.0	11.5	12.5	13.5	9.0	12.5	9.0	7.0	8.0
Vol. Retained on Surfaces / ml	1.0	0.5	0.5	1.0	1.0	1.0	0.5	0.5	0.5	1.0

The 12 mm x 12 mm mesh has sufficiently large holes that the majority of the water is collected in the beaker, rather than running off the mesh and into the trough. With so little mesh material present, most water passes cleanly through the double mesh layer without making any contact with the mesh.

Table 34: Amount of water collected layered mesh consisting of two layers, Chi = 70°, 3 mm mesh spacing, 17 mm x 17 mm at 45° mesh. Beta = 0°

	1	2	3	4	5	6	7	8	9	10
Vol. Dispensed / ml	21.0	21.0	21.0	21.0	21.0	20.0	21.0	20.0	20.0	21.0
Time Taken / s	7.0	6.6	7.3	6.5	7.8	7.3	7.0	7.3	7.6	7.3
Vol. From Trough / ml	5.0	6.5	6.0	6.0	7.5	10.0	9.5	8.0	5.0	8.0
Vol. From Beaker / ml	15.5	14.0	14.5	14.5	12.5	9.5	11.0	11.5	14.5	12.5
Vol. Retained on Surfaces / ml	0.5	0.5	0.5	0.5	1.0	0.5	0.5	0.5	0.5	0.5

Table 35: Amount of water collected layered mesh consisting of two layers, Chi = 70°, 3 mm mesh spacing, 28 mm x 28 mm at 45° mesh. Beta = 0°

	1	2	3	4	5	6	7	8	9	10
Vol. Dispensed / ml	20.0	21.0	20.0	20.0	20.0	20.0	21.0	21.0	21.0	20.0
Time Taken / s	7.3	7.3	7.2	7.4	7.3	6.3	6.9	7.2	7.3	6.4
Vol. From Trough / ml	1.0	1.0	2.0	4.5	3.5	1.5	0.0	5.0	5.5	4.5
Vol. From Beaker / ml	18.5	14.5	17.5	14.5	15.5	18.0	15.5	16.5	14.5	14.5
Vol. Retained on Surfaces / ml	0.5	0.5	0.5	1.0	1.0	0.5	0.5	0.5	1.0	1.0

3D printed meshes which mimic the surface structure of the overlapping branches of *Thuja plicata* as described in prior art have been successfully designed and produced. Both single layer and double layer meshes were created and tested with the orientation and size of the mesh holes proving extremely important in determining the water collection efficiency of the mesh, whilst the surface chemistry shows to have a negligible effect.[3] This is particularly useful for creating surfaces that may show dual properties, for example fog collecting nets which also channel water, by making the surface hydrophobic, it would cause a reduction in the fog collection efficiency. Therefore the channelling of water off the mesh being independent of surface chemistry is advantageous for such a dual purpose device.

3D printing has proven a useful technique for creating surfaces which mimic leaves as had been demonstrated in the case of *Thuja plicata*. In this case the macro

scale structure of the leaf surface is replicated and the water channelling properties displayed also successfully replicated. It has also been shown that plasma treatment can alter the surface chemistry alowing hydrophilicity/hydrophobicity to be imparted onto the 3D printed surface making this technique very useful for replicating a variety of plant surfaces. The ability to alter the surface chemistry of the 3D printed material is also useful for potential future applications in fog collecting devices. The next stage is to use this technique to replicate the surface nanostructure present on leaf surfaces for 3D printing.

7.4 3D Printed Leaf Surface

A relatively new technique which could be used to replicate plant surfaces is 3D printing, which has previously been used to replicate other biological surfaces such as shark skin.[4] A major advantage of the technique is that fabrication of the surfaces is cheap and quick, as well as scaleable. Which overcomes some limitations of the nanoimprinting process described previously in this thesis. This technique may also prove useful in the fabrication of fog collection nets and surfaces in countries where heavy machinery is otherwise inaccesable. Samples of *Phyllostachys aurea* were placed in an X-ray scanner in order to generate a 3D representation of the leaf surface (**Figure 102**).

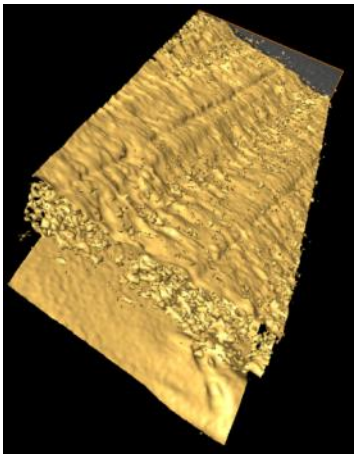

Figure 102: Image showing a small section of a leaf of *Phyllostachy aurea*. Image shown is looking at the adaxial surface of the leaf

The 3D representation of the surface can then be further reduced to a small sub section, this is done in order to reduce the computing power needed to analyse

the surface. The smaller surface is then further processed using NetFabb software to generate a suitable surface that can be 3D printed. Samples were then printed using an Objet Eden 500V 3D printer, at a range of scales. It was found that due to the resolution limits of the 3D printer, a surface which was the same scale and size as the original file could not be printed. The surface microfeatures present in the computer generated file were smaller than the minimum resolution present on the printer, which is an inherent limitation of this technique. By printing the surface at 20–30 times larger, an accurate replica of the surface can be printed. Currently 3D printing remains inaccesible to create exact replicas of the leaf surface as the technology is insufficient to provide the required resolution.

7.5 Laser Cut Meshes

Since the major limitation of the 3D printed leaf surface was the lack of resolution available in current technology additional applications were sought, with one such application could be to combine 3D printing with fog collection. By combining the shape of the 3D printed mesh with samples previously discussed (**Chapter 3**) samples could allow a dual purpose surface to be created; a surface which can collect and channel fog, as well as collect and channel rainwater. This is particularly useful since altering the surface chemistry of the 3D printed meshes showed a negligible effect on the water channelling ability. A 2D replica of the mesh shape was generated in Solidworks and used to laser cut a pattern into a variety of materials (Figure 103). These meshes were subsequently exposed to fog in order to test their fog collection efficiency.

Figure 103: An example of the laser cut mesh. Mesh is 30 x 30 mm and made from non-woven polypropylene sheet material described previously

7.5.1 Non-woven Polypropylene Sheet (Avoco)

A total of three different meshes were laser cut and 30 mm x 30 mm samples cut from them. The mesh was then exposed to fog and showed a steady increase in the amoount of fog collected, with all three samples collecting similar total amounts.

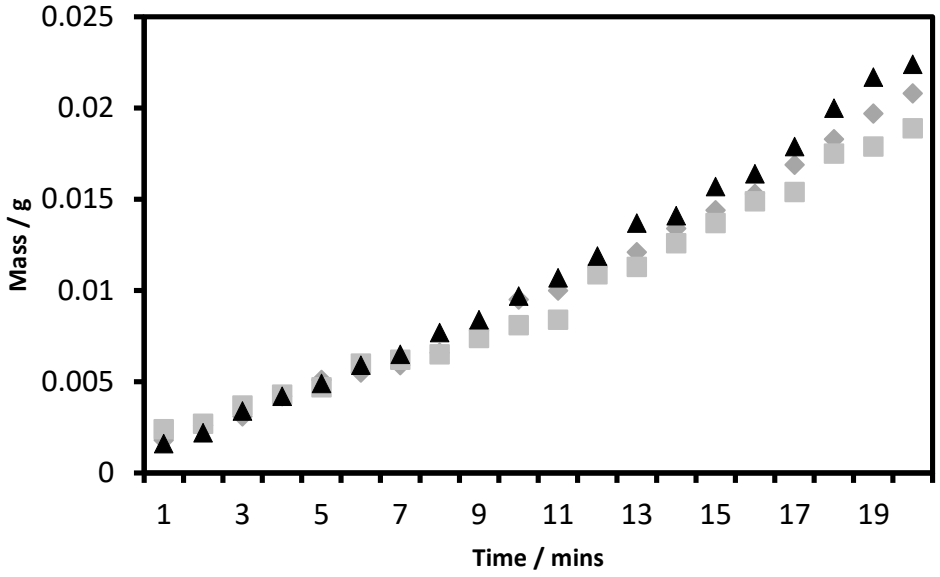

Figure 104: Fog collection measurements on the non-woven polypropylene sheet which has been laser cut to create the same pattern as the 3D printed meshes

7.5.2 Non-woven Polypropylene Mask

The same pattern of behaviour was observed for the non-woven polypropylene mask, with all three samples collecting very similar total masses of water and showing a clear linear increase over time.

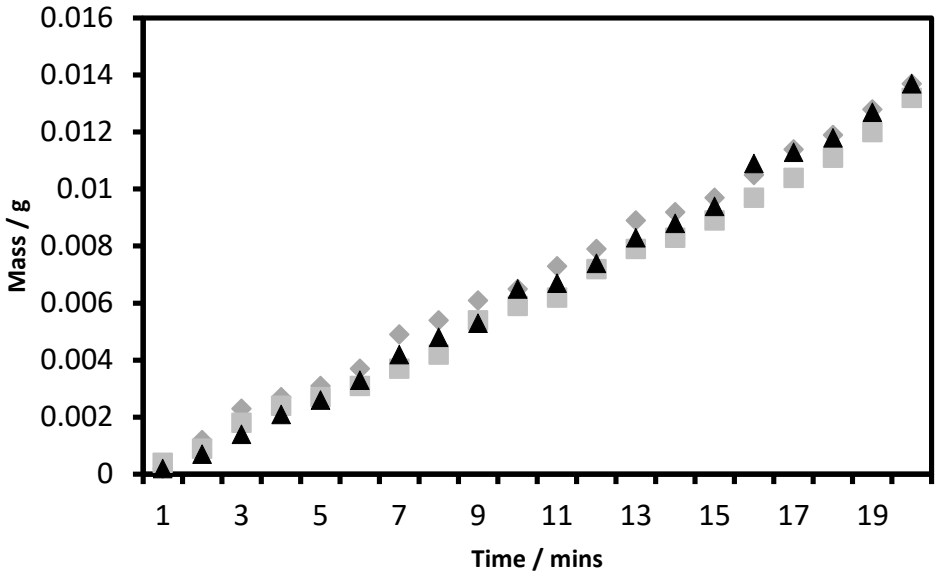

Figure 105: Fog collection measurements on the non-woven polypropylene mask which has been laser cut to create the same pattern as the 3D printed meshes

7.5.3 SP80 Grade

SP80 grade sandpaper also showed a steady linear increase across samples, with the total mass of water collected at the end of the experiment being very similar in value.

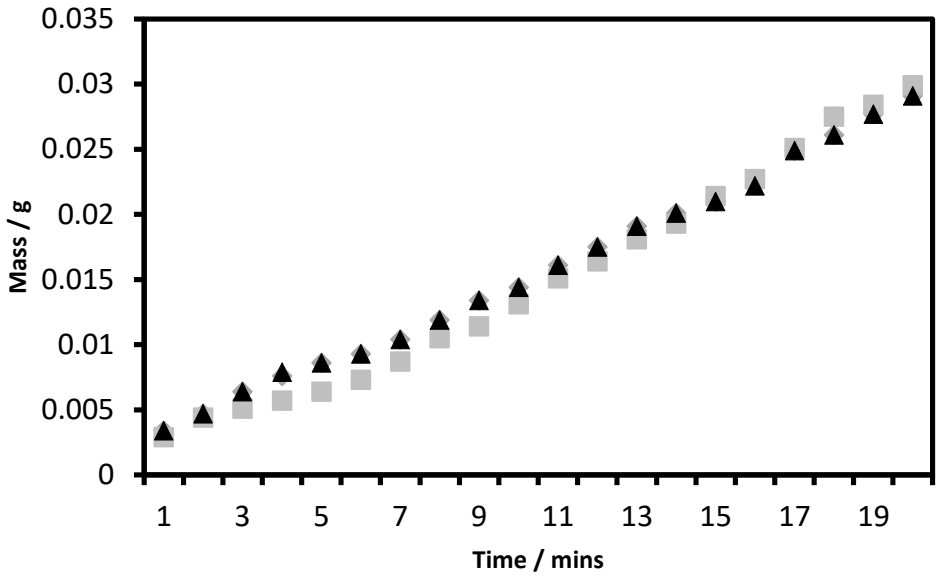

Figure 106: Fog collection measurements on the SP80 grade sandpaper which has been laser cut to create the same pattern as the 3D printed meshes

7.5.4 SP180 Grade

As with the SP80 grade sandpaper, the SP180 showed a similar pattern of behaviour, with all three samples collecting very similar amounts and at a similar rate. The total mass of water collected was also significantly higher than that of the SP80 grade sandpaper.

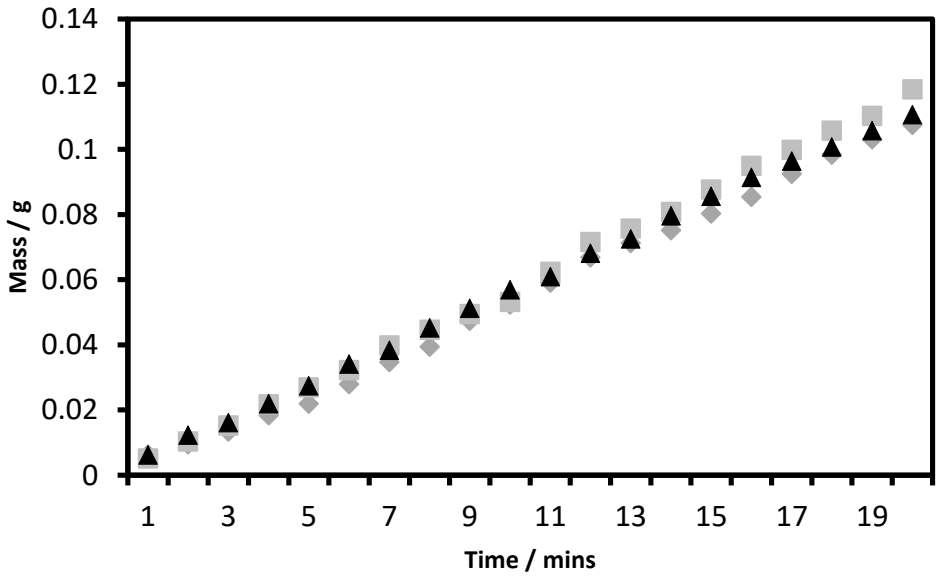

Figure 107: Fog collection measurements on the SP180 grade sandpaper which has been laser cut to create the same pattern as the 3D printed meshes

7.5.5 SP600 Grade

SP600 grade sandpaper showed similar behavior to the previous samples, however one sample showed a slight increase in water collection relative to the other two samples, although the total amount collected is broadly similar across all samples.

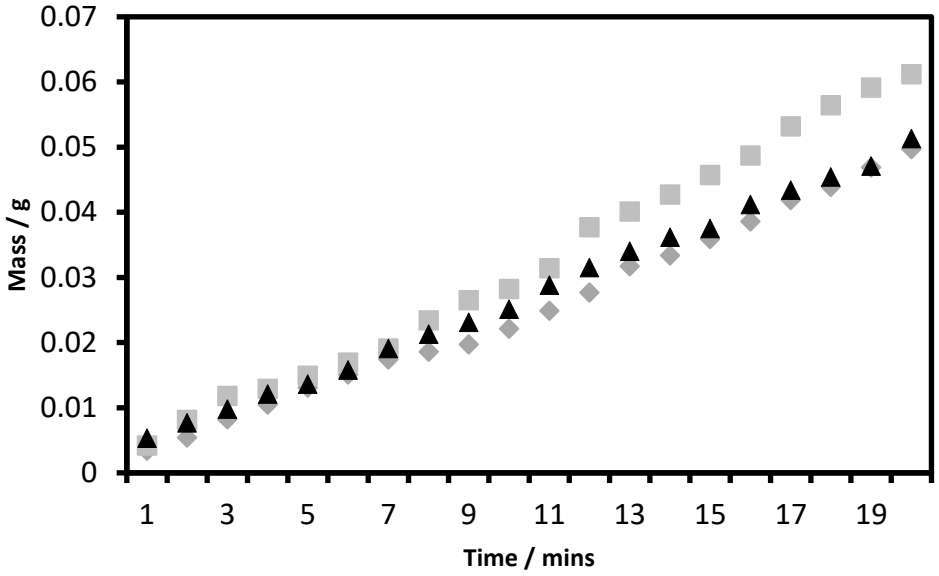

Figure 108: Fog collection measurements on the SP600 grade sandpaper which has been laser cut to create the same pattern as the 3D printed meshes

7.5.6 SP1200 Grade

SP1200 grade sandpaper showed similar behaviour to that of SP600, with one sample collecting slightly more at the end of the experiment relative to the other two samples. They do however all show similar rate of collection and broadly similar total masses collected.

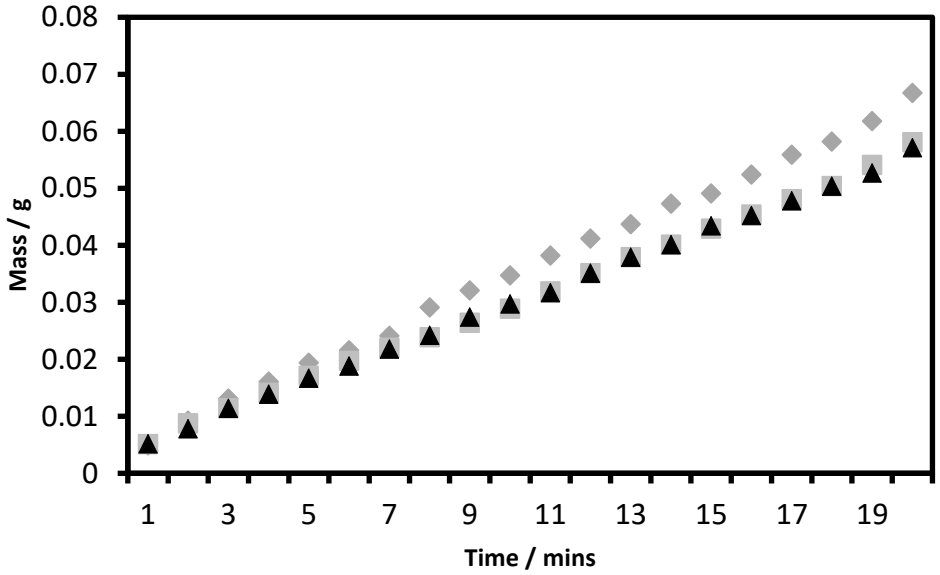

Figure 109: Fog collection measurements on the SP1200 grade sandpaper which has been laser cut to create the same pattern as the 3D printed meshes

7.5.7 Comparison with Uncut Meshes

When comparing the samples prior and post laser cutting, all samples apart from the non-woven polypropylene mask show improvement in the amount of water collected (**Figure 110**). Since the majority of the samples take the form of a solid surface, when the fog stream impacts the surface it rebounds off in all directions. This serves to reduce the flow rate of the fog stream at the surface and therefore the amount of water collected. By laser cutting holes into the surface, the fog stream can flow more easily through the sample which increases the flow rate.[5,6] However, one important aspect to note is that by cutting in the surface, the surface area of the sample decreases, if the holes are made too large, a decrease in collection efficiency will be observed. Therefore a balance between increasing the flow rate across the sample and decreasing the samples surface area needs to be achieved. This likely explains

why one sample showed a decrease in the amount of fog collected. The non-woven polypropylene mask sample, with its fibrous surface did not reduce the flow rate present at the surface as effectively as the other samples, experimentally it was observed that some of the fog stream passed through the sample. The lower amount of mass collected is likely due to the reduced surface area present after laser cutting, which contributes more than the increase in flow rate.

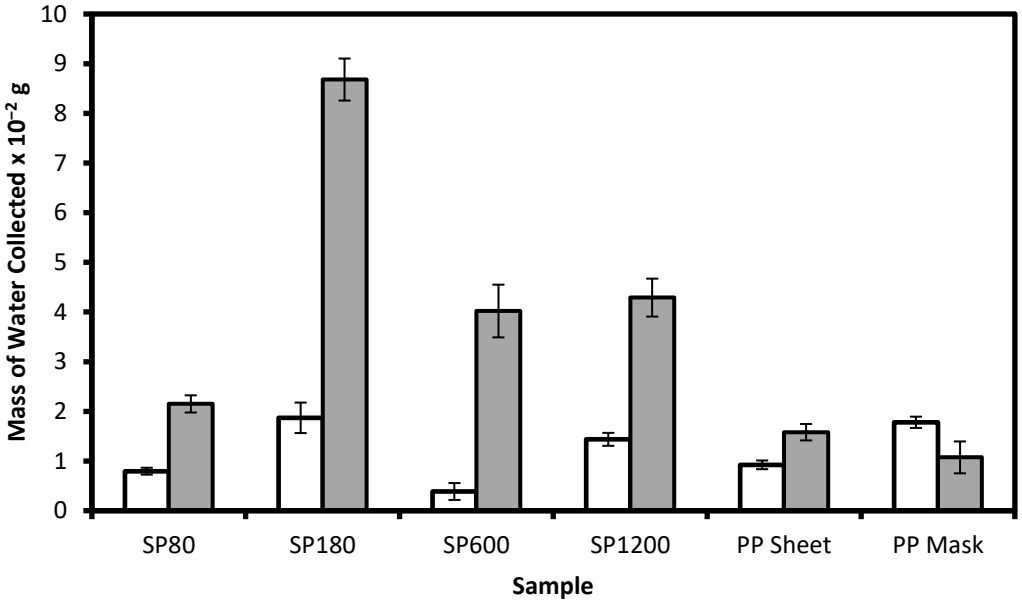

Figure 110: Comparison of the total amount of water collected between 5–20 mins for a range of samples. Grey bars indicate samples after laser cutting, white bars prior to laser cutting. Standard deviations are shown

The largest observed improvement is for the SP180 sandpaper, which shows a significantly improved water collection relative to pre laser cutting. All sandpaper samples showed an increase in the amount of water collected after laser cutting, likely due to the increased flow rate present at the surface. The sandpaper samples had the best structural integrity of all samples and showed the largest amount of deflection of the fog stream (as observed experimentally). There was some charring around the edges of the laser cut holes present on the sandpaper samples, however the amount of charred area was small compared to the overall mesh surface and unlikely to account for the differences seen.

7.6 Conclusion

The use of 3D printing provides a useful replication technique for surfaces which mimic the wetting behaviour of plants. In this case the successful mimicking of the wetting behaviour of the overlapping branches of *Thuja plicata* was achieved by 3D printing meshes based upon the macro structure of the leaves. These meshes were tested for their water channelling ability using both single and dual layer meshes, with the latter showing excellent water channelling properties when exposed to simulated rainfall. Efficient removal of water from a surface, as displayed by the leaves of *Thuja plicata*, would be a useful property for fog collecting devices as it has been shown to increase their fog collection efficiency. By incorporating the materials previously tested for fog collection with the shape and function of the *Thuja plicata* meshes could therefore provide a useful, dual purpose, fog/water collection device. The inclusion of the mesh design via laser cutting showed enhancement of the fog collection ability of the samples tested for all but one sample. The increased flow rate present at the surface, due to the holes laser cut into the surface, serving to increase the fog collection efficiency of the sample

Similar 3D printing techniques were then also applied to directly copy the surface features present on a leaf surface on both a macro and nano scale. Whilst the analysis of the surface, as well as computer processing of the resulting data was successful, 3D printing technology proved a limiting factor in creating replica surfaces. However, it should be noted that should the technology improve sufficiently, these surfaces can easily be fabricated using this new and novel application of 3D printing.

7.7 Reference

[1] Rengier, F.; Mehndiratta, A.; von Tengg-Kobligk, H.; Zechmann, C. M.; Unterhinninghofen, R.; Kauczor, H.-U.; Giesel, F. L. 3D Printing Based on Imaging Data: Review of Medical Applications. *International Journal of Computer Assissted Radiology and Surgery* **2010**, *5*, 335–341.

[2] Gross, B. C.; Erkal, J. L.; Lockwood, S. Y.; Chen, C.; Spence, D. M. Evaluation of 3D Printing and its Potential Impact on Biotechnology and the Chemical Sciences. *Anal. Chem.* **2014**, *86(7)*, 3240–3253.

[3] von Spreckelsen, R. M.; Harris, M. T.; Wigzell, J. M.; Fraser, R. C.; Carletto, A.; Mosquin, D. P. K.; Justice, D.; Badyal, J. P. S. Bioinspired Breathable Architecture for Water Harvesting. *Sci. Rep.* **2015**, *5*, 16798.

[4] Wen, L.; Weaver, J. C.; Lauder, G. V. Biomimetic Shark Skin: Design, Fabrication and Hydrodynamic Function. *J. Exp. Biol.* **2014**, *217*, 1656–1666.

[5] Park, K-Y.; Chhatre, S. S.; Srinivasan, S.; Cohen, R. E.; McKinley, G. H. Optimal Design of Permeable Fiber Network Structures for Fog Harvesting. *Langmuir*, **2013**, *29 (43)*, 13269–13277.

[6] Schemenauer, R. S.; Joe, P. I. The Collection Efficiency of a Massive Fog Collector. *Atmospheric Research* **1989**, *24*, 53–69.

Chapter 8: Conclusions and Future Work

A combination of surface roughness and surface chemistry govern the wettability of plant surfaces, to produce a range of effects that often have biological advantages. The combination of hierarchical surface roughness and aliphatic surface chemistry often produces plants which display superhydrophobicity, whilst fine micro hairs present on the surface of others produce surfaces capable of collecting water from atmospheric fog. These plants provide a useful template for the development of surfaces which display these properties and often inspire useful applications such as self-cleaning surfaces, water resistant electronics (such as mobile phones) and anti biofouling devices provided they can be successfully replicated. There are a variety of techniques such as SEM and ToF-SIMS that can be used to analyse plant surface structure and chemistry and distinguish between differing surfaces of the same leaf species. These coupled with a variety of replication techniques, such as moulding and plasmachemical surface modification, enable the successful biomimicking of these kinds of surfaces.

In this work, the leaves of *Xanthosoma sagittifolium* were found to display a unique capture and release type mechanism with water droplets remaining pinned to surface veins before reaching critical mass and rolling off the leaf surface. This serves to efficiently remove surface water as well as surface contaminants which may be present. It was found that the leaves displayed hierarchical roughness with macro (plant cells) and nano (surface waxes) features. The macro structure varied between the main body of the leaf, margin/lamina, and the central vein region, the midrib. The structure also showed some variation within the margin/lamina region due to the prescence of smaller surface veins which run across the entirity of the leaf surface. The vein regions present displayed underlying cell structure of a different shape, oblong, compared to the more spherical shape found in other parts of the leaf, whilst the surface waxes between all regions showed similar structures. This surface structure remained the same between young and mature leaves.

ToF-SIMS was carried out on the surface of a young leaf to analyse the surface waxes which also indicated that there were differences in the relative intensities of several compounds (likely carboxylic acids) present on the surface of the margin/lamina and midrib regions. This difference, coupled with the difference

in surface macro structure helps to explain the difference in wettability, particularly in contact angle hysteresis observed. Surfaces which mimick this behaviour were successfully replicated using a nanoimprinting process which yielded surfaces with comparble surface roughness and chemistry, with those treated with PFAC-6 showing best results in terms of contact angle and contact angle hysteresis. These techniques were also employed to aid in the understanding and replication of the wetting mechanisms for other plants, such as *Eremopyrum orientale* which resulted in a publication. This work provides useful demonstration and application of replication techniques that have been applied to plant surfaces, as well as further highlighting the usefulness of ToF-SIMS in the analysis of surface waxes. Combining scanning electron microscopy and ToF-SIMS as described, as well as the nanoimprinting process should provide a useful framework for future work analysing and replicating other, unique plant surfaces.

Also investigated was the implementation of a new, novel technique, to aid in the analysis of plant surface waxes using ToF-SIMS. By mechanically removing the plant waxes using a moulding process, it becomes possible to analyse surface waxes of plants without the need to transport samples immediately to the mass spectrometer, which is particularly useful if plant specimens cannot be easily obtained. It also makes possible the analysis of plants found in developing countries that otherwise wouldn't have easy access to ToF-SIMS. The use of the moulding process proved to be an effective way to measure the prescence of surface waxes and showed excellent correlation with previously published work for the leaves of *Phyllostachys aurea* showing the same compounds present on the surface. This novel technique will prove useful in future work studying the surface chemistry of plants in developing countries that lack access to the necessary equipment as well as those plants located in isolated geographical locations. This combined with the successful, and novel, 3D printing of a leaf sample of *Phyllostachy aurea* could also allow biomimicking surfaces to be cheaply and readily distributed to those regions.

Finally, the development of a new fog collection methodology for use in testing plant surfaces for water harvesting was also achieved, which was subsequently used and validated by testing plant samples, replicas, and inorganic samples for their fog collection efficiency. The technique was used to test the fog collection ability of a variety of meshes based on the overlapping branch structure of *Thuja plicata* from previously published work in an attempt to improve the water

collection efficiency of the material. Envisioned was the creation of a dual purpose device, which can both collect fog and channel surface water simultaneously, which should improve the fog collection efficiency of any devices. The inclusion of the mesh design into the surfaces showed enhancement of the fog collection of all samples barring one, due to increased flow rate of the fog stream through the mesh surface.

Future work in this area will involve additional analytical experimentation to better understand the surface waxes present on leaves of *Xanthosoma sagittifolium*, particularly utilising ToF-SIMS. It is possible to raster the ToF-SIMS analysis across the surface of the sample and resolve individual mass ions which would prove useful in analysing the wax chemistry in the vein/no vein regions previously described. Work would focus on accurately characterising the surface waxes and their spatial resolution using ToF-SIMS as well the inclusion of GC-MS to identify individual compounds. Finally, atomic force microscopy would be used to characterise the surface roughness between the vein and no vein regions. Negative moulds of the surface of *Xanthosoma sagittifolium* would then be created and analysed using the same techniques to further develop the use of the moulding process for ToF-SIMS analysis. Additionally, a 3D scan of a leaf of *Xanthosoma sagittifolium* would be taken in order to create a replica of the surface that could be succesfully 3D printed utilising similar techniques to *Phyllostachys aurea*. This work would serve to completely characterise the surface structure and waxes of *Xanthosoma sagittifolium* and give a greater insight into its wetting properties as well as provide a toolkit for future work on new plant species.

As well as completing the wax characterisation of *Xanthosoma sagittifolium* additional fog experiments on a wider range of surface will be conducted. These include experiments on laser cut inorganic and biological samples which mimic the surface of *Thuja plicata*, as well as additional plant species such as *Verbascum thapsus* which displays unique surface hairs. In particular, work will be undertaken to create large scale replicas of plant surfaces that are suitable for field testing under a variety of fog conditions.

Finally, using the techniques developed in this thesis, multiple different plant species with unique surface wettabilities will be characterised and replicated. These species include *Verbascum thapsus*, *Eriobotrya japonica*, and *Tylecodon singularis*

which all display interesting surface properties that could provide further insight into biomimetic fog collecting devices. *Tylecodon singularis* for example is native to the fog regions of Namibia, with the ultimate goal to create full scale fog collecting devices that are commercially viable.

Throughout this thesis, it has been demonstrated that multiple plant surfaces, such as *Xanthosoma sagittifolium* and *Eremopyrum orientale*, can be successfully analysed and replicated to mimic the surface properties of their parent plant both structurally and chemically. New wetting mechanisms, capture and release, as well as new analytical, ToF-SIMS, and replication, 3D printing, techniques were also developed to produce the surfaces for several different plants. This work resulted in multiple collaborative publications and provides a useful reference point for future analysis of new plant species.

Appendix

Figure No.	Source
1	wikimedia commons
2	Power Point 1
3	Power Point 1
4	Power Point 1
5	Power Point 1
6	Power Point 1
7	Power Point 1
8	Power Point 1
9	N/A
10	N/A
11	N/A
12	N/A
13	N/A
14	N/A
15	N/A
16	wikimedia commons
17	Power Point 1
18	Power Point 1
19	Power Point 1
20	Power Point 1
21	N/A
22	Power Point 1
23	Folder 1
24	Folder 1
25	Excel 1
26	Folder 2
27	Folder 2
28	Folder 2
29	Folder 2
30	Folder 2
31	Folder 2
32	Folder 2
33	Folder 2
34	N/A
35	Folder 3
36	N/A
37	Excel 4
38	N/A
39	N/A
40	N/A
41	N/A

42	N/A
43	Folder 5
44	Folder 5
45	Folder 5
46	Folder 5
47	Folder 5
48	Folder 5
49	Folder 6
50	Folder 6
51	Folder 6
52	Folder 6
53	Folder 6
54	Folder 6
55	Folder 6
56	Folder 6
57	Excel 5
58	Excel 5
59	Excel 5
60	Excel 5
61	Excel 5
62	Folder 4
63	Excel 5
64	Folder 4
65	Excel 5
66	N/A
67	Excel 6
68	Excel 6
69	Excel 6
70	Excel 6
71	Excel 6
72	Excel 6
73	Excel 6
74	Excel 6
75	Excel 6
76	Excel 7
77	Excel 7
78	Excel 7
79	Excel 7
80	Excel 7
81	Excel 7
82	Excel 7
83	Excel 7
84	Excel 8
88	Power Point 2

86	Excel 8
87	Excel 8
88	Excel 8
89	Excel 8
90	Excel 8
91	Excel 8
92	Excel 8
93	Excel 8
94	Excel 8
95	Excel 8
96	Excel 8
97	Excel 8
98	Excel 8
99	Excel 8
100	N/A
101	N/A
102	N/A
103	N/A
104	Excel 10
105	Excel 10
106	Excel 10
107	Excel 10
108	Excel 10
109	Excel 10
110	Excel 10

Supplementary S 1: Data archive for figures where applicable

Table No.	Source
1	N/A
2	N/A
3	N/A
4	Excel 1
5	Excel 1
6	Excel 1
7	Excel 1
8	N/A
9	Excel 2
10	N/A
11	N/A
12	Excel 3
13	Excel 3
14	Excel 3
15	Excel 3
16	Excel 3

17	Excel 3
18	Excel 4
19	Excel 4
20	Excel 4
21	Excel 4
22	N/A
23	N/A
24	Folder 5
25	Folder 5
26	Folder 5
27	Folder 5
28	N/A
29	N/A
30	N/A
31	Excel 9
32	Excel 9
33	Excel 9
34	Excel 9
35	Excel 9
36	Excel 9
37	Excel 9

Supplementary S 2: Data archive for tables where applicable.